People's Democratic Republic of Algeria

Ministry of Heigher Education and Scientific Research

University of Kasdi Merbah Ouargla

Faculty of Mathematics and Material Sciences

Department of Physics

Order No :

Serial No :

THESIS

To obtained the diploma of :

3rd cycle DOCTORATE

Sector : Physics

Option : Physics of materials

Presented by :

Fatma ZERIBI

Entitled

Elaboration and characterization of titanium dioxide thin films by Sol-Gel (spin - coating) process for photovoltaic applications

Discussed publicly on : 27/05/2023

Before the jury composed of :

Pr. Fethi KHELFAOUI	Kasdi Merbah University - Ouargla	President
Pr. Ismail CHIHI	Kasdi Merbah University - Ouargla	Examiner
Pr. Rachid GHERIANI	Kasdi Merbah University - Ouargla	Examiner
Pr. Hanane SAIDI	Mohamed Khider University - Biskra	Examiner
Pr. Abdallah ATTAF	Mohamed Khider University - Biskra	Supervisor
Pr. Lazhar BENMEBROUK	Kasdi Merbah University - Ouargla	Co-Supervisor

Academic year :2022/2023


بسم الله الرحمن الرحيم

Dedication

To the person who taught me giving without reward. To the person that I ask God to protect her and to make her see the picking of fruits after long waitness and my words with stay as stars to be followed to day, tomorrow, and forever.

To the person whom here douàa is my success'd secret and her tenderness is my hurts treatment, To my dearest person to my heart.

To my mother : ZERIBI LAATRA

To all persons I grew up with then, and I rely on them, to those I know well the life's meaning and to those I spent my childhood, to my dear brothers and my dear sisters.

And I thank so much to all my family's children of my family.

To my sisters who were not given birth by my mother, to those who were scincere, to those who share with me my happiness and my sadnese, to those who were with me upon the success is street, To all my dear friends.

To those who help us, and provide us with facilitese, ideas and informations, I thank them suicerly especially.

At last, the special thank is addressed to those who did not help us and stood as an obstacle againts our modest research. Without their existence, no sense and no taste to our research.

Acknowledgements

Firstly, I thank **GOD** the whole powerful for having agreed his infinite kindness, courage, the force and patience to complete this modest work.

I wish to make a point of profoundly thanking to my supervisor **Prof. Attaf Abdallah**, dean of Faculty of Exact Sciences and Sciences of Nature and Life in Mohamed Khider University of Biskra, for his acceptance to take charge of my work and suggesting the thesis statement and his help, support, guidance throughout the course of this work.

After that, I make a point of profoundly thanking to my Co-supervisor **Prof. Benmebrouk Lazhar,** Professor at the Faculty of Mathematics and Matter Sciences in Kasdi Merbah University of Ouargla, for his help, support, guidance and encouragement. He has been a great support on all fronts and made my Doctorate thesis journey a memorable experience.

I address my sincere thanks to **Prof. Khelfaoui Fethi** Professor at the Faculty of Mathematics and Matter Sciences in Kasdi Merbah University of Ouargla for the honor that makes to me by accepting the presidency of this jury.

I owe my heartful thanks to **Prof. Chihi Ismail** Professor at the Faculty of Mathematics and Matter Sciences in Kasdi Merbah University of Ouargla, who showed great interest in my research work and accepted to belong to the jury and to examine my work.

I am grateful to **Prof. Gheriani Rachid** Professor at the Faculty of Mathematics and Matter Sciences in Kasdi Merbah University of Ouargla, who agreed to accept to belong to the jury and to examine my work.

I am also thankful to **Prof. Saidi Hanane** professor at the department of sciences of matter at faculty of exact sciences and sciences of nature and life in University Mohamed Khider of Biskra, who agreed to accept to belong to the jury and to examine my work .

I would also like to acknowledge **Prof. Aida Mohamed Salah, Dr. Derbali Ammar** and **Prof. Tibermacine Toufik** for his generous help in the experimental phase.

I would like to thank all people at the Laboratory of thin films and (**LPCMA**) applications, of the University Mohamed Khider-Biskra. Who helped me to carry out structural and optical characterizations.

I would also like to thank all people at the laboratory of the Radiation and Plasmas and Surface Physics **(LRPPS)**, of the university Kasdi Merbah for all their facilities and assistance.

Finally, I wish to address my thanks to all the teachers and students of the department of sciences of matter especially the teachers of physics and the members of thin films laboratory of our university every one by his name.

FATMA ZERIBI

Abstract

Elaboration and characterization of titanium dioxide thin films by Sol-Gel (spin - coating) process for photovoltaic applications.

Titanium oxide thin films have been deposited on glass substrates by sol-gel spin coating method using titanium tetra-isopropoxide (TTIP), absolute methanol and acetylacetone as precursor solution, solvent and catalyzer, respectively. The effect of the number of layers, the mixed solvent's percentage of ethanol and methanol, the drying temperature, the stirring (mixing) time, lanthanum (La) doping and manganes (Mn) doping on the structural, optical and electrical properties of TiO_2 films, these films were annealed at 500 °C.

All films have been characterized by multiple techniques such as X-ray diffraction (XRD), UV-Visible spectroscopy, Fourier transform infrared (FTIR) spectroscopy and four probe method to investigate the physical properties of titanium dioxide films. X-ray diffraction analysis showed that the films are polycrystalline in nature having tetragonal structure of anatase phase with preferred growth orientation along (101) plane. The transmittance of TiO_2 films was high up to 90 % and it is probably related to the good crystalline quality of the films. The band gap was varied between 3.37 and 3.75 eV. Furthermore, the electrical measurements revealed that prepared TiO_2 films at different drying temperatures have a low resistivity (about $11.10 \times 10^2 - 1.22 \times 10^2$ (Ω.cm)) which made these films suitable for photovoltaic and optoelectronic applications.

Keywords: Thin films, Titanium oxide, Sol-Gel, spin coating technique, Doping, Structural properties, Optical properties, Electrical properties**.** Photovoltaic applications.

Résumé

Elaboration et caractérisation des couches minces d'oxyde de titane par voie Sol-Gel (spin - coating) en vue d'applications photovoltaïques.

Des films minces de d'oxyde de titane ont été déposés sur des substrats de verre par la trchnique de revêtement par centrifugation sol-gel en utilisant du tétra-isopropoxyde de titane (TTIP), du méthanol absolu et de l'acétylacétone comme solution précurseur, solvant et catalyseur, respectivement. L'effets de la nombres des couches, du pourcentage d'éthanol et de méthanol du solvant mélangé, la température de séchage, le temps d'agitation (mélange), dopage par lanthane (La) et dopage par manganes (Mn) sur les propriétés structurelles, optiques et électriques des films de TiO_2, ces films ont été recuits à 500 °C.

Tous les films ont été caractérisés par de points pour étudier les propriétés physiques des films d'oxyde de titane. L'analyse par diffraction des nombreuses techniques telles que la diffraction des rayons X (DRX), la spectroscopie UV-Visible, la spectroscopie infrarouge à transformée de Fourier (IR-TF) et la méthode de quatre rayons X a montré que les films sont de nature polycristalline et présentent une structure tétragonale de phase anatase avec une orientation de croissance préférée selon le plan (101). La transmittance des couches d'TiO_2 était élevée jusqu'à 90% et elle est probablement liée à la bonne qualité cristalline des films. La bande interdite variait entre 3.37 et 3,75 eV. De plus, les mesures électriques ont révélé que les films de TiO_2 préparés à différentes températures de séchage ont une faible résistivité (environ $11.10 \times 10^2 - 1.22 \times 10^2$ (Ω.cm)) ce qui rend ces films adaptés aux applications photovoltaïques et optoélectroniques.

Mots-clés: Couche mince, Dioxyde de titane, Sol-Gel, Technique de spin coating, Dopage, Propriétés electrique, Propriétés optique, Propriétés électrique, Applications photovoltaïques.

ملخص

تحضير و توصيف الشرائح الرقيقة لأكسيد التيتانيوم بواسطة تقنية الطرد المركزي سائل ـ هلام من أجل التطبيقات الكهروضوئية

تم ترسيب الشرائح الرقيقة لأكسيد التيتانيوم على ركائز زجاجية بواسطة تقنية الطرد المركزي سائل – هلام باستخدام التيتانيوم رباعي الأيزوبروبوكسيد ، الميثانول وأسيتيل الأسيتون كمصدر، مذيب ومثبت على التوالي. وقد تم دراسة تأثير كل من عدد الطبقات ، نسبة المذيب المختلط من الإيثانول و الميثانول، درجة حرارة التجفيف ، وقت تحريك (خلط) المحلول ، التطعيم باستخدام اللونثانم والمنغنيزعلى الخصائص البنيوية ، الضوئية والكهربائية لشرائح أكسيد التيتانيوم الرقيقة ، حيث تم تلدين هذه الأفلام عند 500 درجة مئوية.

تم توصيف كل الشرائح باستعمال عدة طرق مثل انعراج الأشعة السينية ، المطيافية فوق البنفسجية والمرئية، مطيافية الأشعة تحت الحمراء(FTIR) وتقنية المسابير الأربعة. أظهرت تحاليل نتائج إنعراج الأشعة السينية أن الشرائح ذات طبيعة متعددة البلورات ببنية رباعية الشكل وفق الطور أناتاز مع اتجاه مفضل للنمو وفق المستوي (101). إضافة إلى ذلك كانت نفاذية شرائح أكسيد التيتانيوم عالية بحيث وصلت إلى النسبة % 90 وقد يعود ذلك للتبلور الجيد لهذه الشرائح. كما تتراوح قيم فجوة النطاق الممنوع ما بين 3.37- 3.75 إلكترون فولط. علاوة عن ذلك، أظهرت القياسات الكهربائية أن أغشية أكسيد التيتانيوم المحضرة عند درجات حرارة تجفيف مختلفة تملك أقل مقاومية من بين الشرائح المحضرة (تتراوح ما بين 1.22×10^2 - 11.10×10^2 أوم.سم) مما يجعلها صالحة للاستعمال في التطبيقات الكهروضوئية و الإلكتروضوئية.

الكلمات المفتاحية : الشرائح الرقيقة، أكسيد التيتانيوم ، سائل – هلام، تقنية الطرد المركزي، تطعيم،خصائص هيكلية ، خصائص ضوئية، خصائص كهربائية ، التطبيقات الكهروضوئية .

Table of contents

List of Figures

List of Tables

General introduction

General introduction

Solid thin films represent a class of materials that has aroused growing interest both from a fundamental and technological point of view since the beginning of the 1980 s. They can be produced from conductive, insulating, semi-conductive and polymeric materials. The thickness of films deposited on substrates can vary from an atomic plane (a few Angstroms) to several micrometers. Their physical properties are closely related to the deposition parameters. Where, in the last decades, a growing interest paid to thin films of transparent conducting oxides (TCO) which degenerate semiconductors with a large gap ($\geq$ 3eV) [1]. Due to the interest of transparent conductive oxides, many research works is devoted to the study and synthesis different physical and chemical properties of these materials such as In_2O_3, TiO_2, SiO_2, ZnO and Bi_2O_3 etc [2,3]. Titanium dioxide (TiO_2) is one of the most important group II–VI semiconductor materials on the part of both industry and science fields because of its flexible properties that include a high refractive index, a wide band gap (3.2 eV), and high physical and chemical stability and non-toxic nature [4,5]. Furthermore, titanium oxide can be grouped into three crystalline phases: rutile, anatase and brookite [6,7]. The presence of any one or more than one phase in the material can effect on the micro-structural, optical and electrical properties of the material [8]. Among these phases rutile is the most stable phase and it is usually obtained after annealing at temperature above 500 ^oC [9]. While the other two phases are metastable which are difficult to synthesize and are continuously studied [10]. In addition, titanium dioxide has been extensively investigated nano-materials owing to their great potential application in this field: photo-catalysis [11], photonic device and solar cell [12], optical filters, antireflection coatings [13], ferroelectric and gas sensing [14]. In order to obtain enhanced their properties of titanium dioxide (TiO_2), several working have been widely studied the effect of different parameters on the physical properties of TiO_2 thin films have been reported by various method [15,16]. In order to obtain high quality optoelectronic devices based on TiO_2, usually the perfect film thickness is necessary for best device performance. Furthermore, it is highly motivating to study the influence of film thickness on the structural, optical and electrical properties due to the most important decisive of this factor for film physical properties.

Conventional technique can be achieved to the fabrications of titanium dioxide films include, ultrasonic spray pyrolysis [17], radio frequency (RF) magnetron sputtering [18],

chemical vapor deposition (CVD) [19], pulsed laser deposition (PLD) [20] and sol-gel process [21].

The sol-gel method allows the production of a wide variety of oxides in different configurations (monoliths, thin films, fibers, powders). This great diversity, both in materials and in shaping, has made this process very attractive in technological fields such as optics [22] electronics [23], biomaterials [24]. It also has the advantage of using a soft chemistry and being able to lead to very pure and stoichiometric materials [25]. The basic principle of the sol-gel process corresponding to the abbreviation of "solution-gelation" is as follows: a solution based on precursors in the liquid phase is transformed into a solid by a set of chemical reactions of the polymerization type at ambient temperature. Moreover, among of these methods, sol-gel method offers several advantages including simplicity of equipment and ease of implementation of the material, low energy cost, high purity and better homogeneity of the material, and realization of multi-component deposits in a single operation [26].

This thesis contains the following seven chapters:

Chapter I : This chapter is concerned with studying of the transparent conductive oxides (TCO) and presents the definition of it, their properties and applications. In addition, a brief overview of titanium dioxide's structural, optical, and electrical properties is offered, with a focus on its photovoltaic applications.

Chapter II : This is chapter discusses the different techniques used for the deposition of titanium oxide (TiO_2) thin films. And in particular, the technique of Sol-Gel (spin coating). This chapter also discusses the analysis techniques used in the characterization of the samples, which characterized using X-ray diffractometer (XRD), spectroscopy and fourier transform infrared spectroscopy (FTIR). On the other hand, for the study of the optical properties, UV-VIS spectroscopy was used and the four-point technique for the study of the electrical properties. Furthermore, the study of different relationship of calculation of the deposit's characteristics (crystallite size, Strain, dislocation density, stress, conductivity and optical gap...etc.).

Chapter III **:** Deals with the preparation and characterization of titanium oxide (TiO_2) films deposited by sol - gel (spin coating) method on glass substrates with different number of spin-coated layers. In addition, this is chapter devoted to studied the influence of the mixed

solvent's (ethanol + methaol) ratios on the crystalline structure, optical, and electrical properties of TiO_2 thin films

Chapter IV : The influence of drying temperature and stirring time on the properties structural, optical and electrical of prepared titanim dioxide thin films by sol-gel (spin coating) technique was investigated.

Chapter V : Gives an account of lanthanum and manganese doped titanium dioxide (TiO_2) films prepared by sol-gel (spin coating) on glass substrates at equal to 500 °C with different mol.% of La and Mn doping. The films were prepared in well conditions.

The thesis objective :

The main objective of this thesis work is the synthesis and the study of the structural, optical and electrical properties of TiO_2 thin films and to optimize the growth conditions of TiO2 thin films for photovoltaic applications (front electrodes for solar cells, photocatalysis, gas sensors…etc.), which are grown on glass substrates and cost effective technique's use which is Sol-Gel spin-coating process.

General introduction's references

[1] Z.-F. Bi, L. Wang, X.-H. Liu, S.-M. Zhang, M.-M. Dong, Q.-Z. Zhao, X.-L. Wu, and K.-M. Wang, "Optical wave guides in TiO_2 formed by He ion implantation." Opt. Express, 20, 6712 (2021).

[2] A. Sanchez-Juarez, A. Tiburcio-Silver, and A. Ortiz, "Properties of fluorine-doped ZnO deposited onto glass by spray pyrolysis." Sol. Energy Mater. Sol. Cells, 52, 301 (1998).

[3] W.-J. Wu, W.-L. He, H.-Y. Yu, H.-X. Huang, and M. Chen, "Synthesis and photopsyhical properties of pyerene-functionalized nano-SiO_2 hybrids in solutions and doped-PMMA thin films." Material Chemistry and Physics, 186 (2017).

[4] A. J. Haider, R. H AL-Anbari, G. R Kadhim, and C. T Salame, "Exploring potential environmental applications of TiO_2 nanoparticles." Energy Procedia, 119, 332 (2017).

[5] Y. Venkatesh, R. S. Dubey, and K. Brijesh, "Morphological and optical properties of dielectric multilayer structures prepared with distinct precursor concentrations." Nanosystems: Physics, Chemistry, Mathematics, 10, 355 (2019).

[6] Dorian A, Hanaor H, Sorrell Charles C. Revew of the anatase to rutile p transformation. J. Mater Sci, 2011; 46:855-47.

[7] Beltran A, Gracia L, Andres J. Density functional theory stdy of the brookite surfaces phase transition between natural titania polymorphs, J. Phys Chem, B 2006; 110 :23417

[8] Wang Liqin, Fu Xiujun, Han Yang, Chang E, Wu Haitao, Wang Haiying, Li Kuiying, Xiaowen Q. Preparation, characterization, and phtocatalytic activity of TiO_2/ZnO nanocomposites. J. Nanomater, 2013:1-6.

[9] Kajitvichyanukul P, Ananpattarachai J, and Pongpom 2005 Sci Technol. Adv Mater, 6 352.

[10] Landmann M, Rauls E, Schmidt WG. The electronic structure and optical respons rutile, anatase and brookite TiO_2. J. Phys Condens Matter, 2012; 24(1-6):195503.

[11] A. L. Linsebigler, G. Lu, and J. T. Yates, "Photocatalysis on TiO_2 surfaces: principles, mechanisms, and selected results." Chem. Rev., 95, 735 (1995).

[12] U. Deneb Menda, G. Ribeiro, D. Nunes, T. Calmeiro, H. Aguas, E. Fortunato, R. Martins, and M. J. Mendes, "High-performance wide band gap perovskite solar cells fabricated in ambient high-humidity conditions.",Materials Advances, 2, 6344 (2021).

[13] S. Haque, M. J. Mendes, O. Sanchez-Sobrado, H. Águas, E. Fortunato, and R. Martins, "Photonic-structured TiO_2 for high-efficiency, flexible and stable

perovskite solar cells." Nano Energy, 59, 91 (2019).

[14] A. Szeghalmi, M. Helgert, R. Brunner, F. Heyroth, U. Gösele, and M. Knez, "Atomic layer deposition of Al_2O_3 and TiO_2 multilayers for applications as band pass filters and antireflection coatings." Appl. Opt., 20, 48 (2009).

[15] N. Chen, D. Deng, Y. Li, X. Liu, X. Xing, X. Xiao, and Y. Wang, "TiO2nanoparticlesfunctionalized by Pd nanoparticles for gas-sensing application with enhanced butane response performances." Sci. Rep., 7, 7692 (2017).

[16] L. Zou, "Multi level resistive switching performance of TiO_2-based flexible memory prepared by low-temperature sol-gel method with UV irradiation." Curr. Appl Phys., 24, 32 (2021).

[17] E. Carlos, R. Branquinho, R. Martins, A. Kiazadeh, and E. Fortunato, "Recent progress in solution-based metal oxide resistive switching devices." Adv. Mater., 33, 2004328 (2020).

[18] M. Kitano, K. Funatsu, M. Matsuoka, M. Ueshima, and M. Anpo, "Preparation of nitrogen substituted TiO_2 thin film photocatalysts by the radio frequency magnetron sputtering deposition method and their photocatalytic reactivity under visible light irradiation." J. Phys. Chem. B, 110, 25266 (2006).

[19] S. C. Jung, "Photocatalytic activities and specific surface area of TiO_2 films prepared by CVD and sol–gel method." Korean J. Chem. Eng, 25, 364 (2008)

[20] K. I. Jang, E. Hong, and J. H. Kim, "Improved electrochemical performance of dyesensitized solar cell via surface modifications of the working electrode by electrodeposition." Korean J. Chem. Eng, 30, 620 (2013).

[21] A. B. Haugen, I. Kumakiri, C. Simon, and M.-A. Einarsrud, "TiO_2, TiO_2/Ag and TiO_2/Au photocatalysts prepared by spray pyrolysis."J.Eur.Ceram.Soc. 31,291(2011).

[22] J.P.Boilot, F.Chaput, L.Mailer, A.Brun, Y.lévy et J-P.Galup. Image de la PhySIQUE. 44 (1998).

[23] B.Darracq, F.Chaput, K.Lahlil, J.P.Boilot, Y.Levry, V.Alain, L.Ventelon, M. BlanchardDesce, Optical Materials, 9,265(1998).

[24] D.B. Wolfe, J.C. Love, K.E. Paul, M.L. Chabinyc, G.M Whitesides, Appl. Phys. Let. 80,12 (2002) 2222.

[25] J.Zhang, B.Li, Z.Wang, G.Cheng, S.Dong, Analytica Chimica Acta 388,71 (1999).

[26] J. M. Nedeljkovic, Z. V. Saponjic, Z. Rakocevic, V. Jokanovic, and D. P. Uskokovic, " Ultrasonic spray pyrolysis of TiO_2 nano-particles." Nano structured Materials, 9, 125 (1997)

Chapter I

Titanium dioxide Thin Films and their Applications: an overview

I.1. Introduction

Transparent conductive oxides are degenerate semiconductors with a large gap (≥ 3eV), it also constitutes a special type of material that combines two physical properties together, high optical transparency and high electrical conductivity. This unusual set of physical features is produced by creating free electron or hole carriers in a material with a big enough energy band gap to be non-absorbing or transparent to visible light. Due to the interest of transparent conductive oxides, a lot of research work are devoted to the study and synthesis of these materials. Metal oxides are generally big gap semiconductors. They can be represented by MOn (with M denotes the metal atom and O an oxygen atom), and the Titanium dioxide is one of transparent conductive oxides (TCO_S) [1].

Titanium dioxide is a unique material because of its flexible properties that include a high refractive index, a wide band gap (3.2 eV), and resistance to chemical and physical impacts. In addition, titanium dioxide has very good semiconducting properties, including photocatalysis, photonic device and solar cell, optical filters, antireflection coatings, ferroelectric and sensors. This wide range of the application of TiO_2 is due to its unique electronique and structural properties. TiO_2 can be grouped into three crystalline phases: rutile, anatase and brookite. The presence of any one or more than one phases in the material can affect on the micro-structural, optical and electrical properties of the material. Among these phases rutile is the most stable phase and it is usually obtained after annealing at temperature above 500 °C. While the other two phases are metastable which are difficult to synthesize and are continuously studied [2].

This chapter is concerned with studying one of the transparent conductive oxides, titanium oxide, and studying the most important general properties of it and its various appliations.

I.2. Transparent conductive oxides (TCO_S)

I.2.1. Definition of TCO_S

Transparent Conductive Oxides (TCO_s) are promising materials. Since the discovery of the dual property of electrical conductivity and transparency in the visual domain at the turn of the century [3] , and also they are defined as oxides which are made from metal oxides of single, binary and more recently multiple elements. They are applied as thin films using various deposition techniques such as jet pyrolysis, evaporation, sputtering, and laser ablation, molecular beam epitaxy [4,5].

Transparent conducting oxides (TCOs) have the unique combination of transparency and electronic conductivity and are key enablers of technologies like pressure-sensitive displays. The combinations of indium (In_2O_3), zinc (ZnO) and tin oxide (SnO_2), and cadmium oxide (CdO) dominate on TCOs, with indium-tin oxide (ITO) prevalent (Pasquarelli et al, 2011) [6]. In addition that TCOs generally have relatively high melting points but also high density, low hardness and high refractive indices. However, they transmit in the visible and can feature luminescence, high electron mobilities and semiconductor and piezoelectric behavior (Weber, 2003) [7]. As a result, three different electrical states are attainable: conductor, semiconductor and insulator, according to the energy band theory, (Figure I.1). In the conductor, the valence band (VB) and the conduction band (CB) overlap, as a result, electrons can freely flow. The semiconductor has, for its part, a prohibited band which separates CB and VB commonly called gap. The electrons cannot take the located energies in this band. They need to acquire energy to move into the CB. For a gap greater than 4 eV, we speak of insulation because even at room temperature, CB is empty [8].

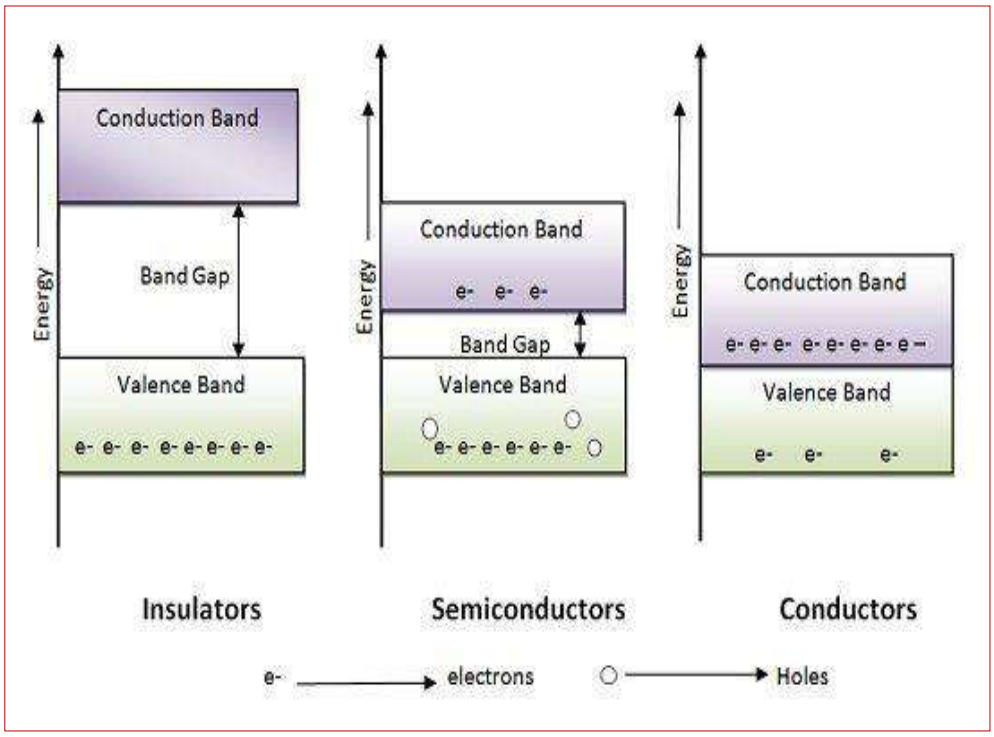

Figure I.1. The classification of materials based on bands theory (e^- = electrons, o = holes) [9].

I.2.2. Properties of TCOs

Historically, Karl Baedeker observed the first cohabitation of electrical conductivity and optical transparency in the visible range in 1907 [10] on thin layers of cadmium oxides CdO [11] , which could be considered to be the first oxide that appeared to be transparent and

conductive. But, the first TCOs useful for practical applications was tin-doped indium oxide [(In_2O_3: SnO_2) (90wt%: 10wt%)], commonly known as ITO. It was developed in the early 1950s, and remained among the materials offering the best optical and electrical performance [12,13]. It has been the TCOs of choice for the past 50 years intended for applications requiring high conductivity and transparency in the visible region. Research in the early 1980s focused on intrinsically doped ZnO thin films [14,15], only their electrical properties were found to be unstable above 150 °C [16]. This problem has been solved by employing the extrinsically doped films [16].

I.2.2.1. Optical properties

The existence of an optical window covering the entire visible domain is characteristic of TCOs. Optical transmission is defined as the ratio between the intensity of the incident light and the intensity of the light transmitted through the material under consideration. The absorption spectrum is deduced from the transmission and reflection spectra [17]. For exemple TCOs are produced polycrystalline or amorphous and are often doped with several elements, such as fluorine (F) [18], antimony (Sb) [19], titanium (Ti) [20] and galium (Ga) [21].Visible transparency can be up to 90% (thin coatings) with transmission windows spanning from 0.35 to 3.5 µm . Moreover, they can absorb UV and reflect IR wavelengths, making them useful heat reflectors with UV protection.

I.2.2.2. Electrical properties

The physics of large gap semiconductors describes the electrical properties of TCOs. The conductivity σ expressed in $\Omega^{-1}.cm^{-1}$ is the product of the density of charge carriers n_V in cm^{-3}, the mobility µ of these charges in $cm^2.V^{-1}.s^{-1}$ and the elementary electric charge of the electron q (formula I.1). Resistivity ρ, defined as the inverse of conductivity, is expressed in Ω.cm [22].

$$\sigma = q\, n_v\, \mu = \frac{1}{\rho} \qquad \text{(I.1)}$$

An important surface electrical property in the field of TCOs is the surface resistance R_S defined as the ratio of the resistivity to the thickness of the layer according to the relation (I.2) [22]:

$$R = \rho / e \qquad \text{(I.2)}$$

I.2.2.3. General properties of TCO

In addition to good optical and electrical properties, other factors influence the materials and deposition procedures that are used. The etching of the layers, The cost of production, as well as the toxicity, are essential considerations. The plasma frequency, the hardness of the layers and the adhesion, the thermal and chemical resistance of the layers are also essential parameters. Gordon has studied the different influences of all these parameters giving criteria for various applications [23].

Control of the parameters of the deposition method is of great importance for the growth of high quality TCO films. The physical properties of the TCO thin film are strongly related to the structure, morphology and composition of the deposit. These factors are effected by the deposition parameters of the different methods. For TCOs, a wide variety of deposition techniques are used.

TCOs must have a strong electrical conductivity and low visual absorption in the visible range. This is why tests for the quantitative evaluation of the quality of TCO have been proposed in the form of "figures of merit" [Haacke, 1976], an example of which is described by Gordon's equation (I.3) [24].

$$\frac{\sigma}{\alpha} = -\frac{1}{Rsq\ \ln(T+R)} \qquad (I.3)$$

where : σ is the conductivity ($\Omega^{-1}.cm^{-1}$), α is the absorption coefficient (cm^{-1}), Rsq is the square resistance (Ω), T [%] is the coefficient of transmission, and R [%] is the coefficient of reflection.

I.3. Titanium dioxide

I.3.1. Generality

Titanium dioxide (TiO_2) is a unique material due to its flexible properties which include a high refractive index, a wide forbidden band (3.2 eV), and resistance to chemical and physical impacts. In addition, titanium dioxide has very good semiconductor properties, which has generated significant enthusiasm on the part of scientists for various applications, and in particular for photocatalysis, antireflection coatings, optical waveguides, photonic crystals, devices based on a metal, insulator, ferroelectric, semiconductor structure [25]. Moreover the properties of titanium oxide (TiO_2) depend on several parameters, namely the nature of the phase, the microstructure, the crystallinity and the chemical composition. These parameters can be modified either by the method of preparation or by heat treatment or by

additions. The modification of the properties of TiO_2, using a doping metal, depends both on the type of metal of its concentration and on its distribution [15].

Titanium oxide (TiO_2) has been the subject of several studies because with interesting physicochemical properties due to its chemical stability, low cost and many other aspects presented in what follows. In 2010, the world production of TiO_2 used as pigment is estimated at 5.3 million tons, 55 to 60% by the chlorine process, 40 to 45% by the sulfuric process, mainly in China. This production reached 6.55 million tonnes in 2012 and the market is expected to reach 6.8 million tonnes in 2016. Titanium oxide is very chemically stable, non-volatile and non-flammable. It is non-toxic and has both a very high refractive index and a very high dielectric constant. It is obtained from titanium ore, about 95% of the amount of ore extracted is used for the production of the pigment and only 5% for the preparation of the metal [26].

I.3.2. structural properties of TiO_2

Titanium dioxide exists in several forms, the three main ones being anatase, rutile and brookite [27] :

I.3.2.1. Anatase structure

Anatase crystallizes in a quadratic or tetragonal system, whose lattice parameters are a = b = 3.784 Å and c = 9.515 Å [28], it has a theoretical density of 3.79 (g/cm^3), is also an insulator with a band gap of about 3.2 eV [29] .When heated to 700 °C, it turns into rutile. The crystal structure of anatase is far more complicated than that of rutile, the octahedra there have been "deformed". Figure I.2 shows the structure of anatase. The crystal structure of anatase is formed of octohedra linked together by edges, these octahedra being elongated along the c axis. It has its own 2 atoms of titanium and 4 atoms of oxygen where the mean Ti-O distances (1.917 Å). This structure is formed at temperatures lower than those of rutile formation and those of broukite, it crystallizes at about 400 °C and it shares several properties with rutile such as hardness and density [30].

I.3.2.1. Rutile structure

The rutile is most thermodynamically stable phase , derives its name from the latin rutilus, which means red, in reference to the observation of a red shade transmitted through this structure, where it strongly refracts light, with a high refractive index of value between (2.7-3.1) [31], so it has been widely applied in pigments and in opacifieds. The mesh of rutile

is quadratic or tetragonal system, whose lattice parameters are (a = b = 4.5936 Å, c = 2.9587 Å) [28]. The rutile mesh is shown in Figure I.2. Moreover, each titanium (Ti) atom is coordinated with six (O) oxygen atoms and is surrounded by three coplanar titanium atoms at the vertices of an almost equilateral triangle, the average inter-ionic distance in rutile is 1.959 Å for Ti-O bonds and 2.960 Å for Ti-Ti bonds [32]. This form is produced at high temperature [33].

I.3.2.3. Broukite structure

Broukite crystallizes in the orthorhombic crystal system. Its mesh parameters are: a = 9.184 Å; b = 5.447 Å; c = 5.145 Å [28] (Figure I.2). Brookite has a more complex structure, although the Ti – O distances are similar to other structures [32]. Almost all studies relating to the synthesis of TiO_2 brookite reveals the presence of brookite and rutile and/or anatase phases at the same time. The brookite phases transform into rutile phases at high temperatures, starting around 750 °C. [34].

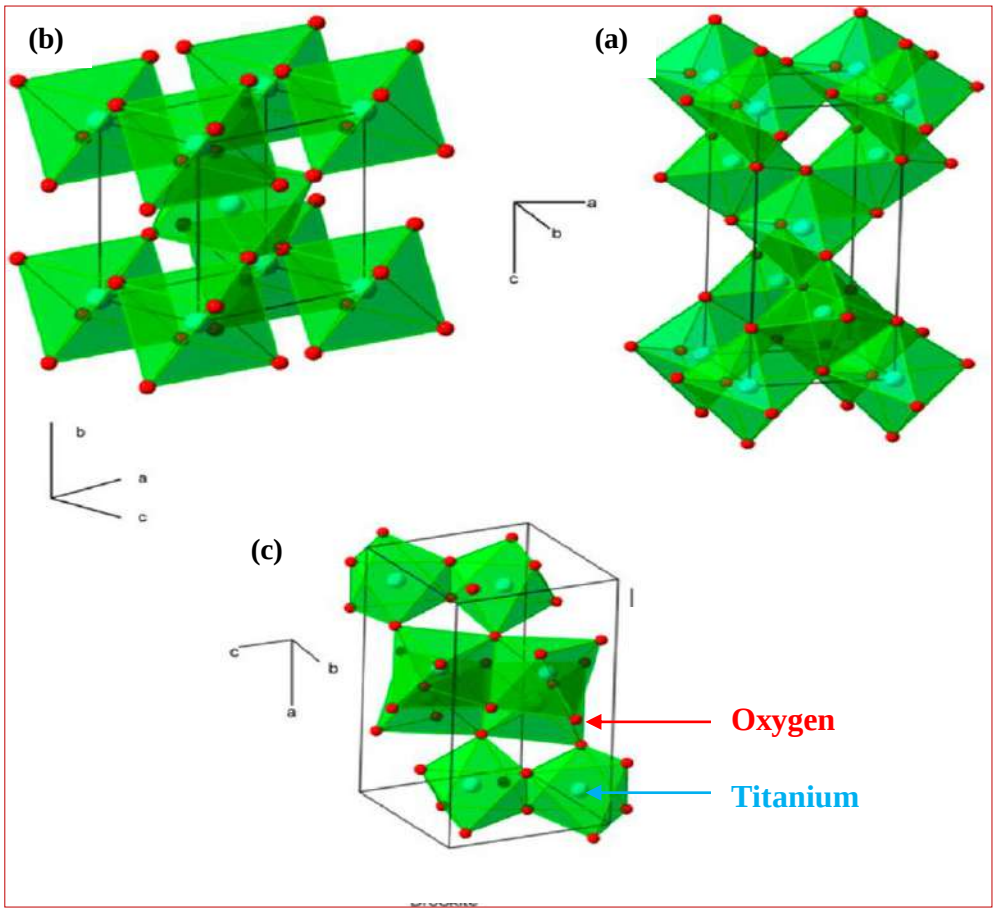

Figure I.2. Crystalline structures of titanium dioxide (TiO_2) in different phases: (a) anatase, (b) rutile, (c) brookite [35].

Table I.1. Properties of the different phases of titanium dioxide [36].

Phase	Anatase	Rutile	Broukite
Crystal structure	tetragonal	tetragonal	orthorhombic
Lattice constants (Å)	a = b = 3.784 c = 9.514	a = b = 4.5936 c = 2.9587	a = 9.184 b = 5.447 c = 5.145
Molecule/cel	4	2	8
The density (g/cm^3)	3.79	4.13	3.99
Volume/molecule ($Å^3$)	34.061	31.216	32.172
***O - Ti - O* bond angle**	77.7° 92.6°	81.2° 90°	77° ~ 105°
***Ti-O* bond length (Å)**	1.937 (4) 1.965 (2)	1.949 (4) 1.980 (2)	1.87 ~ 22.04
Hardness (Mohs)	5.5 - 6.0	6 - 6.5	5.5 - 6.0
Refractive index	2.48 – 2.56	2.61 – 2.89	2.58 – 2.70
Atomic radius (Å)	r (Ti^{4+}) = 0.605 r (O_2^-) = 1.36	r (Ti^{4+}) = 0.605 r (O_2^-) = 1.36	r (Ti^{4+}) = 0.605 r (O_2^-) = 1.36
d (Ti^{4+} - O_2^-) (Å)	1.93 – 1.98	1.95 – 1.99	1.86 – 2.04
Coordination	[Ti^{4+}] = 6 [O_2^-] = 3	[Ti^{4+}] = 6 [O_2^-] = 3	[Ti^{4+}] = 6 [O_2^-] = 3
Compactness	0.645	0.708	0.655

I.3.3. Optical properties of TiO_2

I.3.3.1. Refractive index of TiO_2

In the visible spectrum, several kinds of titanium oxide have a high refractive index n. rutile has the highest index (n ~ 2.66) of the three stable crystalline phases, which is higher than that of anatase (n ~ 2.54). This, paired with a high visible light dispersion coefficient, makes the rutile phase a popular white pigment of choice for industry (paints, food or pharmaceutical dyes, etc.) [37,38].

I.3.3.2. Gap of TiO_2

As a result, TiO_2 is portrayed as a semiconductor with a broad prohibited band (band-gap). The Rutile, Anatase and Brookite gaps have a value of 3 eV, 3.2 eV and 3.1 eV respectively (Eg between the valence band (corresponding to the O2p orbital) and the conduction band (corresponding to orbital Ti3d). Transitions corresponding to photons in the ultraviolet domain result from these gap values [39].

I.3.4. Electrical properties of TiO_2

Titanium dioxide is an n-type semiconductor, TiO_2 single crystals have a resistivity of about 10^{13} Ω.cm at room temperature, and about 10^7 Ω.cm at 250 °C. These values are similar to conductivities reported for a rutile single crystal : while the conductivity was 5×10^{-14} $(\Omega.cm)^{-1}$ at 30 °C, it is increased to 3.3×10^{-9} $(\Omega.cm)^{-1}$at 260 °C. Therefore, TiO_2 is generally considered to be an insulator at temperatures below 200 °C. Highly insulating TiO_2 films have a variety of applications, including serving as a dielectric "gate" in metal-oxide-semiconductor field-effect transistor (MOSFET) devices. The electrical properties of the TiO_2 sheet, furthermore, can be changed to make it particularly conductive for a variety of applications, including humidity and gas sensors [40].

I.3.5. Electronic properties of TiO_2

TiO_2 can be considered either as a wide band gap n-type semiconductor or as a narrow band gap oxide. It has a band gap slightly greater than 3eV. In its stoichiometric state, occupied states derive mainly from oxygen atoms; free states derive from Ti atoms. When reduced, the material contains oxygen vacancies [17]. For the three crystalline forms of TiO_2 mentioned above, the valence band is formed by the overlap of orbitals eg of titanium and 2p of oxygen (Figure I.2). The conduction band is formed by the eg and t2g orbitals of titanium [39].

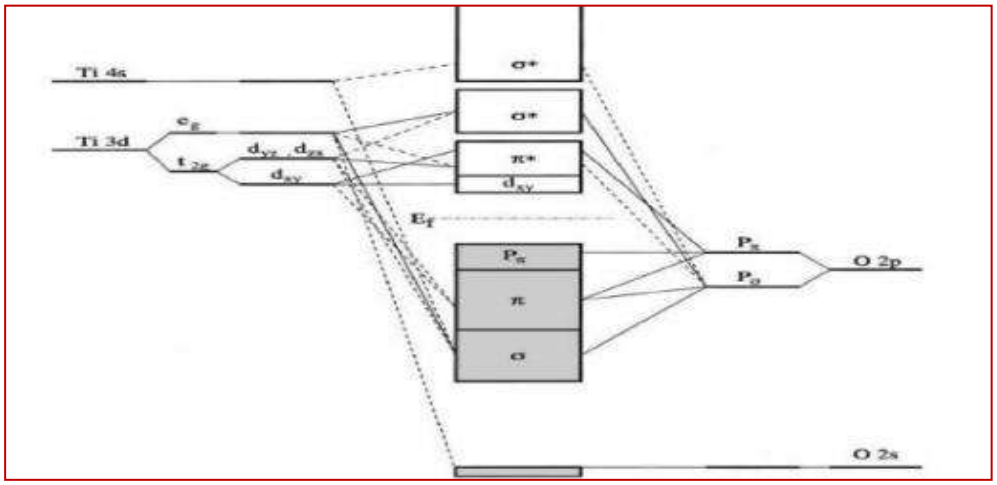

Figure I.3. Schematic representation of the electronic structure of TiO_2 [25].

I.4. Stability of crystalline phases

Rutile is the stable phase at high temperature, the anatase phase is mainly obtained during syntheses by soft chemistry. The anatase phase is stabilized in nanomaterials. This reversal of stability is due to the surface energy of materials.

The particular behavior of nanomaterials has been explained by the surface effect. At the nanoscale, a large number of atoms are found on the surface of the grains. As a result, the material properties show significant changes compared to the same coarse-grained materials. Thus, the surface energy, called γ, for a phase to be thermodynamically stable outside the classical stability domains is expressed as follows:

$$\boldsymbol{\gamma = \alpha V + \beta S} \qquad (I.3)$$

with α and β the free energies respectively by volume V and by surface S.

where we find that the free energy in volume is less in the case of rutile , the trend is reversed in the case of free surface energy . In the case of small crystals, the role of surface energy is enhanced: free energy is then minimized in the case of anatase which is stabilized.

Banfield et al. [41] studied the stability of various polymorphic phases of TiO_2 by X-ray diffraction during isochronous and isothermal reactions. Banfied showed that rutile is energetically stable when the particle size is greater than 35nm, and that the brookite phase is energetically stable between 11 and 35 nm, and that anatase is energetically favored for the smallest particles less than 11nm (see Figure I.4) [42].

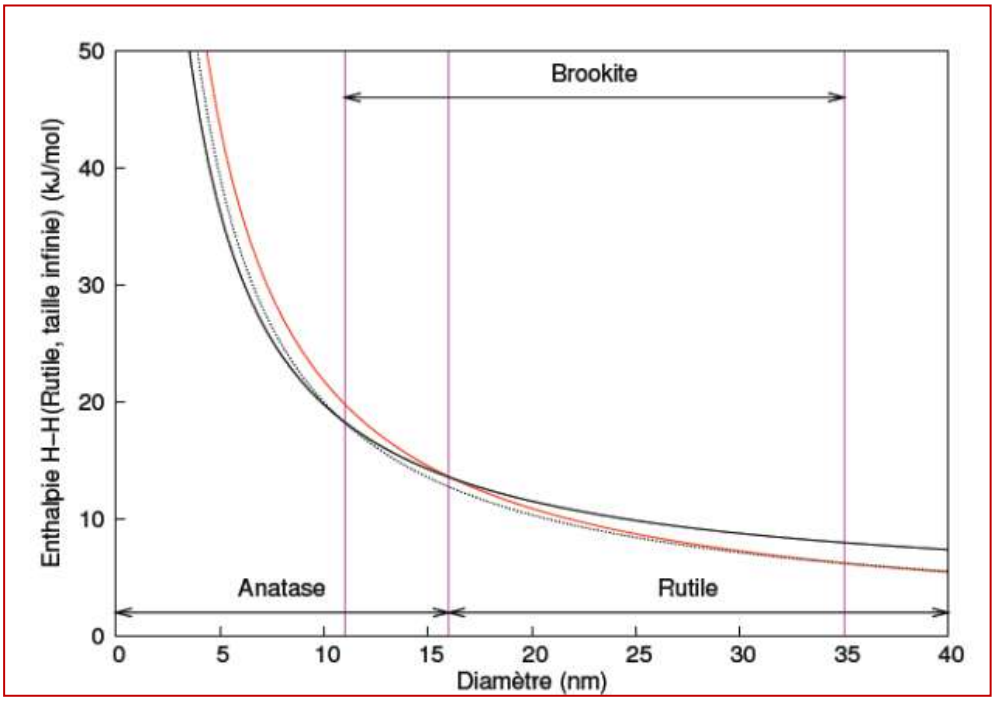

Figure I.4. Evolution of the enthalpy of anatase (thick line), rutile (thin line) and brookite (dotted line) as a function of the size of the nanocrystals. The vertical lines correspond to the brookite-anatase transition for a diameter of 11 nm, the anatase-rutile transition for a diameter of 16 nm and the broukite rutile transition at 35 nm [42].

Finally, experimental analyzes, thermodynamic calculations and calculations are based on the structure that confirm the properties of TiO_2 which are in the form of thin layers and strongly depend on the phase of its microstructure. These vary according to the techniques and the conditions of preparation, as well as by the heat treatments.

I.5. The titanium-oxygen phase diagram

From the phase diagram, rutile is the most stable structure, it exists in a temperature range below 1870 °C, which is the melting temperature of TiO_2. Which disappears completely at a temperature above 700 °C during the anatase structure after an irreversible of anatase-rutile transformation. This transformation can take place at temperatures lower or higher than 700 °C, namely the type and the percentage of impurities which contains the TiO_2 matrix. When the stoichiometry of titanium dioxide varies from 0 to 2, we find the following phases: Ti, Ti_2O, TiO, Ti_2O_3, Ti_3O_5, Ti_nO_{2n-1} and TiO_2 (see Figure I.5) [19].

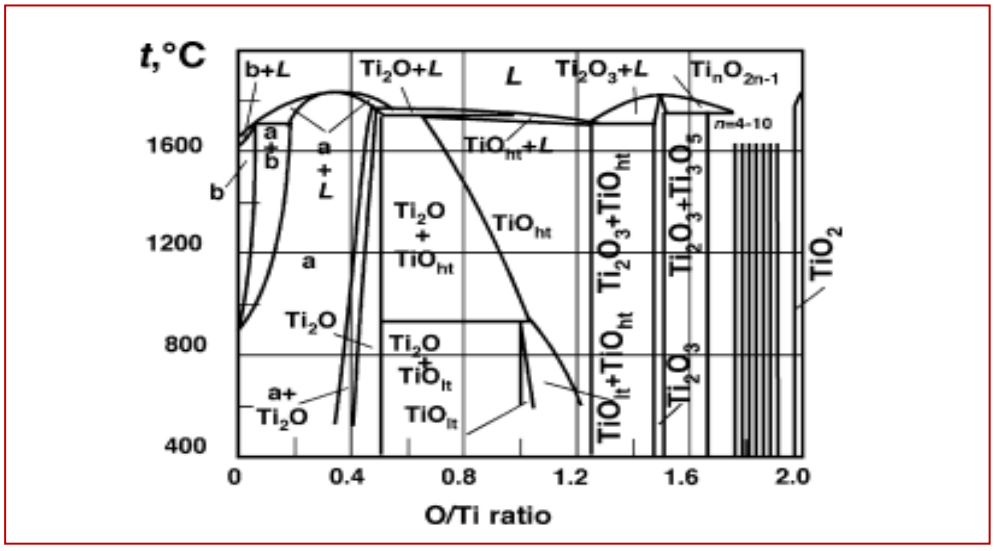

Figure I.5. Phases diagram of titanium-oxygen [43].

I.6. Doping of titanium dioxide (TiO_2)

Several studies have been devoted to doping and its influence on the structural properties of thin titanium oxide films obtained by different methods. The modulation of these properties does not only depend on the type of dopant, but also on its concentration, its

distribution in the TiO_2 network, the technique and the conditions of preparation. The doping of TiO_2 thin films is accompanied by significant changes in structure and morphology, such as the transformation of the anatase structure to the rutile structure, the transformation of the brookite structure to the rutile structure and the appearance of new phases.

One of the most essential ways is to doping TiO_2 dioxide with transition metals [44], and multiple studies have been carried out with various metals: iron (III) (Fe), zirconium (Zr), cerium (Ce), manganese (Mn), chromium (Cr) and cobalt (Co), tungsten (W) , silver (Ag), zinc (Zn), copper (Cu) [45,46], other metals, for example: magnesium (Mg), strontium (Sr), barium (Ba), calcium (Ca), lead (Pb).

Several authors claim that this form of cationic doping lowers TiO_2 energy barrier by narrowing the width prohibited band's [47]. However, the majority of works adhere to the fact that this doping increases the recombination of charges (electrons and holes) [48].

The effect of lanthanum (La-TiO_2) and manganese (Mn-TiO_2) doping on titanium dioxide is investigated in this thesis.

I.6.1. Lanthanum properties

Lanthanum takes its name from the greek word « lanthanum » which means hiding, because this element has long remained hidden in cesium oxide. Lanthanum comes in the form of a malleable, ductile, silvery-gray metal which, like sodium, is soft enough to be split with a blade. It oxidizes both in air and in water. (Table I.2).

Table I.2. Lanthanum properties.

Sympol	La
Atomic number	57
Atomic mass	138.91 ($g.mol^{-1}$)
Density	6.18 ($g.cm^{-3}$) at 20°C
Melting point	920°C
Boiling point	3463°C
Electronic configuration	[Xe] $5d^1 6s^2$
Group, Periode, Bloc	3, 6, f

I.6.2. Manganese properties

Manganese is a chemical element with the symbol Mn and is a pinkinsh-gray, chemically active element. It is a hard metal and is very brittle. It is hard to melt, but easily oxidized. Manganese is reactive when pure, and as a powder it will burn in oxygen, it reacts with water (it rusts like iron) and dissolves in dilute acids. (Table I.4).

Table I.3. Manganese properties.

Sympol	Mn
Atomic number	25
Atomic mass	54.9380 ($g.mol^{-1}$)
Density	7.43 ($g.cm^{-3}$) at 20°C
Melting point	1247°C
Boiling point	2061°C
Electronic configuration	[Ar] $3d^5 4s^2$
Group, Periode, Bloc	7, 4, d

I.7. Applications of TiO_2 thin films

I.7.1. Photocatalyst

Like all transition metal oxides, titanium dioxide has many applications, in catalysis, electronics and optics. Since the discovery of the photoelectrochemical properties of TiO_2, in particular the capacity to decompose water by producing hydrogen in 1972, photocatalysis begun to have more attention, therefore, research intensifies, and the applications of this emerging technology are diversifying (Table I.4). The electronic properties of TiO_2, its low economic cost, its chemical stability and its non-toxicity, make it a occupies a privileged place among these oxides and a catalyst of choice for this technology [49].

But what exactly is the process of photocatalysis and the photocatalysts that make it happen?

A photocatalyst is a coating agent containing titanium dioxide as its active component. An oxidation-reduction chemical reaction occurs when light comes into contact with the photocatalyst. When applied to surfaces it functions to purify air so as to prevent the contamination of the surface. Moreover, this technology functions as a revolutionary catalyst for protecting the environment.

Table I.4. Summary of TiO_2 applications in photocatalysis [50].

Category	Application	Properties
Building Materials	Cements, roof tiles, window tents, plastic sheets, coated, aluminum panels, curtains	• Self-cleaning. • Antibacterial. • Air purification. • Water purification.
	Soundproof walls, coated, tunnel walls, signage and reflectors, deposit on tunnel lamps.	
	Wallpaper, window shade	
Effluent purification system	Air purifier, air conditioners, purification system for used water and sewage, purification for swimming pools.	
Hospitals	Tile, operating room walls, tools, uniforms.	• Sterilization. • (TiO_2 – Cu). • Self-cleaning.

The correct definition of photocatalysis includes the process of photosensitization by which photochemical damage is performed on a chemical species resulting from the initial absorption of radiation by other chemical species called photosensitizers. Heterogeneous photocatalysis that has been the subject of numerous research studies involves photo-reactions at the surface of the catalyst. As with any process involving heterogeneous phase reactions. Hence, the photocatalytic process can be divided into five steps : transfer of reactive molecules dispersed in the fluid to the surface of the catalyst, adsorption of reactive molecules on the surface of the catalyst, reaction on the surface of the adsorbed phase, desorption of products and removal of products from the fluid / catalyst interface [51].

Photocatalytic reactions with TiO_2 are limited to wavelengths below 400 nm, in the UV ultraviolet. Figure (I.6), it is also materials that can work in the visible are more desirable in terms of using natural light. Indeed, only 5% of sunlight is used in the case of anatase. For this reason, the doping of TiO_2 anatase has been studied to move its gap in the visible. This has shown that doping with different transition metals such as V, Cr, Mn, Fe and Ni, allows a

visible shift of the absorption band of TiO_2. This shift depends on the amount of dopant introduced. The efficiency in the shift is as follows: V, Cr, Mn, Fe, Ni. This allows sunlight to be used more efficiently and up to 20% to 30% better [52].

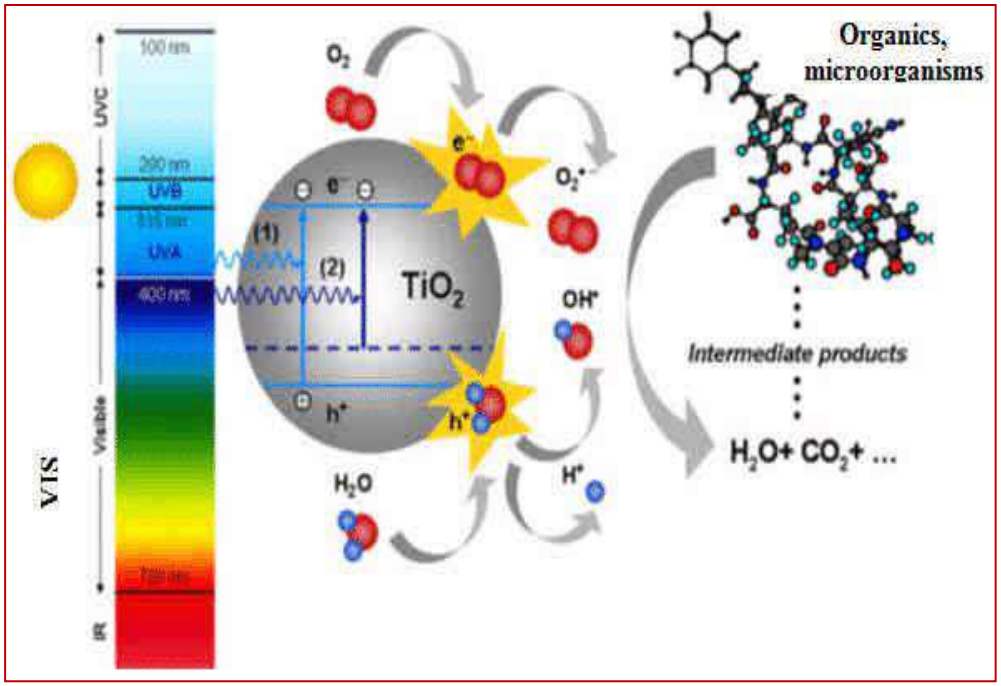

Figure I.6. Scheme of the photocatalytic action of TiO_2 under UV (1) and visible (2) irradiation [53].

The photocatalytic method is based on the excitation of TiO_2 by light radiation with a wavelength of less than 387 nm, which equates to an energy larger than or equal to the forbidden band width (3.2 eV):

$$\mathbf{TiO_2 + h\nu \rightarrow h^+ + e^-} \qquad \text{(I.4)}$$

An electron from the valence band is promoted to the conduction band with the formation of a positive hole (h^+). The holes react with water and organic pollutants adsorbed on the surface of TiO_2, according to reactions (I.5) and (I.6):

$$\mathbf{H_2O + h^+ (valence\ band) \rightarrow OH + H^+} \qquad \text{(I.5)}$$

$$\mathbf{h^+ (valence\ band) + pollutant \rightarrow pollutant^+} \qquad \text{(I.6)}$$

The hydroxyl radicals formed in the reaction (I.5) also participate in the degradation of pollutants:

$$\mathbf{OH + pollutant \rightarrow CO_2 + H_2O} \qquad \text{(I.7)}$$

We must also consider the electron-hole recombination reaction in the volume of the particle or on the surface:

$$h^+ + e^- \rightarrow \text{heat} \qquad \text{(I.8)}$$

The rate of creation of electron-hole pairs under the influence of reaction photons (equation I.4) is determined by the incident light intensity as well as the photocatalyst's optical and physical properties. The speed of diffusion of the pairs and their rate of recombination depend on several factors, mainly structural: the allotropic composition [54], the crystallinity [55], the size of the crystallites [56], and the ionic doping rate [57]. These factors influence the photocatalytic activity as well. On the other hand, photocatalytic activity depends on the chemical nature of the pollutant and the chemical complexity of its molecule [52].

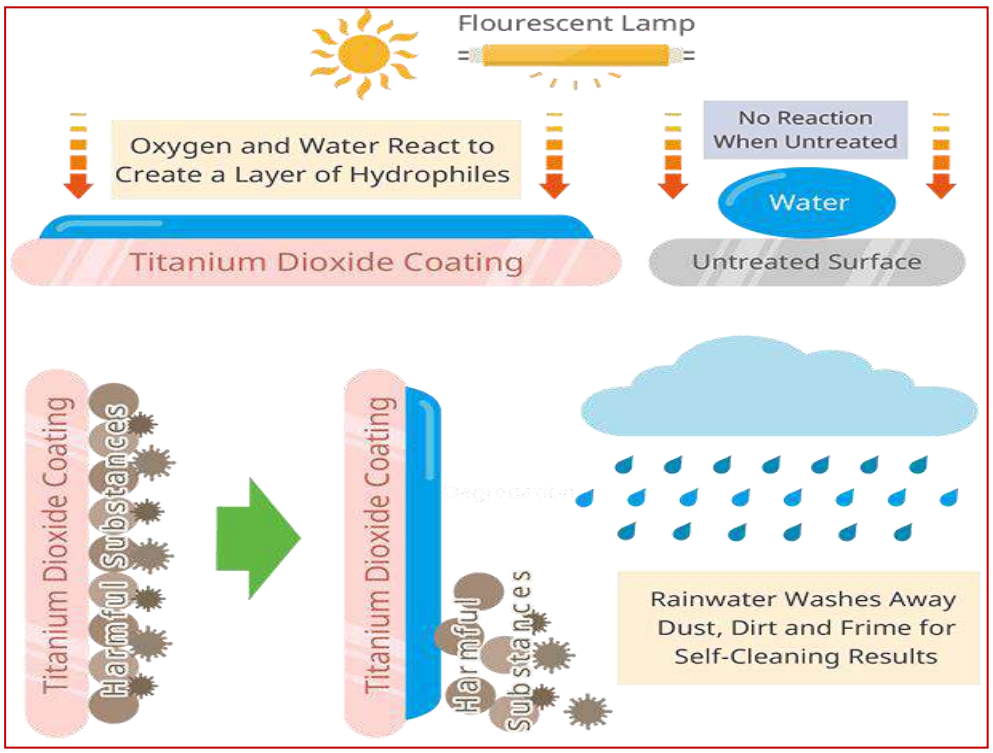

Figure I.7. Principle of photocatalysis of titanium dioxide (TiO_2).

I.7.2. Dye sensitized solar cells

I.7.2.1. What is dye sensitized solar cells ?

Dye-sensitized solar cells (DSCs) have exhibited solar energy conversion efficiency of over 10% and remain one of the most promising candidates, as they possess advantages of being flexible, inexpensive, and easier to manufacture than brittle silicon solar cells [58,59]. A very important feature of DSCs is the photoelectrode, which includes mesoporous wide band

gap oxide semiconductor films with an enormous internal surface area, typically a thousand times larger than those of bulk films [60,61].To date, the highest solar-to-electric conversion efficiency has been achieved with films that consist of 20 nm TiO_2 nanocrystallites sensitized by ruthenium-based dyes. Hence, solar cells play a vital role in converting solar energy into electrical energy, which is known as the PV effect. Solar cells exposed to sunlight will see changes in electrical characteristics such as voltage, resistance, and current.

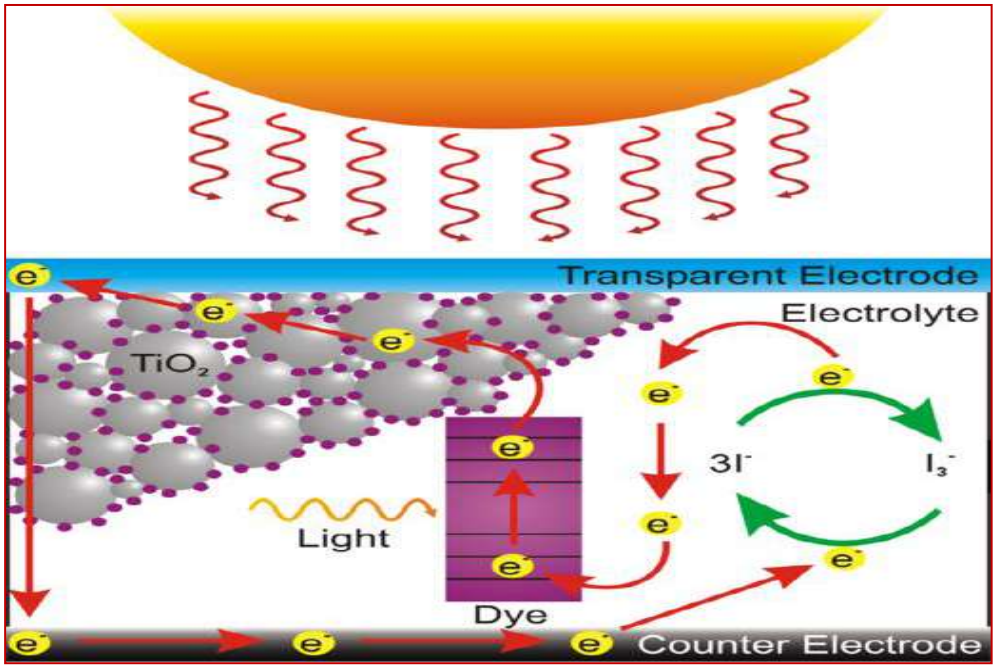

Figure I.8. Schematic illustration of a generic dye-sensitized solar cell [62].

I.7.2.2. How do dye sensitized solar cells work?

The working principle of DSSC involves four basic steps: light absorption, electron injection, transportation of carrier, and collection of current. The following steps are involved in the conversion of photons into current (as shown in Figure I. 8) [63]:

1- Firstly, the incident light (photon) is absorbed by a photosensitizer, and thus, due to the photon absorption, electrons get promoted from the ground state (S^+/S) to the excited state (S^+/S^*) of the dye, where the absorption for most of the dye is in the range of 700 nm which corresponds to the photon energy almost about 1.72 eV.

2- Now, the excited electrons with a lifetime of nanosecond range are injected into the conduction band of nanoporous TiO_2 electrode which lies below the excited state of the dye, where the TiO_2 absorbs a small fraction of the solar photons from the UV region. As a result, the dye gets oxidized.

$$S + h\nu \rightarrow S^* \quad \text{(I.9)}$$

$$S^* \rightarrow S^+ + e^- \ (TiO_2) \quad \text{(I.10)}$$

3- These injected electrons are transported between TiO_2 nanoparticles and diffuse towards the back contact (transparent conducting oxide [TCO]), through the external circuit, electrons reach at the counter electrode.

4- The electrons at the counter electrode reduce I^-_3 to I^-; thus, dye regeneration or the regeneration of the ground state of the dye takes place due to the acceptance of electrons from I^- ion redox mediator, and I^- gets oxidized to I^-_3 (oxidized state).

$$S^+ + e^- \rightarrow S \quad \text{(I.11)}$$

5- Again, the oxidized mediator (equation I− 3) diffuses towards the counter electrode and reduces to I ion.

$$I_3^- + 2e^- \rightarrow 3I^- \quad \text{(I.12)}$$

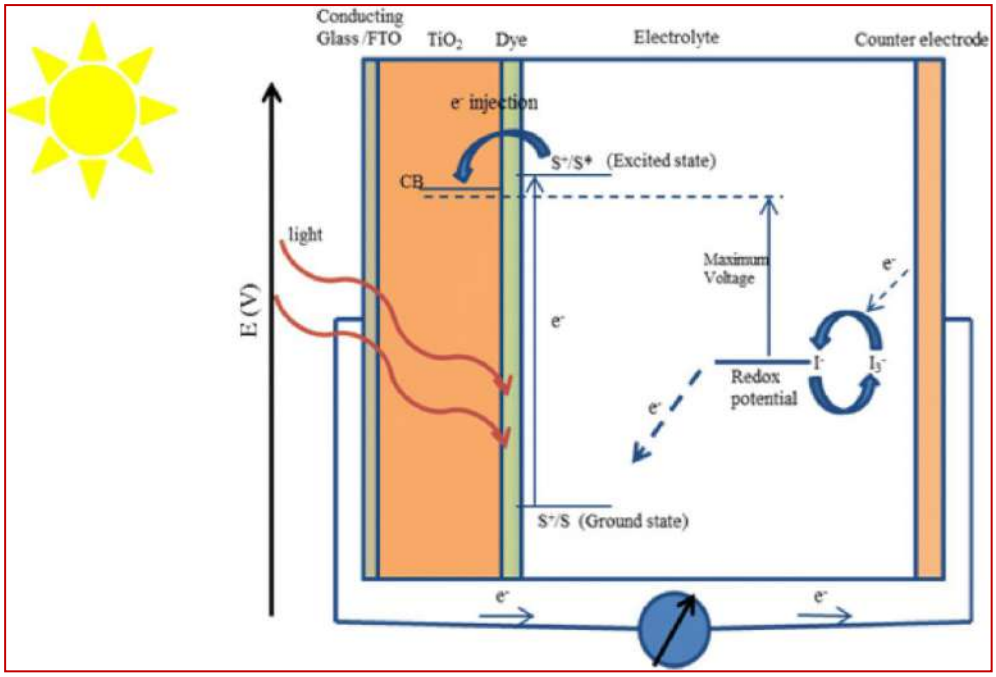

Figure I.9. Construction and working principle of the dye-sensitized nanocrystalline solar cells [63].

I.7.2.3. Advantages and disavantges of dye sensitized Solar Cells

I.7.2.3.1. The advantages

- Dye sensitized solar cells are the most efficient third-generation solar technology available is greatly used in applications like rooftop solar collectors. The power production efficiency is around 11%, as compared to thin-film technology cells which are between 5% and 13%, and traditional commercial silicon panels which operate between 12% and 15%.
- In a silicon solar cell, it acts both as a source of electrons as well as an electric field provider, whereas in a DSSC, the semiconductor is used mainly for charge transport & the photo electrons are supplied by a different source (dye).
- DSSCs work even in low-light conditions. Hence they are very popular under cloudy weather conditions and non-direct sunlight, where traditional cells would be a failure. The cutoff in DSSC is so low, they have been proposed for indoor usage, to collect energy for small devices from the lights in houses.
- A traditional solar cell is encased in glass with a metal at back for increasing its strength. Such setup may cause a decrease in its efficiency, as the cells heat up internally. However DSSCs are built up with only a thin layer of conductive plastic on the front side to allow radiation of heat much easily & quickly and therefore operate at low internal temperatures. Also the cell's mechanical structure is such that it indirectly leads to higher efficiencies in higher temperatures [64,65].

I.7.2.3.2. The disavantages

- DSSCs are not considered as an option, for large-scale deployments where higher-cost higher-efficiency cells are more viable. DSCC is not manufactured in commercial scale yet.The sharp cut in silicon solar panels costs have led other types of solar technology like Solar Thermal and Thin Film Technology taking a back seat.
- Another major drawback is the electrolyte solution, which contains volatile organic solvents and must be carefully sealed. Replacing the liquid electrolyte with a solid has been a major ongoing field of research [66,67].

Chapter I's references :

[1] Zhuan-Fang Bi, Lei Wang, Xiu-Hong Liu, Shao-Mei Zhang, Ming-Ming Dong, Quan-Zhong Zhao,Xiang-Long Wu, and Ke-Ming Wang, " Optical waveguides in TiO_2 formed by He ion implantation", 12March 2012 / Vol. 20, No. 6 / OPTICS EXPRESS 6712.

[2] Landmann M, Rauls E, Schmidt WG. " The electronic structure and optical response of rutile, anatase and brookite TiO_2 ". J Phys Condens Matter 2012; 24(1-6):195503.

[3] S. E. Park, H. Joo, J.W. Kang, Solar Energy Materials and Solar Cells, 83 (2004) 39-53.

[4] K. Ellmer, Journal of Physics D: Applied Physics 33 (4) (2000) R17.

[5] V. Cracium, J. Elders, J. G. E. Gardeniers, J. Geretovsky, I. W. Boyd, Thin Solid Films 259 (1), (1995) 1.

[6] H.Hartnagel, "Semiconducting Transparent Thin Films." Institute of Physics Publications, Phila delphia (1995).

[7] Xiao Wei Sun and Yi Yang," ZnO Nanostructures and Their Applications, Pan Stanford Publishing." Taylor & Francis Group, Boca Raton (2012).

[8] Amir FATH ALLAH, " Regroupement de techniques de caractérisation de matériaux destinés à l'énergie solaire pour optimisation et mesures industrielles." Thèse de Doctorat, Université Paris Sud, 2015.

[9] Public.iutenligne.net/chimie/valls/chimie-du-solide/propri_semiconducteurs_1.htm

[10] K. Badeker, Annals of Physics 22 (1907) 749.

[11] S. H. Oh, D. J. Kim, S. H. Hahn, E. J. Kim, " Comparison of optical and photocatalytic properties of TiO_2 thin films prepared by electron-beam evaporation and sol–gel dip-coating. " J. Materials letters.Vol. 57, pp. 4151- 4155 (2003).

[12] K. L. Chopra, S. Major, and D. K. Pandya, Thin Solid Films 102 (1983) 1.

[13] R. G. Gordon, MRS Bulletin**,** 25 (8) (2000) 52.

[14] S. Maniv, C. J. Miner, and W. D. Westwood, Journal of Vacuum Science and Technology A1 (3) (1983) 1370.

[15] T. Minami, H. Nanto, S. Takata, Applied Physics Letters 40 (10) (1982) 961.

[16] T. Minami, H. Nanto, S. Shooji, S. Takata, Thin Solid Films 111 (2) (1984) 167.

[17] S.C. Dixon, D.O. Scanlon, C.J. Carmalt, I.P. Parkin," n-Type doped transparent conducting binary oxides: an overview." J. Mater. Chem. C. 4 (2016) 6946–6961.

[18] A. E. Rakhshani, Y. Makdisi, H. A. Ramazaniyan, Journal of Applied Physics 83 (2)

(1998) 1049.

[19] C. Terrier, J. P. Chatelon, J. A. Roger, Thin Solid Films 295(1-2) (1997) 95.

[20] Wang, T. Brezesinski, M. Antonietti, B. Smarsly, ACS Nano 3(6) (2009) 1373.

[21] V. Assunçao, E. Fortunato, A. Marques, H. A. Guas, I. Ferreira, M.E.V. Costa, and R. Martins. " Thin Solid Films 427(1-2) (2003) 401-405.

[22] H.Dixit,"First-Principles Electronic Structure Calculations of Transparent Conducting Oxide Materials." Doctorate Thesis, University Antwerpen, Belgium, 2012.

[23] K. Badeker, "Electrical Conductivity and Thermo-Electromotive Force of Some Metallic Compounds."Ann. Phys. 22, 749, 1997.

[24] G.Haacke,"New figure of merit for transparent conductors ", J. Appl. Phus. 47 (1976) 4086.

[25] K.G. Budinski," Surrface Engineering for Wear Resistance. (Retroactive Coverage) ".Prentice-Hall, Inc, Englewood Cliffs, New Jersey 07632, United States, 1988.420 (1988).

[26] J. Barksdale, " Titanium, Its Occurrence. " Chemistry, and Technology, 2nd Edition, Roland Press Company, New York (1966).

[27] L. Vayssieres. " On solar hydrogen and nanotechnology. Wiley (2011).

[28] Sarah Bouhadoun."Synthèse de nanoparticules de dioxyde de titane par pyrolyse laser et leur application en photocatalyse. " Thèse de doctorat. Université Paris-Sud.2015.

[29] C.W. Bunn, "The lattice-dimensions of zinc oxide." NATURE,VOL.238 JULY 7 1972.

[30] Alan M. " The crystallization of anatase and rutile from amorphous titanium dioxide under hydrothermal conditions. " American Mineralogist. Vol 61; pp. 419-424, 1976.

[31] Kakkar,A.K;Yitzchaik,S ;Roscose,S.B ;Marks,T.J ;Lin,WP ;Wong,G.K.Thin Solid Films 1994,242,142.

[32] Castaneda L, Alonso J.C, Ortiz A, Andrade E, Saniger J.M, and Banuelos J.G. "Spray pyrolysis deposition and characterization of titanium oxide thin films." Materials Chemistry and Physics 77 (2002) 938–944.

[33] Luttrell T, Halpegamage S, Tao J, Kramer A, Sutter E and Batzill M. "Why is anatase a betterphotocatalyst than rutile?- Model studies on epitaxial TiO_2 films." Scientific Reports, Vol 4; pp. 40-43, 2014.

[34] N.Rahimi, R.A. Pax, E.M. Gray, " Review of functional titanium oxides. I: TiO_2 and its modifications. " Progress in Solid State Chemistry (2016), 07.002.

[35] Lan Y, Lu Y. and Ren Z. " Mini review on photocatalysis of titanium dioxide nanoparticles and their solar applications." Nano Energy. Vol. 2(5); pp. 1031-1045, 2013.

[36] S. D. Mo and W. Y. Ching, " Electronic and optical properties of three phases of titanium dioxide: Rutile, anatase, and brookite." Physical review B, 51 (1), (1995).

[37] S. Pardis, " Synthèse de nanoparticules d'oxyde de titane par pyrolyse laser : étude des propriétés optiques et de la structure électronique", Thèse de Doctorat, Université Paris Sud XI, France (2001).

[38] B. Thomas, "Des nanotitanates de soduim aux dioxydes de titane : électrode négative à base de TiO_2 (B) nanométrique pour accumulateur lithium ion", Thèse de Doctorat, Matériaux. Université de Nantes, 2009. Français.

[39] Tong Z. and Shang-Peng. " The Stability, Electronic Structure, and Optical Property of TiO_2 Polymorphs." Journal Physical Chemistry C. Vol 118 (21); pp. 11385-11396, 2014.

[40] B. S. Richards, "Novel uses of titanuim dioxide for silicon solar cells ", Thèse de doctorat, Université de New South Wales Sydney2052- Australie, (2002).

[41] H. Zhang and J. Banfield,"Understanding polymorphic phase transformation behavior during growth of nanocrystalline aggregates : insights from TiO_2." Journal of Physical Chemistry B 104, 3481 (2000).

[42] Catherine Pighini. " Synthèses de nanocristaux de TiO_2 anatase a distribution de taille contrôlée. Influence de la taille des cristallites sur le spectre Raman et étude des propriétés de surface ". Thèse de Doctorat.Université de Bourgogne. 2006.

[43] G. V. Samsonov, " The Oxide Handbook, IFI/Plenum Press ", New York, 1982.

[44] X.H. Wang, J.G. Li, H. Kamiyama, Y. Moriyoshi et al, J. Phys. Chem. B, 110 (2006) 6804.

[45] Z. Ambrus, N. Balázs, T.Alapi, N. Wittman, et al. Applied Catalysis B: Environmental, 81(1-2) 27-37 (2008).

[46] H.E. Chao, Y.U. Yun, H.U. Xingfang, and A. Larbot, Journal of the European Ceramic Society, 23 (2003) 1457-1464

[47] H. Yamashita, M. Harada, J. Misaka, M. Takeuchi, Y. Ichihashi, F. Goto, M. Ishida, T. Sasaki and M. Anpo J. Synchrotron Rad., 8 (2001) 569.

[48] A.D. Paola, G. Marc, L. Palmisano, M. Schiavello, K. Uosaki, S. Ikeda, B. Ohtani, J. Phys. Chem. B, 106 (2002) 637–645.

[49] B. R. Sankapal, M. C. Lux-Steiner, A. Ennaoui, Applied Surface Science, 239 (2005) 165.

[50] Fujishima, A., Zhang, X. and Tryk, D. A, Surface Science Reports, 2008. 63(12): p. 515-582.

[51] D. M. Blake, P. C. Maness, Z. Huang, W. A. Jacoby, Journal of Separation and Purification Methods, 28 (1999) 1-50.

[52] M.Anpo, P. Tundo, P.Anastas, Eds.; In Green Chemistry; Oxford University Press, 2000.

[53] Herrmann, J. M, Catalysis. Today, 1999. 53: p. 115-129.

[54] K. M. Schindler, M. Kunst, J. Phys. Chem. 94 (1990) 8222.

[55] M. Maeda, T. Watanabe, Surface and Coatings Technology. 201 (2007) 9309.

[56] C. B. Almquist, P. Biswas, Journal of Catalysis. 212 (2002) 145.

[57] W. Choi, A. Termin, M. R. Hoffmann, J. Phys. Chem. 98 (1994) 13669.

[58] Michael Gra1tze. " Solar Energy Conversion by Dye-Sensitized Photovoltaic Cells." Inorg. Chem. 2005, 44, 6841-6851.

[59] Nazeeruddin, M.K, DeAngelis, F. Fantacci, S. Selloni, A.Viscadi, G.Liska, P. Ito, S. Takeru, B. Gratzel, M. J. Am. Chem. Soc. 2005,127, 16835.

[60] Keis, Magnusson, E. Lindstrom, H. Lindquist, S. E. Hagfeldt, A. Sol. Energy Mater. Sol. Cells, 2002, 73, 51.

[61] Guo, P.; Aegerter, M. A. Thin Solid Films 1999, 351, 290.

[62] M. S. Roy, Y. S. Deol, M. Kumar, N. Prasad, and Y. Janu, "Dye Sensitized Solar Cells for Solar Energy Harvesting", AIP Conference Proceedings 1391, 46 (2011).

[63] Kusama H, Orita H, Sugihara H (2008) TiO_2 Band Shift by Nitrogen-Containing Heterocycles in Dye-Sensitized Solar Cells: a Periodic Density Functional Theory Study. Langmuir 24: 4411–4419.

[64] Basic Research Needs for Solar Energy Utilization Archived 16 July 2011 at the Wayback Machine, U.S. Department of Energy Office of Basic Energy Sciences, 2005.

[65] Kimberly Patch, " Solar cell doubles as battery ", Technology Research News, 2006.

[66] Ecole Polytechnique Fédérale de Lausanne, " New Efficiency Benchmark For Dye-sensitized Solar Cells", Science Daily, 3 November 2008.

[67] Nathalie Rossier-Iten," Solid hybrid dye-sensitized solar cells: new organic materials, charge recombination and stability ",École Polytechnique Fédérale de Lausanne, 2006

Chapter II

Deposition Thechniques Study on Titanium dioxide

II.1. Introduction

A thin film is a layer of material ranging from fractions of a nanometer (monolayer) to several micrometers in thickness. The controlled synthesis of materials as thin films is a fundamental step in many applications. A familiar example is the household mirror, which typically has a thin metal coating on the back of a sheet of glass to form a reflective interface. The process of silvering was once commonly used to produce mirrors, while more recently the metal layer is deposited using techniques such as sputtering. Advances in thin film deposition techniques during the 20^{th} century have enabled a wide range of technological breakthroughs in areas such as magnetic recording media, electronic semiconductor devices, integrated passive devices, LEDs, optical coatings (such as anti-reflective coatings), hard coatings on cutting tools, and for both energy generation (e.g. thin-film solar cells) and storage (thin-film batteries). It is also being applied to pharmaceuticals, via thin-film drug delivery. A stack of thin films is called a multilayer [1].

Thin film deposition is the process of creating and depositing thin film coatings onto a substrate material. These coatings can be made of many different materials, from metals to oxides to compounds. Thin film coatings also have many different characteristics which are leveraged to alter or improve some element of the substrate performance. For example, some are transparent; some are very durable and scratch-resistant; and some increase or decrease the conductivity of electricity or transmission of signals. Hence, deposition techniques fall into two broad categories, depending on whether the process is primarily chemical or physical [1].

Conventional technique can be achieved to the fabrications of titanium dioxide films include, ultrasonic spray pyrolysis, radio frequency (RF) magnetron sputtering, chemical vapor deposition (CVD), pulsed laser deposition (PLD) and sol-gel process [2]. Among of these methods, sol-gel method offers several advantages including simplicity of equipment and ease of implementation of the material, low energy cost, high purity and better homogeneity of the material, and realization of multi-component deposits in a single operation.

In this chapter, we will make a detailed investigation on the different depositing titanium oxide (TiO_2) thin films. In particular, the technique of sol-gel (spin coating) and different relationships, which are used to describe films.

II.2. What is a thin film ?

Thin films is a thin layers of material and thickness typically less than 1 µm. Thin film devices are typically 5 to 50 µm thick. Thin layer refers to growth that occurs atom by atom or molecule by molecule, while thick layer refers to growth is grain by grain [3]. Coalescence, nucleation, and the growth process all contribute to the production of thin films. Since, the absorbent species are not in thermodynamic equilibrium with the substrate, they migrate across its surface until their temperature matches that of the substrate. As a result of these displacements, when they arrive at favorable places (impurities, crystal defects, etc.) which are called nucleation sites, they create germs which will be growth for the formation of the layer [3]. These thin layers modify the properties of the substrate on which they are deposited. Because of their insulating or conductive qualities, they are mostly utilized in the fabrication of electronic components such as solar cells.

- For objects protection and improved mechanical properties, resistance to wear, corrosion or by serving as a thermal barrier. This is, for example, chrome plating;
- To modify the optical properties of objects. In particular, let us cite decorative coatings (example of gilding) or modifying the reflective power of surfaces (anti-reflective glasses or mirrors) [4].

Since thin films are nano-objects in one direction of space, the physical and chemical properties of thin films can differ from those of macroscopic objects in all their dimensions. For example, an insulating material when it is of macroscopic dimensions can become an electrical conductor in the form of a thin layer due to the tunnel effect .So , generally thin films are typically utilized when an object's surface qualities need to be improved or modified by adding or changing functionality in some way. [5].

II.3. Thin film preparation methods

The deposition of thin films on different substrates is an essential step in the majority of fields of modern technological manufacture of materials which can be semiconductors, metals, insulators, oxides [6]. The thin film production methods are distinguished by two routes:

• Physical methods that combine evaporation, spraying and laser ablation of all of these forms.

• Chemical methods include sol-gel, spray, MOCVD, etc.

There are several techniques for producing thin solid films but practically, there are two main methods of depositing thin films are: deposition by physical process and by chemical process. The classification of techniques is presented in Figure II.1.

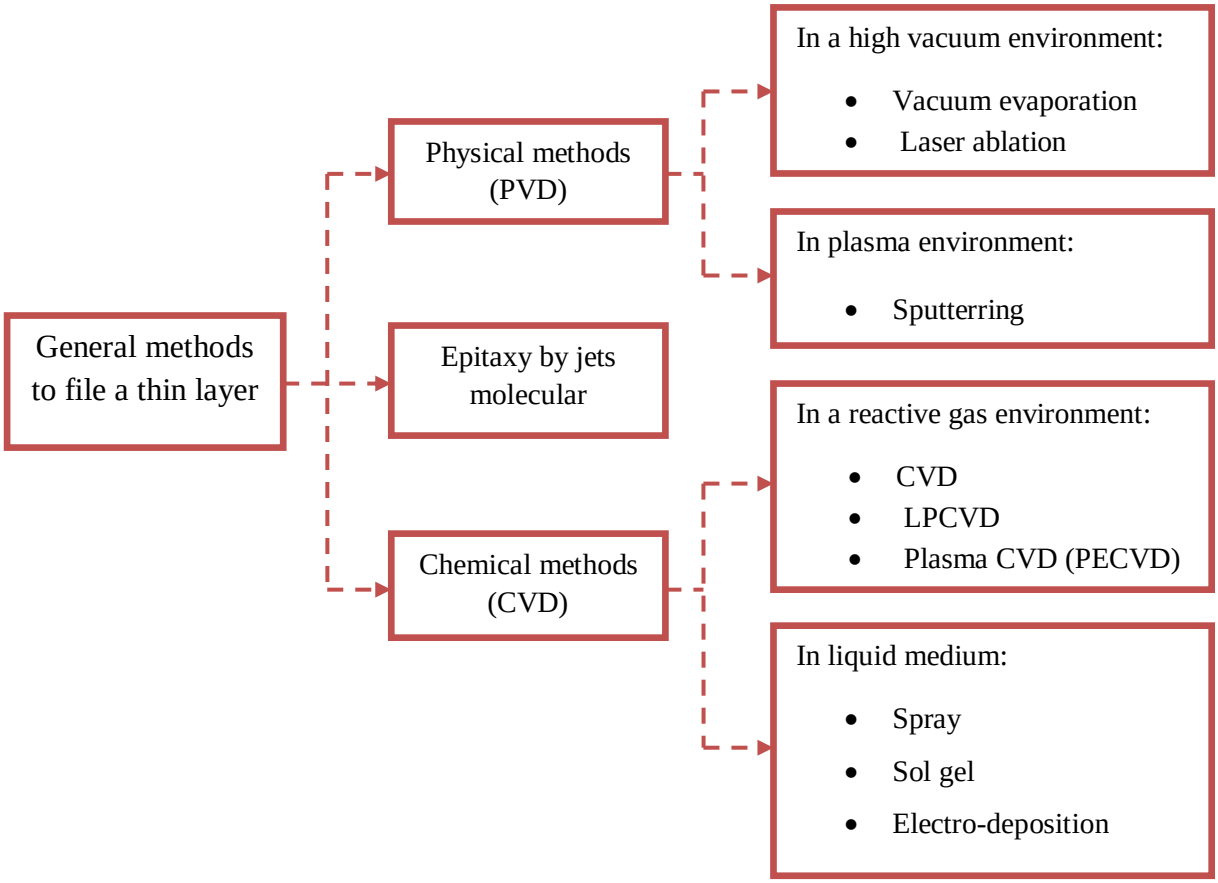

Figure II.1. Presentation of the main thin film deposition techniques [7].

II.3.1. Physical methods

II.3.1.1. Physical vapor deposition (PVD)

The development of vacuum technology has progressed considerably during the last three decades and this has enabled the development of vacuum deposition techniques such as basic PVD techniques the basis of evaporation and spraying under all these shapes. Hence, the physical vapor deposition is easy to control also the layers obtained by PVD are dense. The PVD technique is based on the vaporization or sublimation of the material to be deposited. This is put in a crucible under vacuum, then it is heated to high temperature using a filament or with an intense and energetic beam of electrons or using a laser. Once evaporated, the material in the form of molecules, atoms or clusters is deposited by condensation on the substrate, thus forming the desired thin layer [8].

These techniques have been widely used for obtaining refractory linings resistant to erosion and wear, such as alumina Al_2O_3 and stainless steel [9].

Physical vapor deposition (PVD) has a number advantages over chemical vapor deposition, for example the films are dense, the process is simple to control and there is no pollution [10].

The most widely used PVD processes are:

1- Thermal (or Vacuum) Evaporation
2- Sputtering
3- Laser ablation

II.3.1.1.1. Thermal (or Vacuum) Evaporation deposition

Thermal (or vacuum) evaporation is an old deposition process used for the formation and growth of the thin film on the surface of solid materials. Where the vapors of the material to be deposited are obtained by various methods of heating it: Joule effect, induction (a high-frequency generator's coupling), electron gun, laser beam or electric arc. Evaporation is carried out under high vacuum (pressures ranging from 10^{-3} to 10^{-4} Pa) in order to increase its speed [11], hence in order to achieve homogeneous deposits and uniform thickness, it is important to allow rotational or translational movement of the substrate to the evaporation source [12]. He process is still beneficial in a contemporary environment and widely applicable in the laboratory and industries for thin film deposition. The basic sequential steps for thermal or vacuum evaporation are shown below:

- Steam is created by subjecting the target material to a very high temperature by sublimation or boiling,
- The vapor ejected from the target material is transported to the substrate through a vacuum,
- Condensation of vapor takes place to form a solid thin film on the surface of the substrate, and additional repeatability of deposition cycles results in thin film growth and nucleation

During the thermal evaporation process, the target material vaporized from the thermal process sources gets to the substrate material with minimal interference. The process is often carried out at a high vacuum pressure (HV), and the trajectory of the movement of the target material to the substrate is a straight path trajectory termed line of sight [13]. Vapour flux is created by heating the surface of source material to a sufficiently elevated temperature in a vacuum. The flux can then condense to the surface of the substrate material to form a thin film. The vacuum environment creates a safe zone to reduce gaseous contaminants in the

deposition process to an acceptable and minimal level and allows the evaporated atoms to undergo essentially collisionless transport from the source onto the substrate.The thermal vaporization rate might be very high compared to other PVD processes [13,14]. Tungsten wire coils are commonly used as the source of the thermal heat or by using high energy electron beam for heating the target material to an elevated temperature.

One of the most salient advantages of thermal vacuum evaporation is that it enables fabrication of multilayer devices in which the thickness of each layer can be controlled easily, in contrast to spin-coating , This combinatorial fabrication greatly enhances the efficiency of systematic device fabrication aimed at optimizing the varied parameters.Consequently, the thermal vacuum deposition technique is undergoing major developments. Where, Kido and coworkers [15] have developed a linear deposition procedure with a constantly moving substrate. In this design, the sources evaporate uniformly through long narrow parallel slits as the substrate moves at a constant speed, resulting in uniform multilayer devices

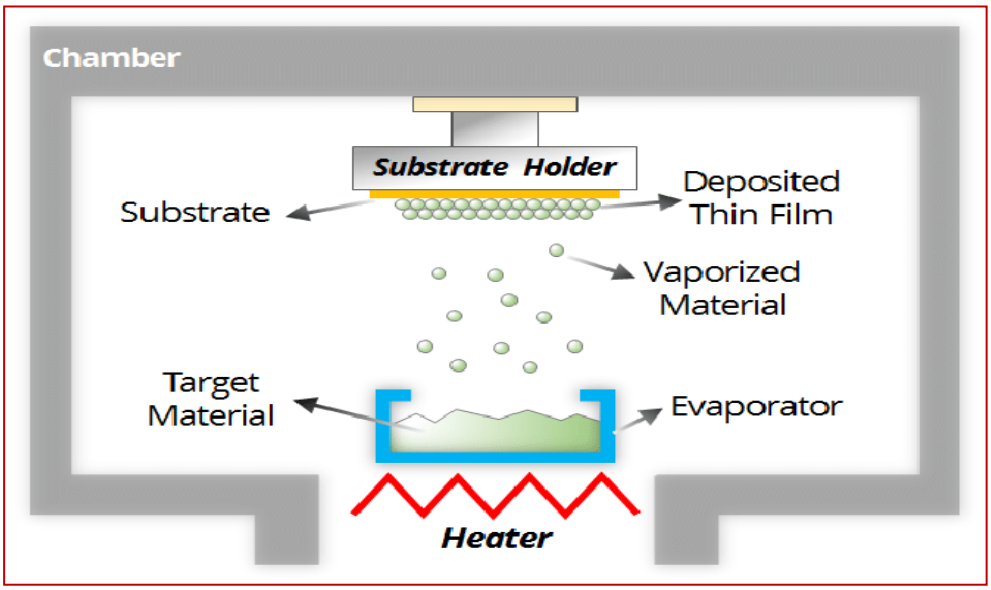

Figure II.2. Scheme of thermal evaporation deposition [16].

II.3.1.1.2. Sputtering deposition

Sputtering is the thin film deposition manufacturing process at the core of today's semiconductors, disk drives, CDs, and optical devices industries. On an atomic level, sputtering is a Physical vapor Deposition method, utilizing argon ions for bombarding a cathodically connected target, made of the coating material, atoms of the target are knocked out by the high energy ions and deposit on the substrate surface such as a silicon wafer, solar panel or optical device [17]. Basically the steps of sputtering process are the following (see Figure II.3) :

1- The neutral gas is ionized by an external power supply, producing a glow discharge or plasma
2- A source (the cathode, also called the target) is bombarded in high vacuum by gas ions due to the potential drop acceleration in the cathode sheath
3- Ions from the target are ejected by momentum transfer and diffuse through the vacuum chamber
4- Ions are deposited on the substrate to be coated and form a thin film

The sputtering process begins when a substrate to be coated is placed in a vacuum chamber containing an inert gas - usually Argon - and a negative charge is applied to a target source material that will be deposited onto the substrate causing the plasma to glow .In addition that , free electrons flow from the negatively charged target source material in the plasma environment, colliding with the outer electronic shell of the Argon gas atoms driving these electrons off due to their like charge. The inert gas atoms become positively charged ions attracted to the negatively charged target material at a very high velocity that "Sputters off" atomic size particles from the target source material due to the momentum of the collisions. These particles cross the vacuum deposition chamber of the sputter coater and are deposited as a thin film of material on the surface of the substrate to be coated [18]. Several different methods of physical vapor deposition are widely used in sputter coaters, including ion beam and ion-assisted sputtering, reactive sputtering in an Oxygen gas environment, gas flow and magnetron sputtering.

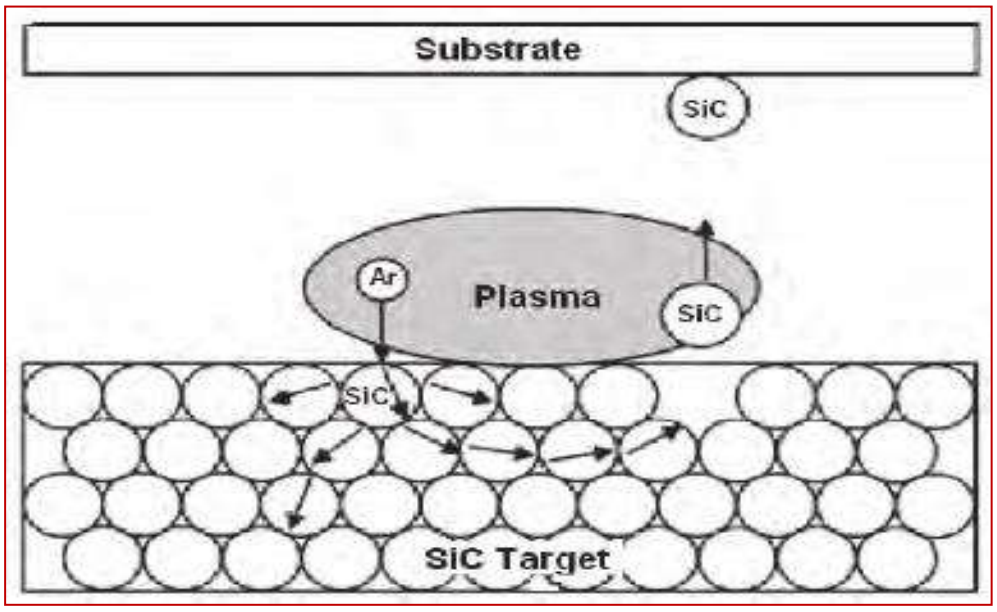

Figure II.3. Schematic of sputtering process [19].

II.3.1.1.3. Laser ablation deposition

Laser ablation (PLD: Pulsed Laser Deposition) is a complex process. The laser penetrates to the sample surface, depending on the wavelength of the laser and the refractive index of the target material. Morever, it is a deposition technique that involves depositing layers by ablating a target of the desired material using a pulsed laser [20]. This process took off at the end of the 1980s with the first realization of thin layers of the new superconducting material YBa2Cu3O4-δ with good crystalline quality, perfect control of stoichiometry and a high critical temperature which had not been reached, laser ablation could achieve a resolution around 25 nm [21].

The principle of laser ablation consist of placing the target and the substrate on which the thin film will be deposited are placed facing each other in a vacuum chamber. Above the ablation threshold, atoms, electrons, agglomerates and clusters are ejected from the surface and a plasma appears which has a very strong particle density and high excitation temperature. The laser fluence (energy per unit area) required to produce the plasma depends on the target material, its morphology and the laser wavelength. The power can reach a few tens, the plasma, generally referred to as the plume, is then condensed on a substrate heated to a high temperature (500 <T <720 ° C) to ensure crystallization of the material [22]. The laser ablation deposition process therefore involves the following steps (see Figure II.4):

1- Interaction of the radiation with the target.
2- Dynamics of materials having undergone ablation.
3- Deposit of materials torn from the target on the substrate.
4- Nucleation and growth of the thin film on the surface of the substrate.

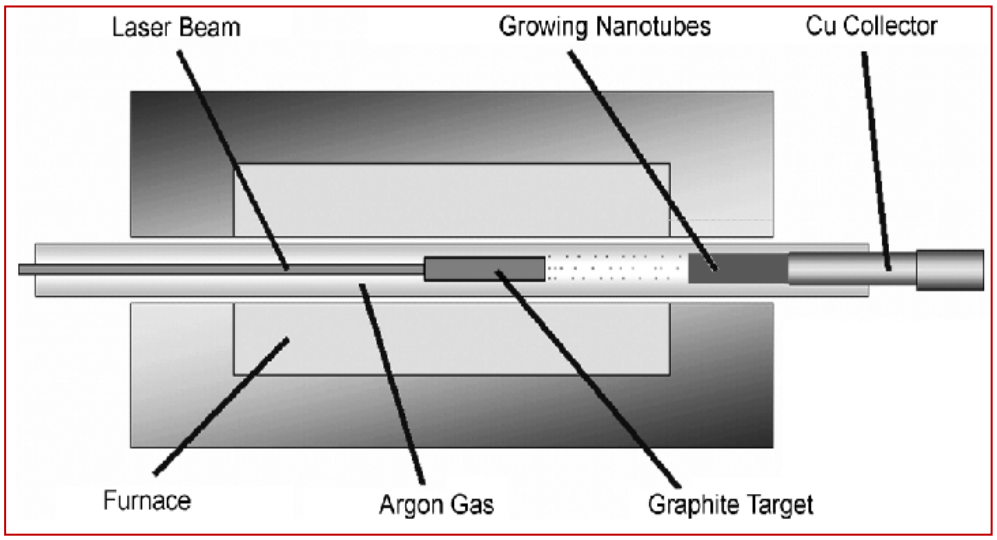

Figure II.4. Schematic diagram of laser ablation method [23].

II.3.2. Chemical methods

II.3.2.1. Chemical vapor deposition (CVD)

The CVD technique is a versatile and quick method to produce high performance, high purity solid materials. This process is often used in the semiconductor industry to produce thin films. In a typical CVD process, the substrate is exposed to one or more gas phase precursors, which react and / or decompose on the surface of the substrate to generate the desired deposit. Where, the composition and morphology of layers varies depending on the chosen precursors and substrate, temperature, chamber pressure, carrier gas flow rate, quantity and ratio of source materials, and source-substrate distance for the CVD process. Atomic layer deposition (ALD), a subclass of CVD, can provide further control of thin film deposition through sequential, self-limiting reactions of precursors on a substrate [24].

Microfabrication processes widely use CVD to deposit materials in various forms: monocrystalline, polycrystalline, amorphous, epitaxial. These materials include silicon, silica, silicon germanium, silicon carbides, carbon diamond, fibers, nanofibers, filaments, carbon nanotubes, tungsten, materials with high electrical permittivity, etc.

Generally, A thermally activated chemical vapor deposition (CVD) process involves seven steps, Explained as follows:

1- Transfer of material in the gas phase, from the inlet of the reactor to the surface of the deposit, supply by convection (forced, natural) of the gaseous species to the vicinity of the substrate.
2- Gas phase reactions during transfer.
3- Adsorption (dissociative or not) of the precursor gas on the surface of the solid.
4- Diffusion of molecules adsorbed on the surface to the growth sites.
5- Possible chemical reactions at the surface: incorporation of the atoms of the deposit (nucleation -growth).
6- Desorption of reaction products.
7- Transfer of material from the reaction products from the deposition zone to the outlet of the reactor; possible diffusion of atoms from the deposit to the substrate (and vice versa) [25].

The variants of the process are:

- LPCVD (Low Pressure Chemical Vapor Deposition), it is the case of hot wall reactor that it is heated directly.

- PECVD (Plasma Enhanced Chemical Vapor Deposition) or PACVD (Plasma Assisted Chemical Vapor Deposition).
- MOCVD: Metal-Organic Chimical Vapor Deposition.

The vapor deposition (CVD) scheme represented in Figure II.5:

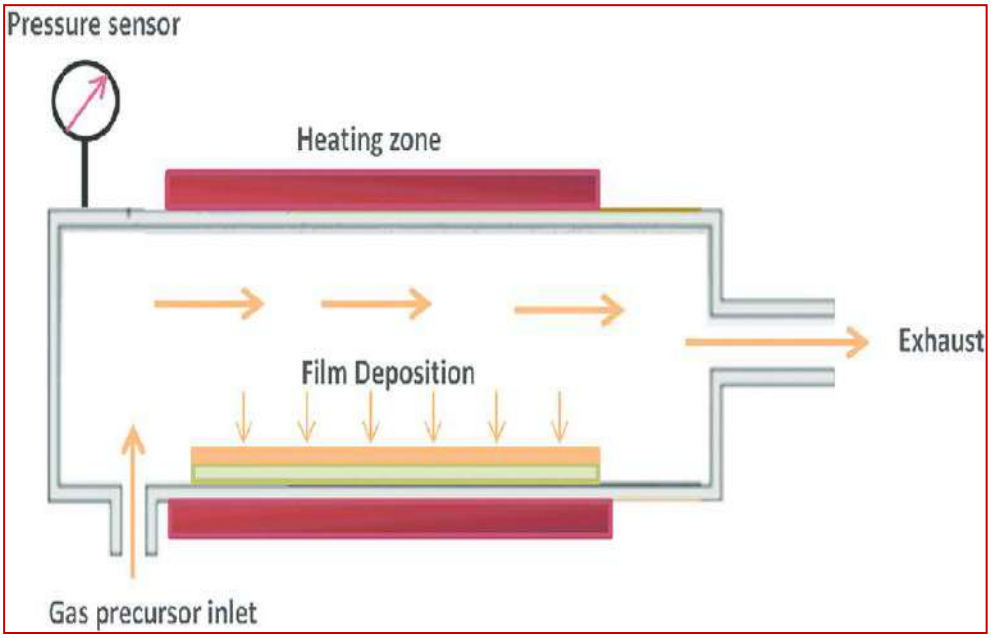

Figure II.5. Shematic diagram of a chemical vapor deposition (CVD) système [26].

II.3.3. Spray pyrolysis technique

Spray pyrolysis is a low-cost and simple technique for the fabrication of high-quality transparent and conducting oxide thin films for different optoelectronic applications. The first introduction of the spray pyrolysis technique by Chamberlin and Skarman [27] in 1966 was for the growth of CdS thin films for solar cell applications.Since then, the process has been investigated with various materials, such as Indium Tim Oxide (ITO) [28], ZnO [29], ZrO_2 [30] and others [31].

The principle of spray pyrolysis is which a solution of two or more reactive compounds is vaporized and then sprayed with an atomizer on a heated substrate. The temperature of the substrate permits the chemical reaction between the reactive chemicals and the substrate to be thermally activated. The experiment can be performed either in air or in a controlled atmosphere [32].

The general simplified scheme for spray pyrolysis deposition is shown in Figure II.6, where is displayed the three processing steps for spray pyrolysis deposition are :

1- Atomization of the precursor solution.

2- Aerosol transport of the droplet.

3- Droplet evaporation, spreading on the substrate, and drying and decomposition of the precursor salt to initiate film growth.

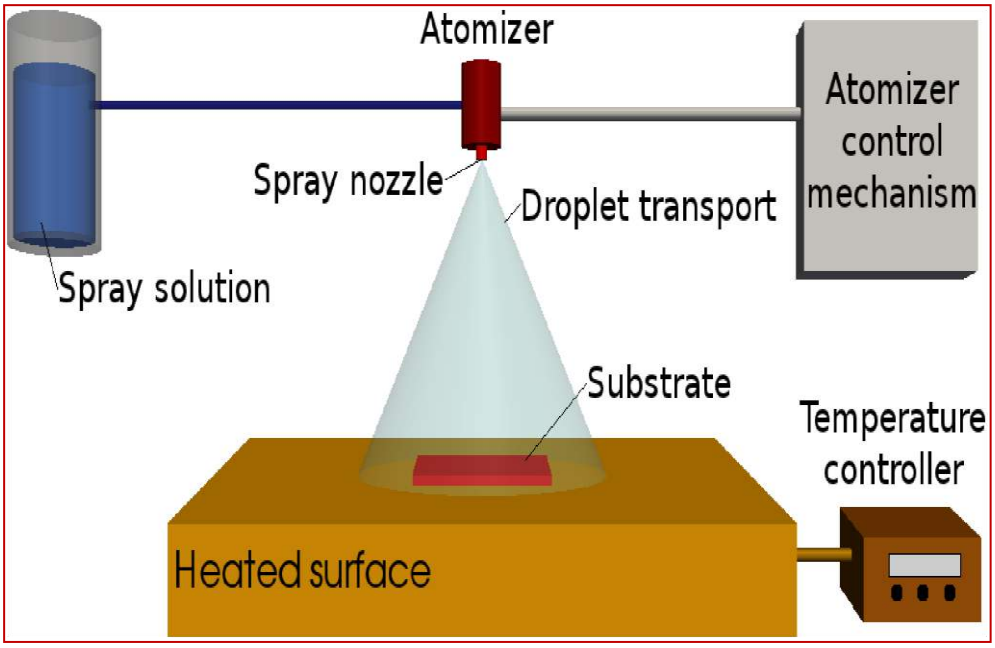

Figure II.6. General schematic of a spray pyrolysis deposition process [33].

II.3.4. Sol-Gel method

II.3.4.1. Historical

The first "sol-gel" synthesis of a silicon glass was described by a French chemist JJ EBELMEN in 1945. According to his observations, "under the action of a humid atmosphere, a silicic ether gradually transforms into a mass. transparent solid which is none other than silica comparable to the most limpid rock crystal "the" solgel "process was born, Mendeleyev [34] proposed the intervention of multiple condensation phenomena to form polysiloxanes of strong masses, but the real beginning of sol-gel materials did not take place until the 1930s. Coinciding with the recognition of the covalent model of polymers, making it possible to establish the fundamental bases in the understanding of the mechanisms of hydrolysis and condensation. But it was not until nearly a century that this idea was taken up by the glass industry. The first "solgel" patent was filed in 1939 in Germany by Schott Glaswerke for the production of mirrors. These mirrors, marketed in 1959, were followed by many other products, in particular anti-reflective coatings which improve the optical properties of building glazing.

II.3.4.2. What is the Sol-Gel method ?

Sol gel is a method for producing solid materials from small molecules. The method is used for the fabrication of metal oxides, especially the oxides of silicon (Si) and titanium (Ti).In addition, sol gel technique is a process for the development of materials allowing the synthesis of glasses, ceramics and organo-mineral hybrid compounds, from precursors in solution. It makes it possible to produce thin layers made up of stacks of metal oxide nanoparticles.

The sol-gel method allows the production of a wide variety of oxides in different configurations (monoliths, thin films, fibers, powders). This great diversity, both in materials and in shaping, has made this process very attractive in technological fields such as optics [35] electronics [36], biomaterials [37]. It also has the advantage of using a soft chemistry and being able to lead to very pure and stoichiometric materials [38]. The basic principle of the sol-gel process (corresponding to the abbreviation of "solution-gelation" is as follows: a solution based on precursors in the liquid phase is transformed into a solid by a set of chemical reactions of the polymerization type at ambient temperature (See Figure II.7).

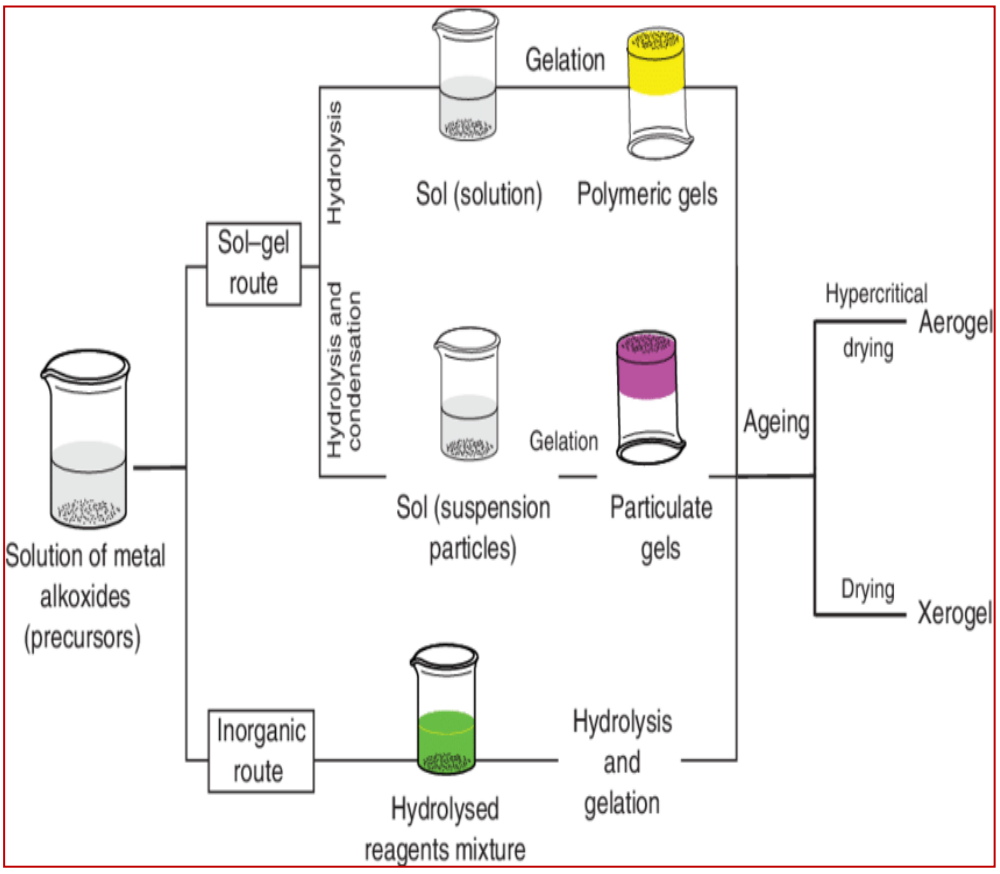

Figure II.7. Schematic diagram of sol-gel process [39].

The principle of the Sol-Gel route is to obtain inorganic materials in the form of films of high optical quality from an organic solution. Obtaining a Sol-Gel film is carried out in three stages as shown in the (Figure II.8) [34]:

1- The first is the development of a metal alkoxide solution.
2- The second is the deposition of the solution, in the form of a thin layer, on a substrate
3- The last step is the heat treatment of the gelled layer in order to remove organic compounds and densify the film

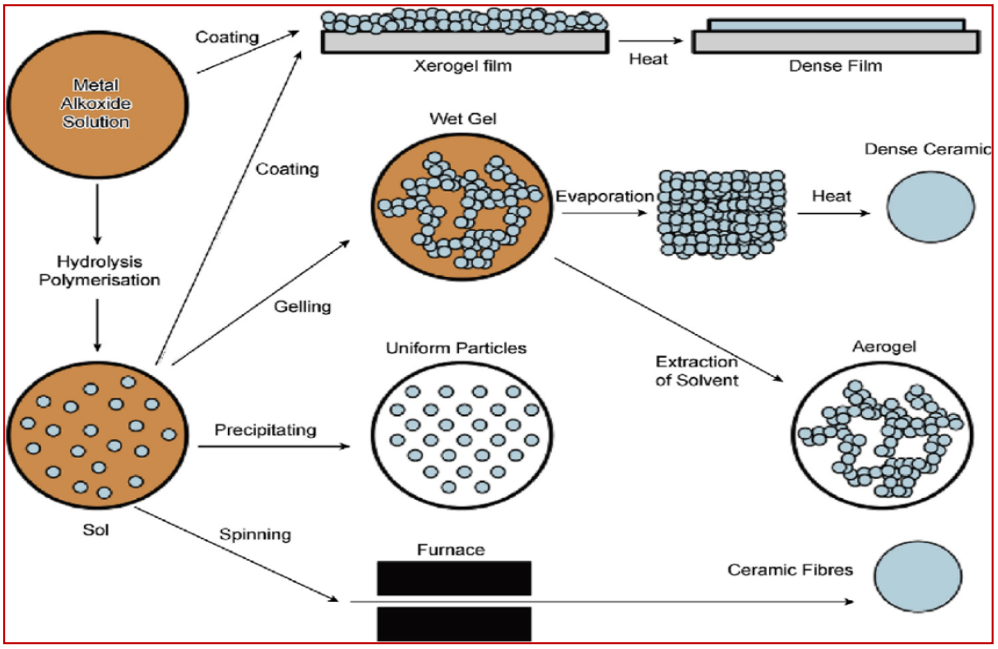

Figure II.8. Different stages and routes of sol-gel synthesis [40].

II.3.4.3. The precursors

The precursors constituting "the soil" can be of two types. They are either colloidal particles dispersed in a liquid, or organometallic precursors in solution in a solvent. What ever its nature, the precursor is dissolved before being hydrolyzed. It is the polymerization of these precursors that results in a solid three-dimensional network that is interconnected and stable through the formation of M-O-M bonds. The system is then in the frozen state [41].

II.3.4.3.1. Inorganic or colloidal precursors

The aqueous solution of an inorganic salt is used. In this solution, the M^{z+} cations are picked up by polar H_2O molecules. An $(M - OH)^{(z-1)+}$ bond is formed when an electron from

a saturated σ orbital is transferred to a lower energy orbital and unsaturated. This in fact resultsin the two partial reactions that follow:

$$M^{z+} + (OH)^{-} \leftrightarrow (M–OH)^{(z-1)+} \quad \text{(II.1)}$$

$$(M–OH)^{(z-1)+} \leftrightarrow (M=O)^{(z-2)+} + H^{+} \quad \text{(II.2)}$$

According to the aforementioned reactions that in an acidic medium, by increasing the pH of the solution, one of the following two types of ligands can be formed:

- Hydroxo ligand : $(M– (OH))^{(z-1)+}$.
- An Oxo ligand : $(M = O)^{(z-2)+}$.

Condensation reactions involving hydroxo $(M– (OH))^{(z-1)+}$ ligands lead to the formation of (M – OH – M) or (M – O – M) bonds. Note, however, that colloidal solutions and stable gels can be obtained by keeping the pH constant. This route is mainly used in industrial powder manufacturing processes [41].

II.3.4.3.2. Organic or polymeric precursor

The most widely used organic precursors are metal alkoxides of generic formula $M(OR)_z$ where M denotes a metal of valence Z and R a radical of an alkyl chain— $(C_n H_{2n+1})$. Metal alkoxides must be of high purity and exhibit high solubility in a wide variety of solvents. This condition of high solubility can generally only be achieved in organic solvents. The main advantage of using organic precursors is that they allow a homogeneous and intimate molecular mixture of different precursors in order to produce glasses and ceramics with several components [41].

II.3.4.4. Reaction mechanisms

Metal alkoxides are first diluted in an organic solvent (usually alcohol). Their sol-gel transformation (solidification) occurs through an inorganic polymerization mechanism [42,43].

The chemical mechanism of transformation breaks down into two reactions:

- ❖ hydrolysis
- ❖ condensation of alkoxides.

II.3.4.4.1. Hydrolysis

In order for the alkoxides to condense at room temperature, hydrolysis of the –OR groups must initiate the reaction process. This step is necessary to give rise to hydroxyl groups –OH:

$$M(OR)_n + H_2O \rightarrow HO - M(OR)_{n-1} + ROH \quad (II.3)$$

Figure (II.9) shows the hydrolysis steps for a metal alkoxide; a nucleophilic substitution (step 1) on the metal atom with proton transfer (step 2) and departure of the leaving group (step 3). Hydrolysis is a nucleophilic substitution of a ligand — OH for a ligand — OR. It is accompanied by the intake of water as well as the ejection of alcohol. During this step, the functionality of the precursor is created with respect to what is called polycondensation.

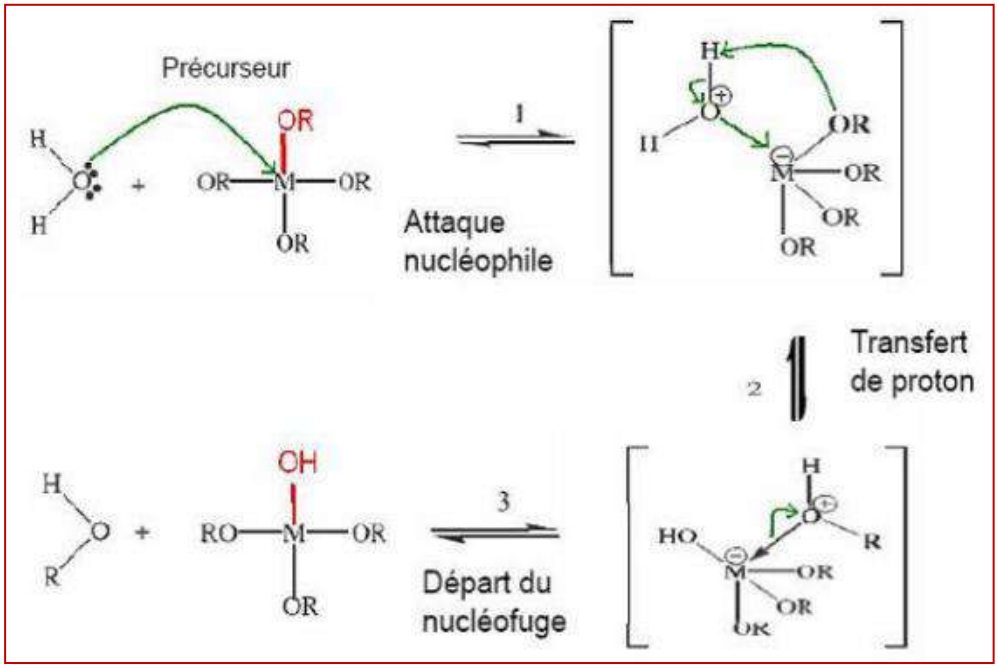

Figure II.9. Mechanism of hydrolysis of metal alkoxides M (OR)n [44].

II.3.4.4.2. The condensation

The condensation reaction, otherwise known as polymerization, is a complex mechanism because four mechanisms (alkoxolation, oxolation, alcoholation, and isolation) can compete for polymerization and formation of a MOM bridge. The relative importance of each of the mechanisms depends on the experimental conditions.

a. Alkoxolation

The reaction occurs between two metal alkoxides, One of them is only partially hydrolyzed. Its method of action is similar to that of hydrolysis. (Figure II.10).

$$(RO)_{n-x}M(OH)_x + M(OR)_n \longrightarrow (RO)_{n-x}(OH)_{x-1}M\text{-}O\text{-}M(OR)_{n-1} + ROH \quad (II.4)$$

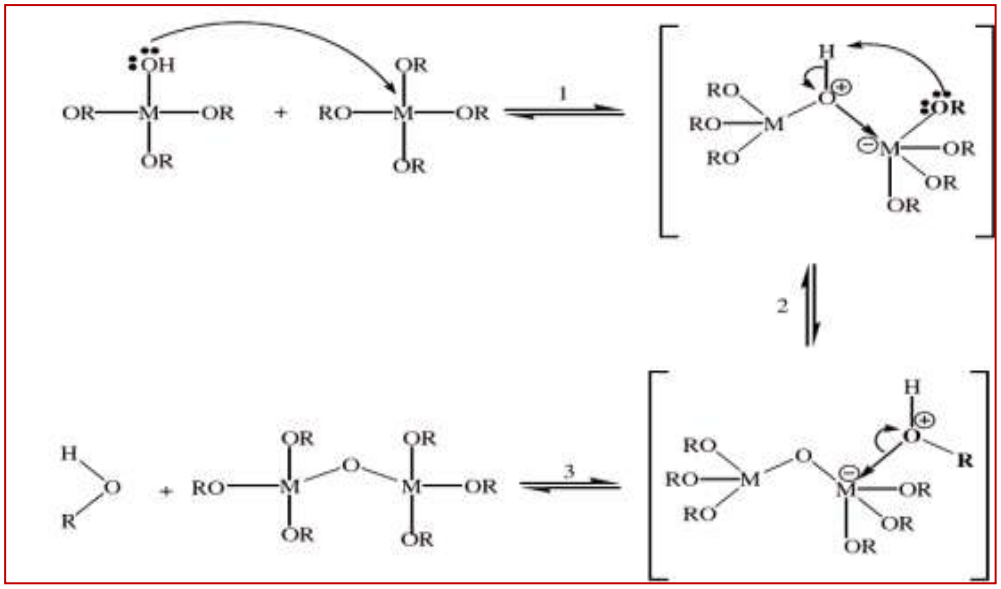

Figure II.10. Mechanism of alkoxolation of metal alkoxide M(OR)n [44].

b. Oxolation

Between two partly hydrolyzed alkoxides, this mechanism occurs:

$$(RO)_{n-x}M(OH)_x+(RO)_{n-y}M(OH)_y \longrightarrow (RO)_{n-x}(OH)_{x-1}M\text{-}O\text{-}M(OH)_{y-1}(OR)_{n-y} + H_2O \qquad (II.5)$$

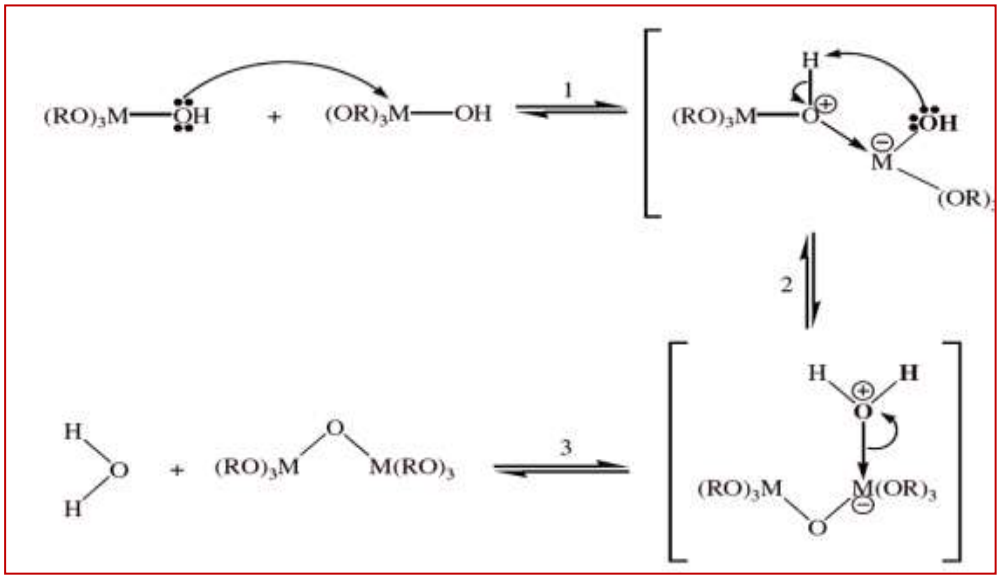

Figure II.11. Mechanism of oxolation of metal alkoxide M(OR)n [44].

c. Alcohol

This reaction does not depend on hydrolysis. Some terminal OR ligands (linked to a single metal center) can act as a bridge between metal centers as shown by the following reaction:

$2M(OR)_n \longrightarrow (RO)_n M\text{-}OR\text{-}M(OR)_{n-1}$ (II.6)

It is alcoholation that induces the molecular complexity of species during polymerization by formation of oligomers before the addition of water. Before the hydrolysis step begins, it is generally difficult to form molecules of large masses, this reaction being highly sensitive to the steric hindrance of the system.

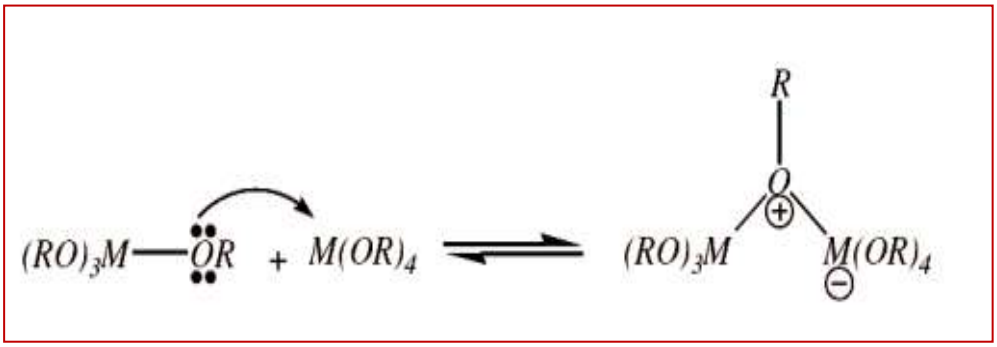

Figure II.12. Mechanism of alcohol of metal alkoxide M(OR)n [44].

d. Isolation

Unlike alcoholation, isolation requires prior hydrolysis of a metal alkoxide. It follows the same mechanism as alcoholation except that the bridge formed is a hydroxyl bridge as shown by the following reaction:

$M\text{-}(OR)_n + (OH)_x\text{-}M(OR)_{n-x} \longrightarrow (OR)_n M\text{-}(OH) - M\text{-}(OR)_{n-x} + (OH)_{x-1}$ (II.7)

Figure II.13. Mechanism of isolation of metal alkoxide M(OR)n [44].

II.3.4.4. The sol-gel transition

The pattern generally adopted for gelation is that of growing polymer chains which agglomerate by polycondensation thus forming clusters [45]. At, as the hydrolysis and condensation reactions progress, polymer clusters are created. When one of these clusters reaches an infinite dimension, the viscosity also becomes infinite: this is the Sol-Gel transition point [45]. The gel is generated when all of the linkages have been utilised. The solid cluster

thus formed is actually an interweaving of macromolecular chains, forming an amorphous solid structure. This structure still contains trapped liquid masses [46], their removal will therefore require a light heat treatment. The morphologies of the polymer chains indicate:

- That an acidic medium promotes hydrolysis, and the gel adopts a chain configuration (reptal model).
- That a basic medium accelerates the condensation, and the gel adopts a configuration in balls (spherical model).

The catalyst therefore acts directly on the microstructure of the material produced. This factor will also play an important role in the porosity of the oxide, which will partially condition the physical properties and therefore the usability of the material in the form of a thin film.

On a macroscopic level, the transition can be followed by the mechanical behavior of the solution. The solution's viscosity then rises as a result of this [47]. The evolution of the viscosity of a sol, and that of its elastic constant are presented schematically in (Figure II.14). Where we notice that with the complete formation of the gel, the viscosity becomes infinite, whereas the elastic constant approaches a finite value G Max. Like any chemical reaction, the Sol-Gel transition is sensitive to its environment such as: temperature and humidity, which can thus modify the kinetics of the reactions challenges.

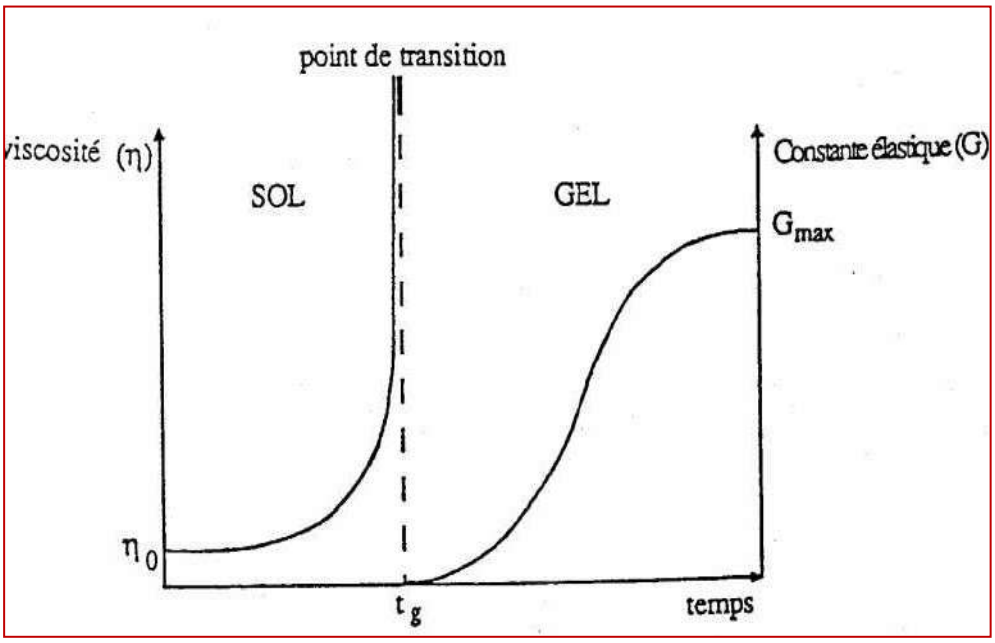

Figure II.14. Evolution of the sol viscosity and the elastic constant of the gel, tg being the time corresponding to the Sol-Gel transition [45].

II.3.4.5. The different methods of thin film deposition by sol-gel

The sol-gel deposition can be carried out in two different ways.

II.3.4.5.1. Spin coating method

Spin coating is a procedure used to deposit uniform thin films onto flat substrates. This method consists in depositing by centrifugation a solution deposited in excess on a substrate. This technique has the advantage of being simple to implemented, for moderate investments. It gives excellent results on flat substrates with dimensions of the order of cm^2 [48]. This deposition method can be broken down into four phases shown schematically in (Figure II.15).

1- ***Deposition***: during this step, the deposition of the solution on the substrate.

2- ***Spin-up***: is the start of rotation, this step causes the liquid to flow out of the substrate.

3- ***Spin-off*** : the constant speed rotation allows the ejection of the excess liquid in the form of droplets and the reduction of the film thickness evenly.

4- ***Evaporation***: during this step, the evaporation of the most volatile solvents accentuates the reduction in the thickness of the deposited film [41].

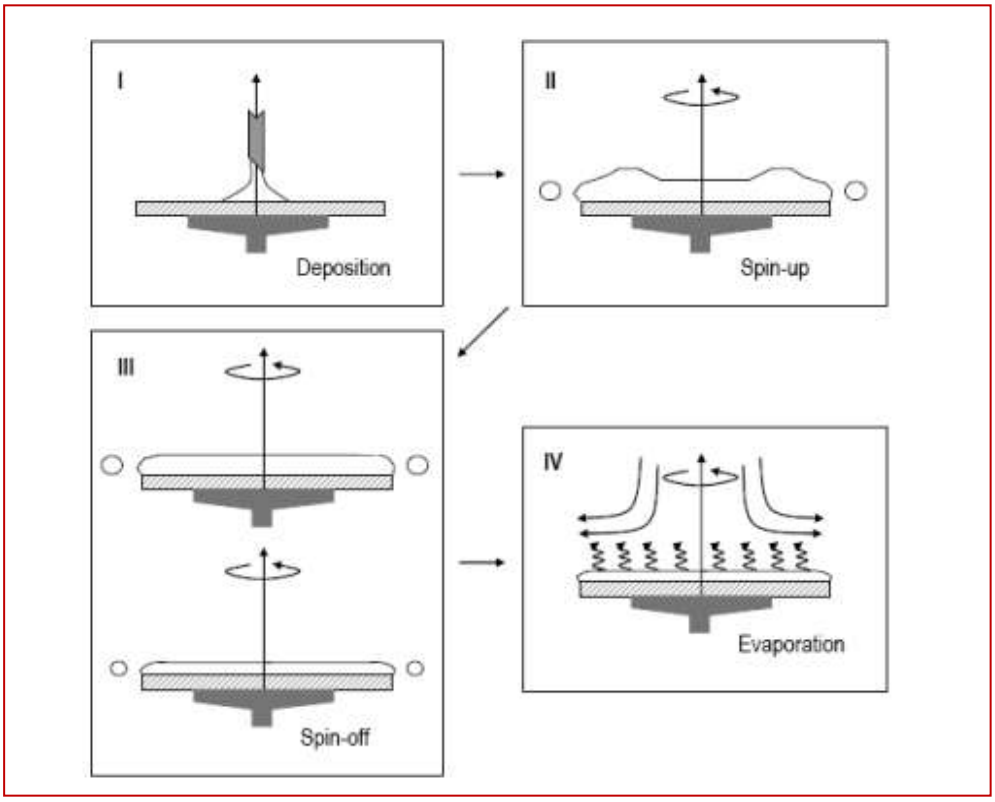

Figure II.15. Stages of spin-coating method : (I) Deposition, (II) Spin-up, (III) Spin-off and (IV) Evaporation [49].

a. Advantages to the technique of spin coating

- There is less loss of materials than with vapor-phase deposition.
- It is a relatively inexpensive technique.
- Aa spinning plate is far cheaper than a vacuum deposition system.
- The spin-coating means we can quickly and easily deposit thin layers.

b. Disadvantages to the technique of spin coating:

- possibility of the presence of contaminants (traces of solvent, oxygen, humidity, etc.).
- difficulty of accurately controlling the deposition (homogeneity, rugosity, etc.).

II.3.4.5.2. Dip-coating method

This method involves immersing the substrate in the solution and removing it at a constant speed to obtain a film of uniform thickness. In addition, dip coating technique is being easy to implement and it has the particularity of allowing layered deposits under a magnetic field, which makes it possible to orient the magnetic nanoparticles within the matrix thus formed.

The dip-coating process can be separated into five stages [50], (see Figure II.16).

1- ***Immersion***: The substrate is immersed in the solution of the coating material at a constant speed (preferably jitter-free).

2- ***Start-up***: The substrate has remained inside the solution for a while and is starting to be pulled up.

3- ***Deposition***: The thin layer deposits itself on the substrate while it is pulled up. The withdrawing is carried out at a constant speed to avoid any jitters. The speed determines the thickness of the coating (faster withdrawal gives thicker coating material).

4- ***Drainage***: Excess liquid will drain from the surface.

5- ***Evaporation***: The solvent evaporates from the liquid, forming the thin layer. For volatile solvents, such as alcohols, evaporation starts already during the deposition and drainage steps.

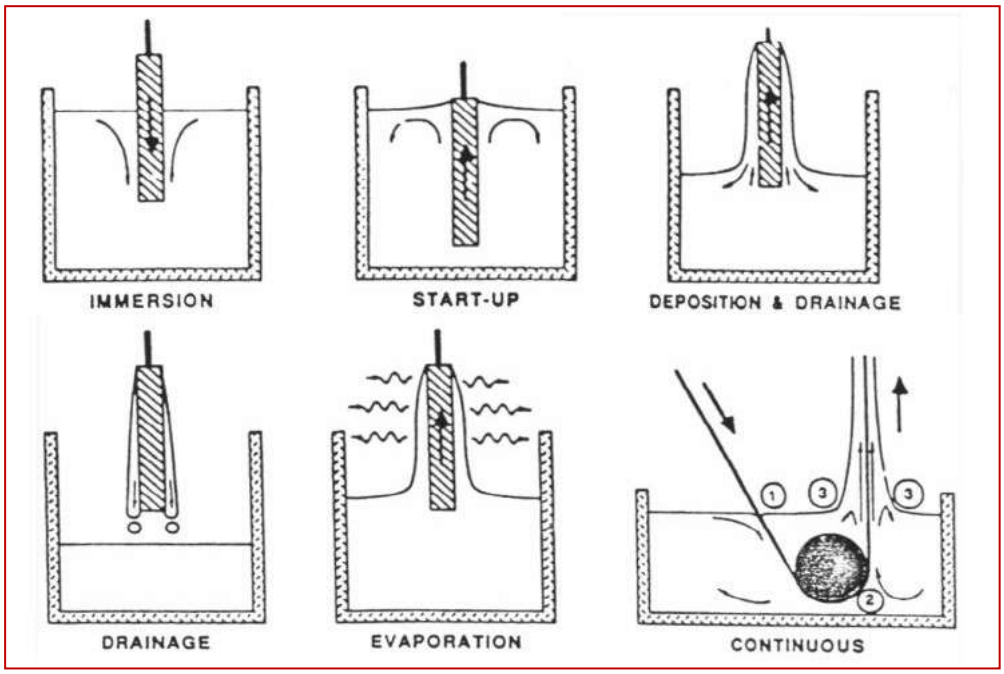

Figure II.16. The different stages of the dip-coating technique [51].

II.3.4.6. What are advantages and disadvantages of the Sol-Gel method ?

a. The advantage

- Versatile: better control of the structure, including porosity and particle size, possibility of incorporating nanoparticles and organic materials into sol-gel-derived oxides.
- Better homogeneity: due to mixing at the molecular level, high purity.
- Simplicity of equipment and ease of use of the material where no need for special or expensive equipment.
- Films are easily anchored on the substrate bearing the complicated shapes and large surfce area
- Suitable for deposition on other substrates like stainless steel plate, aluminium plates, silica glass rashing rings, glass wool.
- Ability to generate thin layers of inorganic oxides on heat-sensitive surfaces at low temperatures.
- Less energy consumption: since the network structure may be formed at relatively low temperatures near Tg, there is no need to attain the melting temperature.
- Ability to optimize the morphology of films based on applications that have been explored.
- Easy to perform in the laboratory [52].

b. The disadvantage

- High cost of alkoxide precursors.
- Delicate control of the process and long process times.
- Handling a large amount of solvents [53].

II.3.4.7. Applications of sol-gel method

The materials resulting from sol-gel technology are found in four main industrial activities, namely:

- ✓ ***Chemical applications***: which include the synthesis of powders, catalysts, membranes, gas barrier, and repellent film.
- ✓ ***Optical and photonic applications***: which include fluorescence solar collector, solar cell, laser element, light guide, optical switching, light amplification, antiereflecting coatings, and non-linear optical effect (second generation).
- ✓ ***Biochemical applications***: which include the formulation of drugs, the development of new treatments, cosmetic formulations, artificial bone tissues, dentistry ... These applications, although few in number on the market, are promised significant development. However, they will require the most severe production constraints (GMP in the pharmaceutical sector).
- ✓ ***Structural applications***: for the manufacture of glass, ceramics, insulation, refractory or composite materials, fibers, abrasives and coatings. Among these materials, it is also necessary to include electronic applications for the synthesis of dielectric, ferromagnetic and electro-chromic materials.
- ✓ ***Thermal application*** : which include the refractory ceramics, fibers wood, aerogels, and low expansion ceramics.
- ✓ ***Mechanical application*** : which include the protection with hard coat, and strong ceramics abrasive.
- ✓ ***Electronique application (ferrolectricity electronic and ionic conduction)*** : which include the capacitor, piezoelectric transfer, non-volatile memory, transparent semiconductors, and solide electrolute (battery,fuel cell).
- ✓ ***Biomedical application*** : which include the entrapment of enzyme, cell, coated implant, and medical test [54].

II.3.5. What is the difference between PVD and CVD?

Table (II.1) presents a comparison between some characteristics specific to the two methods PVD and CVD.

Table II.1. The difference between PVD and CVD method [55].

Process	*PVD*	*CVD*
Definition	PVD is physical vapour deposition	CVD is chemical vapour deposition
Coating Material	Solide form	Caseous form
Method	Atoms are moving and depositing on the substrate	The gaseous molecules will react with the substrate
Deposition temperature	Deposits at a relatively low temperature (around 250 °C-450 °C)	Deposits at relatively high temperatures in the range of 450 °C to 1050 °C
Applications	• Suitable for coating tools that are used in applications that demand a tough cutting edge • TiN, TiAlN, TiCN and CrN coating for cutting tools; • AlSn coating on engine bearings, diamond like coating for valve trains; • Coating for forming tools; • Anti-stick wear resistant coating for injection molds; • Decorative coatings of sanitary and door hardware.	• Maily used for depositing compound protective coating • Integrated circuits; • Optoelectrical devices; • Micromachines; • Fine powders; • Protective coatings; • Solar cells; Refractory coating for jet engine turbine blades

II.4. Characterization techniques

In order to analyze and study the characterization titanium oxide (TiO_2) thin films, several characterization techniques are used such as structural, optical, electrical and surface morphological characterization techniques. The nature of crystal structure and crystalline quality of TiO_2 thin films are studied using X-ray diffraction (XRD), Scanning electron microscopy (SEM) is used to investigate the surface morphology as well as the optical quality of thin film surfaces. In addition that, the optical characteristics have been studied from the transmittance and absorbance using a UV-Visible spectrophotometer and fourier transform infrared (FTIR). The Four point probe technique is carried out to study the measure electrical resistivity and conductivity of the films. We now discuss the different techniques used to characterized titanium oxide thin films.

II.4.1. X-ray diffraction (XRD)

X-ray diffraction (XRD) is an analytical technique based on the study of crystal structure by diffraction of waves: X-rays or electrons. Diffraction depends on the structure studied as well as the wavelength of the radiation used. Indeed, at optical wavelengths the superposition of waves elastically scattered by the atoms of the crystal studied produces classical optical refraction. When this is comparable to the parameters of the crystal lattice, we observe several beams scattered in directions different from that of the incident beam [56].

- **Principle of operation**

In a crystal lattice, the arrangement of atoms is regular and periodic, the distance between the atomic planes of a family of planes (hkl) is called the interreticular distance (Figure III.5). When a rigorously monochromatic x-ray beam (a single wavelength λ) interacts with a solid, there is only diffraction if the atoms of that solid are ordered as a crystal lattice. Part of the incident beam is diffracted by atoms at the same wavelength. If the scattered radiation is in phase, the intensity of the re-emitted X-radiation will be observable and will form a diffracted beam [57].

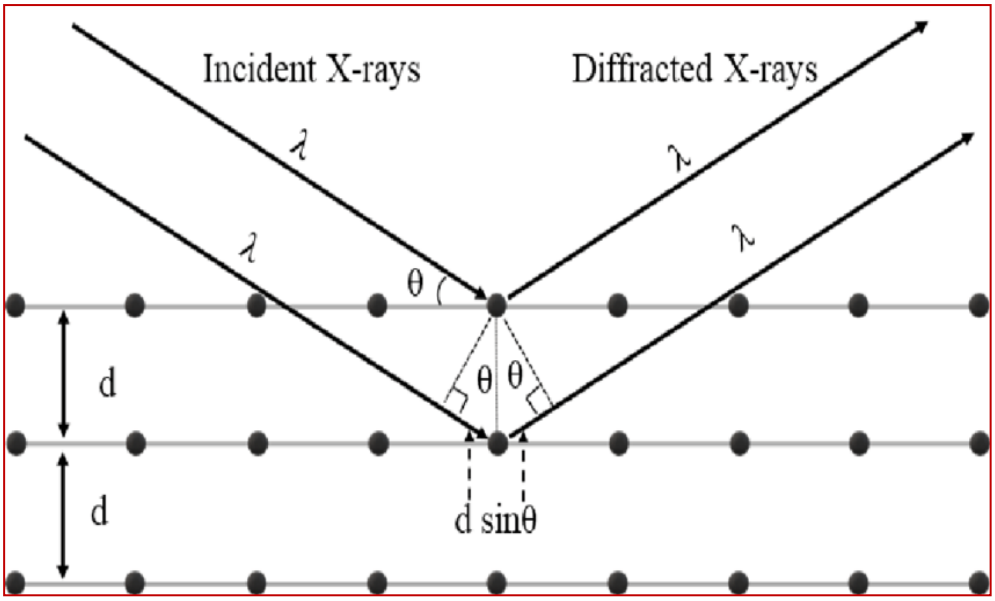

Figure II.17. The principle of Bragg's law [57].

The directions in which the interferences are constructive, called "diffraction peaks", can be determined very simply by the following formula, known as Bragg's law [58]:

$$n\,\lambda = 2d_{hkl}\sin\theta \qquad \text{(II.8)}$$

Where: n is the order of diffraction (whole number) , λ is the wavelength of the x-rays, d_{hkl} is the spacing between consecutive parallel planes and θ is the angle between the incident or diffracted X-rays and the reticular plane.

For the structural characterization of our different thin layers we used the ***BRUKER-AXS type D8*** diffractometer, operating in Bragg - Brentano geometry, according to the following conditions:

- ✓ The X-ray source is produced by a copper anticathode, supplied by a voltage generator - current of 40 kV – 40 mA.
- ✓ The X radiation used is copper Kα (λCuα = 1.54056 Å) obtained by a monocrystalline germanium monochromator.
- ✓ The sample is placed on a goniometric head.
- ✓ The XRD spectra of the samples are recorded for 2θ between 20 ° and 80 ° with a step of 0.02 °.

The identification of the phases and crystal structures of the sample can be done by simply comparing the recorded spectra with the databases of the ASTM files.

II.4.1.1. Determination of the crystallite size (D)

The crystallite size (D) of the film is calculated using Scherrer's formula [59]:

$$D = \frac{0.9\lambda}{\beta.\cos\theta} \qquad \text{(II.9)}$$

Where: λ is the wavelength of the x-ray, β is the full width at half maximum intensity in radians (FWHM), and θ is the Bragg angle.

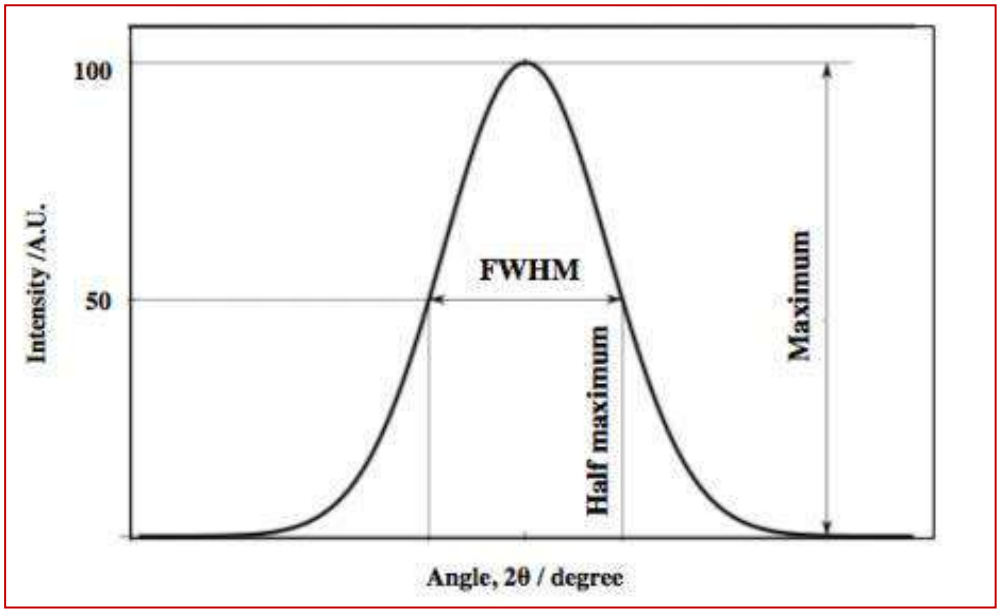

Figure II.18. The definition of FWHM from the X-ray diffraction curve [60].

II.4.1.2. Determination of the lattice parameters (a,c)

The d-spacing and the lattice constants "*a* "and "*c* "of anatase TiO_2 films was calculated from the given relation [61,62]:

$$d_{hkl} = \frac{n\lambda}{2\sin\theta_{hkl}} \qquad \text{(II.10)}$$

$$\frac{1}{d^2} = \frac{h^2+k^2}{a^2} + \frac{l^2}{c^2} \qquad \text{(II.11)}$$

Where: d is the lattice spacing of the crystal planes (h k l).

II.4.1.3. Determination of the strain (ε)

The strain (ε) was determined by using the relation [63] :

$$\boldsymbol{\varepsilon = \frac{\beta.\cos\theta}{\lambda}} \qquad \text{(II.12)}$$

Where: β is the full width at half maximum (FWHM) of the peak and θ is the Bragg's angle.

II.4.1.4. Determination of the dislocation density (δ)

The term "dislocation" refers to a crystallographic defect in materials science. It has an inverse relation with crystallite size and is calculated by using the relation [64]:

$$\boldsymbol{\delta = \frac{1}{D^2}} \qquad \text{(II.13)}$$

II.4.1.5. Determination of the stress (σ)

The residual stress in the plane of the film can be calculated quantitatively using following expression [65]:

$$\boldsymbol{\sigma = \frac{\varepsilon}{2} . E} \qquad \text{(II.14)}$$

Where : ε is the strain, E represents Young's modulus of TiO_2 which is taken as 282.76 GPa [66.67].

II.4.1.6. Determination of the Specific Surface Area (SSA)

The surface states will play an important role in the nanoparticles, due to their large surface to volume ratio with a decrease in particle size [68]. SSA is a material property. It is a derived scientific value that can be used to determine the type and properties of a material. It has a particular importance in case of adsorption, heterogeneous catalysis and reactions on surfaces. SSA is the Surface Area (SA) per mass. Zhang et al. report, the specific surface area and surface to volume ratio increase dramatically as the size of materials decreases. The high surface area of TiO_2 nanoparticles facilitates the reaction / interaction between TiO_2 based devices and the interacting media, which mainly occurs on the surface or at the interface and strongly depends on the surface area of the material [69]. Mathematically, SSA can be calculated using formula [70]:

$$\mathbf{SSA} = \frac{\mathbf{6.10^3}}{\mathbf{D.\rho}} \qquad \text{(II.15)}$$

Where : SSA are the specific surface area, D is the crystallite size, and ρ is the density of TiO_2 (4.23 $g.cm^{-3}$).

II.4.1.7. Determination of the volume of the unit cell (V)

The volume of the unit cell is evaluated by the relation [71]:

$$\mathbf{V = 0.866.a^2.c} \qquad \text{(II.16)}$$

Where : 'a' and 'c' is the lattice constant.

II.4.1.8. Determination of the X-ray density

X-ray density was assessed by using relation [72]:

$$\mathbf{X\text{-ray density} = 8M / N_a.a^3} \qquad \text{(II.17)}$$

Where : M is the molecular weight, Na is the Avogadro number and 'a' is the lattice constant.

II.4.1.9. Determination of the degree of crystallinity (Xc)

The degree of crystallinity can be calculated using formula [72]:

$$\mathbf{X_C = (0.24/ \beta)^2} \qquad \text{(II.18)}$$

Where : β is the full with of half maximum of preferred orientation which is (101) in this case.

II.4.2. Scanning Electron Microscope (SEM)

II.4.2.1. What is a SEM ?

SEM stands for scanning electron microscope. The SEM is a microscope that uses electrons instead of light to form an image. Since their development in the early 1950's, scanning electron microscopes have developed new areas of study in the medical and physical science communities. The SEM has allowed researchers to examine a much bigger variety of specimens.SEM is widely used to investigate the microstructure and chemistry of a range of materials.

The SEM has a large depth of field, which allows a large amount of the sample to be in focus at one time. The SEM also produces images of high resolution, which means that closely spaced features can be examined at a high magnification. Preparation of the samples is relatively easy since most SEMs ony require the sample to be conductive. The combination of

higher magnification, larger depth of focus, greater resolution, and ease of sample observation makes the SEM one of the most heavily used instruments in research areas today [73].

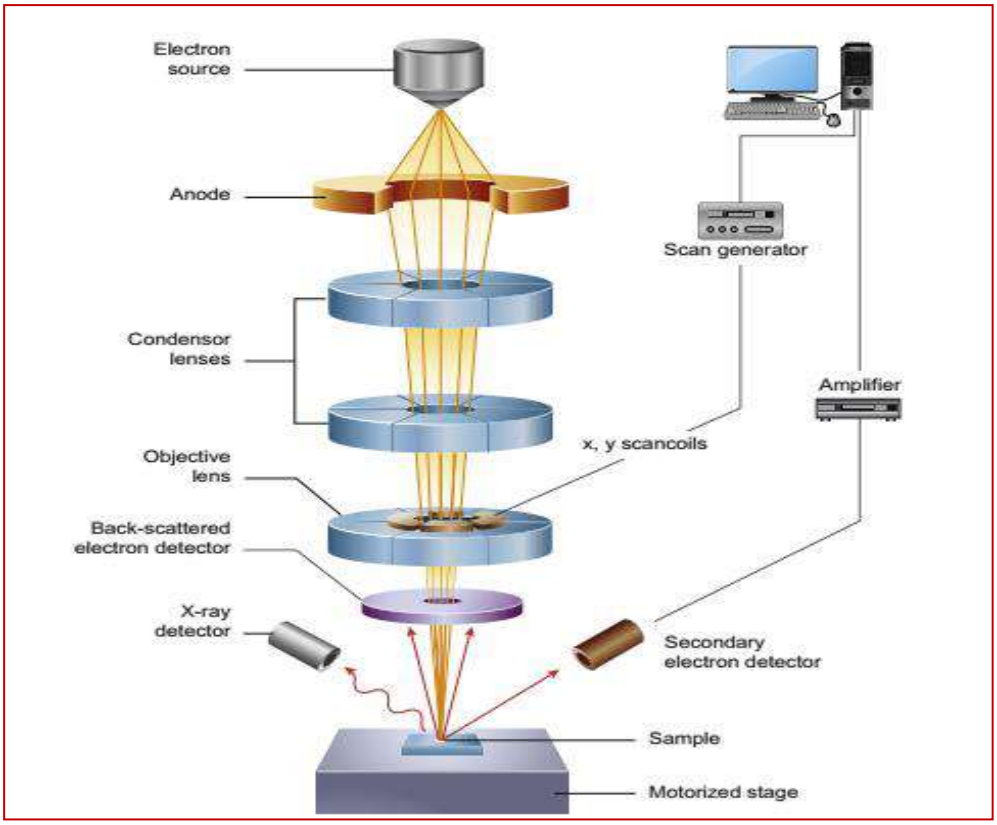

Figure II.19. Schematic diagram of the core components of an SEM microscope [74].

II.4.2.2. How does a SEM work ?

The main components of the SEM include a source of electrons, electromagnetic lenses to focus electrons, electron detectors, sample chambers, computers, and displays to view the images. Electrons, produced at the top of the column, are accelerated downwards where they passed through a combination of lenses and apertures to produce a fine beam of electrons which hits the surface of the sample. The sample is mounted on a stage in the chamber area and, unless the microscope is designed to operate at low vacuums, both the column and the chamber are evacuated by a combination of pumps. The level of the vacuum will depend on the design of the microscope. The electron beam hits the surface of the sample mounted on a movable stage under vacuum. The sample surface is scanned by moving the electron-beam coils. This beam scanning enables information about a defined area of the sample. The interaction of the electron beam with the sample generates a number of signals, which can then be detected by appropriate detectors [75].

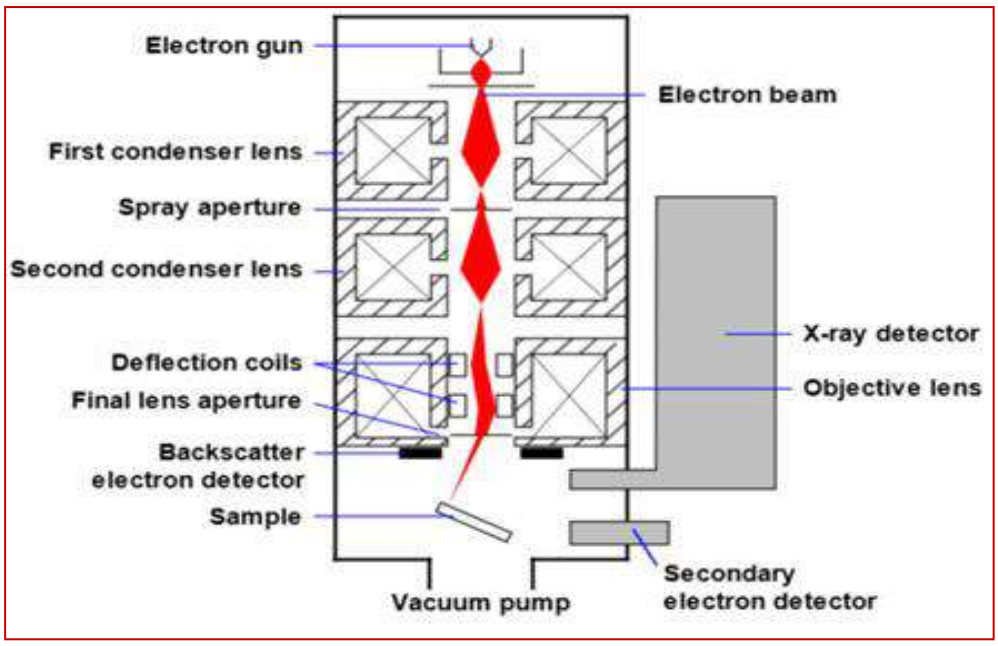

Figure II.20. Schematic of a Scanning Electron Microscope [75].

II.4.2.3. What are advantages and disadvantages of the Scanning Electron Microscope ?

The advantages of SEM include the detailed three-dimensional (3D) topographical imaging and the versatile information obtained from different detectors. The microscope is easy to operate and associated software is user-friendly. The SEM is also widely used to identify phases based on qualitative chemical analysis and/or crystalline structure. Precise measurement of very small features and objects down to 50 nm in size is also accomplished using the SEM. Backescattered electron images (BSE) can be used for rapid discrimination of phases in multiphase samples. SEMs equipped with diffracted backscattered electron detectors (EBSD) can be used to examine microfabric and crystallographic orientation in many materials [73].

The disadvantages of SEM are its size and cost. SEM is expensive to operate. The preparation of samples can result in artifacts. A critical disadvantage is that SEM is limited to solid, inorganic samples small enough to fit inside a vacuum chamber that can handle moderate vacuum pressure [73].

II.4.3. Fourier Transform Infrared Spectroscopy (FTIR)

II.4.3.1. What is a FTIR ?

Fourier transform infrared spectroscopy (FTIR) uses the mathematical process (Fourier transform) to translate the raw data (interferogram) into the actual spectrum. FTIR analysis is

used for the identification of organic, inorganic, and polymeric materials utilizing infrared light for scanning the samples. Alterations in the characteristic pattern of absorption bands clearly indicate a change in the material composition. FTIR is useful in identifying and characterizing unknown materials, detecting contaminants in a material, finding additives, and identifying decomposition and oxidation [76].

II.4.3.2. How does of Fourier transform infrared spectroscopy works ?

A typical FTIR spectrometer includes a source, sample cell, detector, amplifier, A/D convertor, and a computer. Radiation from the sources reach the detector after it passes through the interferometer. The signal is amplified and converted to a digital signal by the A/D convertor and amplifier, after which the signal is transferred to the computer where the Fourier transform is carried out. (Figure II.21), shows the schematic diagram of FTIR spectrometer.

Infrared radiation of about 10,000–100 cm^{-1} is sent through the sample with part of the radiation absorbed and some passing through. The radiation that is absorbed is converted by the sample to vibrational or rotational energy. The resultant signal obtained at the detector is a spectrum generally from 4000 to 400 cm^{-1}, which represents the samples' molecular fingerprint. Every molecule has a unique fingerprint, which makes FTIR an invaluable tool for chemical identification [77].

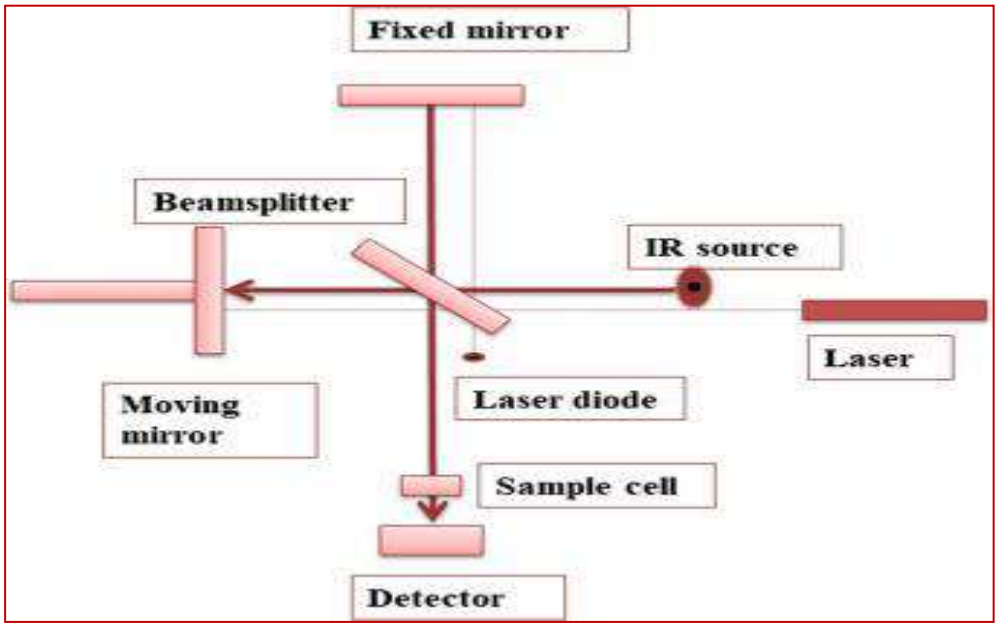

Figure II.21. Schematic diagram of FTIR [77].

II.4.4. Ultraviolet - Visible Spectroscopy

UV-Visible spectroscopy is a method of non-destructive optical analysis that relies on the transition from a ground state to an excited state of an electron, an atom or a molecule by excitation by an electromagnetic wave.

The Principle of UV-Visible Spectroscopy is based on the absorption of ultraviolet light or visible light by chemical compounds, which results in the production of distinct spectra. Spectroscopy is based on the interaction between light and matter. When the matter absorbs the light, it undergoes excitation and de-excitation, resulting in the production of a spectrum.

When matter absorbs ultraviolet radiation, the electrons present in it undergo excitation. This causes them to jump from a ground state (an energy state with a relatively small amount of energy associated with it) to an excited state (an energy state with a relatively large amount of energy associated with it). It is important to note that the difference in the energies of the ground state and the excited state of the electron is always equal to the amount of ultraviolet radiation or visible radiation absorbed by it [78].

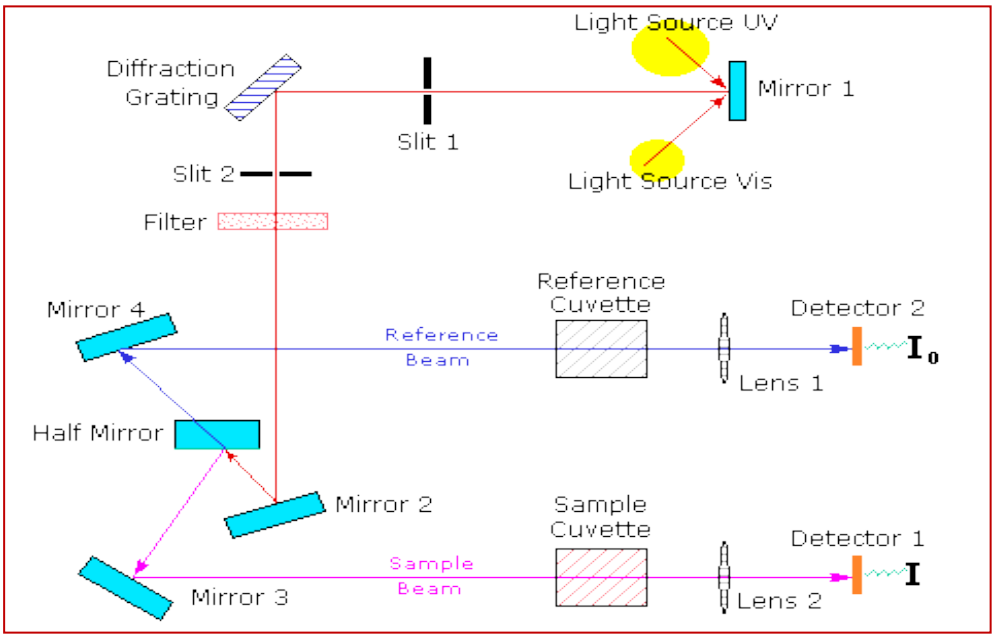

Figure II.22. The principle of operation of UV-visible Spectrophotometer [78].

II.4.4.1. Determination of Films' thickness (d) (Swanepoel method)

On based the pattern of transmittance in the transparent region, we used the optical interference fringes method to evaluate the thickness d of the TiO_2 films according to the following relationship [79,80]:

$$\mathbf{d} = \frac{\boldsymbol{\lambda_1 \lambda_2}}{\mathbf{2(\lambda_1 n_2 - \lambda_2 n_1)}} \quad \text{(II.19)}$$

$$\mathbf{n_{1,2}} = \left[(\mathbf{N_{1,2}} + (\mathbf{N_{1,2}^2} - \mathbf{n_0^2 n_s^2})^{\frac{1}{2}}\right]^{\frac{1}{2}} \quad \text{(II.20)}$$

$$\mathbf{N_{1,2}} = \frac{\mathbf{2n_0 n_s(T_M - T_m)}}{\mathbf{T_M T_m}} + \frac{(n_0^2 + n_s^2)}{\mathbf{2}} \quad \text{(II.21)}$$

Where T_m and T_M are the minimum and maximum transmission for the same wavelength, M is the number of oscillations between the two extreme; λ_1, n_1 and λ_2, n_2 are the corresponding wavelengths and indices of refraction, n_s is the refractive index of the glass substrate and $n_0 = 1$ is the refractive index of the air.

II.4.4.2. Determination of absorption coefficients (α)

In the spectral domain where the light is absorbed, and knowing the thickness of the layer,The absorption coefficient for each value of the transmittance T in (%) can be calculated using the following expression [81]:

$$\boldsymbol{\alpha} = \frac{\mathbf{1}}{\boldsymbol{d}} \mathbf{ln}\left(\frac{\mathbf{100}}{\boldsymbol{T}}\right) \quad \text{(II.22)}$$

where T(%) is the transmittance, and can be directly measured by [81] :

$$\mathbf{T} = \frac{\boldsymbol{I}}{\boldsymbol{I_\circ}} \times \mathbf{100} \quad \text{(II.23)}$$

II.4.4.3. Determination of optical gap (Eg)

The optical gap is calculated using the Tauc model proposed, in which Eg is related to the absorption coefficient α by [82]:

$$\mathbf{(\alpha h\nu)^n = A\,(h\nu - E_g)} \quad \text{(II.24)}$$

Where: $h\nu$ is the photon energy, Eg is optical gap n and A are constants, n characterizes the optical type of transition and takes the values 2, 1/2 (2 for allowed direct transitions or 1/2 for allowed indirect transitions).

Thus, if we plot $(\alpha h\nu)^2$ as a function of the energy of a photon $E = h\nu$ [knowing that $h\nu$ (ev) = hc / λ (Å) = 12400 / λ (Å)] and that I' we extrapolate the linear part of $(\alpha h\nu)^2$ to the x-axis (i.e. for $(\alpha h\nu)^2 = 0$), we obtain the value of Eg [83], (Figure II.23).

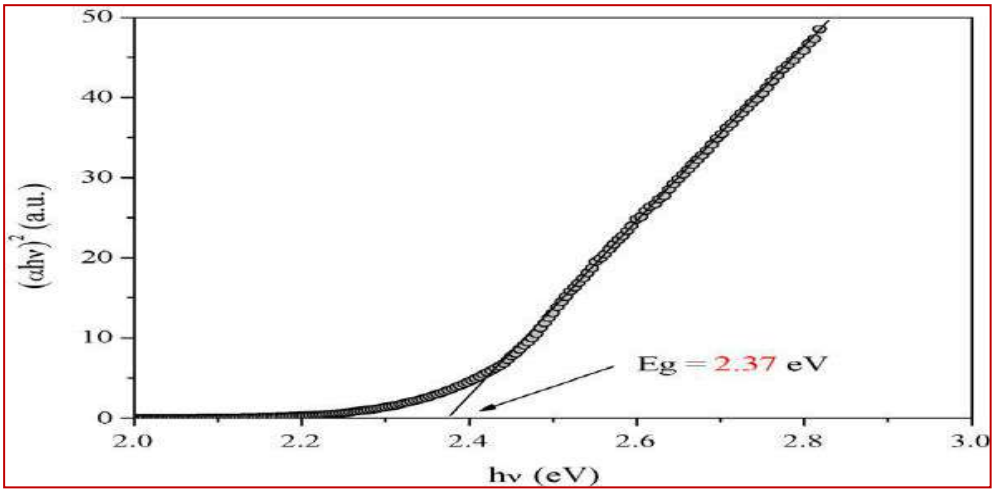

Figure II.23. Determination of optical gap (Eg) [83].

II.4.4.4. Determination of urbach energy (Eu)

The parameter which characterizes the disorder of the material is the tail energy of Urbach (Eu). According to Urbach's law, the expression of the absorption coefficient is of the form [84]:

$$\alpha = \alpha_0 . \exp\left(\frac{h\nu}{E_u}\right) \quad \text{and } E_u = \left(\frac{d[\alpha h\nu]}{d[h\nu]}\right)^{-1} \qquad \text{(II.25)}$$

where : α_0 is a constant and Eu is Urbach energy.

We can determine Eu value as the reciprocal of the linear part slope by plotting $ln\ (\alpha)$ versus $h\nu$ (Figure II.24):

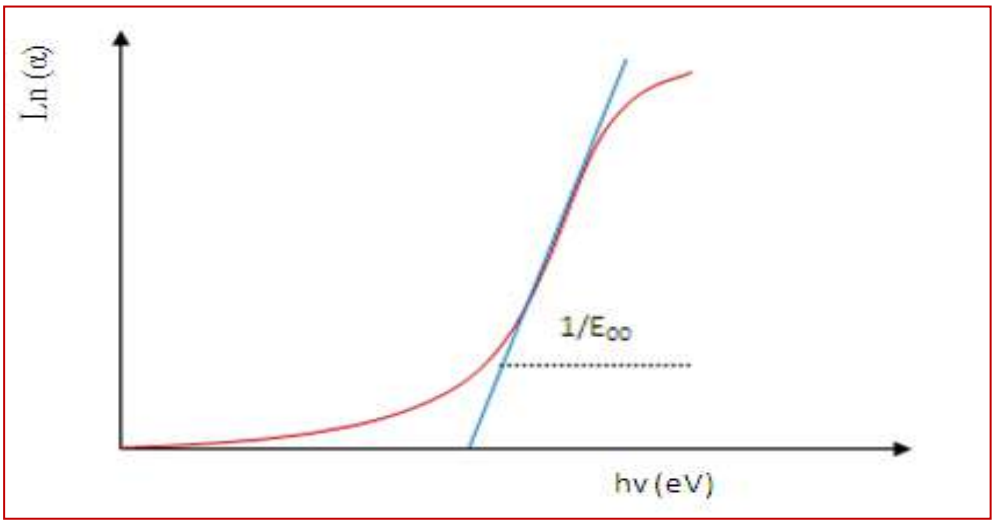

Figure II.24. Determination of urbach energy (E_{00}) [84].

II.4.5. Four point prob method with electrical caracterisation

The four-point technique can be used either for a thick material or for a thin layer deposited on an insulating substrate or isolated by a junction.Apply the four points in a

straight line to the film that has been deposited on the insulating substrate (glass). In the configuration of the four aligned tips, the two external tips serve to bring the current I while the two internal tips allow the measurement of the potential difference U. These electrodes are arranged equidistantly and have a distance "d " (Figure II.25).

When the distance a between the terminals is significantly more than the thin film's thickness, i.e. e << d (the thickness is negligible compared to the other dimensions), the lateral dimensions can be considered as infinite. In this case, a two-dimensional conduction model is used "a cylindrical propagation of field lines in the thin film" and gives [85].

$$\frac{U}{I} = K\,\frac{\rho}{e} \qquad \text{(II.26)}$$

Where : ρ is the resistivity of the layer, e is the thickness, and k is coefficient ($\mathbf{K} = \frac{\mathbf{Ln\ 2}}{\boldsymbol{\pi}}$).

The $\frac{\rho}{e}$ ratio characterizing the layer is denoted R_S and is expressed in Ω.

With a coefficient K ready, R_S is the ratio between the voltage U and the current I. From the previous considerations, using the following relationship, we can calculate the resistivity of the four point measurement knowing the thickness:

$$\boldsymbol{\rho} = \left(\frac{\boldsymbol{\pi.U}}{\mathbf{Ln2.I}}\right).\mathbf{e} = \mathbf{Rs}.\mathbf{e} \qquad \text{(II.27)}$$

So, the conductivity is given by the following expression:

$$\boldsymbol{\sigma} = \frac{\mathbf{1}}{\boldsymbol{\rho}} \qquad \text{(II.28)}$$

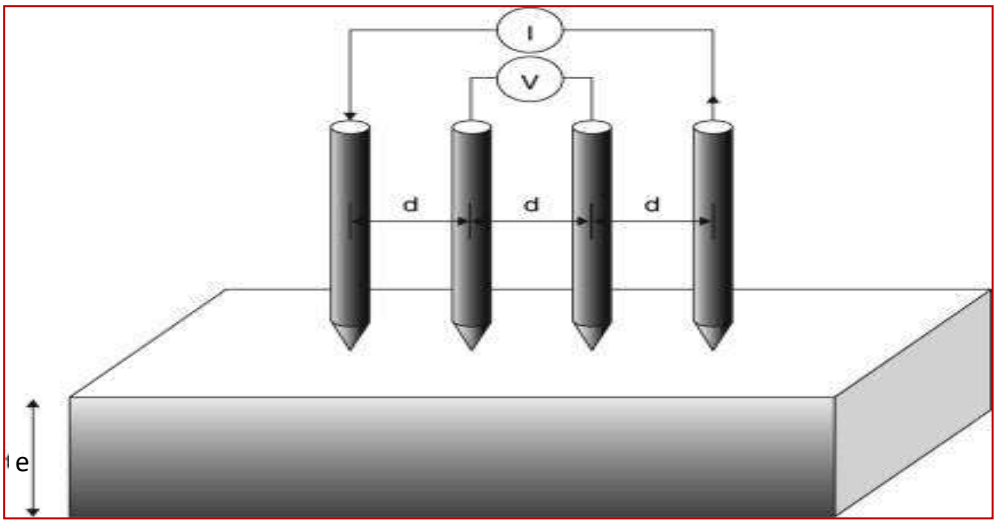

Figure II.25. Schematic representation of a four-point probe in contact with a conductive plate [86].

Chapter II's references :

[1] Knoll, Wolfgang Knoll; Advincula, Rigoberto C., eds. (7 June 2011). " Functional Polymer Films, 2 Volume Set 1st Edition. Wiley-VCH. ISBN 978-3527321902.

[2] S. Hu, F. Li, Z. Fan, " The comparison of property and visible light activity between bulk and surface doped N-TiO_2 prepared by sol-gel and N2-plasma treatment." Bull. Korean Chem. Soc, 33 (2012) 199-203.

[3] A. Aldrin, "Preparation and characterization of certain II-VI, I-III-VI2 semiconductor thin films and transparent conducting oxides." PhD thesis, Cochin University of Science and Technology, Kerala, India, 2004.

[4] L. Holland, " Vacuum deposited thin films." Chapman & Hall, London (1966).

[5] K. S. Shamala, Indian Academy of Sciences Bulletin; of Materials Science, 27 (2004) 295-301.

[6] L.Pawlowski, " dépôts physique ", Presses Polytechniques et Universites Romandes, 2003.

[7] Mahmoudi Sana, " Etude comparative entre deux méteaux passifs en milieux neutre, alcalin et acide: un acier inoxydable 304 L et un alliage de titane Ti6Al4V." Mars 2008.

[8] Milton Ohring, " The Materials Science of Thin Films." Academic Press San Diego NewYork Boston London Sydney Tokyo Toronto, (1992).

[9] Liu X, Chu P, Ding C. "Surface modification of titanium, titanium alloys, and related materials for biomedical applications." Mater. Sci. Eng. R 2004; 47: 49–121

[10] Hanawa T, Asami K, Asaoka K. " Repassivation of titanium and surface oxide film regenerated insimulated bioliquid." J. Biomed. Mater. Res. 1998; 40(4): 530–538.JIAN 92.

[11] A. Derbali, " The effect of the distance of the Bec and the temperature of the substrate on the properties of thin films of zinc oxide (ZnO)." magister thesis, Mohamed Khider Biskra University, (2011).

[12] D.M. Mattox, V.H. Mattox, 50 years of vacuum coating technology and the growth of the Society of Vacuum Coaters, Society of Vacuum Coaters, (2007).

[13] Mattox DM (2010) Handbook of physical vapor deposition (PVD) processing, William Andrew.

[14] Mattox DM (1998) Atomistic Film Growth and Some Growth-Related Film Properties, Handbook of Physical Vapor Deposition (PVD) Processing.

[15] H. Koinuma, N. Kanda, J. Nishino, A. Ohtomo, H. Kuboto, M. Kawasaki, M. Yoshimto, " Laser MBE of ceramic thin films for future electronics. "App. Surf. Sci, 109-110 (1997) 514-519.

[16] L. Eckertová, Physics of Thin Films, Springer Science & Business Media, 2012.

[17] R. Behrisch, " Sputtering by Particle Bombardment I: Physical Sputtering of Single-Element Solids." Springer-Verlag, 1981.

[18] W. Westwood, " Sputter deposition." AVS Education Committee, 2003.

[19] M. Ohring, "Materials Science of Thin Films Deposition and Structure.",2nd Edition, Academic Press, (2002).

[20] T. Guo, P. Nikolaev, A. Thess, D.T. Colbert and R.E. Smalley, " Catalytic growth of single-walled nanotubes by laser vaporization."Chem. Phys. Lett., 1995, 243, 49-54.

[21] D. Dijkkamp, T. Venkatesan et al, Applied Physics Letters, 51 (1987) 619.

[22] Faouzi HANINI,"Etude des propriétés physiques de couches minces TiO2 élaborées par différentes techniques." Thèse de Doctorat, Université Constantine 1, 2014.

[23] Sylvain TRICOT."Comparaison des procédés d'ablation par faisceau laser et par faisceau d'électrons pour la croissance de couches minces." Thèse de doctorat. Université D'ORLÉANS.2008.

[24] C. Blouet, D. Chambonnet, D. Keller and C.Villard, Ann. Phys, C1 (1997) 153.

[25] Ratner B. " Titanium in Medicine: Material Science, Surface Science, Engineering, Biological Responses and Medical Applications (eds. Brunette D M, Tengvall P, Textor M, Thompson P). " Springer-Verlag, Berlin and Heidelberg 2001; 1–12.

[26] T. Iwashita, S. Ando, Thin Solid Films, 520 (2012) 7076.

[27] R.R.Chamberlin and J.S.Skarman" Chemical spray deposition process for inorganic films." Journal of the Electrochemical Society, 113(1) :86-89,1996.

[28] J.Manifacier, J.Fillard, and J.Bind," Deposition of In_2O_3-SnO_2 layers on glass substrates using a spraying method." Thin Solide Films, 77(1-3) :67-80,981.

[29] F. Paraguay D., W. Estrada L., D. Acosta N., E. Andrade, and M. Miki-Yoshida. " Growth, structure and optical characterization of high quality ZnO thin films obtained by spray pyrolysis." Thin Solid Films, 350(1-2):192-202, 1999.

[30] G.L.Messing, S-C Zhang, and G.V. Jayanthi. "Ceramic powder synthesis by spray pyrolysis." Journal of the American Ceramic Society, 76(11) :2707-2726,1993.

[31] J.B.Mooney, and S.B.Radding," Spray pyrolysis processing". Annual Review of Materials Science, 12(1) :81-101,1982.

[32] S.Major, A.Banerjee, and K.Chopra, " Highly transparent and conducting induim-doped zinc oxide films by spray pyrolysis.".Thin Solid Films, 108(3) :333-340,1983.

[33] W.Siefert, Thin Solid Films, 120 (1984) 275–282

[34] Mendeleyev D. I, Khim. Zhur. Sok. i. Eng, 4 (1860) 65.

[35] J.P.Boilot, F.Chaput, L.Mailer, A.Brun, Y.lévy et J-P.Galup. Image de la PhySIQUE. 44 (1998).

[36] B.Darracq, F.Chaput, K.Lahlil, J.P.Boilot, Y.Levry, V.Alain, L.Ventelon, M.BlanchardDesce, Optical Materials, 9,265(1998).

[37] D.B. Wolfe, J.C. Love, K.E. Paul, M.L. Chabinyc, G.M Whitesides, Appl. Phys. Let. 80,12 (2002) 2222.

[38] J.Zhang, B.Li, Z.Wang, G.Cheng, S.Dong, Analytica Chimica Acta, 388,71 (1999).

[39] C.J. Brinker et G.W. Scherer, "Sol → gel → glass : I. Gelation and gel structure." Journal of Non-Crystalline Solids, 70 (3) (1985) 301.

[40] https://en.wikipedia.org/wiki/Sol-gel, (accessed 30.12.16).

[41] Rabaste SEBASTIEN, "Microcavités optiques élaborées par voie sol-gel : applications aux ions terre rare d'Eu^{3+} et aux nanocristaux semi-conducteurs de CdSe." Thèse de Doctorat, Université Claude Bernard - Lyon 1, 2003.

[42] C.J. Brinker, Sherrer G.W, " Sol-Gel Science, the Physic and Chemistry Sol-Gel Processing", Academic Press, San Diego, 1989.

[43] H. Cattey, Thèse, Université de Franche-Comté, Besançon, 1997

[44] M. S. SALLARD, thèse de doctorat, L'école normale Superieure de Cachan(2007).

[45] M. Bathat, Thèse de doctorat, Université Claude Bernard Lyon.1 (1992).

[46] D.Gallagher and T.A. Ring, sol-gel processing of ceramics films.

[47] D. Gallagher, T.A. Ring, " Sol-gel processing of ceramics films". Chimia 43 (1989) 298.

[48] Cohen, Edward; Lightfoot, E. J. (2011), "Coating Processes", Kirk-Othmer Encyclopedia of Chemical Technology, New York: John Wiley.

[49] C.J.Brinker, A.J.Hurd, G.C.Frye, P.R.Shunkard, et C.S.Ashley. J Ceram.Soc.Japan, 99 (1991) 862.

[50] Rahaman, M.N. (2007). Ceramic Processing. Boca Raton: CRC Press. pp. 242–244. ISBN 978-0-8493-7285-8.

[51] C. J. Brinker, A. J. Hurd, P. R. Schunk, G. C. Frye, et C. S. Ashley. J. Non Cryst. Sol, 147 (1992) 424-436.

[52] L.L. Hench, D.R. Ulrich, Ultrastructure Processing of Ceramics, Glasses and Composites, Wiley-Interscience, 1984.

[53] Salim CHELOUCHE, "Propriétés des fenêtres optiques ZnO:Al pour cellules solaires en couches minces à base de CIGS." Mémoire de Magister, Université Ferhat Abbas–Setif, 2012.

[54] C. J. Brinker; G. W. Scherer, " Sol-gel science: the physics and chemistry of sol-gel processing. " Academic press, Cambridge MAUS, 2013.

[55] R. Morent, N. De Geyter, in Functional Textiles for Improved Performance, Protection and Health, 2011.

[56] Ron Jenkins and R. L. Snyder. " Introduction to X-ray powder diffractometry. Number v.138 in Chemical analysis. " Wiley, New York, (1996).

[57] Yacine Benlatraeche," Contribution à l'amélioration de la durée de vie d'outils carbure pour l'usinage du MDF (Medium Density Fiberboard) par application de dépôts ternaires (CrAIN, CrVN) et modification de l'aréte de coupe." Thése de Doctorat, institut des scirnces et technologies, Paris, 2011.

[58] Y.P. Venkata Subbaiah, P. Prathap, K.T. Ramakrishna Reddy, "Structural, electrical and optical properties of ZnS films deposited by close-spaced evaporation." Applied Surface Science, 253 (2006) 2409–2415.

[59] M. Devika, K.T.R. Reddy, Appl.Phys, 100 (2006) 023518.

[60] H, Yilmazer., M, Niinomi., T, Akahori., M, Nakai and Y, Todaka, " Effect of high–pressure torsion processing on microstructure and mechanical properties of a novel biomedical β–type Ti–29Nb–13Ta–4.6 Zr after cold rolling." International Journal of Microstructure and Materials Properties, 7 (2-3), (2012) 168-186.

[61] Kamal A. Aly, N.M. Khalil, Yousif Algamal, Qaid M.A. Saleem, " Estimation of lattice strain for zirconia nano-particles based on Williamson- Hall analysis." Materials Chemistry and Physics, 193 (2017) 182−188.

[62] D. Komaraiah, E. Radha, J. James, N. Kalarikkal, J. Sivakumar, M.V. Ramana Reddy, R. Sayanna, " Effect of particle size and dopant concentration on the Raman and the photoluminescence spectra of TiO_2:Eu^{3+} nanophosphor thin films." J. Lumin, 211 (2019) 320–333.

[63] T. Prasada Rao, M.C. Santhoshkumar. " Effect of thickness on structural, optical, electrical properties of nanostructured ZnO thin films by spray pyrolysis." Applied Surface Science, 255(2009) 4579-4584.

[64] F. Szekely, I. Groma, J. Lendvai, " Characterization of self-similar dislocation structures by X-ray diffraction. " Mater. Sci. Eng. A, 324 (2002) 179–182.

[65] S Asha Bhandarkar, Prathvi, Akshayakumar Kompa, M.S. Murari, Dhananjaya Kekuda, Rao K. Mohan, " Investigation of structural and optical properties of spin coated TiO_2:Mn thin films. " Optical Materials, 118 (2021) 111254.

[66] A. Arunachalam, S. Dhanapandian, C. Manoharan, and G. Sivakumar, " Physical properties of Zn doped TiO_2 thin films with spray pyrolysis technique and its effects in antibacterial activity. " Spectrochimica Acta Part A: Molecular and Biomolecular Spectroscopy, 138 (2015) 105.

[67] B.D. Cullity, S.R. Stock, Elements of X-ray Diffraction, Addison-Wesley Publishing Company, Reading, MA, (1978).

[68] Chen J, Yaling Li, Wang Y, Yun J,Cao D. " Preparation and characterization of zinc sulfide nanoparticles under hight-gravity enviroment." Mat.Res.Bull, 2004 ; 39 (2): 185 -194 .

[69] R. Bomila, S. Srinivasan, S. Gunasekaran, A. Manikandan,"Enhanced photocatalytic degradation of methylene blue dye, opto-magnetic and antibacterial behaviour of pure and La-doped ZnO nanoparticles. "J. Supercond. Magn, 31 (3) (2018) 855–864.

[70] Jo-Yong Park, Yun-Jo Lee, Ki-Won Jun, Jin-Ook Baeg, and Dae Jae Yim," Chemical Synthesis and Characterization of Highly Oil Dispersed MgO Nanoparticles. " J. Ind. Eng. Chem , Vol. 12, No. 6, (2006) 882-887.

[71] C-J. Chung, H-I. Lin, P-Y. Hsieh, K-C. Chen, J. L. He, A. Leyland, A. Matthews, "Growth behavior and microstructure of arc ion plated titanium dioxide." Surf. Coat. Technol, 204 (2009) 915–922.

[72] Zohra Nazir Kayani, Sidra Rahim, Riffat Sagheer, Saira Riaz, Shahzad Naseem, "Assessment of antibacterial and optical features of sol-gel dip coated La doped TiO_2 thin films. " J. Materials Chemistry and Physics, 250 (2020) 123217.

[73] Stokes, Debbie J. (2008). "Principles and Practice of Variable Pressure Environmental Scanning Electron Microscopy (VP-ESEM)." Chichester: John Wiley & Sons. ISBN 978-0470758748

[74] B.J.Inkson."Scanning electron microscopy (SEM) and transmission electron microscopy (TEM) for materials characterization. "Materials Characterization Using Nondestructive Evaluation (NDE) Methods,10 (2016).

[75] M. Walock,“ Nanocomposite coatings based on quaternary metalnitrogen.” PhD Thesis, University of Alabama, 2012.

[76] P.Mohamed Shameer, P.Mohamed Nishath. “ Exploration and enhancement on fuel stability of biodiesel : a step forward in the track of global commercialization.” Advanced Biofuels. (2019) 181-213.

[77] Taha M, Hassan M, Essa S, Tartor Y. “ Use of Fourier transform infrared spectroscopy (FTIR) spectroscopy for rapid and accurate identification of yeasts isolated from human and animals. ” Int J Vet Sci Med, 2013;1(1):15–20.

[78] S. Sheth, “Synthesis and Characterization of Catalysts for Photo-oxidation of Water.” PhD Thesis, University of Paris-Sud, 2013.

[79] Abdelhak Jrad, Tarek Ben Nasr, Najoua Turki-Kamoun, “ Effects of Al content on physical properties of ZnS thin films prepared by chemical bath deposition. ”J Mater Sci: Mater Electron, 26 (2015) 8854–8862.

[80] Fouad Bouaichi, Hanane Saidi, Abdallah Attaf, Mohamed Othmane, Nadia Lehraki, Malika Nouadji, Marcel Poulain and Said Benramache,“ The synthesis and characterization of sprayed ZnO thin films: As a function of solution molarity. ” Main Group Chemistry, 15 (2016) 57–66.

[81] A. Yahia, “ Optimization of indium oxide thin films properties prepared by sol gel spin coating process for optoelectronic applications. ” Doctorate these, University of biskra, 2020.

[82] J.Tauc, R.Grigorovici, and A.Vancu, “ Optical properties and electronic structure of amorphous germanium. ” Physica Status Solidi (B), 15(2), (1966) 627- 637.

[83] D. Beena, K. J. Lethy, R. Vinodkumar, V. P. Pillai, V. Ganesan, D. M. Phase, S. K. Sudheer, “ Effect of substrate temperature on structural, optical and electrical properties of pulsed laser ablated nanostructured indium oxide films.” Applied Surface Science, 255(20) (2009), 8334-8342.

[84] T.P. Rao, M.S. Kumar, “ Physical properties of Ga-doped ZnO thin films by spray pyrolysis.” J. Alloys Compd, 506 (2010) 788–793.

[85] S. Rahmane, “ Elaboration et caractérisation de couches minces par spray pyrolyse et pulvérisation magnétron”, Thèse de Doctorat, Université Mohamed Khider Biskra, (2008).

[86] S. Kasap and P. Capper, “Springer Handbook of Electronic and Photonic Materials”, Springer Science and Business Media, (2006).

Chapter III

Effect of the number of layers and the mixed solvent on structural, optical and electrical properties of spin-coated TiO2 thin films

III.1. Effect of the number of layers

III.1.1. Introduction

The aim of this work is to develop titanium oxide (TiO_2) thin films, deposited by the sol-gel method (spin-caoting) on substrates of glass using titanium (IV) isopropoxide as a precursor. Analysis and discussion of the results concern the influence of the number of layers, on the structural, optical and electrical properties of the layers produced.

III.1.2. Experimental details

III.1.2.1. Apparatus used (Spin coater)

The deposition of thin layers of TiO_2 by the Sol-gel route is carried out using a ***spin coater*** device designed and produced at the level of the thin film laboratory. The substrate is placed and held by vacuum on a turntable at a constant speed in order to spread the deposited material (in gel form) uniformly by centrifugal force. The machine used for this operation are shown in Figure III.1:

Figure III.1. Holmarc spin coater.

III.1.3. Preparation of the substrate

III.1.3.1. Choice of substrate

The substrates are industrial glass slides; with a refractive index of 1.52 and a square area of 2.5 x 2.5 cm diamond tip.

- Glass is the most often selected substrate.

- It allows films' a good optical characterization.
- After deposition, the sample (substrate + layer) will undergo cooling to room temperature which causes compressibility of the two materials constituting the sample.
- Financial cost.

III.1.3.2. Cleaning of the substrate

The quality of the sample deposition depends on the cleanliness and surface condition of the substrate. The cleaning of the substrates is a very important step which is carried out in a clean place, because this step determines the qualities of adhesion and homogeneity of the deposited layers. The process used for cleaning glass substrates is described by the following steps:

- The substrates are cut using a pen with diamond point.
- Cleaning with soap solution.
- Rinsing with the distilled water and then with acetone during 5 min.
- Rinsing with distilled water.
- Rising with methanol during 5 min at ambient temperature.
- Cleaning in distilled water bath.
- Drying using a drier.

III.1.4. Materials and TiO_2 thin film preparation

Titanium oxide (TiO_2) thin films were deposited by using sol-gel spin coating process. Sol–gel method considered as a facile process for the fabrication high quality thin films of metal oxide materials which is easy to synthesize of thin films in bulk with different layers with sufficiently demonstrate physical and chemical properties. It was prepared a starting solution with a concentration of 0.2 (mol/l) and a pH = 6 was prepared by dissolving 0.605 ml of titanium tetra and distilled iso-prop-oxide (TTIP) as the solutein 10 ml of ethanol which was used as a solvent and 0.210 ml of acetyl acetone as a catalyst. The prepared mixture solution was maintained under agitation at a temperature of 50 °C for 3 hours. This solution is transparent yellowish color and slightly viscous. Soda-lime glass plates ($2.5\times2.5\times 0.15$ cm^3) are used as the substrates, which it was cleaned with ethanol, acetone water during 5 min into each process and subsequently dried in air. The precursor solution was deposited on clean substrates using a spin coating system, and then the prepared solution were injected onto the center of the glass substrate, and it was rotated at a spinning speed of 4000 rpm for 30 s. After

30 s, the deposited films were dried at 250 °C for 10 min in a furnace to evaporate the organic solvent. This step was repeated for **(3-5-7-11-13-15 times)** in order to obtain a multilayer film. Finally, TiO_2 films were calcined for 2 h at 500 °C in the furnace. The schematic diagram of the process used in the preparation of the TiO_2 thin films is illustrated in Figure III.2.

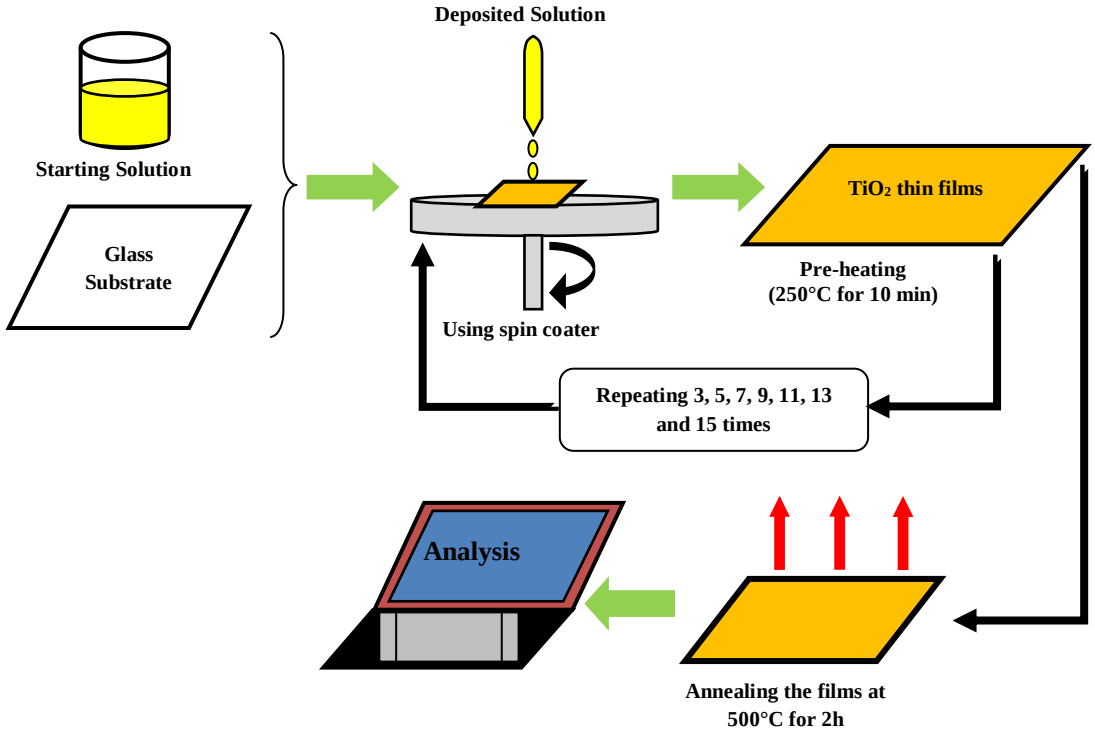

Figure III.2. Schematic diagram of the preparation steps of TiO_2 thin film procedure at different number of spin-coated layers.

III.1.5. Characterization methods

The synthesized structural, optical and electrical properties of TiO_2 films were characterized using various techniques. Firstly, the structure of the prepared films was acquired by X-ray diffractometer (XRD) spectra (Model: Bruker D8) using Cu Kα (λ =1.5418 Å) radiation within the 2θ range of 10° – 90°, with the steps of 0.02°. Besides, Perkin Elmer Lambda 950 UV/VIS spectrometer using a blank substrate as the reference position examined the optical properties of deposited thin film (film thickness, transmittance, gap energy, Urbach energy, refractive index) ranging from 300 to 1100 nm. Furthermore, the FT-IR spectra were obtained with a Fourier transform infrared spectrometer (Perkin Elmer UATR Two). The scanning wavelength of infrared was 400 – 4000 cm^{-1}. Finally, four-point method,

using“KEYSIGHT B1500A Semiconductor Device Analyzer” and “CPS PROBE STATION” apparatus at room temperature was performed to estimate the electrical resistivity.

III.1.6. Results and discussion

III.1.6.1. Adhesion test

Bibliographic research on adhesion tests for thin layers shows that there are a great many works on adhesion verification, which is justified by the growing interest in this field of activity. Adhesion, although not directly part of the desired properties, is an important parameter in the reliability of the deposited layer. Adhesion characterizes the behavior of a set of two materials united by adhesion, which represents the surface bond of one material to another.

Two main families of tests can be distinguished; the test that damages the sample “destructive methods”, and that which keeps the sample intact “non-destructive methods”, But as long as we do not have this type of expensive material at our disposal. The adhesive strength between the films and the substrates was tested using the Scotch tape test on the deposited films before any characterization on the as prepared and heat treated films. Adhesion strength is generally deemed "excellent" if the film sticks to the substrate and does not rip away from it. In our search. In our research, we found that our layer adhered well to the substrate in all films.

III.1.6.2. Thin Film Thickness

Based on the pattern of transmittance in the transparent region, we used the optical interference fringes method to evaluate the thickness d of the TiO_2 films according to the relationship (II.15).

The film thickness verses number of layers of TiO_2 thin films are shown in Figure III.3 As expected from the Figure III.3, the films thickness increases with number of layers, from about 243.72 nm for 3 layers to around 1543.83 nm for 15 layers. This increase in film thickness is reasonable due to the increase in the quantity of the deposited material. Similar results behaviour have been reported by other works [1,2]. Indeed, it is well argued in thin film growth mechanism that the film formation passes through three steps : (i) nucleation (ii) cross linking and finally vertical growth .The two first steps are controlled by the substrate temperature, while the vertical growth increases with the deposition time, i.e film thickness.

The vertical growth is also called columnar growth, hence the top of the film surface is composed by aggregation formed by the column, this is at the origin of agglomeration and clusters on the top surface and surface roughness.

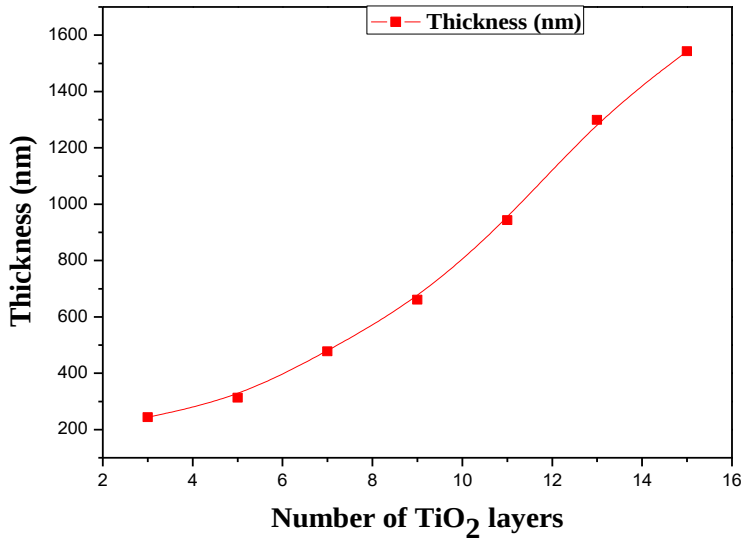

Figure III.3. The thickness of the TiO_2 thin film as a function of the number of spin-coated layers.

III.1.6.3. Structural properties

The XRD patterns of TiO_2 films grown at various number of layers are illustrated in Figure III.4. Generally, titanium dioxide can crystallizes in three different phases: rutile, anatase and brookite [3]. Rutile is the most stable one, while the other two phases are metastable which can transform into rutile when heated [4,5]. As shown from Figure III.4, the XRD results indicated that the films have a single anatase phase (JCPDS card No. 21-1272) [6], where as no other phases are revealed (rutile or brookite). Similar structure phase was observed by other literature [7,8]. From XRD results, it is noteworthy that at up to 9 layers one peak located at $2\theta = 25.35°$ assigned to (101) diffraction plane. While, over 11 layers three peaks have obtained at 2θ values equal to 25.35°, 37.93°and 48.11° with (101), (004) and (200) planes of reflections, respectively. Furthermore, as shown in Figure III.4, all samples have only preferred orientation growth along the (101) plane, which can be attributed to the minimal value of the free surface energy for this plane [9]. That gives the atoms sufficient mobility to move to positions of less energy leading to the highest atomic density achieved along the (101) direction [10,11]. In addition, as the number of layers increase, the intensity of (101) peak is enhanced, indicating improved the crystallinity of the TiO_2 thin

films with increasing number of layers. However, at large number of layers, the diffraction angle (101) of TiO_2 thin films has shifted of 0.04° to 0.15°, this may originate from the occurrence of residual stresses in the films, reflected to change in d-spacing of a typical (101) plane.

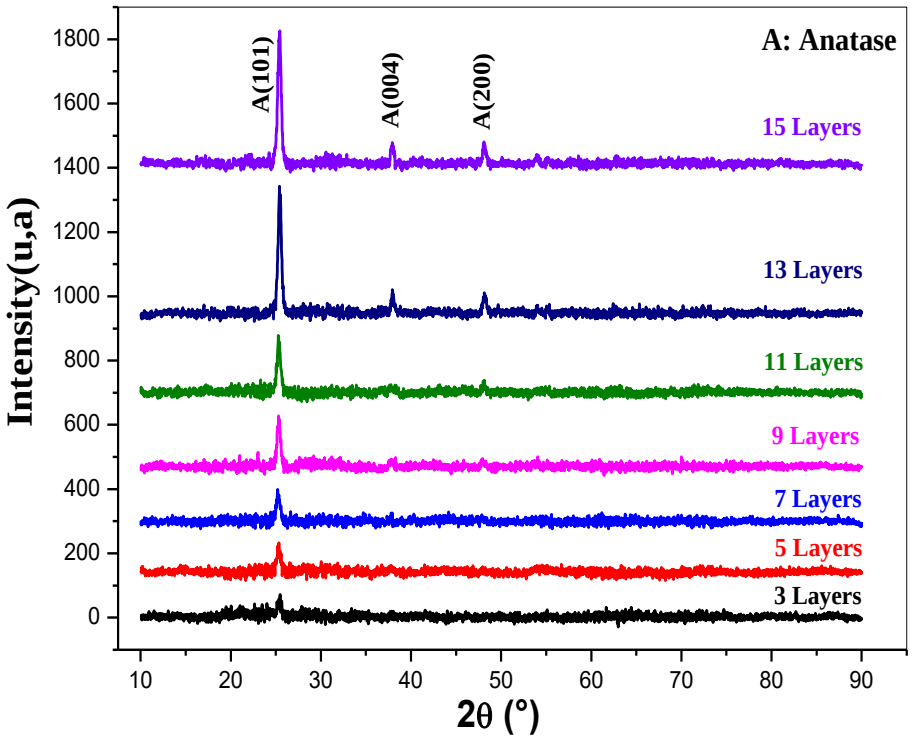

Figure III.4. XRD patterns of TiO_2 thin film with different number of spin-coated layers.

Can be estimated that the crystallite size using the well known debye-scherrer equation (II.9). In addition, the dislocation density (δ) and lattice strain (ε) have also been estimated for all the films by applying relations (II.13) and (II.12).

The variation of crystallite size, dislocation density and the strain with number of layers of TiO_2 films are represented in Table III.1 and Figure III.5. As can be seen from these values, the crystallite sizes increases when the number of layers increase, while, the strain decreases. Lin et al. [12] also reported the same increases of crystallite size for ZnO films with different thicknesses. This may be due to the collectively fusion of small crystallite into the bigger crystallites, as the result, the density of nucleation centers in films decrease which in turn generates of internal strain [13,14].

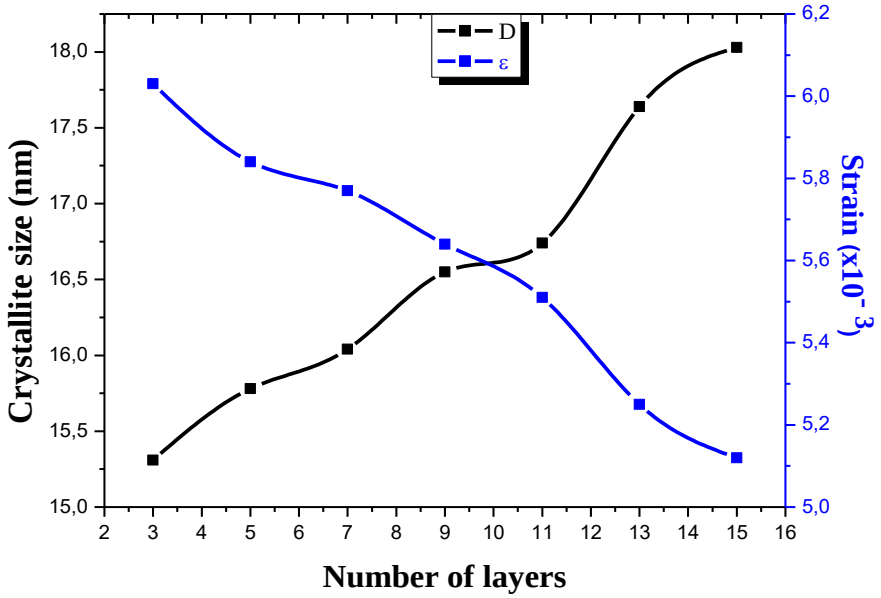

Figure III.5. Crystallite size and strain of TiO_2 thin film as a function of the number of spin-coated layers.

Table III.1: Crystallite sizes, dislocation density and strain values of TiO_2 thin films extracted from XRD analysis at different number of spin-coated layers.

Number of Layers	Peak (hkl)	2θ°	FWHM (β°)	D (nm)	δ x10^{15} (Lines /m^2)	ε x10^{-3}
3	(101)	25.40	0.53	15.31	4.26	6.03
5	(101)	25.38	0.51	15.78	4.01	5.84
7	(101)	25.20	0.50	16.04	3.88	5.77
9	(101)	25.35	0.48	16.55	3.65	5.64
11	(101)	25.32	0.47	16.74	3.56	5.51
13	(101)	25.42	0.46	17.64	3.21	5.25
15	(101)	25.43	0.45	18.03	3.07	5.12

The d-spacing and the lattice constants *a* and *c* of anatase TiO_2 films was calculated from the given relation (II.11) and the residual stress in the plane of the film can be calculated quantitatively using expression (II.14). The obtained structural parameters for the deposition of TiO_2 are provided in Table III.2.

The values of residual stress of TiO_2 thin films deposited at various number of layers are illustrated at Figure III.6. We can deduce from Figure III.6 that the residual stress of the

films prepared at number of layers 3, 5, 9, 11, 13 and 15 have a compressive stress. In contrast, the films deposited at number of layers 7 were found to have a tensile stress. These obtained results are in good agreement with those published in other works [15,16]. This variation in residual stress can be related to lattice mismatch, and the different thermal expansion coefficients between the films and the substrates [17,18].

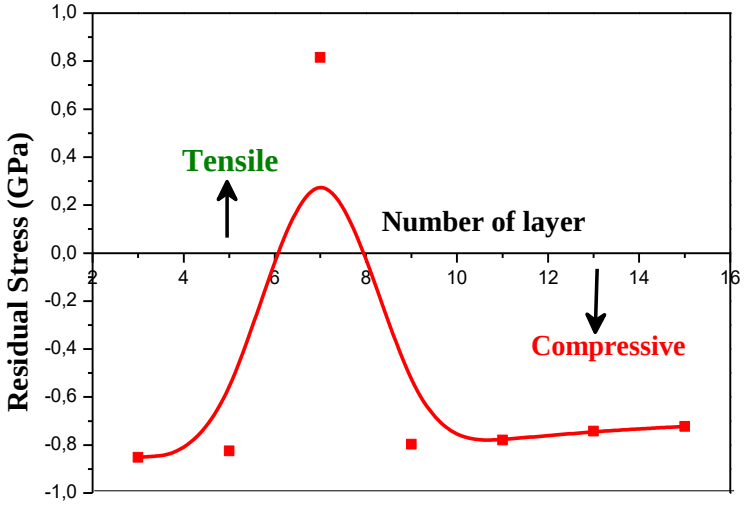

Figure III.6. The residual stress of TiO_2 thin film as a function of the number of spin-coated layers.

Table III.2. Structural parameters information of prepared TiO_2 thin films for different number of spin-coated layers.

Number of Layers	*h k l* planes	2θ (degree)	Calculated parameters			Reference parameter (JCPDS card No 21-1272)	Stress (Gpa)
			d-spacing (Å)	Lattice constant *a* (Å)	Lattice constant *c* (Å)		
3	(101)	25.40	3.5027	3.7681	9.5006		-0.852
5	(101)	25.38	3.5062	3.7760	9.4860		-0.825
7	(101)	25.20	3.5301	3.8017	9.5105	a_0 = 3.7852 Å	0.815
9	(101)	25.35	3.5099	3.7785	9.4790	c_0 = 9.5135 Å	-0.797
11	(101)	25.32	3.5134	3.7834	9.4716	d_0 = 3.521 Å	-0.779
13	(101)	25.42	3.5010	3.7676	9.4757	2θ = 25.28°	-0.742
15	(101)	25.43	3.4993	3.7649	9.4848		-0.723

III.1.6.4. Optical properties

The effect of number of layers on the optical transmittance spectra of TiO_2 thin films in the wavelength range of 300 – 1100 nm for the all samples are presented in Figure III.7. As it is shown transmittance spectrum can be divided in to two prominent regions: first region have a high absorption (λ< 385 nm), this is caused by the fundamental absorption of the light in thin films of TiO_2; which is meant to the electronic transition between valence and conduction band of TiO_2 [19]. Furthermore, it should be mentioned that the absorption edge shifts towards longer wavelength (i.e. red shift) with increasing numbers of layers (see the insert image in Figure III.7), which suggesting to narrowing the band gap energy of our films. Second region of strong transmittance, it is higher than 70% in the visible region (400 – 800 nm) for all films. Since the excellent optical transmittance, these films can be useful for optical coating applications like: anti-reflective, wavelength-selective films and UV-protected films for optoelectronic devices [20]. Also, all the deposited films have interference fringes in the visible region owing to the difference of the refractive index value between air-film and film-substrate interfaces [21]. Additionally, the transmittance of the films decreases with increasing the number of layers caused by the increased in the films thickness.

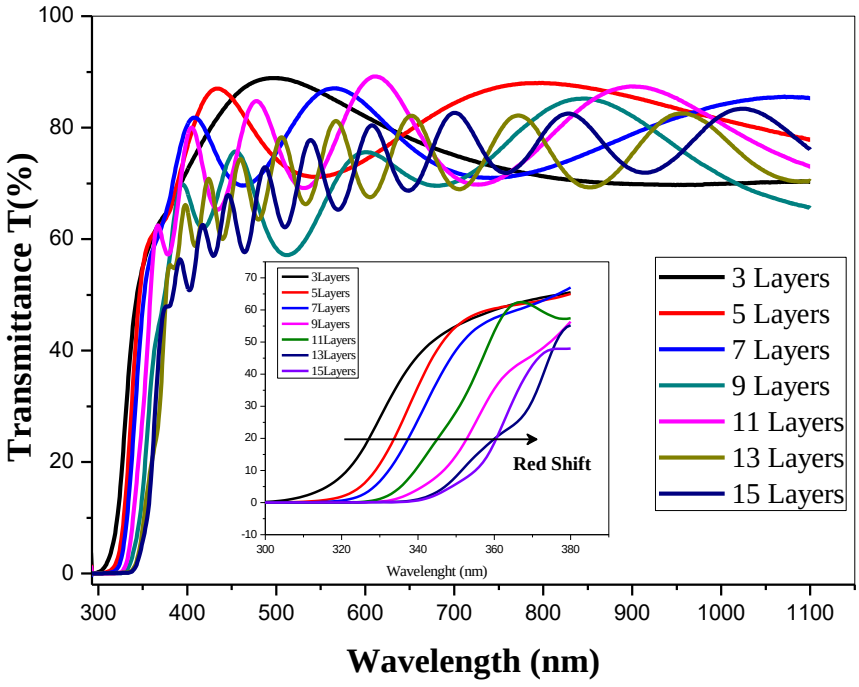

Figure III.7. Optical transmittance of TiO_2 thin film at various number of spin-coated layers.

The optical band gap energy of 3, 5, 7, 9, 11, 13 and 15 layers of TiO_2 thin films is deduced d by plotting a curve between $(\alpha h\nu)^2$ and $(h\nu)$ as shown in Figure III.8. The Tauc's equation was used to determine the band gap energy, according to the following relation (II.20).

The Urbach energy (band tail width), (E_u) is the disorder in film network. It is determined using the expressions (II.21).

The calculated optical band gap energy and the Urbach energy for 3, 5, 7, 9, 11, 13 and 15 layers of TiO_2 thin films are summarized in Table III.3. These results indicate that the band gap energy (E_g) decreases from 3.67 to 3.52 eV as the number of layers increases. In contrast, the Urbach energy increases from 0.288 to 0.315 eV with increasing the number of layers. These obtained values are in good agreement with the previously reported values [22,23]. The gradual decrease in the band gap energy is related to the quantum confinement effect caused by the crystallite sizes enlargement [24,25], which is correlated to low band gap energy. In other side, the increase of the band tail width (E_u) can be attributed to the increase of the density of oxygen vacancy atoms into the TiO_2 film [26,27].

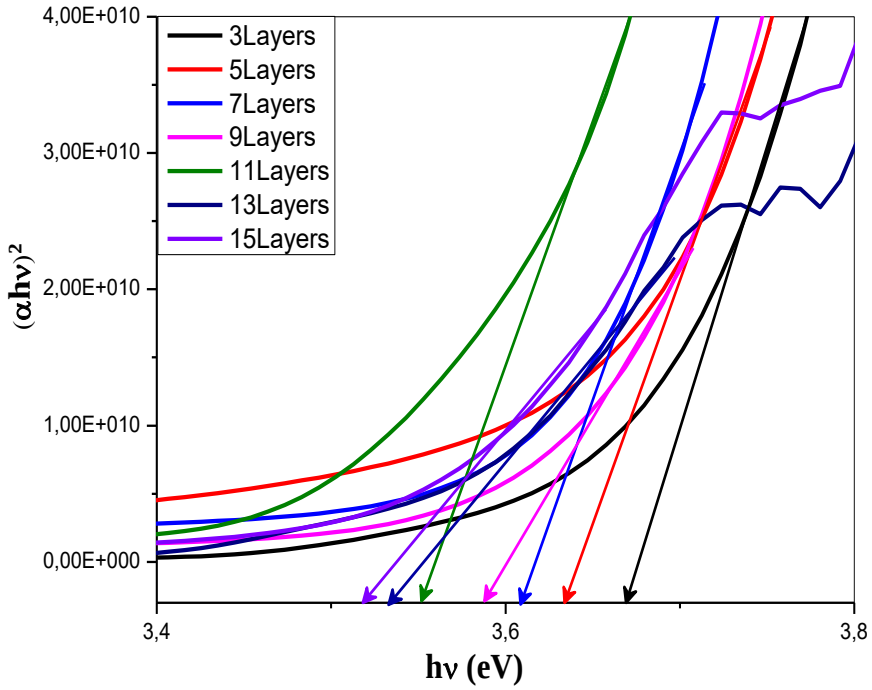

Figure III.8. The plot of $(\alpha h\nu)^2$ versus hν of anatase TiO_2 thin films deposited on glass substrate using different number of spin-coated layers.

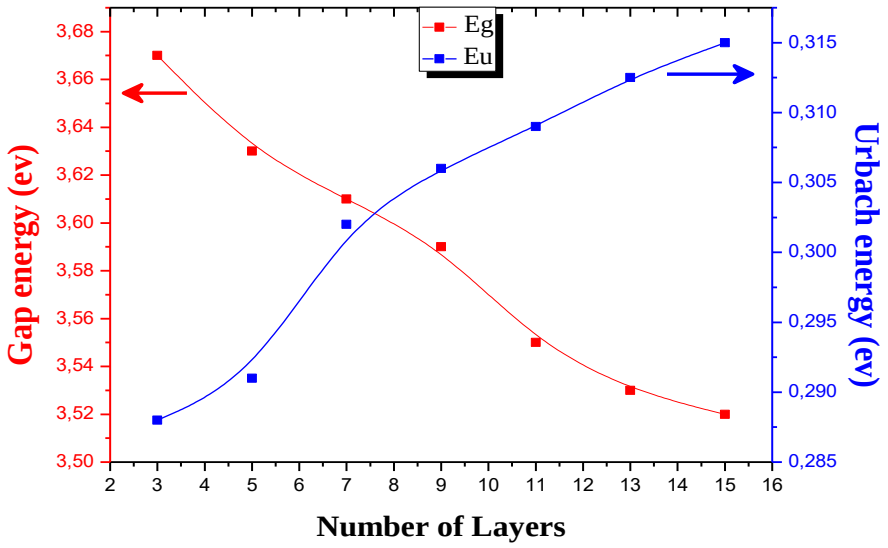

Figure III.9. Optical band gap and Urbach energy of TiO_2 films as a function of the number of spin-coated layers

Table III.3. Optical band gap energy and Urbach energy values of TiO_2 thin films deposited using sol-gel spin coating method with different number of spin-coated layers.

Number of Layers	Thickness (nm)	Band Gap Energy (eV)	Urbach Energy (eV)
3	243.72	3.67	0.288
5	313.20	3.63	0.291
7	477.22	3.62	0.302
9	661.32	3.59	0.306
11	924.78	3.55	0.309
13	1299.14	3.53	0.312
15	1543.83	3.52	0.315

III.1.6.5. Fourier Transform Infrared (FTIR) Spectroscopic Analysis

FTIR spectroscopy is an excellent tool to finding the nature of structural and chemical bonding in the titanium oxide (TiO_2) thin films. Figure III.10 represents the FTIR spectra of titanium oxide (TiO_2) thin films with various numbers of layers in the range of 400 – 4000 cm^{-1}.The characteristic absorption bands in the pure TiO_2 film, as shown in Figure III.10, include two strong broad peaks. One is around 764 cm^{-1}, which is assigned to the stretching vibration of Ti–O groups, and the other is around 907cm^{-1}, which is assigned to the stretching vibration mode of Ti–O–Ti groups. By the way, absorption intensity of the two peaks

increases with increasing number of layers which indicated to the enhancement of the crystallization degree [28], that supported by DRX results. Also, the peak of feeble absorption intensity located at 1563 cm^{-1} is associated to water molecules H–O–H stretching vibrations (pertaining to the adsorbed water) [29]. Also, there are traces of CO_2 (2354 cm^{-1}). This last band is due to the fact that the FTIR analysis of TiO_2 thin films was carried out in ambient air [30]. On the other hand, we observe tow other peaks locate at 2852 and 2922 cm^{-1}, these peaks are observed due to the C–H stretching bonds of the organic compounds [31].

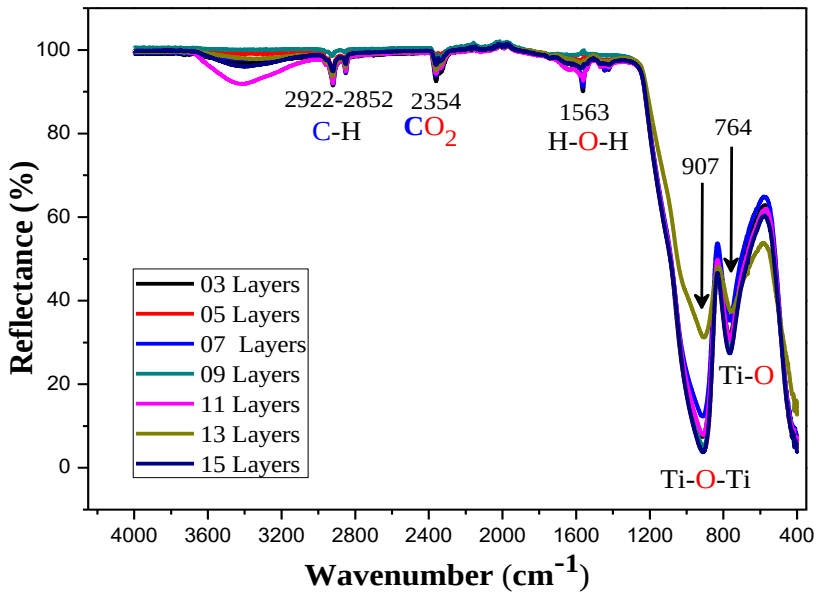

Figure III.10. FTIR reflectance spectra of TiO_2 thin films deposited on glass substrate using different number of spin-coated layers.

III.1.6.6. Electrical properties

The electrical properties of the obtained TiO_2 thin films as a function of number of layers were measured by using four probe techniques at room temperature. The value of the electrical resistivity ρ is obtained according to equation (II.22).

Figure III.11 shows the electrical resistivity of TiO_2 thin films as a function of the number of layers. As we can see, the measured values of ρ were found to be in the order of 10^3 Ω.cm for all films. As the number of layers increases, ρ gradually increases from 2.51×10^3 Ω.cm until a maximum value of 13.06×10^3 Ω.cm for 15 layers. This resistivity is greater than those found in the literature for pure TiO_2 obtained by sol-gel process (resistivity ~10^4 Ω·cm) [32,33], while, it is lower than that reported by Muaz et al. [34] for TiO_2 synthesized by the sol–gel method (resistivity ~10^7 Ω·cm). The electrical resistivity rise may ascribed to inherent

defects in TiO_2 films such as Ti interstitials and/or O vacancies (VO), these defect be have as an acceptor ones, that may play an important role in the free electrons concentration reduction and consequently the films resistivity increase.

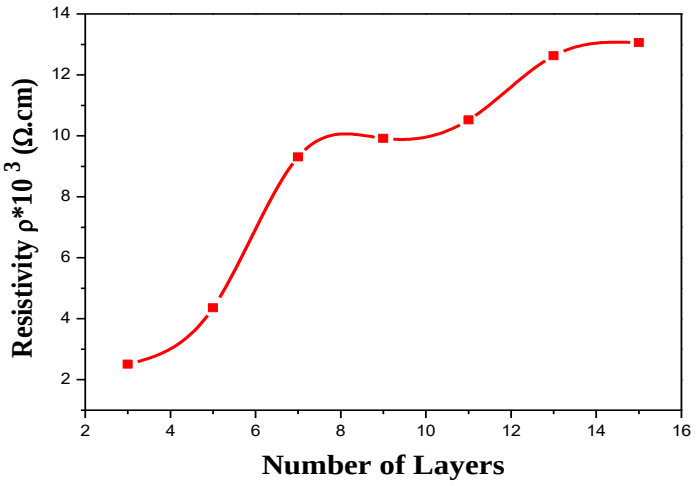

Figure III.11. Electrical resistivity variations of TiO_2 thin films as a function of the number of spin-coated layers.

Conclusion

In conclusion, high quality nano-crystalline TiO_2 thin films were deposited on glass substrate via a sol-gel spin coating method. Their physico-chemical properties variation with number of layers were investigated. The X-ray diffraction analysis showed that the only detectable crystal structure is the one of anatase with strong (101) as preferential orientation, while the films crystallite size varies from 15.31 to 18.03 nm. In addition, all TiO_2 thin films are highly transparent in the visible region where the absorption band shifts to wards higher wavelength (Red Shift), suggesting the reduction in the optical band gap energy by increasing the layers. The FTIR measurements confirmed the presence of functional groups and chemical bonding in these films. Moreover, the electrical resistivity varies with the number of layers, it rise with number of layers from 2.51×10^3 to 13.06×10^3 Ω.cm. These properties make it useful for many applications such as antireflection coating, self-cleaning glass, gas sensors, dielectrics materials, blocking layers (buffer film) in DSSC, photo catalysis, and antibacterial.

Finally, these multi-layers TiO_2 thin films may be a potential candidate in optoelectronics devices due to their attractive properties, such as strongly absorb UV radiations, high transmittance visible light, single anatase phase and suitable crystallite size.

III.2. Effect of mixed solvent

III.2.1. Introduction

The deposition parameters of the Sol-Gel (spin coating) process are closely related to the characteristics of TiO_2 films generated by this technology. As a result, deposition conditions have been widely studied in attempt to improve TiO_2 film characteristics. Moreover, the choice of solvent is also dictated by process requirements (ease of drying, integrity of the final material), possible toxicity or environmental constraints (emission of volatile organic compounds).

The solvent have been studied by Artaki et al. [35]. He classified them into three categories:

- protic and polar solvents (methanol, formamide)
- aprotic and polar solvents (dimethyl formamide, acetonitrile)
- aprotic and apolar solvents (dioxane).

The most favorable solvents in this works are polar and protic solvents. Indeed, in acid catalysis, these solvents stabilize the all intermediates by a better, as they form hydrogen bonds with them. On the other hand, in basic catalysis, they inhibit the reactivity of nucleophiles by protonating them. Under these conditions, the most suitable solvents are therefore the polar aprotics which stabilize the charged transition state and which solvate the reactants and the worst solvents are the apolar aprotics which do not stabilize the reaction intermediates and which poorly solvate the catalysts. Also, Artaki also showed that the morphology of the networks created was different depending on the solvent. Polar solvents give more linear structures and apolar solvents denser and spherical structures which is explained by a greater reactivity in the network than at the periphery.

In this chapter, we will studied the effect of the mixed solvent (ethanol + methaol) on the structure, optical, and electrical properties of TiO_2 thin films, and we evaluated the relationship between these properties in general.

III.2.2. Experimental details

III.2.2.1. Preparation of TiO_2 films

The sol-gel (spin coating) procedure was used to deposite TiO_2 thin films as a function of concentration solution at room temperature. The solution was prepared by mixing titanium

Tetra isopropoxide (Ti $[OCH(CH_3)_2]_4$) ($Molecular\ weight$ = 284.25 $g.\ mol^{-1}$) which was used as precursor and acetyl acetone (CH_3COCH) used as a stabilizer and mixing ethanol (C_2H_5OH) with methanol (CH_3OH) used as a solvent as follows : ***[(0% of methanol, 100% of ethanol), (25% of methanol, 75% of ethanol), (50% of methanol, 50% of ethanol), (75% of methanol, 25% of ethanol) and (100% of methanol, 0% of ethanol)]***.

The mixture was then agitated for 3 hours at 50 °C with a magnetic stirrer until a clear, yellowish, and slightly viscous solution was achieved. Soda-lime glass plates (2.5×2.5×0.15 cm^3) are used as the substrates, which it was cleaned with ethanol, acetone and distilled water during 5 min into each process and subsequently dried in air.

Now the glass substrate is fixed on spin coating system, and then the prepared solution was dropped onto cleaned glass substrate with rotation speed of 4000 rpm for 30 s in order to obtain a well coated thin film on glass substrates. After each coating, the coated film was dried at 250 °C for 10 min on a furnace to evaporate the organic solvent. This technique was repeated for seven times to produce a multilayer film that was annealed in an air furnace for 2 hours at 500 °C.

Figure III.12 shown the overall procedure for preparing and characterisation of TiO_2 thin films using the sol-gel (spin coating) technique.

III.2.2.2. Characterization of thin film

The synthesized structural, optical and electrical properties of TiO_2 films were characterized using various techniques. Where the film adherence to the substrate was evaluated using the tape method. The X-ray diffraction (XRD) studies were conducted in a BRUKER–AXS type D8 diffractometer (CuKα1 radiation, 1.5406 A°) radiation with in the 2θ range of 10°–90°, with the steps of 0.02°. A Perkin Elmer Lambda 950 UV/VIS spectrometer was used to measure the films transmittance and absorbance spectra in the 300–1100 nm wavelength range. Moreover, the FTIR spectra were obtained with a Fourier transform infrared spectrometer (Perkin Elmer UATR Two). The scanning wavelength of infrared was 400 – 4000 cm^{-1}. The resistivity was achieved by the four aligned probe method.

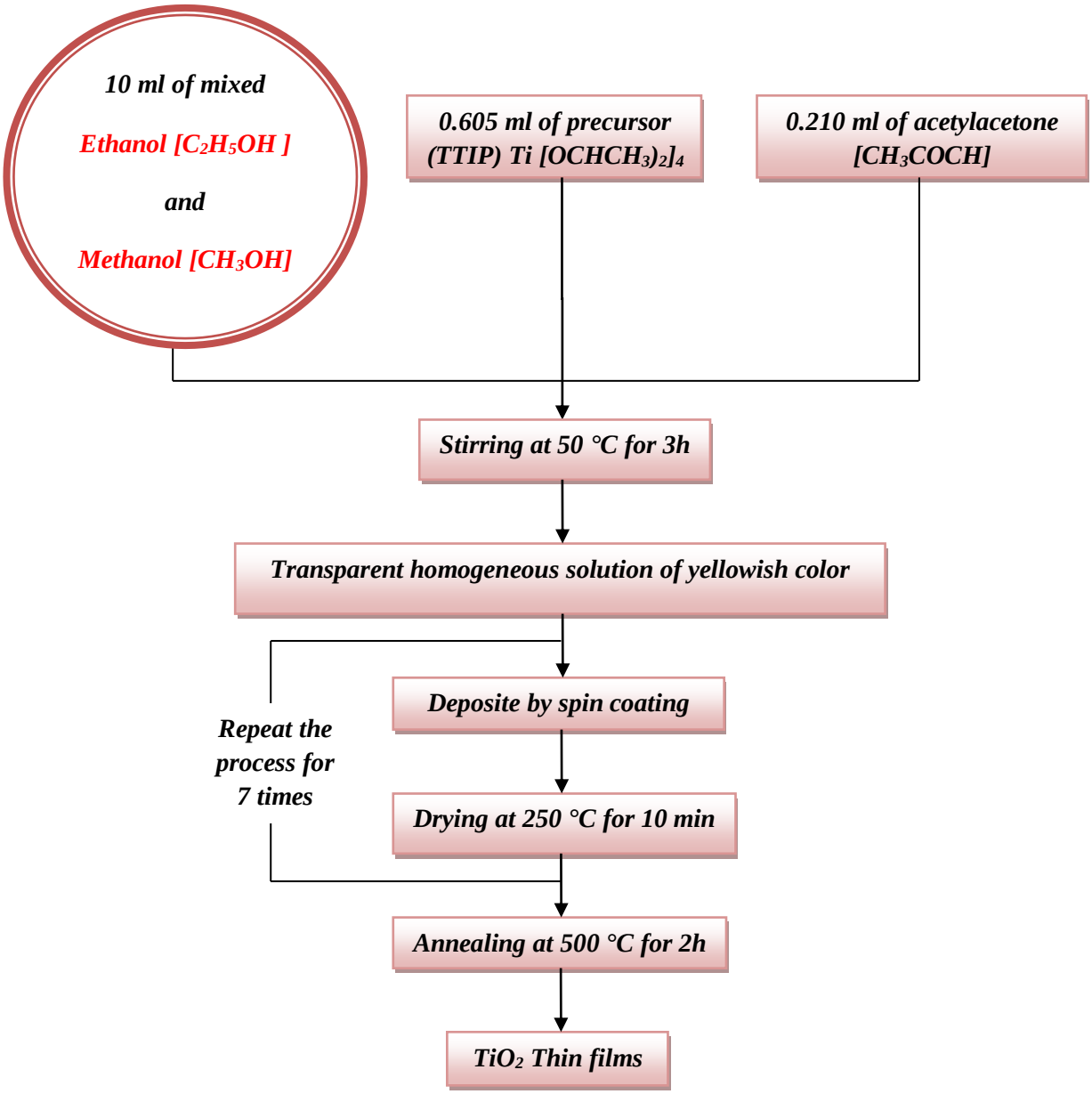

Figure III.12. The schematic diagram of the preparation steps of TiO_2 thin films at different percentages of the methanol and ethanol solvent.

III.2.3. Results and discussion

III.2.3.1. Film thickness study

The variation in titanium dioxide (TiO_2) film thickness as a function of various ethanol and methanol ratios was presented in Figure III.13. It can be noticed, that the film thickness increases with increasing the percent of methanol from 477.22 to 940.78 nm. Moreover, it is clearly observed that the methanol solvent shows the higher thickness than the ethanol. The

increase in film thickness of the films probably due to crystallite sizes. These results are in good agreement with those published by A. K. M. Muaz et all. [36].

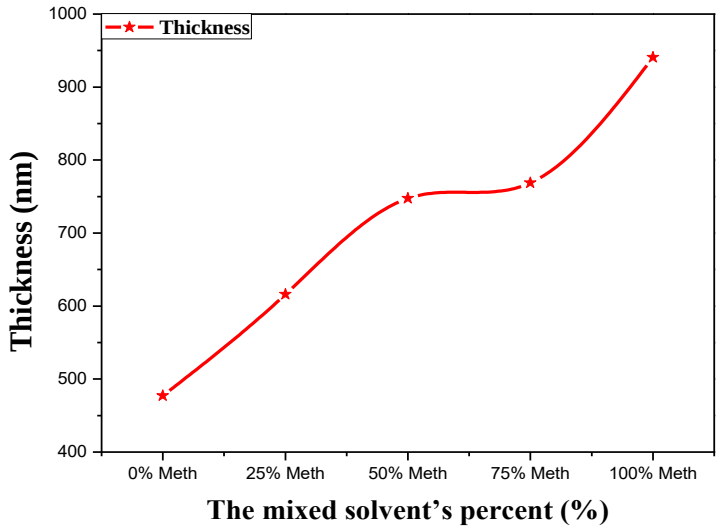

Figure III.13. Films thickness's as a function of the mixed solvent's percentage.

III.2.3.2. Structural characteristics

The structural characterization is very important in explaining optical and electrical properties of thin TiO_2 films. The X-ray diffraction patterns were recorded with various ratios of ethanol and methanol which was represented in Figure III.14. The XRD results show that all the TiO_2 films deposited from a mixture of ethanol and methanol was so interesting results. When deposited of TiO_2 thin films on the glass substrates, the XRD patterns of the all samples grown using methanol and ethanol as a solvent showed reflections exclusively related to the anatase phase (Figure III.14). Peaks in XRD correspond to the (101), (004), (112), (200) and (211) reflections at diffraction angle of 25.33°, 37.92°, 38.01°, 48.13° and 54.08°. Respectively, This is in accordance with JCPDS (n°: 21-1272). Moreover, no other phases (rutile or brookite) are detected in our results. countrary to the results of XRD pattern of as deposited TiO_2 film on glass substrate at 550 °C of methanol and ethanol that carried solvent ratios obtained by Cynthia Edusi et al [37], suggest that the films produced with a (50% of methanol : 50% of ethanol) and a (75% of methanol : 25% of methanol) mixture showed the presence of only the rutile phase. Also, the films produced with 100% of methanol gives only the rutile phase. While the results of our work are consistent with the results obtained by Cynthia Edusi et all [37]. When 100% ethanol is used as solvent, gives exclusively anatase.

As can be seen from the Figure III.14 the intensity of the (101) peak generally increases with the increase of methanol ratios out from 0% to 100%. In the same time , it decreases with the increase of ethanol ratios out from 0% to 100% and this indicates the increase of the percentage of the methanol solvent improved the TiO_2 thin films crystallinity, where we find the maximum crystallization intensity at that the films produced of (100% of methanol: 0% of ethanol), in another meaning because of the increase of nucleation sites. Furthermore, we notice that the samples have a strong preferred orientation in the (101) direction, the peak becomes narrower, intense when the methanol solvent ratios increases, and this indicate the enhancement of the films crystallinity. It might be the reasons of film growth at the (101) direction since it requires the lowest free surface energy [38], which leads to the highest atomic density achieved at the (101) direction. Thus, it appears from this investigation that a mix of two phases with pureforms, with a certain degree of control over the ratio of two phases, can be achieved by controlling the solvent mixture ratio, which could be beneficial for the manufacture of specific titanium dioxide films.

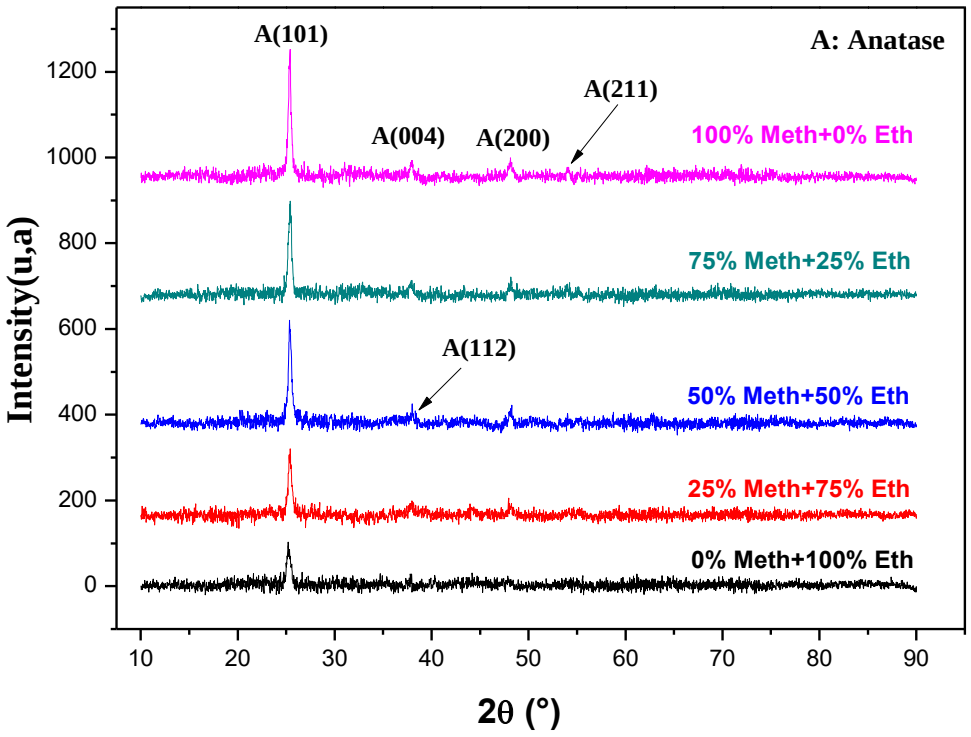

Figure III.14. The XRD patterns of TiO_2 thin films deposited with the percentage of the mixed solvent.

The microstructural parameters of TiO_2 thin films prepared using different ratios of solvents ethanol and methanol are grouped in Table III.4, exhibit the highest XRD diffraction peaks on the (101) plane, so the crystallite sizes of the TiO_2 are highlighted on it. Therefore, the crystallite size along this plane was estimated using Debye–Scherrer equation (II.9). The strain (ε) was determined by the formula (II.12). The quantity of defects (δ) in TiO_2 thin film (the dislocation density) was estimated by the Williamson and Smallman's equation (II.13). From Figure III.15 which shows the crystallite sizes at different ethanol and methanol ratios and Table III.4, we can observe crystals increasing in size from 16.04 nm to 21.77 nm (lower defects). The result shows that the TiO_2 thin films prepared using 100% of ethanol solvent produce the smallest crystallite size (16.04 nm). Correspondigly, the TiO_2 thin films prepared using 100% of methanol solvent produce the largest crystallite size (21.77 nm). The largest crystalline size displayed by the film prepared using methanol solvent at ratio of 100% can be attributed to higher viscosity of methanol compared with other solvent (ethanol) [39]. while the strain decreased by the increase in the percent of methanol solvent from 2.15 x 10^{-3} to 1.59 x 10^{-3}. This is due to the increase of crystallite size that led to reduction in inter-crystalline barriers as grain boundary area in the layers. On the other hand, as for the dislocation density it decreased from 3.88 × 10^{15} to 2.10 × 10^{15} (lines/m^2) with the increase in the percentage of methanol solvent and the decrease in the percentage of ethanol solvent (see Figure III.16) . So, we can conclude that the use of methanol instead of ethanol reduces the structural defects, indicating the improvement in the crystallinity. These results are supported by the variation of XRD data. As reported Youssef Doub et al. [40], S. Benramache et al. [41] and A. Begum et al. [42].

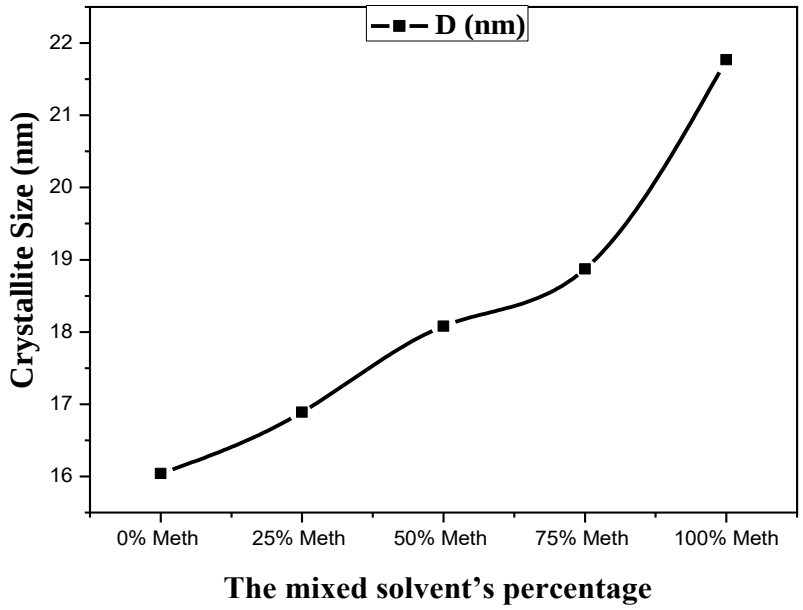

Figure III.15. The Crystallite size of TiO_2 thin films with different the percentage of the methanol and ethanol solvent.

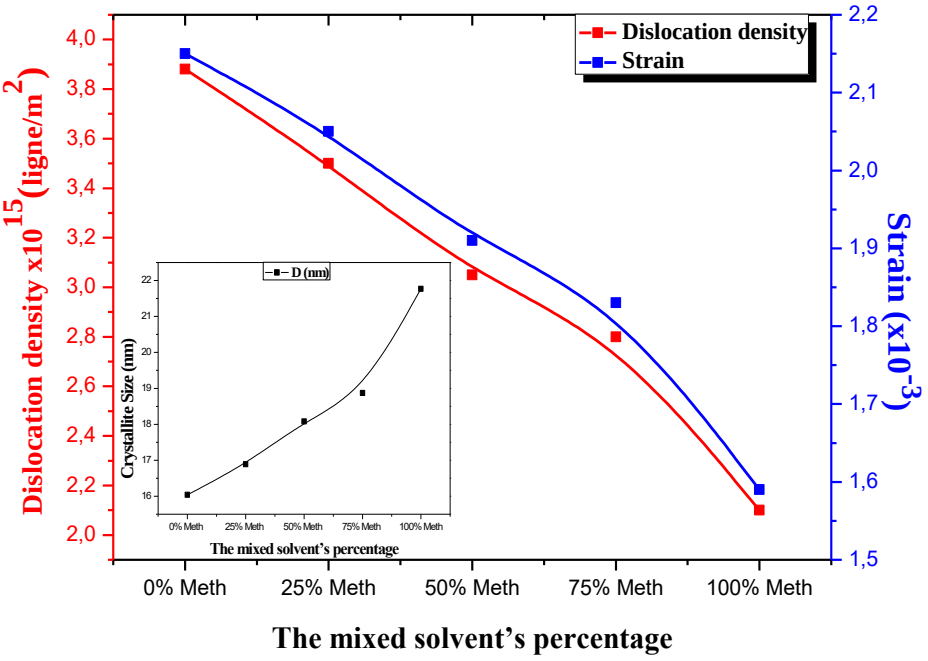

Figure III.16. Dislocation density δ and strain ε in terms of the various ratios of methanol and ethanol.

Table III.4. The crystallite sizes, dislocation density and strain parameters of TiO_2 thin films at different percentages of the methanol and ethanol solvent.

The mixed solvent's percentage	Peak (hkl)	2θ°	FWHM (β°)	Crystallite size D (nm)	Dislocation density(δ)x10^{15} (Lines /m^2)	Strain (ε)x10^{-3}
0% Methanol+100% Ethanol	(101)	25.20	0.50	16.04	3.88	2.15
25% Methanol+75% Ethanol	(101)	25.35	0.48	16.89	3.50	2.05
50% Methanol+50% Ethanol	(101)	25.33	0.45	18.08	3.05	1.91
75% Methanol+25% Ethanol	(101)	25.44	0.43	18.87	2.80	1.83
100% Methanol+0% Ethanol	(101)	25.37	0.37	21.77	2.10	1.59

The lattice parameters a = b≠c for tetragonal structure, d_{hkl} is given by the formula (II.11):

The resolution of the two equation (II.10) and (II.11) for two (hkl) planes allowed us to determine the lattice parameters "a" and "c". The 2θ values chosen for the calculation were 25°, 37° and 48° positions corresponding to (101), (004), and (200) planes, respectively, for the samples prepared by various ethanol and methanol ratios. The lattice parameters of TiO_2 thin films varied slightly with the change of the solvents percent. The lattice parameters a, b and c showed in Table III.5 are in accordance with TiO_2 powder crystallized under a tetragonal structure [39].

Table III.5. The structural parameters of TiO_2 films corresponding to (101) plane as a function of the mixed solvent's percentage

The mixed solvent's percentage	hkl planes	2θ°	Calculated parameters			Reference parameter (JCPDS card No 21- 1272)	Stress (Gpa)
			d-spacing (Å)	Lattice constant a (Å)	Lattice constant c (Å)		
0% Methanol+100% Ethanol	(101)	25.20	3.5301	3.8000	9.5376		0.305
25% Methanol+75% Ethanol	(101)	25.35	3.5092	3.7789	9.4592	a_0 = 3.7852Å	-0.289
50% Methanol+50% Ethanol	(101)	25.33	3.5130	3.7829	9.4710	c_0 = 9.5139Å	-0.270
75% Methanol+25% Ethanol	(101)	25.44	3.4982	3.7636	9.4847	d_0 = 3.521 Å	-0.259
100% Methanol+0% Ethanol	(101)	25.37	3.5075	3.7755	3.4774	2θ = 25.28°	-0.224

The residual stress (σ_{stress}) of the prepared films have been calculated using the relation (II.14). From Figure III.17 that shows the values of the stress of TiO_2 thin films deposited at various ratios of solvents ethanol and methanol, and Table III.5, One can deduce the stress of the films prepared at (0% of methanol : 100% of ethanol) were found to have a tensile stress. In contrast, the films deposited at methanol percent from (25%, 50%, 75% and 100%) were found to have a compressive stress, which means the stress changed from tensile (positive) to compressive (negative). Moreover, the stress decreases for TiO_2 thin films deposited from -0.289 Gpa to -0.224 Gpa with the increases of methanol solvent ratios. Also, we notice that the stress have a variation inverse with grain size, when there is an increase in grain size, there is an improvement in crystal quality. So, there will be a decrease in stresses, this is due to the decrease in grain boundaries [43].

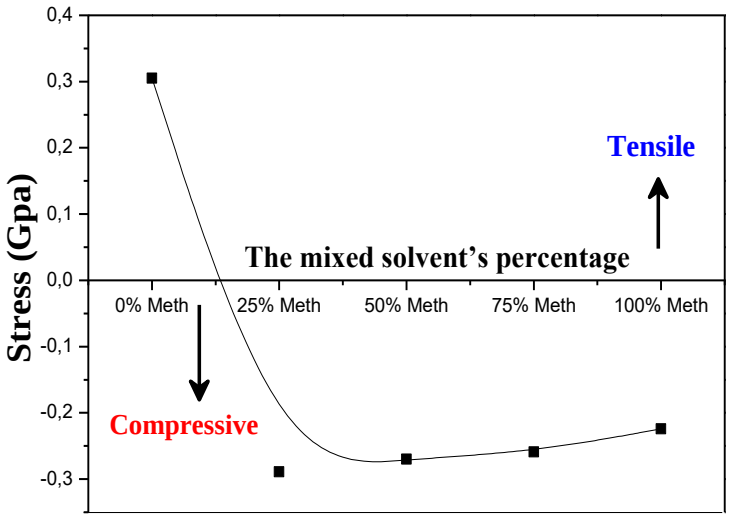

Figure III.17. The stress of TiO_2 thin films in terms of the various ratios of methanol and ethanol.

III.2.3.3. FTIR Spectroscopic Analysis

The Fourier transform infrared (FTIR) spectra of anatase titanium dioxide (TiO_2) produced by sol-gel spin coating are shown in Figure III.18. The FTIR study of these TiO_2 nanoparticles showed the characteristics of the formation of high purity products and the peaks correspond to anatase titania. The spectroscopic band is observed in the range 500 cm^{-1} - 600 cm^{-1} for TiO_2 nanoparticles, which is described as a stretching mode of vibration for the Ti–O bond [44]. Another peak between 600 and 800 cm^{-1} corresponds to the Ti–O–Ti bond's

stretching vibration [45], and the other is around 897 cm^{-1} can be attributed to the Ti–O stretching mode, which involves nonbridging oxygen atoms. As reported by Carolina M. Rodrigues et al. [46] and Daniela Cordeiro Leite Vasconcelos et al. [47]. Besides, we observe two bands at around 1430 and 1588 cm^{-1} corresponding to the simple bending C–H vibration of the organic compounds. As reported by Tessy Lopez et al. [48] and E. Zanchetta et al. [49]. Moreover, additional peaks are noted at 2924 cm^{-1} (CH_2 asymmetric stretching mode) and at 2856 cm^{-1} (CH_2 symmetric stretching mode) of the alcoxide [50,51]. Also, The C=O vibration band at 1704.3 cm^{-1} is found for TiO_2 thin films. As reported by Jianhong Wei et al. [52]. On the other hand, there are also traces of CO_2 (2361 cm^{-1}). This last band is due to the fact that the FTIR analysis of TiO_2 thin films was carried out in ambient air [30].

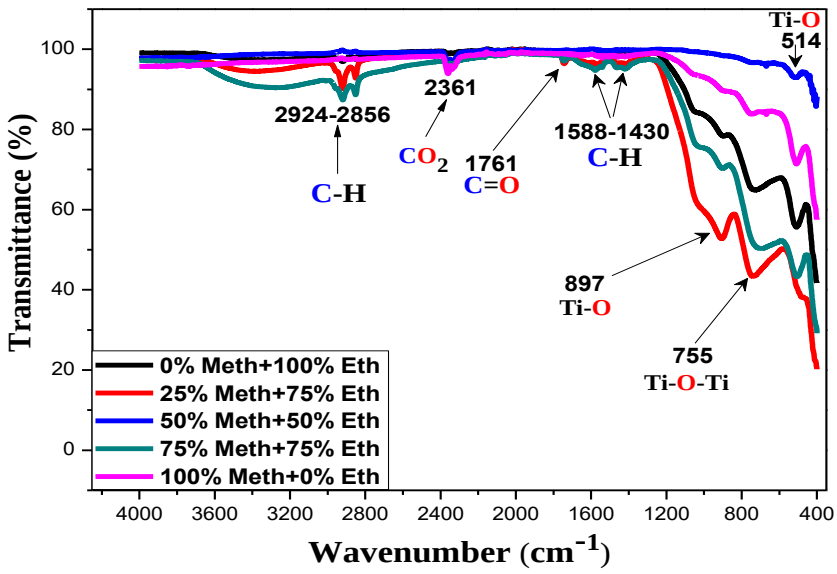

Figure III.18. FTIR spectra for TiO_2 thin films deposited as a function of the ratio of the mixed solvent.

III.2.3.5. Optical characteristics

The ability to knowledge optical characteristics of materials is critical in the design and analysis of optoelectronic devices [53]. Figure III.19 shows the transmittance spectra of TiO_2 thin films prepared at 500 °C by spin coating technique with different percentages of the mixed solvent in the wavelength range of 300 – 1100 nm. All samples have good absorption in the UV range (λ< 385 nm), and this is caused by the fundamental absorption of the light in thin films of TiO_2. On the other hand, there is a shift in the short absorption towards longer

wavelengths (i.e. red shift) when the percent of the mixed solvent of the solution were increased from 0% to 100% (See the insert image in Figure III.19), which indicates to narrowing the band gap energy of films. It is found that the TiO_2 films deposited at different percentages of the mixed solvent (methanol + ethanol) exhibit a high optical transparency more than 72% for all films, which gives the thin layers of TiO_2 the character of transparent films in the visible region. The highly transmittance of these films can be appropriated as transparent electrode of the solar cell application. On the other hand, in the visible region all of the samples indicate the existence of interference fringes in the transmission spectra ; this can be attributed to the decreased light scattering of incident light in the material due to uniform and homogenity of a smooth surface area consequently of interference oscillation between films and substrate surface [54]. As we also notice the transmittance increases with the increase of the percent of the methanol solvent from 0% to 100%, this last can be explained by an increase in the crystallinity of the films and the improvement of crystallinity, which leads to a decrease in optical scattering and defects. Also, this may be due to the loss of scattering light because of the oxygen vacancies and the growth of crystallite sizes in the principle causes to the improvement in the transmittance value [55].

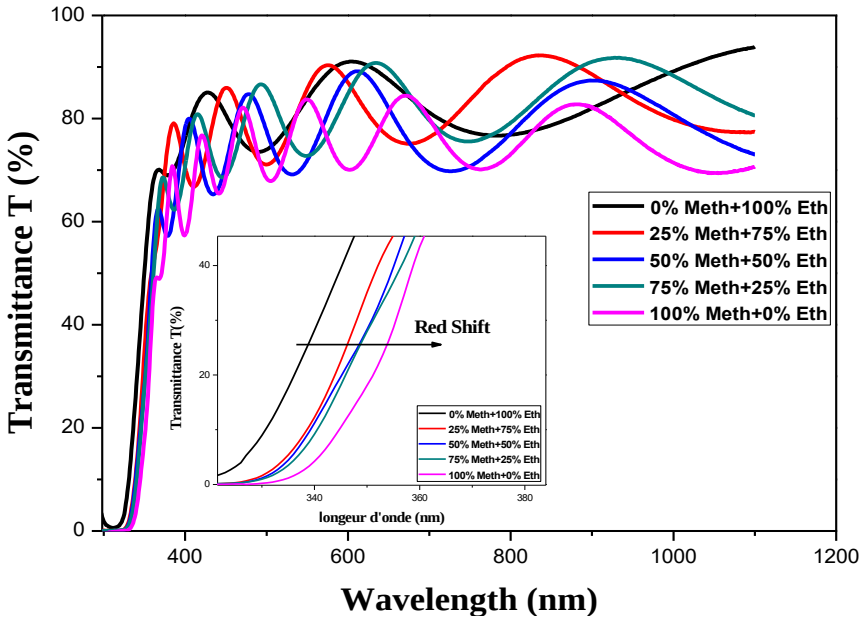

Figure III.19. Transmittance spectra of TiO_2 thin films as a function of the mixed solvent's percentage.

the extrapolation of the linear region of the curves to intersect at hν axis. From Figure III.20 and Table III.6. it decreased is possibly due to the generation of micro deformations and the decrease of interatomic can be seen that the energy band gap of TiO_2 samples decreased from 3.68 to 3.56 eV with increasing the percent of the methanol solvent. The reduction of energy band gap of TiO_2 thin films with the increase of methanol ratios was carried out could be owing to the associated to the increase of crystallite size. This decrease of optical band gap when the crystallite size spacing [56].

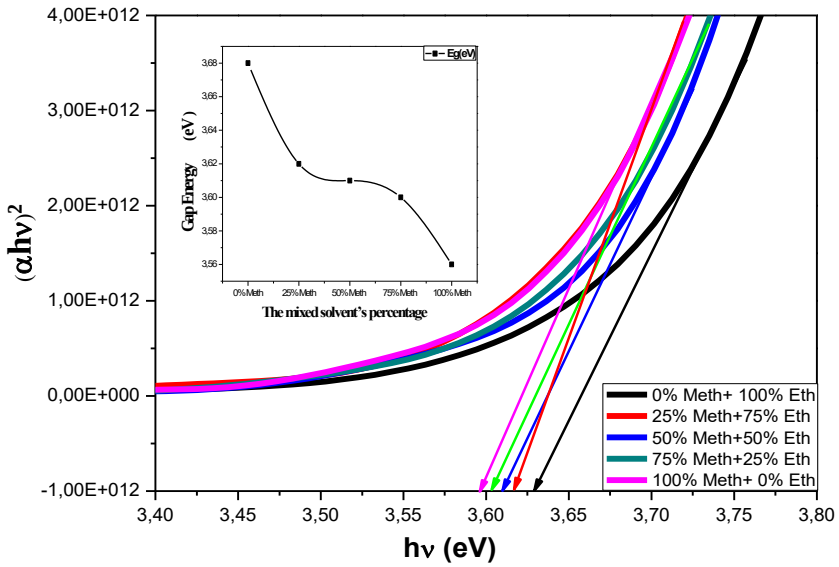

Figure III.20. Plots of $(\alpha h\nu)^2$ against hν of TiO_2 films as a function of the mixed solvent's ratios.

The Urbach energy is estimated by plotting Ln(α) vs. (hν) and fitting the linear portion of the curve with a straight line. As illustrated in Figure III.21, the reciprocal of the slope of this linear section produces the value of Eu.

As can be seen in Figure III.21, the Urbach energy or the width of the band tail decreased from 0.302 eV to 0.154 eV with the increases of methanol solvent ratios. This behavior proves that the degree of structural disorder decreases with the increase of the percent methanol solvent. Moreover, that a minimum Urbach energy were reached at the percentage of 100 % of TiO_2 thin films. This could be owing to improved crystallinity and minimization of strain and dislocation density, resulting in fewer defects in TiO_2 thin films

this means the ideal, good and adequate the solvent ratio for less structural disorder is at methanol solvent at 100 percentage.

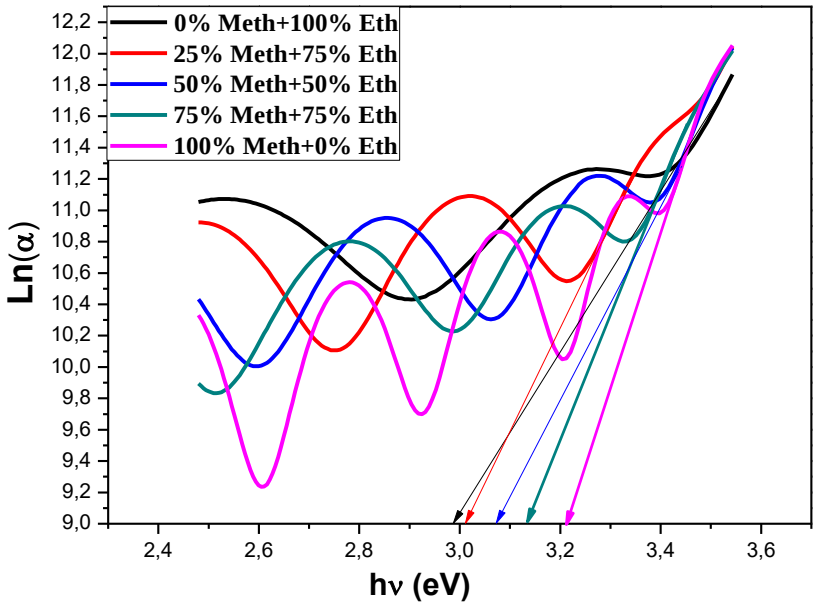

Figure III.21. Ln(α) vs hν plots of the films with different methanol and ethanol solvent's ratios.

Table III.6. Optical and electrical properties values of TiO_2 thin films deposited using sol-gel spin coating method with different ratios of methanol and ethanol.

The mixed solvent's percentage	Thickness (nm)	Band Gap Energy (eV)	Urbach Energy (meV)	Rsheet $x10^6$ (Ω/sheet)	Electrical resistivity $x10^2$ (Ω.cm)	Electrical conductivity $x10^{-3}$ $(Ω.cm)^{-1}$
0% Methanol+100% Ethanol	477.22	3.68	0.302	19.52	93.15	0.11
25% Methanol+75% Ethanol	616.12	3.62	0.167	3.25	2.02	4.95
50% Methanol+50% Ethanol	747.67	3.61	0.159	2.32	1.73	5.78
75% Methanol+25% Ethanol	768.60	3.60	0.156	2.05	1.57	6.36
100% Methanol+0% Ethanol	940.78	3.56	0.154	1.30	1.22	8.19

III.2.3.6. Electrical characteristics

Table III.6 illustrates the variation in resistivity (ρ) of thin films with the mixed solvent's percentage. As shown in Figure III.22 and Table III.6, the electrical resistivity decreased from 93.15×10^2 (Ω.cm) at (0% of methanol + 100% of ethanol) to 1.22×10^2 (Ω.cm) at (100% of methanol + 0% of ethanol). Reduction in the electrical resistivity can be attributed to the increase of the degree of crystallinity of the films, which leading to increasing crystallite sizes, as the result, decreases the scattering at grain boundaries [57] which corresponds with the present XRD results, and consequently increased carrier concentration and free carrier mobility for electrical conduction. On the other hand, this may be due to the increasing film thickness's ,which scatters grain boundary of free electrons in thicker films is less than in thinner films because of larger crystallite sizes . Since resistivity is directly proportional to the electron scattering frequency, as reported S. RaviShankar et all. [58].

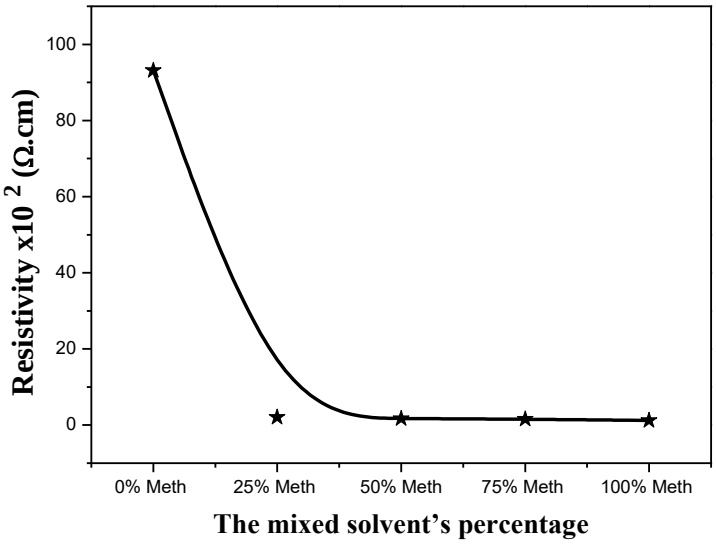

Figure III.22. Electrical resistivity as a function of the mixed solvent's percentage of methanol and ethanol.

Conclusion

High quality TiO_2 nanocrystal's thin films were resulted by the use of sol-gel (spin coating) method on glass substrates, which were annealed at 500 °C. The mixed solvent's percentage was studied at TiO_2 films' structural, optical, and electrical properties. The film thickness measured by Swanepoel method, where we notice an increase in the thickness of TiO_2 thin films with increasing methanol solvent ratio from 477.22 to 940.78 nm. In addition, all films have polycrystalline having tetragonal structure of anatase along (101) plane. However, we notice an increase in the preferential growth in the (101) plane for films with increasing methanol solvent ratio. Furthermore, we observe an increases in the crystallite size from 16.04 to 21.77 nm for TiO_2 nanoparticles. Correspondly, we observe a decrease in the dislocation density and strain with an increse in the ratio of methanol solvent from 3.88 x 10^{15} - 2.10 x 10^{15} (lines/m^2) to 2.15 x 10^{-3}- 1.59 x 10^{-3}, respectively. Besides, the stress of TiO_2 thin films changed from tensile to compressive. On the other hand , it is found that the TiO_2 films deposited at different percentages of the mixed solvent (methanol + ethanol) shows a high optical transparency than 72% for all films, which gives the thin layers of TiO_2 the character of transparent films in the visible region. The highly transmittance of these films can be appropriated as transparent electrode of the solar cell application. In addition, we noticed that the optical band gap energy (Eg) decreases from 3.68 to 3.56 eV where the absorption band shifts to wards higher wavelength (Red Shift). Correspondingly, urbach energy decreases from 0.302 to 0.154 eV. Hence, The FTIR measurements confirmed the presence of functional groups and chemical bonding in these films. of : Ti–O (at 514 cm^{-1}- 897 cm^{-1}), Ti–O–Ti (at 755 cm^{-1}), C=O (at 1761 cm^{-1}), CO_2 (at 2361 cm^{-1}) and C–H (2856 cm^{-1} - 2924 cm^{-1}, 1430 cm^{-1} - 1588 cm^{-1}). Electrical measurements showed that methanol solvent effectively increases the electrical conductivity from 0.11 to 8.19× 10^{-3} $(\Omega.cm)^{-1}$. From these findings, these TiO_2 thin films may be a potential candidate in optoelectronics devices due to their attractive properties.

Chapter III's references :

[1] J. Lungu, N. Stefan, G.Proden, A.Georgescu, A. Mandes, V. Ciupină, I.N. Mihăilescu, and M. A. Gîrţu, " Characterization of spin-coated TiO_2 bffer laters for dyesensitized solar cells", Digest Journal of Nanomaterials and Biostructures, 10, 967 (2015).

[2] I. Alhomoudi, J. Thakur, R. Naik, G. Auner, and G. Newaz, "Anatase TiO_2 films based CO gas sensor: Film thickness, substrate and temperature effects." Appl. Surf. Sci., 253, 8607 (2007).

[3] M. Landmann, E. Rauls, and W. G. Schmidt, " The electronic structure and optical response of rutile, anatase and brookite TiO_2." J. Phys. Condens. Matter, 24, 195503 (2012).

[4] S. Segota, L. Curkovic, D. Ljubas, V. Svetlicic, I. F. Houra, and N. Tomasic, "Synthesis, characterization and photocatalytic properties of sol–gel TiO_2 films." Ceram. Int., 37, 1153 (2011).

[5] S. Riaz and S. Naseem, "Controlled nanostructuring of TiO_2 nanoparticles: a sol–gel approach." J. Sol-Gel Sci. Technol., 74, 299 (2015).

[6] T. Giannakopoulou, N. Todorova, M. Giannouri, J. Yu, and C. Trapalis, "Optical and photocatalytic properties of composite TiO_2/ZnO thin films." Catal. Today, 230, 174 (2014).

[7] Z. Ding, X. Hu, P. L. Yue, G. Q. Lu, and P. F. Greenfield, "Synthesis of anatase TiO_2 supported on porous solids by chemical vapor deposition." Catal. Today, 68, 173 (2001).

[8] M. I. Khan, K. A. Bhatti, R. Qindeel, H. Saeed Althobaiti, and N. Alonizan, "Structural, electrical and optical properties of multilayer TiO_2 thin films deposited by sol-gel spin coating." Results in Physics, 7, 1437 (2017).

[9] T. B. Ghosh, S. Dhabal, and A. K. Datta, "On crystallite size dependence of phase stability of nano-crystalline TiO_2." J. Appl. Phys., 94, 4577 (2003).

[10] M. M. Hasan, A. S. M. A. Haseeb, R. Saidur, H. H. Masjuki, and M. Hamdi, "Influence of substrate and annealing temperatures on optical properties of RFsputtered TiO_2 thin films." Journal of Optical Materials, 32, 690 (2010).

[11] A. Derbali, H. Saidi, A. Attaf, H. Benamra, A. Bouhdjer, N. Attaf, H. Ezzaouia, L. Derbali, and M. S. Aida, "Solution flow rate influence on ZnS thin films properties

grown by ultrasonic spray for optoelectronic application." J. Semiconduct, 39, 093001(1-7) (2018).

[12] S.-S. Lin and J.-L. Huang, "Effect of thickness on the structural and optical properties of ZnO films by r.f. magnetron sputtering." Surface& Coatings Technology, 185, 222 (2004).

[13] M. I. Khan, S. Imran, D. Shahnawaz, M Saleem, and S U Rehman, "Annealing effect on the structural, morphological and electrical properties of TiO_2/ZnO bilayer thin films." Results in Physics, 8, 249 (2018).

[14] I. Ben Miled, M. Jlassi, I. Sta, M. Dhaouadi, M. Ha jji, G. Mousdis, M. Kompitsas, and H. Ezzaouia, "Influence of In-doping on microstructure, optical and electrical properties of sol–gel derived CdO thin films." J. Mater. Sci., Mater. Electron., 29, 11286 (2018).

[15] E. Nishimura, T. Sasabayashi, I. Norihiro, Y. Sato, K. Utsumi, K. Yano, A. Kaijo, K. Inoue, and Y. Shigesato, "Structure and internal stress of tin-doped indium oxide and indium–Zinc oxide films deposited by DC magnetron sputtering." Jpn. J. Appl. Phys., 46, 7806 (2007)

[16] S. Rahmane, M. A. Djouadi, M. S. Aida, and N. Barreau, "Oxygen effect in radio frequency magnetron sputtered aluminium doped zinc oxide films." Thin Solid Films, 562, 70 (2014).

[17] T. P Rao, M. C. S Kumar, and V. Ganesan, "Effect of annealing on the structural, optical and electrical properties of ZnO thin films by spray pyrolysis." India J. Phy, 85, 1381 (2011).

[18] Y. Shen, H. Yu, J. Yao, S. Shao, Z. Fan, H. Hea, and J. Shao, "Investigation on properties of TiO_2 thin films deposited at different oxygen pressures." Optics& Laser Technology, 40, 550 (2008).

[19] R. Mechiakh, N. Ben Sedrine, and R. Chtourou, "Sol–gel synthesis, characterization and optical properties of mercury-doped TiO_2 thin films deposited on ITO glass substrates." Appl. Surf. Sci., 257, 9103 (2011).

[20] N. Witit-anun, P. Rakkwamsuk, and P. Limsuwan, "Characterization of anatase and rutile TiO_2 thin films deposited by two cathodes sputtering system." Advanced Materials Research, 55–57, 469 (2008).

[21] D Wojcieszak, J Michałmazur, A Indyka, M Jurkowska, P Kalisz, D Domanowski,

J Kaczmarek, and Domaradzki, "Mechanical and structural properties of titanium dioxide deposited by innovative magnetron sputtering process." Materials Science Poland, 33, 660 (2015).

[22] M. Sreemany and S. Sen, "A simple spectrophotometric method for determination of the optical constants and band gap energy of multiple layer TiO_2 thin films." Mater. Chem. Phys., 83, 169 (2004).

[23] T. Tański, W. Matysiak, D. Kosmalska, and A. Lubos, "Influence of calcination temperature on optical and structural properties of TiO_2 thin films prepared by means of sol-gel and spin coating." Bulletin of the Polish Academy of Sciences: Technical Sciences, 66, 151 (2018).

[24] T. Ivanova, A. Harizanova, T. Koutzarova, and B. Vertruyen, "Optical and structural characterization of TiO_2 films doped with silver nanoparticles obtained by sol–gel method." Optical Materials., 36 (2013) 207–213

[25] S. Kumar, N. K. Verma, and M. L. Singla, "Sized dependent reflactive properties of TiO_2 nanoparticles and reflectors made there of." Digest Journal of Nanomaterials and Biostructures .Vol. 7, No. 2, April - June 2012, p. 607 - 619, 7, 607 (2012).

[26] M. Caglar and Y. Caglar, "The determination of the thickness and optical constants of the ZnO crystalline thin film by using envelope method." Optoelectron. Adv. Mater, 8, 1410 (2006).

[27] B. Choudhury and A. Choudhury, "Oxygen defect dependent variation of band gap, Urbach energy and luminescence property of anatase, anatase–rutile mixed phase and of rutile phases of TiO_2 nanoparticles." Physica E, 56, 364 (2014).

[28] Z. Yuan, B. Li, J. Zhang, C. Xu, and J. Ke, "Synthesis of TiO_2 thin film by a modified sol-gel method and properties of the prepared films for photocatalyst." J Sol-Gel Sci. Techn, 39, 249 (2006).

[29] L-L Yang, Y.-S. Lai, and J. S. Chen, "Compositional tailored sol-gel SiO_2–TiO_2 thin thin films: Crystallization, chemical bonding configuration, and optical properties." J. Mater. Res., 20, 3141 (2005).

[30] S .Chelbi, L. Hammiche, D. Djouadi, A. Chelouche, "Caracterisations structurale et optique de l'aerogel de TiO elabore dans l'ethanol supercritique." Rev. Alg. Phys, Vol. 2, N° 2, 2015.

[31] Z. Jiwei, Y. Xi, Z. Liangying, S. Bo, H. Chen, "Orientation control and dielectric

properties of sol–gel deposited Ba (Ti, Zr) O_3 thin films." J. Cryst. Growth. 262 (2004) 341–347.

[32] I. Senain, N. Nayan, and H. Saim, "Structural and electrical properties of TiO_2 thin film derived from sol-gel method using titanium (IV) but oxide." International Journal of Integrated Engineering, 2, 29 (2010).

[33] A. Valour et al, "Optical, electrical and mechanical properties of TiN thin film obtained from a TiO_2 sol-gel coating and rapid thermal nitridation." Surface & Coatings Technology, 413, 127089 (2021).

[34] A. K. M. Muaz, U. Hashim, F. Ibrahim, K. L. Thong, M. S. Mohktar, and W- W. Liu, "Effect of annealing temperatures on the morphology, optical and electrical properties of TiO_2 thin films synthesized by the sol–gel method and deposited on Al/TiO_2/SiO_2/p-Si." Microsyst. Technol., 22, 871 (2016).

[35] Artaki, T. W. Zerda and J. Jonas, "Solvent effects on the condensation stage of the sol-gel process." J. NonCryst. Sol. (1986) 81; 381-395.

[36] A. K. M. Muaz, U. Hashim, M. K. Md. Arshad, A. R. Ruslinda, R. M. Ayub, Subash C. B. Gopinath, C. H. Voon, Wei-Wen Liu, and K. L. Foo, " Study of nanoparticles TiO_2 thin films on p-type silicon substrate using different alcoholic solvents." AIP Conference Proceedings 1733, 020086 (2016).

[37] Cynthia Edusi, Gopinathan Sankar, and Ivan P. Parkin, " The Effect of Solvent on the Phase of Titanium Dioxide Deposited by Aerosol-assisted CVD." Chem. Vap. Deposition 2012, 18, 126–132.

[38] Zhang K H L, Walsh A, Catlow C R A, et al. "Surface energies control the self-organization of oriented In_2O_3 nanostructures on cubic zirconia." Nano Lett, 10 (2010) 3740.

[39] K.L. Foon, M. Kashif, U. Hashim, Wei-Wen Liu, " Effect of different solvents on the structural and optical properties of zinc oxide thin films for optoelectronic applications. " Ceramics International. 2013.06.065.

[40] Youssef Doubi, Bouchaib Hartiti, Hicham Labrim, Salah Fadili, Mounia Tahri, Amine Belafhaili, Maryam Siadat, Philippe Thevenin, "Experimental study of properties of TiO_2 thin films deposited by spray pyrolysis for future sensory applications. " Applied Physics A (2021) 127:475.

[41] S. Benramache, A. Rahal, B. Benhaoua, " The effects of solvent nature on spray-

deposited ZnO thin film prepared from Zn $(CH_3COO)_2$, $2H_2O$. " Optik 125 (2014) 663–666.

[42] A. Begum, A. Hussain, A. Rahman, Beilstein , " Effect of deposition temperature on the structural and optical properties of chemically prepared nanocrystalline lead selenide thi films. " J. Nanotechnol. 2(3), 438–443 (2012).

[43] Abdelkarim Allag, Saad Rahmane,"Les propriétés structurales, optiques et électriques des couches minces de ZnO : Al élaborées par spray pneumatique." Courrier du Savoir – N°20 (2015) pp.119-122.

[44] Zuoli He, Wenxiu Que, Jing Chen, Yucheng He, Gangfeng Wang, " Surface chemical analysis on the carbon-doped mesoporous TiO_2 photocatalysts after post-thermal treatment: XPS and FTIR characterization." J. Phy. Chem.Solids, 74 (2013) 924–928.

[45] Q. Li, C. Zhang, J. Li, " Photocatalysis and wave-absorbing properties of polyaniline/ TiO_2 microbelts composite by in situ polymerization method. " Appl. Surf. Sci. 257 (2010) 944–948.

[46] Carolina M. Rodrigues, Odair P. Ferreira and Oswaldo L. Alves, "Interaction of Sodium Titanate Nanotubes with Organic Acids and Base: Chemical, Structural and Morphological Stabilities, J. Braz. Chem. Soc., Vol. 21, No. 7, 1341-1348, 2010.

[47] Daniela Cordeiro Leite Vasconcelos, Vilma Conceição Costa, Eduardo Henrique Martins Nunes, Antônio Claret Soares Sabioni, Massimo Gasparon, Wander Luiz Vasconcelos, "Infrared Spectroscopy of Titania Sol-Gel Coatings on 316L Stainless Steel. Materials Sciences and Applications, 2011, 2, 1375-1382.

[48] TESSY LOPEZ∗ AND R. GOMEZ," Photocatalytic Activity in the 2,4-Dinitroaniline Decomposition Over TiO_2 Sol-Gel Derived Catalysts." Journal of Sol-Gel Science and Technology, 22, 99–107, 2001.

[49] E. Zanchetta, V. Auzelyte , J. Brugger , A.V. Savegnago , G. Della Giustina , G. Brusatin, " Highly inorganic titania based sol–gel as directly patternable resist for micro- and nano- structured surfaces." Microelectronic Engineering 98 (2012) 176–179.

[50] M. Burgos and M. Langlet, " The Sol-Gel Transformation of TIPT Coatings: A FTIR Study," Thin Solid Films, Vol. 349, No. 1-2, 1999, pp. 19-23.

[51] R. Urlaub, U. Posset and R. Thull, "FT-IR Spectroscopic Investigations on Sol-Gel-Derived Coatings from AcidModified Titanium Alkoxides," Journal of Non-

Crystalline Solids, Vol. 265, No. 3, 2000, pp. 276-284.

[52] Jianhong Wei, Lihong Zhao, Suili Peng, Jing Shi ,Zhengyou Liu, Weijia Wen , "Wettability of urea-doped TiO_2 nanoparticles and their high electrorheological effects. " J Sol-Gel Sci Technol (2008) 47:311–315.

[53] S.Y. Kuo, W.C. Chen, F.I. Lai, C.P. Cheng, H.C. Kuo, S.C. Wang, W.F. Hsieh, "Effects of doping concentration and annealing temperature on properties of highly-oriented Al-doped ZnO films." J. Cryst. Growth. 287 (2006) 78–84.

[54] B. Touati, A. Gassoumi, I. Dobryden, M. Maria Natile, A.Vomiero, N. K. Turki, "Engineering of electronic and optical properties of PbS thin films via Cu doping, Superlattices and Microstructures." 97 (2016) 519-528.

[55] M. Gulen, G. Yildirim, S. Bal, A. Varilci, I. Belenli, M. Oz, "Role of annealing temperature on microstructural and electro-optical properties of ITO films produced by sputtering. " J Mater Sci: Mater Electron, 24 (2013) 467–474.

[56] F. Zahedi, R.S. Dariani, S.M. Rozati, " Structural, optical and electrical properties of ZnO thin films prepared by spray pyrolysis: Effect of precursor concentration, Bull. Mater. Sci. " Vol. 37, No. 3, May 2014, pp. 433–439.

[57] M. Jlassi, I. Sta, M. Hajji, H. Ezzaouia," Effect of nickel doping on physical properties of zinc oxide thin films prepared by the spray pyrolysis method." Appl. Surf. Sci, 301 (2014) 216–224.

[58] S. RaviShankar, A.R. Balu, M. Anbarasi, V.S. Nagarethinam, " Influence of precursor molar concentration on the structural, morphological, optical and electrical properties of PbS thin films deposited by spray pyrolysis technique using perfume atomizer. " Optik 126 (2015) 2550–2555.

Chapter IV

Influence of drying temperature and the stirring time on titanium dioxide thin films properties

IV.1. Influence of drying temperature

IV.1.1. Introduction

The temperature is the first parameter to consider, which is involved in any chemical reaction. As soon as the solution is prepared, the temperature affects on the hydrolysis and condensation rates. Hence, in our case, the drying temperature is one of the important process that influences the stoichiometry, structure and characteristics of films. To optimize the drying temperature for obtaining films with the best characteristics structural, optical and electrical properties, its effects on the TiO_2 film characteristics have been studied.

IV.1.2. Experimental details

IV.1.2.1. Deposition of Titanium dioxide

The coating solution was obtained by dissolving first 0.605 ml Titanium Tetra Isopropoxide Ti $[OCH(CH_3)_2]_4$, 10 ml of methanol (CH_3OH) and 0.210 ml of acetylacetone (CH_3COCH) as precursor, solvent and stabilizer, respectively. The solution was then stirred for 3 h using a magnetic stirrer at 50 °C. This solution is transparent yellowish color and slightly viscous. Hence, the prepared solutions were deposited on glass substrates which were previously cleaned with ethanol, acetone and distilled water during 5 min into each process and subsequently dried in air at spin speed 4000 rpm for 30 s. To dry the films, the samples were placed in furnace for 10 min at different temperatures 50, 100, 150, 200 and 250 °C. The spin coating process was repeated seven times to achieve the desired thickness. After that, the annealing process was carried out at 500 °C for 2 h to obtain good crystalline films.

IV.1.2.2. Characterization methods

The tape method was used to check the films' adhesion to the substrate. X-ray diffraction (XRD) studies were conducted in a BRUKER–AXS type D8 diffractometer (CuKα1 radiation, 1.5406 A°) radiation with in the 2θ range of 10° – 90°, with the steps of 0.02°. A Perkin Elmer Lambda 950 UV/VIS spectrometer was used to measure the films' transmittance and absorbance spectra in the 300 – 1100 nm wavelength range, Moreover, the FT-IR spectra were obtained with a Fourier transform infrared spectrometer (Perkin Elmer UATR Two). The scanning wavelength of infrared was 400 – 4000 cm^{-1}. Besides, the electrical resistivity was achieved by the four aligned probe method was carried by

"KEYSIGHT B1500A Semiconductor Device Analyzer" and "CPS PROBE STATION". Figure IV.1 shows the flow chart of the preparation of TiO_2 thin films.

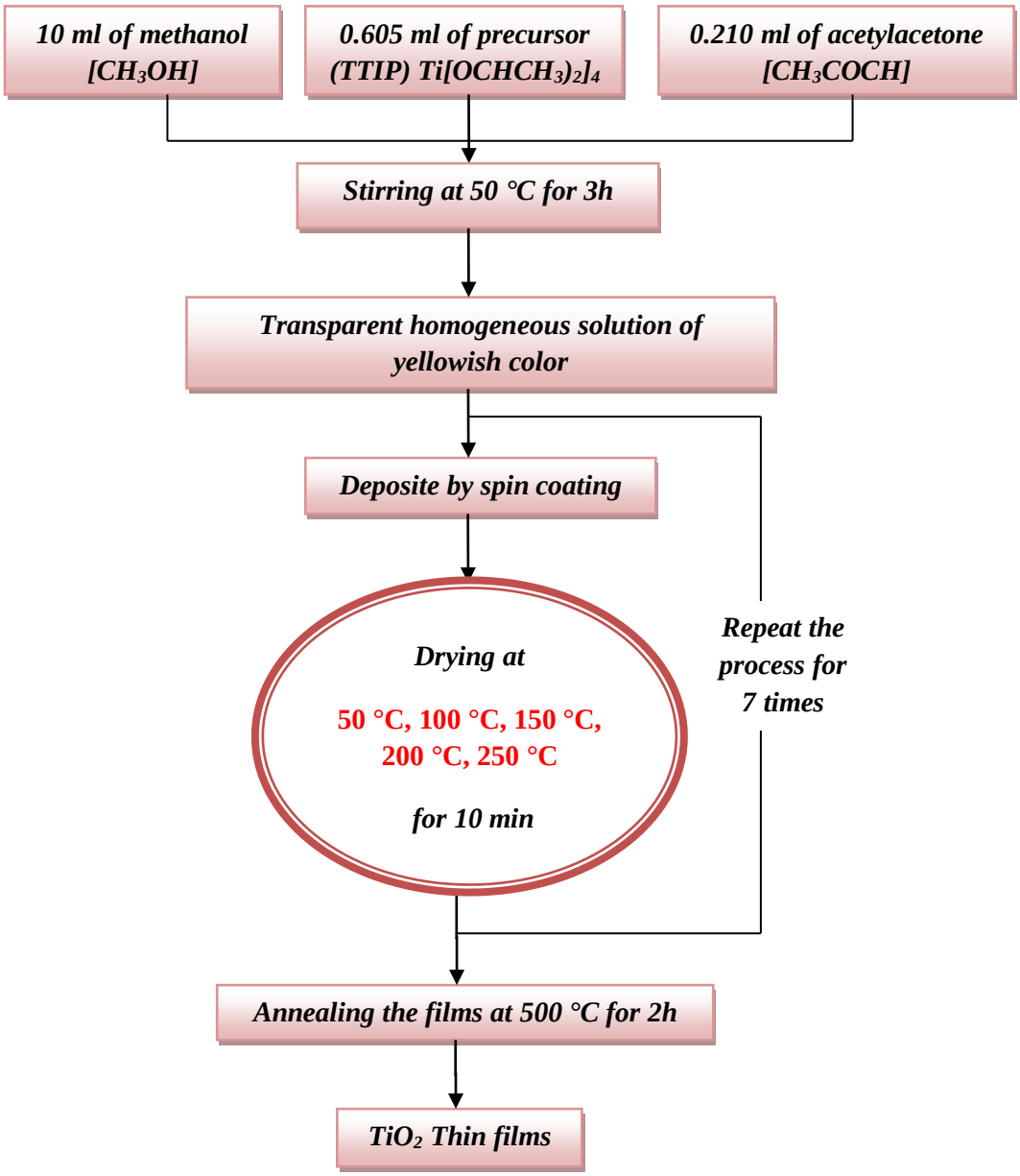

Figure IV.1. Flow chart of sol–gel method for preparation of TiO_2 thin films at different drying temperature.

IV.1.3. Results and discussion

IV.1.3.1. Film thickness study

Swanepoel method (see paragraph II.4.4.1) was used to calculate the films thickness's at the drying temperatures 250 °C and 200 °C and the weight difference method used by Yahmadi et al. [1]. They were used to estimate the thickness (d) of TiO_2 thin films at the

drying temperatures 50 °C, 100 °C and 150 °C due to the absence of interference fringes according to the following relationship:

$$d = \frac{m}{S.\rho} \qquad \text{(IV.1)}$$

where m is the mass of the film (expressed in gram), ρ is the density of the TiO_2 in the bulk form (ρ = 4.23 g/cm^3) and S (cm^2) is the area of the glass substrate.

As Figure IV. 2 illustrates, the thickness decreases from 1346.22 nm to 940.78 nm as drying temperature increases from 50 °C to 250 °C .This reduction in thickness is attributed to the evaporation of water molecules and the removal of all organic species such as hydroxyl (O–H), carboxilate (C=O) and alkane groups (C–H) from all TiO_2 films samples. Therefore, when the drying temperature is getting higher, the film is thinner. These results are supported by the variation of FTIR data.

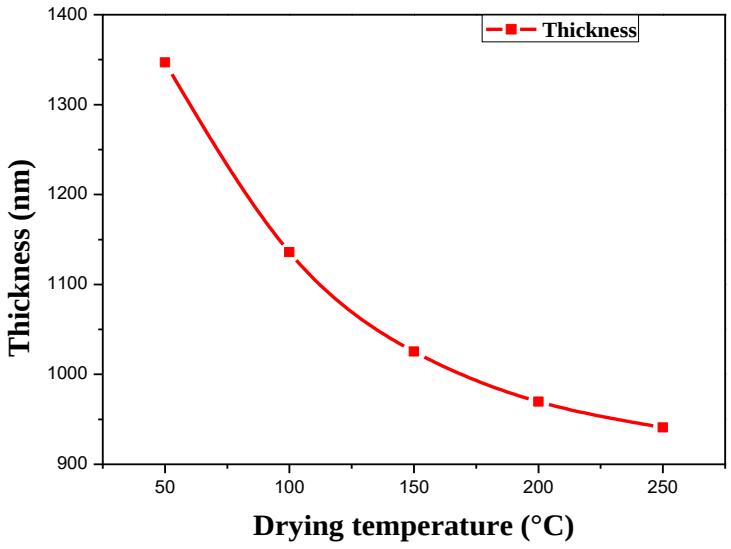

Figure IV.2. Effect of drying temperature on the thickness of TiO_2 thin films.

IV.1.3.2. Structural characterization

The XRD patterns of TiO_2 films deposited on glass substrates with different of drying temperature are illustrated in Figure IV.3. From Figure IV.3, we notice that the XRD results indicated that all the films are crystallized, revealing XRD lines related to anatase phase, no other phases (rutile or brookite) are detected. From XRD results, it is noteworthy that at up

to 200 °C one peak located at 2θ = 25.37° assigned to (101) diffraction plane. While, over 200 °C four peaks have obtained at 2θ values equal to 25.35°, 37.94°, 48.13° and 54.05° with (101), (004), (200) and (211) planes of reflections, respectively. These peaks are in excellent agreement with the standard JCPDS data (n°: 21-1272) file for TiO_2 [2]. Furthermore, Figure IV.3 reveals that the samples have a strong preferred orientation in the (101) direction, it has a higher intensity and narrow, which can be attributed to the value of the free surface energy is minimal for this plane [3]. This gives the atoms sufficient mobility to move to positions of less energy leading to the highest atomic density achieved along the (101) direction [4]. On the other hand, when the drying temperature increases from 50 °C to 250 °C, the intensity of (101) peak is increased and this indicates the enhancement of the films crystallinity of the TiO_2 thin films, where we find the maximum crystallization's intensity at drying temperature of 250 °C. However, as the drying temperature increases, the diffraction angle (101) of TiO_2 thin films changes from 0.07° to 0.13°, which could be due to residual stresses in the films, resulting in a shift in d-spacing of a typical (101) plane.

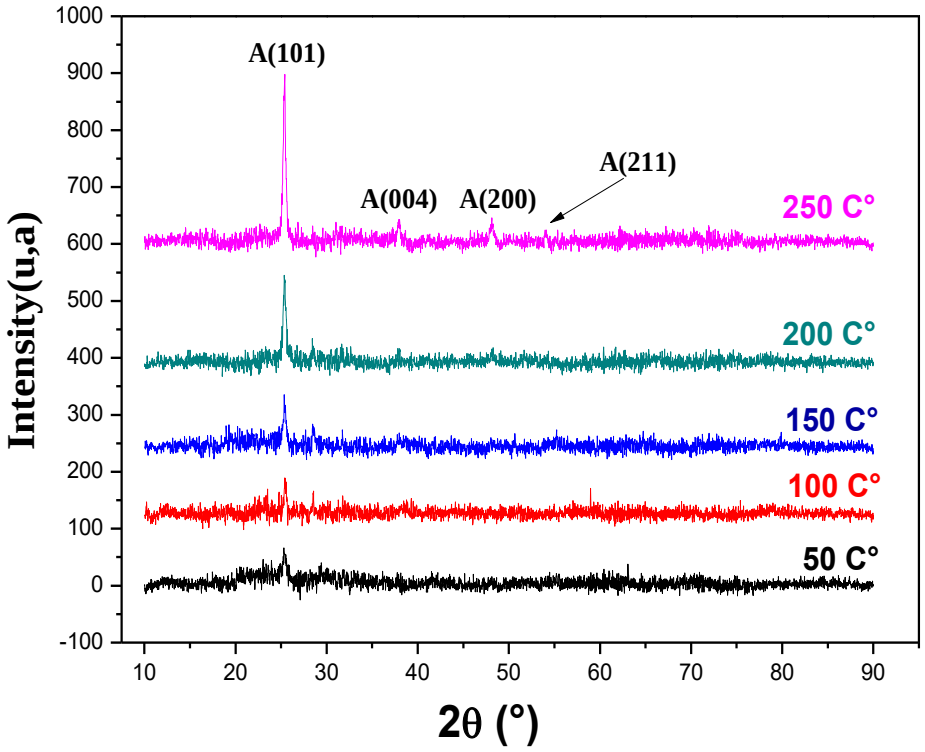

Figure IV.3. Variation of XRD patterns of TiO_2 thin films prepared at different drying temperatures.

The crystallite size (D) and strain (ε) of the TiO_2 samples were from the XRD data using the equation (II.9) and (II.12) respectively. The variation of crystallite size and the strain with drying temperature of TiO_2 films are represented in Table IV.1 and Figure IV.4. As can be seen from these values, the crystallite sizes increases from 13.93 to 21.77 nm, while the strain from 2.48 x 10^{-3} to 1.59 x 10^{-3} is decreased with the drying temperature's increase. Rosari .Saleh et al. [5] also reported the same increases of crystallite size for ZnO films with different drying temperature. This may be due to the collectively fusion of small crystallite into the bigger crystallites, as the result, the density of nucleation centers in films decrease which in turn generates of internal strain [6,7].

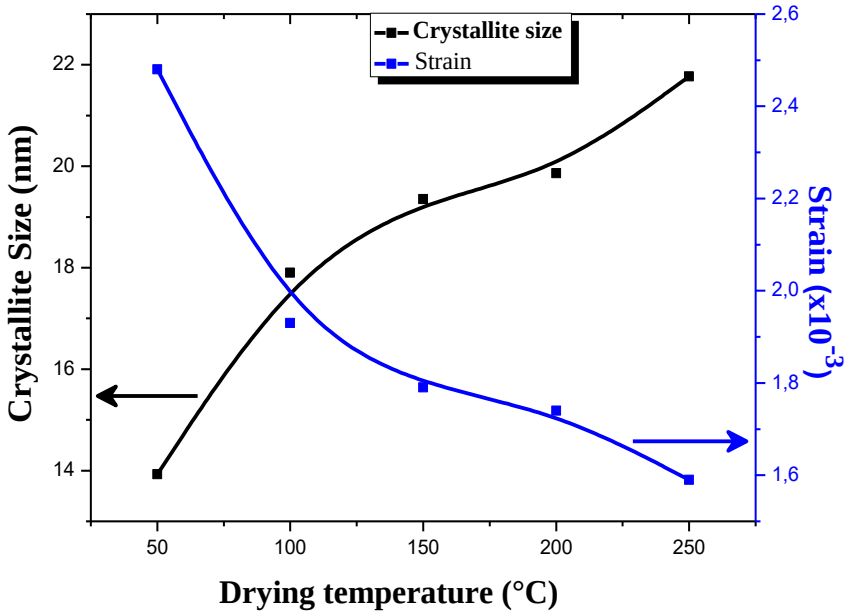

Figure IV.4. Crystallite size and the strain as a function of drying temperature.

In addition, the dislocation density (δ) have also been estimated for all the films by applying the relations (II.13). As it can be seen in the Figure IV.5 and Table IV.1 the increase of crystallite sizes of TiO_2 nanoparticles leds to a the dislocation density decreased as the drying temperature increased of TiO_2 thin films by Sol-Gel (spin - coating) technique from 5.15 × 10^{15} to 2.10 × 10^{15} lines/m^2 .This reduction in the dislocation density is attributed to decrease in grain boundaries and it decreased dislocation defect inside the crystal lattice of the samples with increases in crystallite size in TiO_2 thin films at different drying temperature, that supported by DRX results. Where, it was shown for all samples that the reflection peaks became sharper and that the full-width at half maximum (FWHM)

decreased slightly with increasing drying temperature, indicating the enhancement of crystallinity. Thus reducing dislocation defects within the crystal lattice.

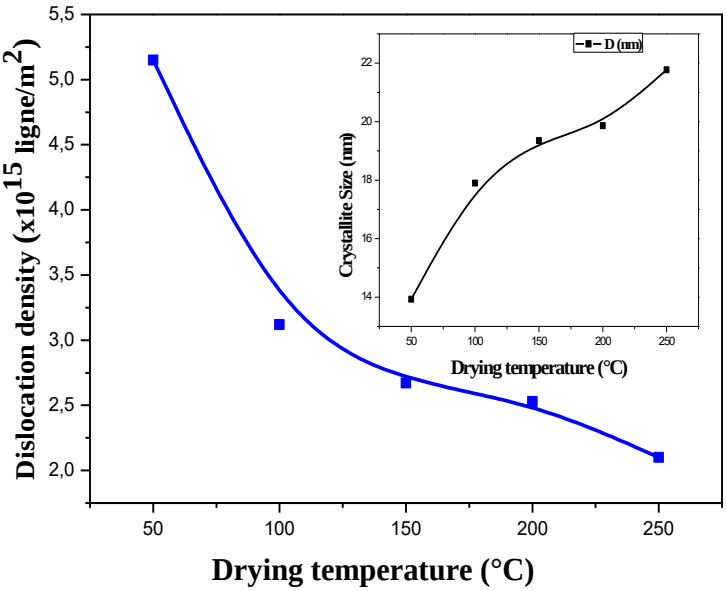

Figure IV.5. The dislocation density of TiO_2 films at different drying temperature.

Table IV.1. Crystallite sizes, dislocation density and strain values of drying temperatures TiO_2 thin films extracted from XRD analysis.

Drying temperature (°C)	Peak (hkl)	2θ°	FWHM (β°)	Crystallite size D (nm)	Dislocation density(δ)x10^{15} (Lines /m^2)	Strain (ε)x10^{-3}
50	(101)	25.38	0.58	13.93	5.15	2.48
100	(101)	25.35	0.45	17.90	3.12	1.93
150	(101)	25.41	0.42	19.35	2.67	1.79
200	(101)	25.38	0.40	19.86	2.53	1.74
250	(101)	25.37	0.37	21.77	2.10	1.59

The d-spacing and the lattice constants a and c of anatase TiO_2 films was calculated from the given relation (II.10) and (II.11) respectively, and the residual stress in the plane of the film can be determinite using the relationship (II.14). From Table IV.2, we observed that the ‘a’ and ‘c’ values are less than the standard values of TiO_2 (a = 3.7852 nm and c = 9.5139 nm) JCPDS (n^o : 21-1272). As shown in the figure (IV.6)

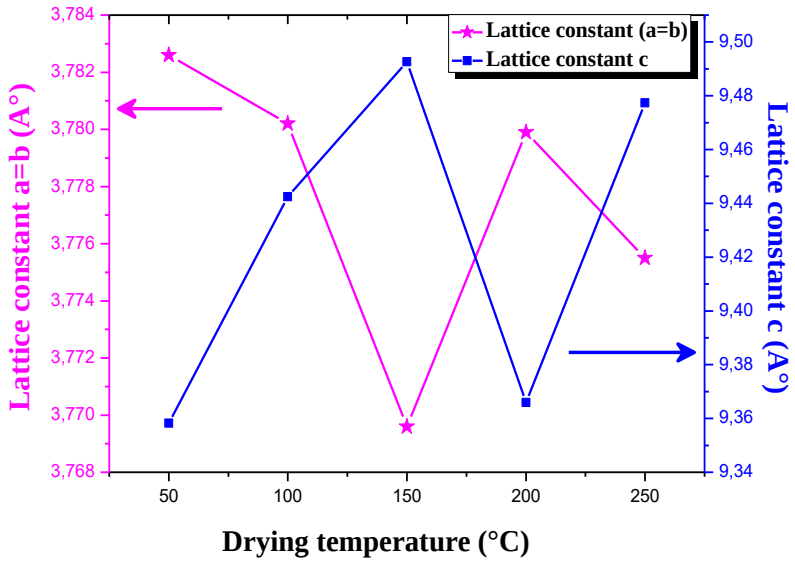

Figure IV.6. Lattice constant graph in termes of the drying temperature.

The values of residual stress of TiO_2 thin films deposited at various dyring temperature are illustrated in Figure IV.7. One can deduce from Figure IV.7, the residual stress of the films prepared at drying temperature 50, 100, 150, 200 and 250 °C were found to have a compressive stress. Besides, we notice that the stress decreases from -0.351 GPa to -0.224 GPa for the TiO_2 thin films. This reduction in stress is attributed to increase in the grain size, therefore an improvement in the crystalline quality and the decrease in the stresses, this is due to the decrease in the grain boundaries [40].

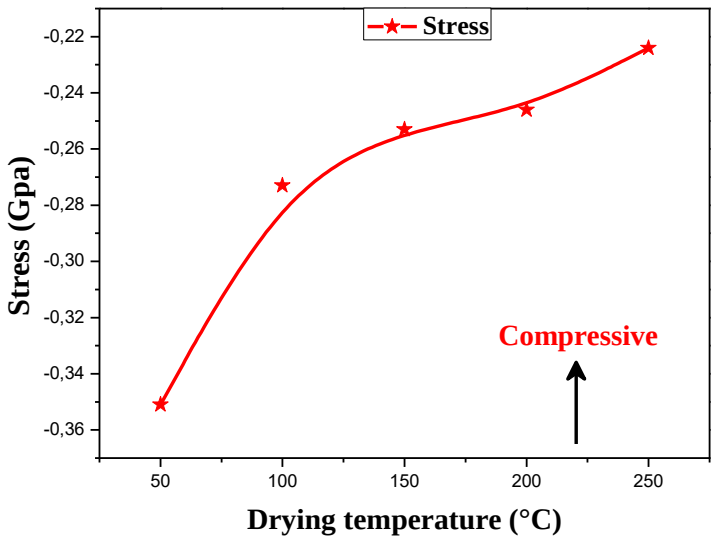

Figure IV.7. The stress of TiO_2 thin films at different drying temperature.

Table IV.2. Micro-structural parameters of TiO_2 thin films formed at different drying temperatures.

Drying temperature (°C)	hkl planes	2θ°	Calculated parameters			Reference parameter (JCPDS card No 21-1272)	Stress (Gpa)
			d-spacing (Å)	Lattice constant a (Å)	Lattice constant c (Å)		
50	(101)	25.38	3.5061	3.7826	9.3582		-0.351
100	(101)	25.35	3.5094	3.7802	9.4425	a_0 = 3.7852 Å	-0.273
150	(101)	25.41	3.5019	3.7696	9.4926	c_0 = 9.5139 Å d_0 = 3.521 Å	-0.253
200	(101)	25.38	3.5052	3.7799	9.3659	2θ = 25.28°	-0.246
250	(101)	25.37	3.5075	3.7755	9.4774		-0.224

IV.1.3.3. FTIR spectroscopy

To gain information on chemical bonding and the existence of particular functional groups in the films, the FTIR technique is utilized at the range of 400 – 4000 cm^{-1}. The FTIR spectra of titanium oxide films with various drying temperatures are shown in Figure IV.8. The films reveal absorption bands at 507, 755 and 897 cm^{-1}. The band at 507 cm^{-1} range due to the vibration of Ti–O bonds in TiO_2 lattice as reported in literatures [8,9]. This bond appears at the drying temperature of 250 °C only for TiO_2 films, the presence of a band at 755 cm^{-1} due to symmetric stretching vibrations of the Ti–O–Ti bonds [10]. On the other hand, the band observed at 897 cm^{-1} can be attributed to the Ti–O stretching mode which involves nonbridging oxygen atoms [11]. Besides, the FTIR analysis of TiO_2 thin films shows traces of CO_2 at (2361 cm^{-1}) because the analysis is treated in a location which contains CO_2 [12]. Furthermore, we also note the absence of associated with the H–O–H bending vibration of the absorbed water molecules and OH group in almost all samples of titanium films because due to the evaporation of water and combustion of organic molecules with increasing drying temperature from 50 °C to 250 °C.

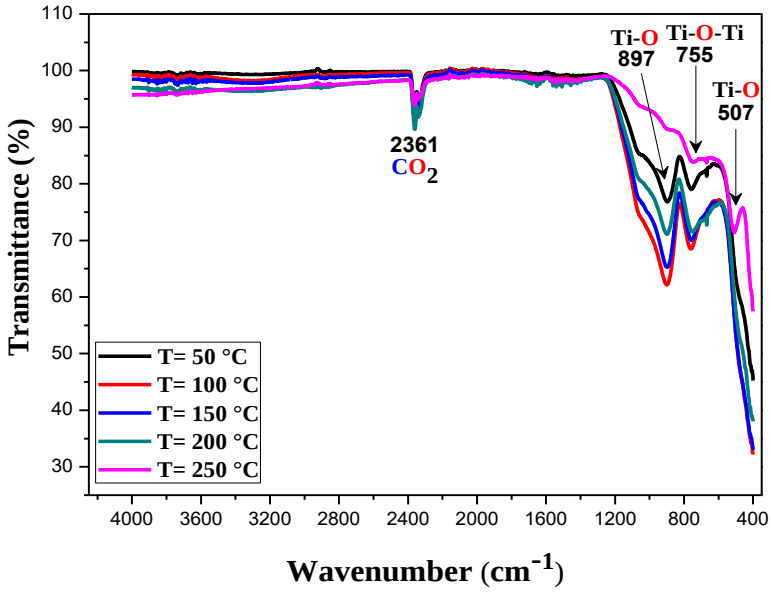

Figure IV.8. FTIR transmittance spectra of TiO_2 thin films deposited on glass substrate using different drying temperatures.

IV.1.3.4. Optical characterization

The transmission spectra of TiO_2 thin films provide information about their band gap and structure, which is important for their applications. The chemical composition, crystal structure, energy of incident photon, and film thickness all influence the transmittance spectra. For a given film, the chemical composition and crystal structure are fixed and hence in such a case the film thickness, crystallinity, and surface and structural homogeneity are factors that greatly influence the transmittance of the film.

Figure IV.9 shows the optical transmittance and absorbance spectra of TiO_2 films at various drying temperatures, with wavelengths ranging from 300 to 1100 nm. It is found that the TiO_2 films deposited at different drying temperature exhibit a high optical transparency about 71-84 % in the visible wavelength region (400 – 800 nm), which gives the thin layers of TiO_2 the character of transparent films in the visible and can therefore be dedicated to the use as optical windows for the cells solar. Moreover, we notice that the presence of interference fringes in transmission spectra in the visible region for the deposited films at 200 °C and 250 °C , this is due to the fact that the prepared films are uniform and homogenous with a smooth surface area consequently of interference oscillation between films and substrate surface [13]. On the other hand, we note the absence of interference

fringes in the long wavelength region at drying temperatures 50 °C, 100 °C and 150 °C. This can be attributed to the scattering of incident light in the material due to the air/film interface roughness. In general, transmittance of the TiO_2 films increases in the visible region (400 – 800 nm) with increase of drying temperature from 50 °C to 250 °C. Many authors report that the increase in transmittance of the films obtained by drying temperature is related to an increase in crystallinity of the films and the improvement of crystallinity and that improving crystallinity reduces optical scattering, flaws, and films surface homogeneity [14,15], that supported by DRX results. Also, can be explained by the decrease in films thickness (Beer-Lambert law). Furthermore, due to the excitation and transition of electrons from the valence band (V_B) to the conduction band (C_B), the transmittance spectra reveal a strong absorbance for all films in the range of ($\lambda <$ 385 nm). This last phenomenon is very important characteristic for a semiconductor corresponding to the optical band gap energy (Eg).

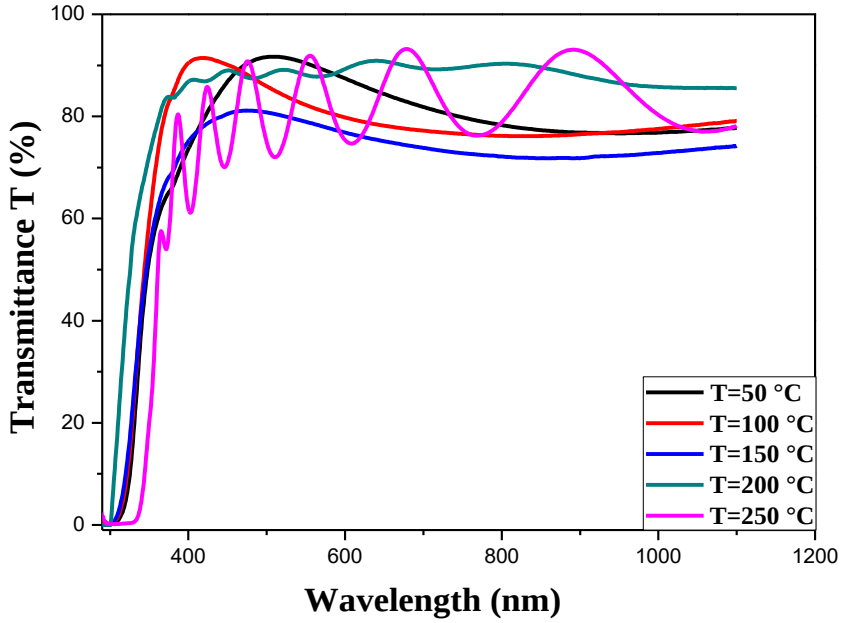

Figure IV.9. Transmittance spectra of TiO_2 thin films with different drying temperatures.

The plots of $(\alpha h\nu)^2$ against $(h\nu)$ in Figure IV.10 are used to estimate the band gap values of the deposited films. The band gap was estimated by extrapolating the straight line to intersect the photon energy axis on the $(\alpha h\nu)^2$ versus $(h\nu)$ curve, which has a straight line section. The band gap value in eV is the point of intersection of Figure IV.10 shows the variations in the optical band gap energy of TiO_2 thin films at various drying temperatures.

In general, in polycrystalline semiconductors, the energy band gap can be impacted by the disorder and dislocation density at the grain boundaries [16]. Also, the quantum size effect and changes in the film's preferred orientation [17,18]. From Figure IV.11 and Table IV.3 it can be seen that the energy band gap was increase (from 3.37 to 3.56 eV) with increasing drying temperature from 50 °C to 200 °C. The results obtained by S. Rabaoui et al. [19]. and then it starts to decrease to the value of 3.56 eV for 250 °C. The increase in energy gap Eg explained by the basis of the Burstein–Moss (BM) effect [20], an energy band widening effect resulting from the increase in the Fermi level in the conduction band of degenerated semiconductors so that high energy is needed for electrons in the valence band to move to higher energy states in the conduction band. Hence, Eg increased tremendously due to the high electron density. It applies that higher electron concentration density dominates over crystal defects which increased band gap. Furthermore, the band gap value decreases with the increase of drying temperature at 250 °C. This may be because when TiO_2 thin films are dried at the temperature 250 °C process improves the crystallinity and increases crystallite size of the films that results in decreasing defects concentration as well as reduce the strain in the films , lowering the optical band gap energy [21,22]. In finally, suggest to that the appropriate drying temperature and the ideal to prepare TiO_2 films is 250 °C.

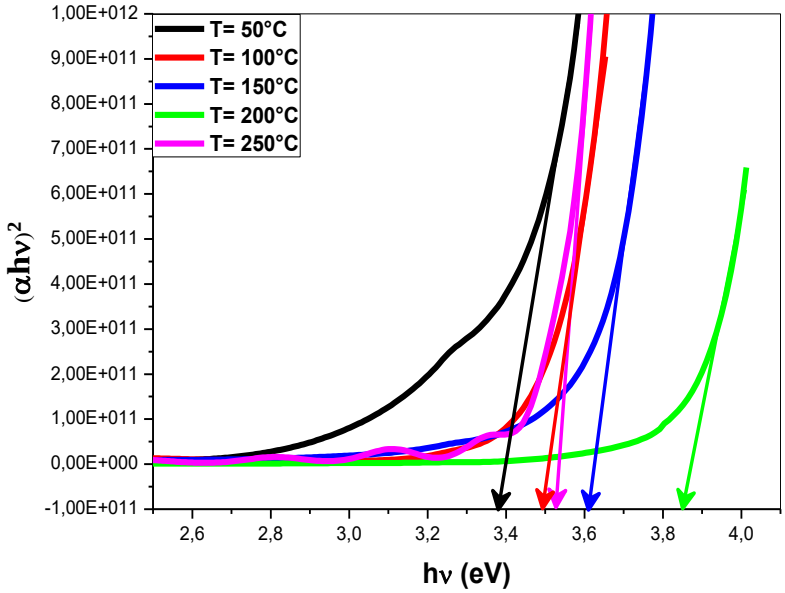

Figure IV.10. The plots of $(\alpha h\nu)^2$ versus photon energy (hν) for the prepared TiO_2 thin films at various drying temperatures.

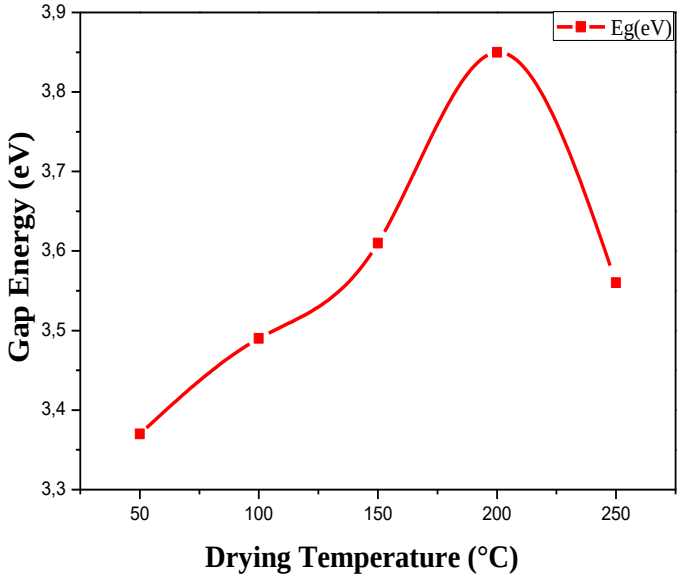

Figure IV.11. The energy band gap of TiO_2 thin film at different drying temperatures.

The Urbach energy (Eu) is the band tail width that describes the disorder in a film network. It is calculated by taking the inverse of the linear part's slope from plots of Ln(α) vs hv (Figure IV.12).

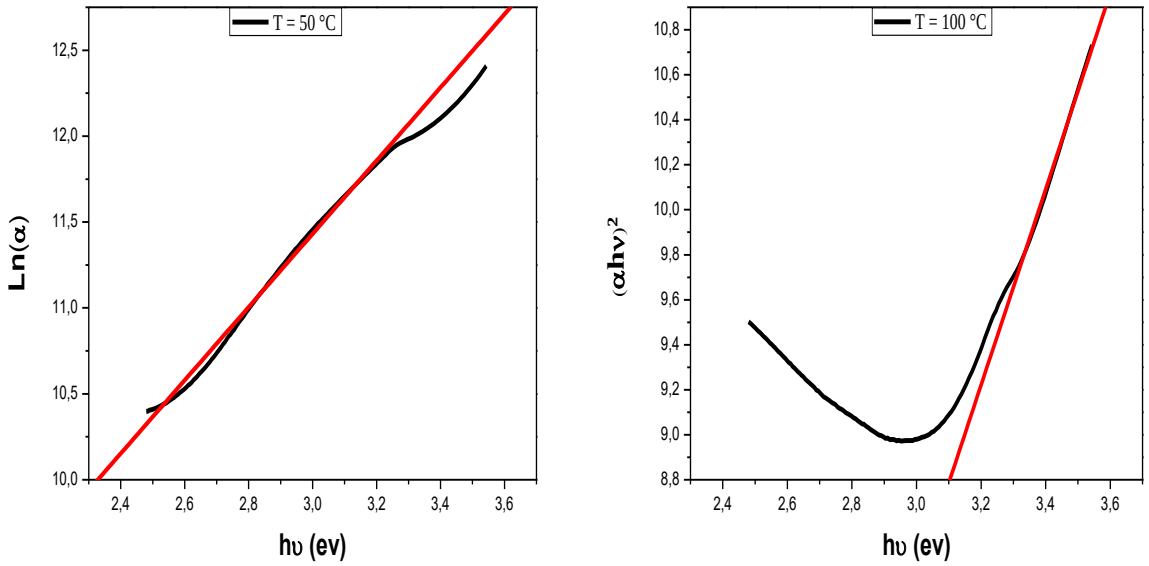

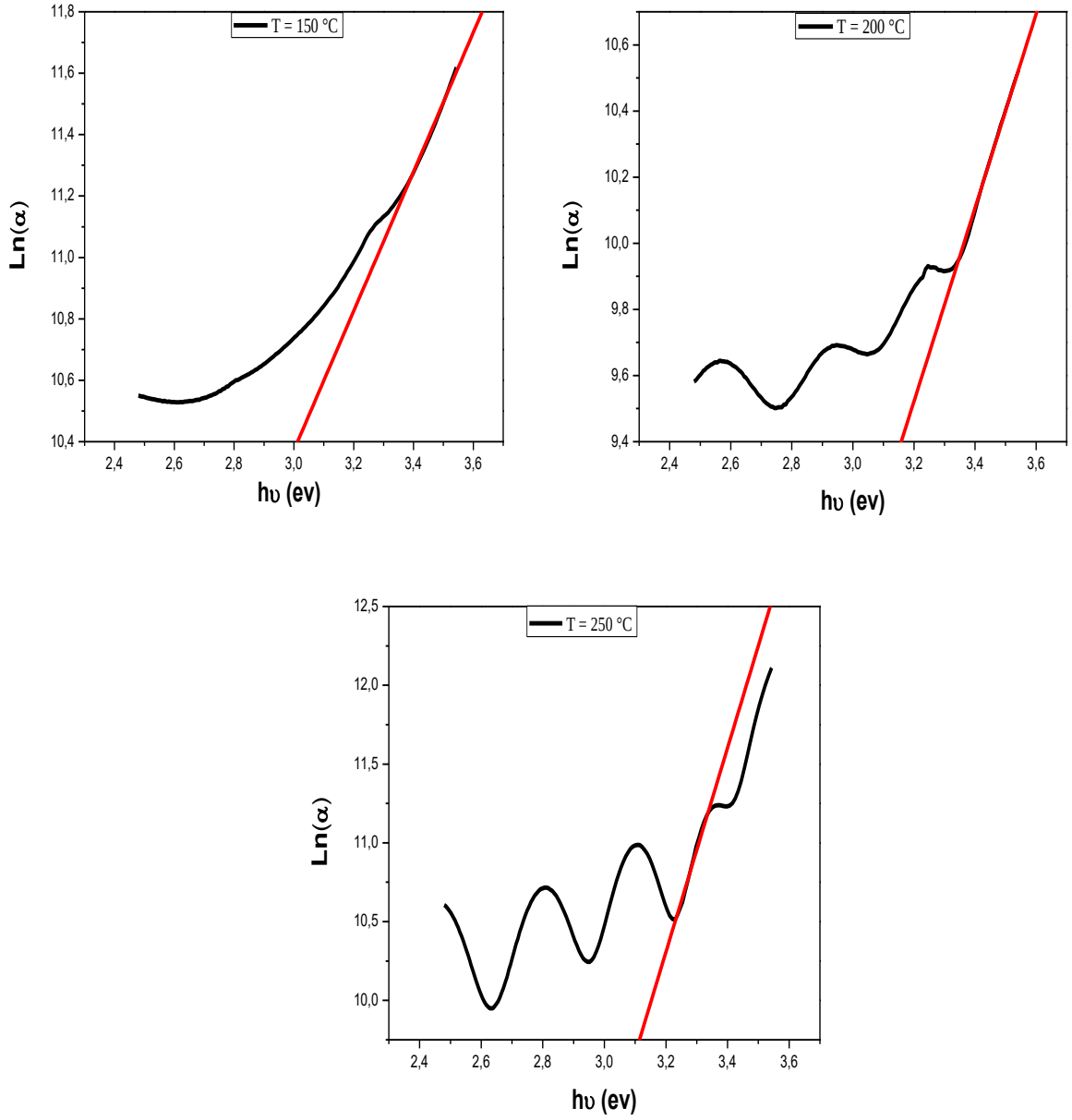

Figure IV.12. Ln (α) vs hν of TiO_2 thin films at different drying temperatures.

As shown in Figure IV.13 and Table IV.3. We notice that the Urbach energy decreases with the increase of drying temperature from 50 °C to 250 °C. This reduction in Urbach energy is due to a decrease in the degree of structural disorder as the drying temperature increase. It is obvious that the film exhibit minimum structural disorder when the films are dried at 250 °C. This could be owing to improved crystallinity and lower strain and dislocation density, resulting in reducing the defects in annealed TiO_2 thin films. Moreover, the lower Urbach energy indicates to increase in crystallinity, thus improvements of the films crystal quality. Also, the degree of disorderliness decreases, and a relaxation of the

distorted bonds, that supported by DRX results (Decrease in Urbach energy can be correlated with the XRD result).

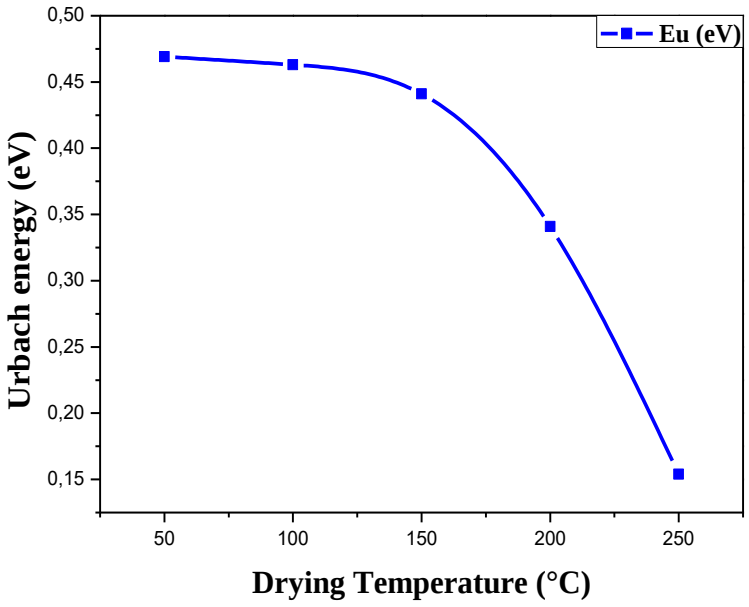

Figure IV.13. The Urbach energy of TiO_2 thin films at various drying temperatures.

Table IV.3. Optical band gap energy, Urbach energy values and electrical resistivity and conductivity of TiO_2 thin films deposited using sol-gel spin coating method with different drying temperatures.

Drying temperature (°C)	**Thickness (nm)**	**Band Gap Energy (eV)**	**Urbach Energy (meV)**	**Rsheet $x10^6$ (Ω/sheet)**	**Electrical resistivity $x10^2$ (Ω.cm)**	**Electrical conductivity $x10^{-3}$ $(Ω.cm)^{-1}$**
50	1346.22	3.37	0.469	8.25	11.10	0.90
100	1135.89	3.49	0.463	8.72	9.90	1.01
150	1025.36	3.61	0.441	2.37	2.43	4.11
200	969.77	3.85	0.341	1.43	1.38	7.24
250	940.78	3.56	0.154	1.30	1.22	8.19

IV.1.3.5. Electrical characterization

The variation of TiO_2 films electrical resistivity and electrical conductivity as a function of drying temperature is shown in Figure IV.14. We can notice from this figure, The electrical resistivity decreases from 11.10×10^2 Ω.cm to 1.22×10^2 Ω.cm with drying temperature increases from 50 to 250 °C. Correspondingly, the electrical conductivity increases from 0.90 to 8.19 x 10^{-3} $\Omega.cm^{-1}$. The increase in conductivity of the films with drying temperature is due to the growth of crystallite size and improvement of crystallinity [23]. This conclusion, that the crystallinity of the films improves as the annealing temperature increases, is supported by the current XRD results. Furthermore, this behavior could be explained by the fact that the drying procedure increases the crystallite size and crystallinity of the film, which therefore results in less grain boundary scattering of free electrons [24].

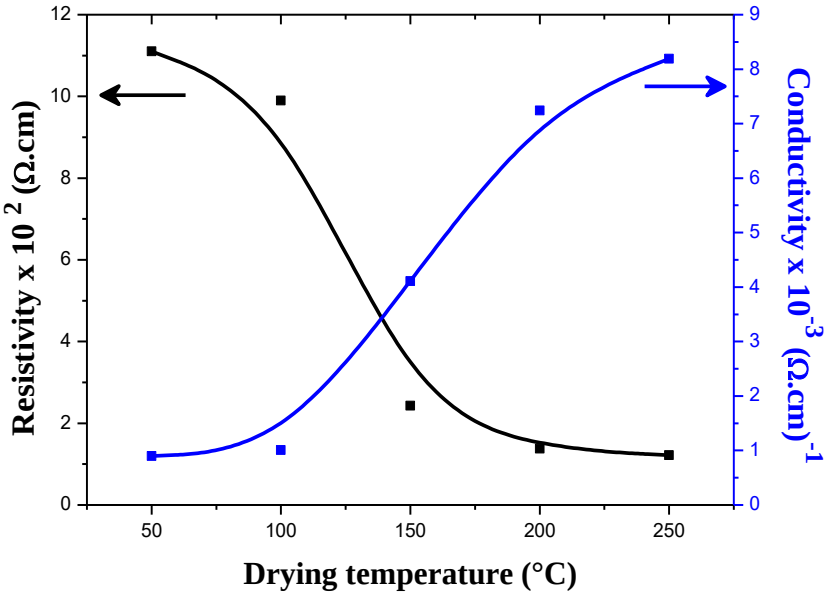

Figure IV.14. Electrical resistivity and conductivity of TiO_2 thin films with different drying temperatures.

Conclusion

In conclusion, TiO_2 thin films were successfully deposited on glass substrates using the sol gel spin coating process at 500 °C. The films were dried in a furnace at various temperatures (50, 100, 150, 200 and 250 °C). The film thickness is measured by weight difference method at 50 °C, 100 °C and 150 °C due to the absence of interference fringes and Swanepoel method was used to calculate it at the drying temperatures 250 °C and 200 °C due to the presence of interference fringes, where we notice a decrease in the thickness of TiO_2 thin films with increasing drying temperature from 1346.22 to 940.78 nm. The deposited thin films feature a polycrystalline anatase tetragonal structure, according to the XRD data. As the drying temperature increase, the crystallinity and crystallite size increase from 13.93 to 21.77 nm. Besides, the stress of the all samples of TiO_2 thin films were found to have a compressive stress. The film transmission in visible region is about 84% at 250°C sample. Also, we observe that the energy band gap was increase (from 3.37 to 3.56 eV) with increasing drying temperature from 50 °C to 200 °C and then it starts to decrease to the value of 3.56 eV for 250 °C. Correspondigly, urbach energy decreases from 0.469 to 0.154 eV. Furthermore, Fourier transform infrared transmittance spectra (FT-IR) confirmed the presence of Ti–O, Ti–O–Ti and CO_2 stretching vibration bonds. Moreover, electrical studies show that as the drying temperature rises, the electrical resistivity falls, with a minimum electrical resistivity of 1.22×10^2 Ω.cm which was obtained for the film coated at 250 °C. As a result, of the current study, it is obvious that the drying temperature has a significant impact on the physical properties of thin films. Finally, we can state that we have created excellent optical and electrical properties's TiO_2 thin films that can be employed in a variety of optoelectronic and photovoltaic applications.

IV.2. Influence of the stirring time

IV.2.1. Introduction

As it is well known, the TiO_2 thin films properties are significant effected by technique of elaboration and deposition parameters. As a result, deposition parameters has been extensively studied in order to improve TiO_2 films electrical characteristics. However, very few studies have been devoted to the influence of Stirring time or mixing time. Danckwerts was the first to discuss the effect of stirring (mixing) on precipitation and reactions in 1958. Indeed, for chemical reactions which characteristic times are shorter than the mixing times, or in the same order of magnitude, the latter have a significant role on the path followed by the precipitation reaction and thus consequently on the yield, purity and physical quality of the produced suspension. The stirring time is the time needed to achieve a certain degree of homogeneity of a tracer in a vessel.

In this chapter, TiO_2 thin films were deposited on glass substrates by Sol-Gel (spin coating) method. Stirring time influence on crystalline structural, optical and electrical properties of TiO_2 films have been investigated.

IV.2.2. Experimental procedures

IV.2.2.1. Preparation of thin films

Using the sol-gel spin coating process, titanium oxide films were prepared on a glass substrate. Where, we used 0.605 ml Titanium Tetra Isopropoxide (TTIP) Ti $[OCH(CH_3)_2]_4$ Titanium Tetra Isopropoxide as precursor, 10 ml methanol (CH_3OH) as solvent and 0.210 ml of acetylacetone (CH_3COCH) as a stabilizer. Then the mixture was stirred constantly at different time : ***1 hour***, ***2 hours***, ***3 hours*** and ***4 hours*** at 50 °C to yield a clear, transparent, and homogeneous solution (with a concentration of 0.2 mol. l^{-1} and a pH= 6).

The aged titanium oxide solutions were deposited on microscopic glass substrates ($2.5\times2.5\times0.15$ cm^3), which it was cleaned with ethanol, acetone and distilled water during 5 min into each process and subsequently dried in air. The precursor solution was deposited on clean substrates using a spin coating system, and then the prepared solution were injected onto the center of the glass substrate, by using a spin coating technique with a controlled rotation speed of 4000 rpm for 30 s at room temperature. The films dried at 250 °C for 10 min to evaporate the solvent and remove organic residuals. This process was repeated seven times to

get well coated films with the desired thickness. Then the films subjected to annealing treatment at temperatures 500 °C for 2 h in a furnac.

The overall process used for the preparation and characterization of TiO_2 thin films based on the sol-gel (spin coating) method is shown in Figure IV.15:

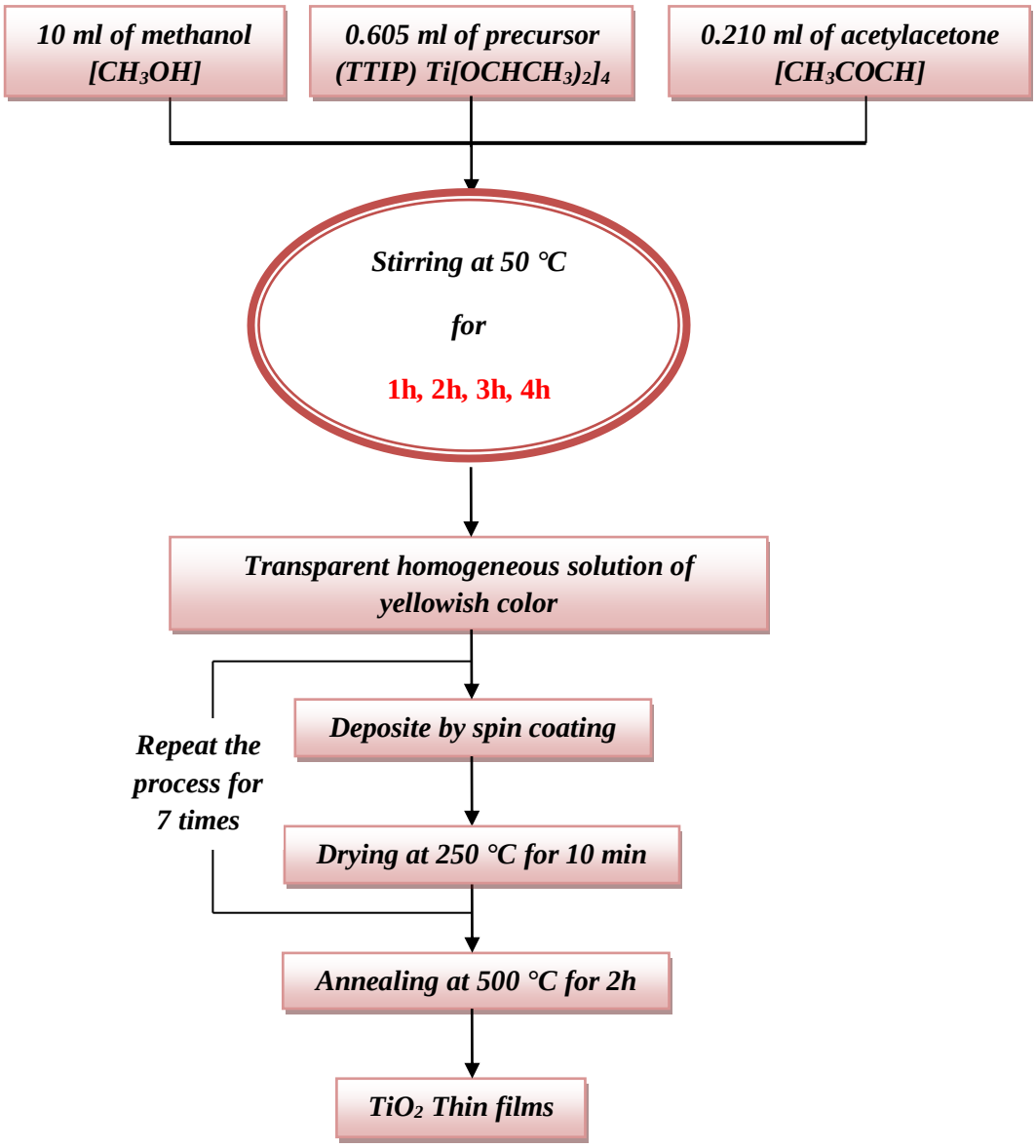

Figure IV.15. The schematic diagram of the preparation steps of TiO_2 thin films at different stirring time.

IV.2.2.2. Films Characterization

The prepared films were characterized by an X-ray diffractometer (X'PERT PRO) using Cu Kα (λ =1.5418 A°) radiation within the 2θ range of 10°– 90°, with the steps of 0.02° to define the crystallite state and structural properties. UV-Visible spectrophotometer (Perkin

Elmer LAMBDA 950 UV/VIS) and fourier transform infrared (FTIR) was carried by (Perkin Elmer UATR Two) spectrometer. On the other hand, electrical resistivity was achieved using four probe method.

IV.2.3. Results and discussion

IV.2.3.1. Film thickness study

The thickness of the films was calculated starting from Swanepoel method (see paragraph II.4.4.1). As Figure IV.16 shows the film thickness's grow up from 787.44 to 986.23 nm as the stirring time augment from 1 hour to 4 hours. Because of the increase in ionization. Where, as the stirring time of the solution increases, the presence of Ti^{4+} ions increases, which then binds with O^{2-} ions, forming the precipitation layer of TiO_2 films. Thus, the thickness of TiO_2 thin films increases.

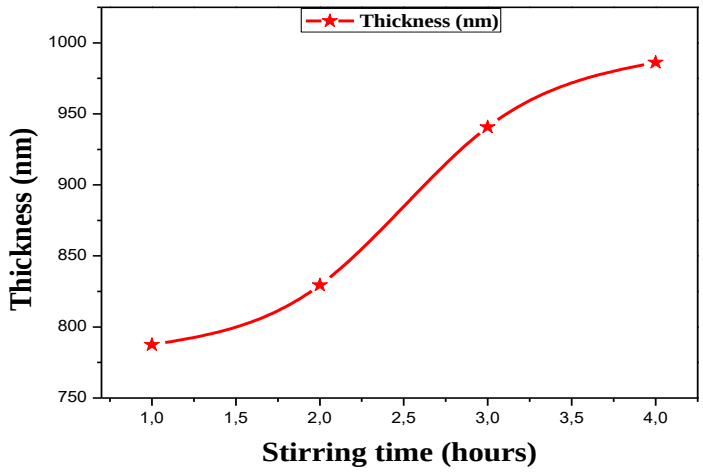

Figure IV.16. The thickness of the TiO_2 thin film as a function of the stirring time.

IV.2.3.2. Structural studies

The crystal structure and orientation of the TiO_2 thin film were investigated by X-ray diffraction (XRD) pattern. The XRD pattern of all TiO_2 films prepared at different of stirring time (1, 2, 3 and 4 hours) on glass substrate are shown in Figure IV.17. The material studied was discovered to be TiO_2 polycrystalline with an anatase tetragonal structure. This is in good agreement with JCPDS data (n°: 21-1272). The films with ***1 hour*** of stirring time present a three peaks of anatase phase at diffraction angle of 25.37°, 38.00° and 48.16° with (101), (112) and (200) planes of reflection. Besides, for the films with ***2 hours*** of stirring times

present a three peaks of anatase phase are shown at diffraction angles of 25.42°, 37.96° and 48.13° with (101), (004) and (200) planes of reflections, respectively. On the other hand, in ***3 hours*** of stirring times of TiO_2 thin film, four peaks of anatase phase have obtained at 2θ values of 25.37°, 37.94°, 48.13°and 54.08° with (101), (004), (200) and (211) planes of reflections. In addition to this, in ***4 hours*** of stirring times , three peaks of anatase phase have obtained at 2θ values of 25.39°, 37.94° and 48.10° with (101), (004) and (200) planes of reflections.

The plan diffraction (101) has a much higher intensity than the diffraction of the other planes ((112), (004), (200), (204) and (211)), which shows a growth in the orientation (101), since the value of free surface energy for this plane is the minimal [25] .We can also observe that there is an evolution of the lines which is reflected by an increase in the diffracted intensity of the anatase plane (101) with the increase in the stirring time from 1 to 4 hours, where the full width at half maximan (FWHM) value decreases, thus indicating the increase in crystallinity of the thin films , this is due to increased number of mixing hours which increases chemical interactions and thus improves the purity of the final mixture [26] . Also, most probably longer stirring time leads to the increase in grain mobility and thus formation of bigger crystallizaion sites which lead to bigger crystals and higher crystallinity of the final product [11,27], and that means that the crystalline state of our films will getting better because of the increase of the stirring time.

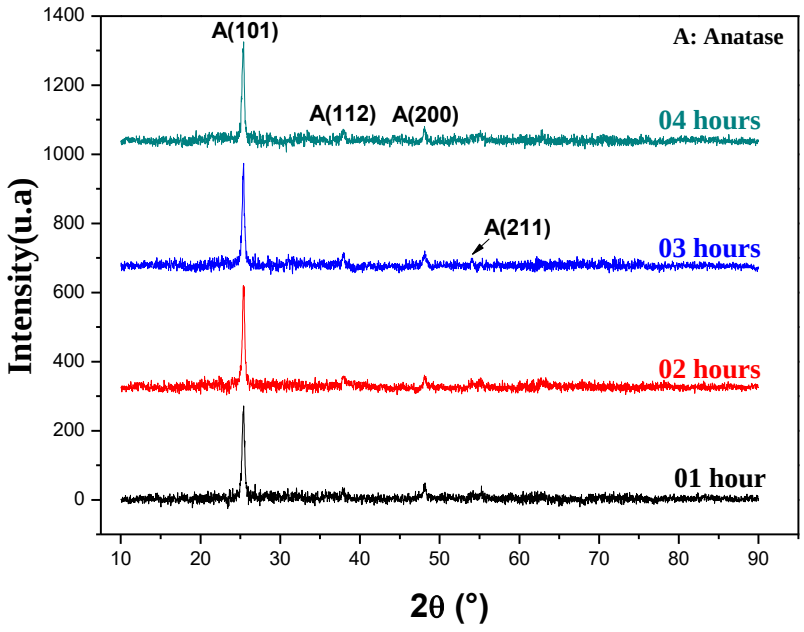

Figure IV.17. XRD patterns of TiO_2 thin films at different stirring times.

The crystallite size of the samples is determined from the broadening of the most intense peak (110) in the XRD pattern using Debye–Scherrer‘s equation (II.9). From Figure IV.17, we notice that the all the diffraction peaks become slightly sharper and intense as the stirring time increases from 1 to 4 hours. This indicates that the crystallite size of the sample increases with increase in stirring time. Crystallite size of the TiO_2 nanoparticles calculated is about 21.27, 21.43, 21.77 and 22.07 nm for 1, 2, 3, and 4 hours samples respectively (As seen in Figure IV.18 and Table IV.4). This increase in crystallite size is attributed to the simultaneous occurrence of particle growth, nucleation. The particle growth and nucleation both govern the particle size. Where the nucleated small crystallites tend to aggregate together to form more thermodynamically stable particles. Furthermore, the concentration of hydroxyl ions can influence the crystallite size and its shape. In our current study the aggregation of nanoparticles is expected due to the presence of substantial OH ions in the samples, that supported by FTIR results, where the vibration expansion of the hydroxyl O–H groups of TiO_2 thin films was found significantly and clearly in all samples. On the other hand, from the earlier reported studys, it was found that the presence of too much OH concentration enhances the agglomeration of the nanocrystals to a great extent. As reported by Dinesh Varshney et al. [28] and L.H. Jiang et al. [29].

The nucleation begin to occur through the following reactions :

$$Ti_4^{+} + 4\ HO^{-} \longrightarrow TiO_2 + 2\ H_2 \qquad (IV.1)$$

$$Ti_4^{+} + 4\ HO^{-} \longrightarrow Ti(OH)_4 \qquad (IV.2)$$

$$Ti4^{+} + 6\ HO^{-} \longrightarrow Ti(OH)_6)^{\ 2-} \qquad (IV.3)$$

The formation of tin oxide occurs as :

$$Ti(OH)_4 \longrightarrow TiO_2 + 2\ H_2O \qquad (IV.4)$$

$$(Ti(OH)_6)^{2-} \longrightarrow TiO_2 + 2\ H_2O + 2\ HO^{-} \qquad (IV.5)$$

From the previous equations it is clear that nucleation occurs via $Ti(OH)_4$ or $(Ti(OH)_6)^{2-}$ So, it is predicated that extensive concentration of OH^- ions facilitates the growth of nanocrystals and that means the increase in the crystallite size of the crystals thus that nanoparticles are well crystallized.

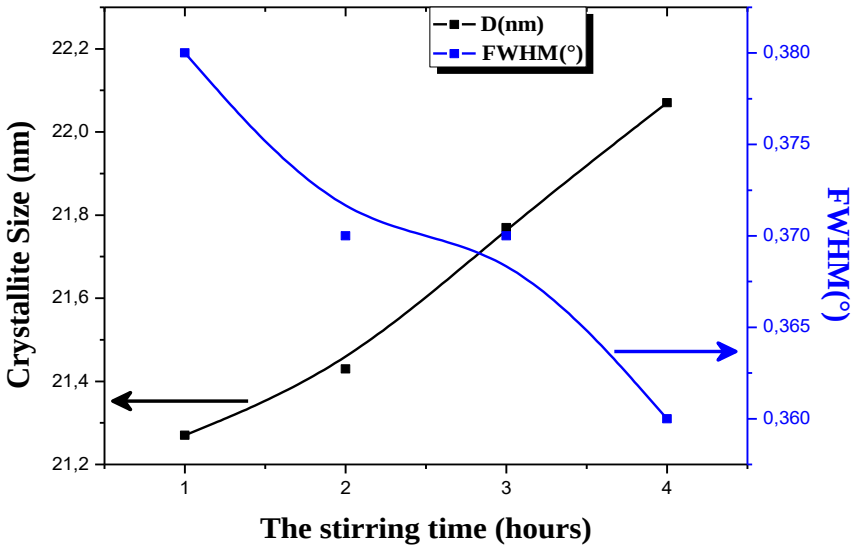

Figure IV.18. Crystallite size (D) and Full width at half maximum (FWHM) of TiO_2 thin film with different of the stirring time.

In addition, the strain (ε) of nanoparticle TiO_2 were determined using the following relations (II.12). The Table IV.4 shows the calculated strain along the orientation (101) crystallographic plane for different the stirring times. The strain values for the TiO_2 films that were deposited during the stirring times of 1, 2, 3 and 4 hours are 1.62, 1.61, 1.59 and 1.56 ($x10^{-3}$) respectively. The strain in TiO_2 thin films was decresing, according to our results. This is due to the reduction in inter-crystalline barriers as grain boundary area in the layers because of to the increase of crystallite size with stirring times. (See in Figure IV.19)

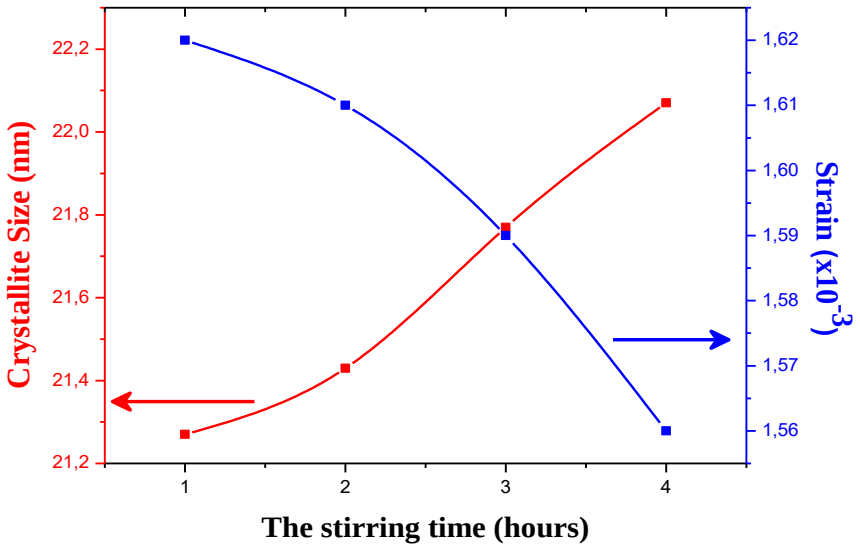

Figure IV.19. Crystallite size and the strain as a function of the stirring time.

A dislocation is a crystallographic flaw, or irregularity, in a crystal structure, and its existence within the crystallite structure has a significant impact on several material properties. The dislocation density (δ), which is defined as the number of dislocation lines per unit volue of the crystal has been computed using grain size values depending on the Williamson and Smallman's relation (II.13). As seen in the Table IV.4 the increase the crystallite size in Titanium oxide nanoparticles between 21.27–22.07 nm leds to a decrease in the dislocation density between $2.21 \times 10^{15} - 2.05 \times 10^{15}$ (lines/m^2) for TiO_2 thin films by spin coating method. This is mainly due to the fact that the increase in crystallite size in TiO_2 thin films with increase of the stirrring times leds to a decrease in grain boundaries and it decreased dislocation defect inside the crystal lattice of the samples and the result of all this was the stress reduced in crystal structure [30].

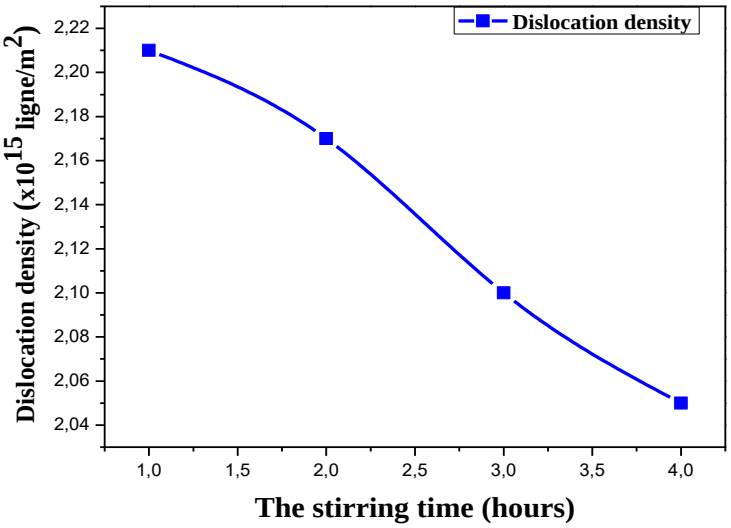

Figure IV.20. The dislocation density of TiO_2 films with different stirring time.

Table IV.4. Crystallite sizes, dislocation density and strain values of the stirring time TiO_2 thin films extracted from XRD analysis.

The Stirring time (hours)	Peak (hkl)	2θ°	FWHM (β°)	Crystallite size D (nm)	Dislocation density(δ)x10^{15} (Lines /m^2)	Strain (ε)x10^{-3}
1	(101)	25.37	0.38	21.27	2.21	1.62
2	(101)	25.42	0.37	21.43	2.17	1.61
3	(101)	25.37	0.37	21.77	2.10	1.59
4	(101)	25.39	0.36	22.07	2.05	1.56

The internal stress (σ) in the plane of the film can be estimated using the equation (II.14). As shown in Table IV.5, the negative sign indicates that the film is in compressive stress. On the other hand, the lattice constants 'a' and 'c' for the films are calculated from formula (II.11). From Table IV.5 and Figure IV.21 we observed that the 'a' and 'c' values are less than the standard values of TiO_2 (a = 3.7852 nm and c = 9.5139 nm), JCPDS card (n° : 21-1272), that's means the lattice was exposed to a compressive stress. Furthermore, It is also shown that the stress decreases from - 0.230 Gpa to - 0.221 Gpa with the increase in the stirring times from 1hour to 4 hours. This behaviour may be due to the size of the crystallites increases, which indicates the improvement of the crystallinity and the number of defects decreases. i.e. the decrease in the stresses [31]. Moreover, this last is confirmed by a shift of the peak (101) to a large angle which indicates a decrease in the plane spacing *d*.

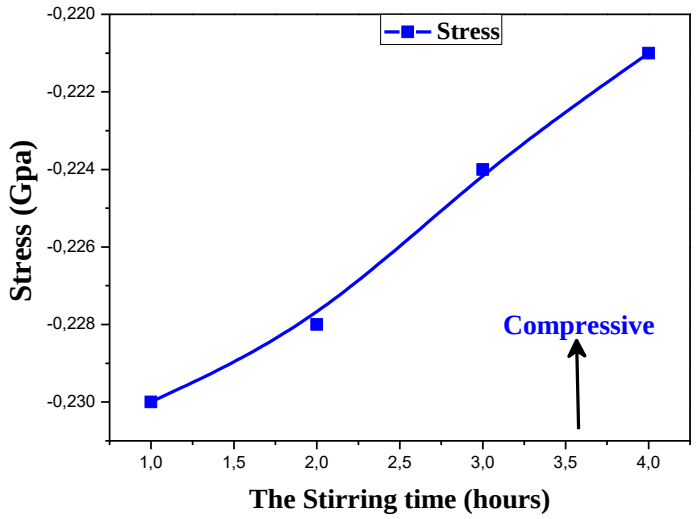

Figure IV.21. The stress of TiO_2 thin films at different stirring time.

Table IV.5. Structural parameters of TiO_2 thin films with the difference of the stirring time.

The Stirring time (hours)	hkl planes	2θ°	Calculated parameters			Reference parameter (JCPDS card No 21- 1272)	Stress (Gpa)
			d-spacing (Å)	Lattice constant a (Å)	Lattice constant c (Å)		
1	(101)	25.37	3.5067	3.7752	9.4678	a_0 = 3.7852 Å	-0.230
2	(101)	25.42	3.5007	3.7674	9.4729	c_0 = 9.5139 Å	-0.228
3	(101)	25.37	3.5075	3.7755	9.4774	d_0 = 3.521 Å	-0.224
4	(101)	25.39	3.5042	3.7715	9.4764	2θ = 25.28°	-0.221

IV.2.3.3. Fourier Transform-Infrared (FTIR)

Fourier transform infrared transmittance spectra (FT-IR) were used to characterize the TiO_2 thin films. The spectra obtained are shown in Figure IV.22. The organic compounds C–H stretching bonds are due to the absorption bands at 2848 and 2927 cm^{-1} [32]. Furthermore, Renard et al. [33] showed that the two bands found at 2850 and 2913 cm^{-1} correspond to the symmetric and asymmetric CH_2 stretching vibration modes. Besides, There are also traces of CO_2 (2361 cm^{-1}). This last band is due to the fact that the FTIR analysis of TiO_2 thin films was carried out in ambient air [12]. Moreover, in the FTIR spectra, main bands were observed at 514, 755 and 897 cm^{-1}. The band at 514 cm^{-1} range due to the vibration of Ti–O bonds in TiO_2 lattice as reported in literatures [8,9], and The band at755 cm^{-1} range due to the vibration of Ti–O–Ti bonds [34]. On the other hand, the band observed at 897 cm^{-1} can be attributed to the Ti–O stretching mode which involves nonbridging oxygen atoms [10,35].

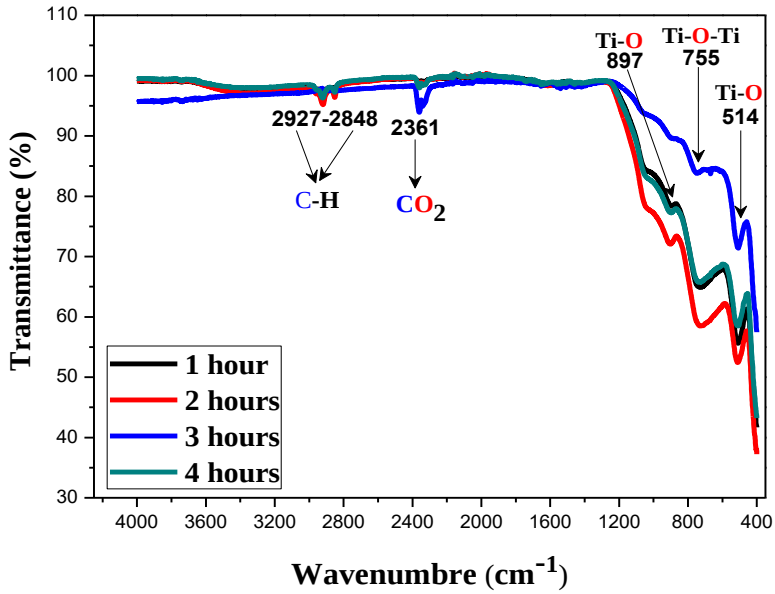

Figure IV.22. FTIR spectra of TiO_2 films at different stirring time.

IV.2.3.4. Optical studies

Figure IV.23 illustrates the transmittance spectra of TiO_2 thin films formed at 500 °C with various stirring times of the solution in the wavelength range of 300 – 1100 nm. On these spectra, two regions can be distinguished :

- A region of high absorption: corresponds to the fundamental absorption (λ< 385 nm) in TiO_2 films, and this is caused by light's fundamental absorption, which is due to the inter-band electronic transition (the valence band and the conduction band). On the other hand, there is a shift in the absorption threshold towards longer wavelengths (i.e. red shift) when the stirring time of the solution were increased from 1 hour to 4 hours (see the insert image in Figure IV.23), which suggesting to narrowing the band gap energy of our films.
- A region of strong transmittance (λ > 385 nm): the transmission value is higher than 72% for all films, which gives the thin layers of TiO_2 the character of transparent films in the visible and can therefore be useful for optical coating applications like: anti-reflective, wavelength-selective films and UV-protected films for optoelectronic devices [36]. On the other hand, we notice that the presence of interference fringes in the visible region of all the deposited films .This is mainly due to the difference of the refractive index value between air-film and film-substrate interfaces [37]. Also, these interference fringes in our samples are due to the decreased scattering light of incident light in the material due to uniform and homogenous with a smooth surface area consequently of interference oscillation between films and substrate surface [38]. As we also notice the transmittance decreases with the increase in stirring time of the solution, which can be explained by the increase in film thickness (Beer-Lambert law).

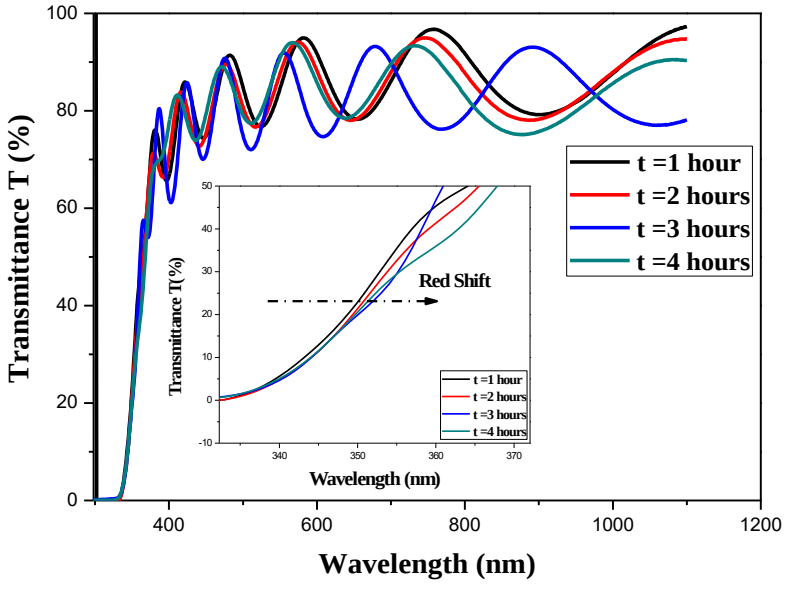

Figure IV.23. The transmittance spectra of TiO_2 thin films deposited at difference stirring time.

The band gap energy of thin films TiO_2 was determined by Tauc plot method according to the relationship (II.20). Based on Figure IV.24, it is obtained that energy gap of TiO_2 thin films prepared with mixing time for 1, 2, 3 and 4 hours are respectively 3.67 eV, 3.65 eV, 3.56 eV and 3.54 eV. These results indicate that the band gap energy (Eg) decreases with increase in the mixing time of the solution. This reduction in energy gap is attributed to the size of the crystal. Larger size of anatase crystals will provide a lower energy gap. This Phenomenon is well-known as a quantum size effect [39]. This effect is known to have important role in controlling the photochemical properties and photocatalytic of semiconductor materials [40].

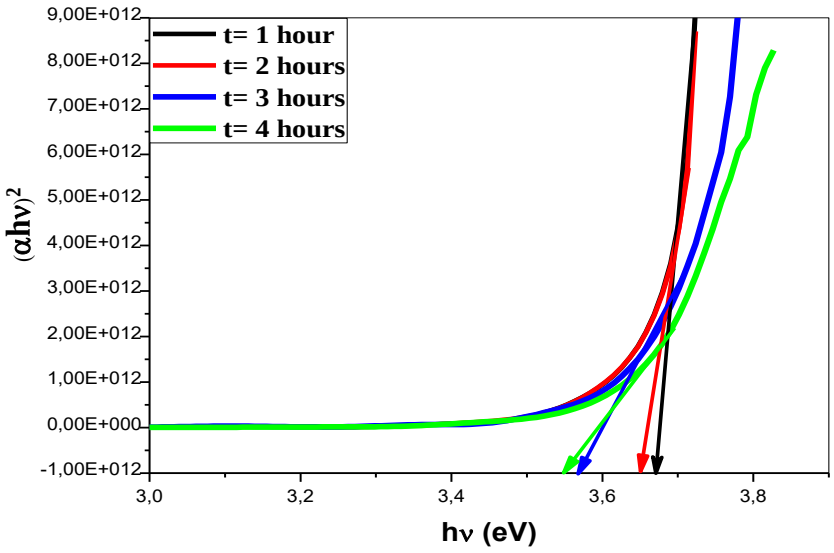

Figure IV.24. The plot of $(\alpha h\nu)^2$ versus hν of anatase TiO_2 thin films deposited on glass substrate with variation of the stirring time.

Disorder or Urbach's (Eu) energy is defined as the bandtailing (electronic states above E_V and below E_C). The Urbach energy of TiO_2 nanoparticles can be determined using the equation (II.21). Hence, according to this definition, Eg and Eu must have an inverse relationship, which is supported by our findings.

Variation in Urbach energy for TiO_2 thin films are summarised in Figure IV.25 and Table IV.6. We have observed an increase in Urbach energy from 0.136 eV to 0.157 eV with increase the stirring time of solution from 1 hour to 4 hours. This may probably be attributed to the reduction of energy band gap with the increase of stirring time of the solution could be

owing to the constitution of localized states in the band gap region. These states could be elicited in the band gap due to structural disorder caused by oxygen vacancies (the increase of the density of oxygen vacancy atoms into the TiO_2 film) [41,42] .

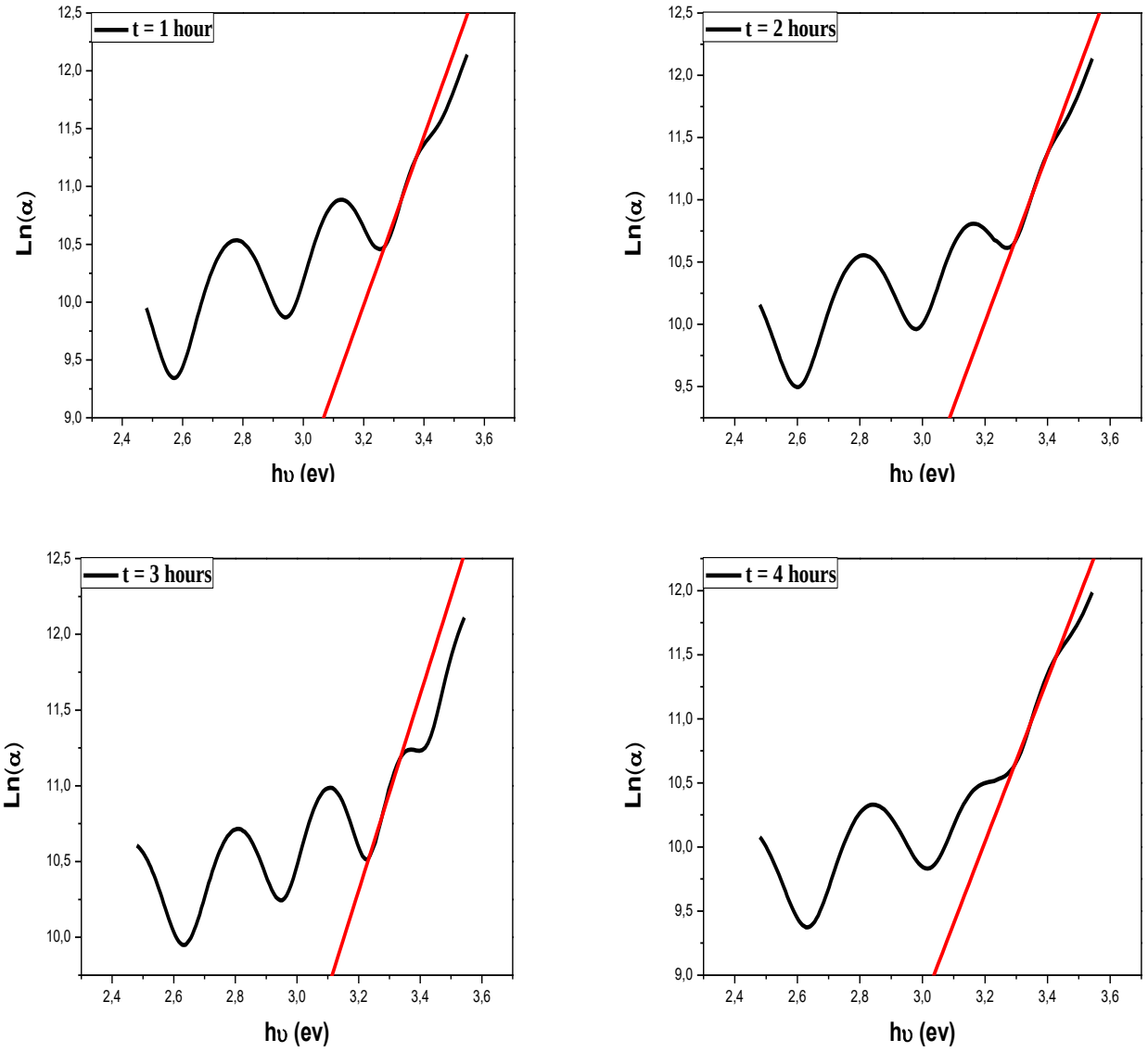

Figure IV.25. The plots of Ln (α) versus photon energy (hv) for the prepared TiO_2 thin films at various stirring times.

IV.2.3.5. Electrical studies

Four point probe technique at room temperature was used to obtain TiO_2 thin films's electrical properties with various stirring times.The value of the electrical resistivity ρ and electrical conductivity σ is obtained according to equation (II.12) and (II.13), the variation of TiO_2 films resistivity and conductivity as a function of stirring time is shown in Figure IV.26.

We can see from this figure, as the stirring time increases from 1 hour to 4 hours, the electrical resistivity gradually increases from 0.66 x 10^2 to 2.90 x 10^2 (Ω.cm). Correspondly, the electrical conductivity decreases from 15.15 x 10^{-3} to 3.44 x 10^{-3} $(Ω.cm)^{-1}$. Electrical resistivity's increase is ascribed to some inherent defects in TiO_2 films such as Ti interstitials and/or O vacancies, this defect behaves as a acceptor defect, which plays an important role in decrease the free electrons concentration and consequently the resistivity of the films increases. Lastly, the minimum value of the resistivity and the maximum value of the conductivity for TiO_2 film at 1 hour of the stirring time makes the film find wide diverse applications in optoelectronics and photovoltaics.

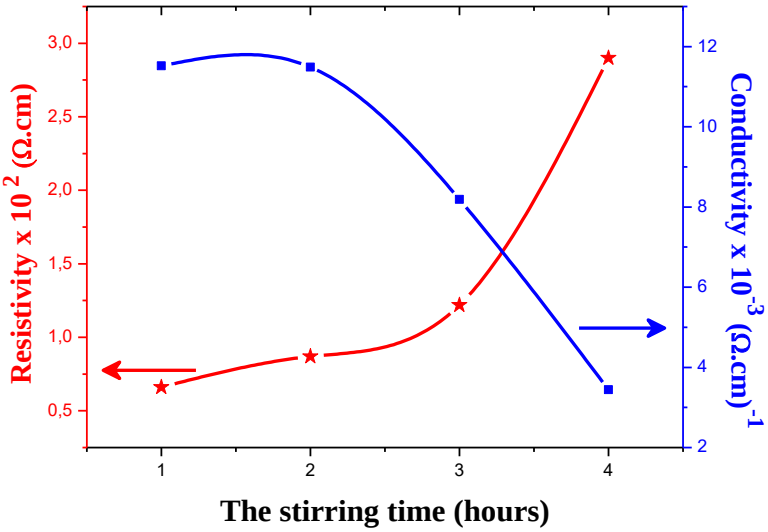

Figure IV.26. Electrical resistivity and conductivity as a function of the stirring time.

Table IV.6. Optical and electrical properties for the stirring time of TiO_2 thin films.

The stirring time (hours)	Thickness (nm)	Band Gap Energy (eV)	Urbach Energy (meV)	Rsheet x10^6 (Ω/sheet)	Electrical resistivity x10^2 (Ω.cm)	Electrical conductivity x10^{-3} $(Ω.cm)^{-1}$
1	787.44	3.67	0.136	0.85	0.66	15.15
2	829.50	3.65	0.147	1.05	0.87	11.49
3	940.78	3.56	0.154	1.30	1.22	8.19
4	986.23	3.54	0.157	2.95	2.90	3.44

Conclusion

On glass substrates, titanium oxide thin films with different stirring time have been effectively deposited using the Sol - Gel (spin coating) process. The influence of stirring time on structural, optical, and electrical properties was studied. XRD patterns revealed that prepared films have a polycrystalline having tetragonal structure of anatase along (101) plane corresponding to TiO_2 structure. We observed an increase in the preferential growth in the (101) plane for films , that means that the crystalline state of our films will getting better because of the increase of the stirring time. Furthermore, we notice a increases in the crystallite size with increasing the stirring time from 21.27 to 22.07 nm for TiO_2 nanoparticles. Besides, the stress of the all samples of TiO_2 thin films were found to have a compressive stress. On the other hand , films exhibited a high optical transparency that reaches up to 82% in the visible range at 1 hour . In addition, we noticed that the optical band gap energy (Eg) drops from 3.67 to 3.54 eV where the absorption band shifts towards higher wavelength (Red Shift). Correspondigly, urbach energy increases from 0.136 to 0.157 eV. Hence, the presence of Ti–O, Ti–O–Ti and CO_2 absorption bands and the stretching bonds of the organic compounds of C–H, due to the symmetric and asymmetric CH_2 stretching vibration modes was confirmed by Fourier transform infrared transmittance spectra (FTIR). In addition, we noticed a increased in the thickness of TiO_2 thin films with increasing stirring time from 787.44 to 986.23 nm. Electrical measurements showed that stirring time increases the electrical resistivity from 0.66 to 2.90×10^2 $(\Omega.cm)^{-1}$. These properties make it useful for many applications such as antireflection coating, self-cleaning glass, gas sensors, dielectrics materials, blocking layers (buffer film) in DSSC, photo catalysis, and Antibacterial.

Finally, we conclude that the prepared TiO_2 films may be a potential candidate in optoelectronics devices due to their attractive properties, such as strongly absorb UV radiations, high transmittance visible light, single anatase phase. Also, the sol gel spin coating process is capable of producing high-quality thin films that are homogeneous and uniform.

Chapter IV's references :

[1] B. Yahmadi, N. Kamoun, C. Guasch, R. Bennaceur, "Synthesis and characterization of nanocrystallized In_2S_3 thin films via CBD technique." Mater. Chem. Phys, 127 (2011) 239–247.

[2] M.Hemissi, H. Amardjia-Adnani, " optical and structural properties of titanium oxide thin films prepared by sol-gel method." Digest Journal of Nanomaterials and Biostructures, Vol. 2, No. 4, December 2007, p. 299-305.

[3] T.B. Ghosh, S. Dhabal, and A. K. Datta, "On crystallite size dependence of phase stability of nano-crystalline TiO_2." J. Appl. Phys., 94, 4577 (2003).

[4] M. M. Hasan, A. S. M. A. Haseeb, R. Saidur, H. H. Masjuki, and M. Hamdi, "Influence of substrate and annealing temperatures on optical properties of RF sputtered TiO_2 thin films." Journal of Optical Materials, 32, 690 (2010).

[5] Rosari Saleh, Nandy Putra, Suhendro Purbo Prakoso, Wayan Nata Septiadi, "Experimental investigation of thermal conductivity and heat pipe thermal performance of ZnO nanofluids." International Journal of Thermal Sciences, 63 (2013) 125e132.

[6] M. I. Khan, S. Imran, D. Shahnawaz, M Saleem, and S U Rehman, "Annealing effect on the structural, morphological and electrical properties of TiO_2/ZnO bilayer thin films." Results in Physics, 8, 249 (2018).

[7] I. Ben Miled, M. Jlassi, I. Sta, M. Dhaouadi, M. Ha jji, G. Mousdis, M. Kompitsas, and H. Ezzaouia, " Influence of In-doping on microstructure, optical and electrical properties of sol–gel derived CdO thin films." J. Mater. Sci., Mater. Electron., 29, 11286 (2018).

[8] Zuoli He, Wenxiu Que Jing Chen, Yucheng He, Gangfeng Wang, " Surface chemical analysis on the carbon-doped mesoporous TiO_2 photocatalysts after post-thermal treatment: XPS and FTIR characterization." Journal of Physics and Chemistry of Solids ,74 (2013) 924–928.

[9] P. Praveen, G. Viruthagiri, S. Mugundan, N. Shanmugam, " Sol–gel synthesis and characterization of pure and manganese doped TiO_2 nanoparticles – A new NLO active material." Spectrochimica Acta Part A: Molecular and Biomolecular Spectroscopy, 120 (2014) 548–557.

[10] Carolina M. Rodrigues, Odair P. Ferreira and Oswaldo L. Alves, " Interaction of

Sodium Titanate Nanotubes with Organic Acids and Base: Chemical, Structural and Morphological Stabilities." J. Braz. Chem. Soc., Vol. 21, No. 7, 1341-1348, 2010.

[11] Q. Li, C. Zhang, J. Li, " Photocatalysis and wave-absorbing properties of polyaniline/ TiO_2 microbelts composite by in situ polymerization method." Appl. Surf. Sci. 257 (2010) 944–948.

[12] S .Chelbi, L. Hammiche, D. Djouadi, A. Chelouche, " Caracterisations structurale et optique de l'aerogel de TiO_2 elabore dans l'ethanol supercritique. " Rev. Alg. Phys, Vol. 2, N° 2, 2015.

[13] X.Y. Li, H.J. Li, Z.J. Wang, H. Xia, Z.Y. Xiong, J.X. Wang, B.C. Yang, " Effect of substrate temperature on the structural and optical properties of ZnO and Al-doped ZnO thin films prepared by dc magnetron sputtering." Opt. Commun, 282 (2009) 247–252

[14] Myo Myo Thu, Atsunori Mastuda, Kuan Yew Cheong ,"Effects of drying temperature on tomato-based thin film as self-powered UV photodetector. " Applied Surface Science ,445 (2018) 186–196.

[15] Sami Saïdi , Aymen Mannaï, Hassen Derouiche, Abdelatif Belhadj Mohamed," Effect of drying temperature on structural and electrical properties of PANI:PVDF composite thin films and their application as buffer layer for organic solar cells." Materials Science in Semiconductor Processing ,19 (2014) 130–135.

[16] S. Lugo-Loredo, Y. Peña-Méndez, M. Calixto-Rodriguez, S. Messina-Fernández, A. Alvarez-Gallegos, A. Vázquez-Dimas, T. Hernández-García, " Indium sulfide thin films as window layer in chemically deposited solar cells." Thin Solid Films, 550 (2014) 110–113.

[17] C.D. Lokhande, A.U. Ubale, P.S. Patil,"Thickness dependent properties of chemically deposited Bi_2S_3 thin films." Thin Solid Films, 302 (1997) 1–4.

[18] R.S. Mane, C.D. Lokhande," Thickness-dependent properties of chemically deposited Sb_2S_3 thin films." Mater. Chem. Phys. 82 (2003) 347–354.

[19] S. Rabaoui , H. Dahman , S. Dekhil , K. Omri , A. Alyamani , L. El Mir, " Effect of drying temperature on the structural and optical characteristics of Cu_2SnS_3 thin films synthesized by simple spin coating technique." J Mater Sci: Mater Electron,(2015) 26:8588–8594.

[20] M. Sahal, B. Hartiti, B. Mari, A. Ridah, M. Mollar, " Etude des propriétés physiques des couches minces de ZnO dopées Al, préparées par la méthode de « sol-gel »

associée au « spin coating ».” Afrique SCIENCE, 02(3) (2006) 245 – 254.

[21] S.H. Sabeeh, R.H. Jassam, “ The effect of annealing temperature and Al dopant on characterization of ZnO thin films prepared by sol-gel method.” Results Phys,10 (2018) 212–216.

[22] G.J. Fang, D. Li, B.-L. Yao, “Influence of post-deposition annealing on the properties of transparent conductive nanocrystalline ZAO thin films prepared by RF magnetron sputtering with highly conductive ceramic target.” Thin Solid Films, 418 (2002) 156–162.

[23] A. Kennedy, K. Viswanathan, “Study of the influence of substrate temperature on structural, optical, and electrical properties of Zn-doped MnIn2S4 thin films prepared by chemical spray pyrolysis.” Phys. Lett. A, 380 (2016) 2842–2848.

[24] S. RaviShankar, A.R. Balu, M. Anbarasi , V.S. Nagarethinam,“ Influence of precursor molar concentration on the structural, morphological, optical and electrical properties of PbS thin films deposited by spray pyrolysis technique using perfume atomizer.” Optik ,126 (2015) 2550–2555.

[25] Y. Takahashi, M. Kanamori, A. Kondoh, H. Minoura, Y. Ohya, Jpn. Jpn. J. Appl. Phys, 33 (1994) 6611-6615.

[26] Y. Al-Douri, M.A. Fakhri, N. Badi, C.H. Voon,“ Effect of stirring time on the structural parameters of nanophotonic $LiNbO_3$ deposited by spin-coating technique.” Optik ,156 (2018) 886–890.

[27] M. M. Abd El-Raheem, and Ateyyah M. Al-Baradi, Internationel Journal of Physical Sciences, 8(31)(2013) 1570-1580.

[28] Dinesh Varshney, Kavita Verma,“ Effect of stirring time on size and dielectric properties of SnO_2 nanoparticles prepared by co-precipitation method.” Journal of Molecular Structure ,1034 (2013) 216–222.

[29] L.H. Jiang, G.Q. Sun, Z.H. Zhou, S.G. Sun, Q. Wang, S.Y. Yan, H.Q. Li, J. Tian, J.S. Guo, B. Zhou, Q. Xin, J. Phys. Chem. B ,109 (2005) 8774.

[30] A. Derbali, A. Attaf, H. Saidi, H. Benamra, M. Nouadji, M.S.Aida, N. Attaf , H. Ezzaouia , “ Investigation of structural, optical and electrical properties of ZnS thin films prepared by ultrasonic spray technique for photovoltaic applications.” Optik, 154 (2018) 286–293.

[31] K. R.Murali, S. Kumaresan,“ Characteristics of brush plated ZnS films. ” Chalcogenide Letters Vol. 6, No. 1, January 2009, p. 17 – 22.

[32] Z. Jiwei, Y. Xi, Z. Liangying, S. Bo, H. Chen, " Orientation control and dielectric properties of sol–gel deposited Ba(Ti, Zr)O3 thin films." J. Cryst. Growth. 262 (2004) 341–347.

[33] L. Renard, J. Brötz, H. Fuess, A. Gurlo, R. Riedel, T. Toupance, " Hybrid organotin and tin oxide-based thin films processed from alkynylorganotins: synthesis, characterization, and gas sensing properties." ACS Appl. Mater. Interfaces, 6 (2014) 17093–17101.

[34] W. Cui, J. He, H. Wang, J. Hu, L. Liu, Y. Liang, " Polyaniline hybridization promotes photo-electro-catalytic removal of organic contaminants over 3D network structure of rGH-PANI/TiO_2 hydrogel." Appl. Catal. B Environ ,232 (2018) 232–245.

[35] Daniela Cordeiro Leite Vasconcelos, Vilma Conceição Costa, Eduardo Henrique Martins Nunes, Antônio Claret Soares Sabioni, Massimo Gasparon3, Wander Luiz Vasconcelos, " Infrared Spectroscopy of Titania Sol-Gel Coatings on 316 L Stainless Steel." J. Materials Sciences and Applications, 2011, 2, 1375-1382.

[36] N. Witit-anun, P. Rakkwamsuk, and P. Limsuwan, "Characterization of anatase and rutile TiO_2 thin films deposited by two cathodes sputtering system." Advanced Materials Research, 55–57, 469 (2008).

[37] D Wojcieszak, J Michałmazur, A Indyka, M Jurkowska, P Kalisz, D Domanowski, J Kaczmarek, and Domaradzki, "Mechanical and structural properties of titanium dioxide deposited by innovative magnetron sputtering process." Materials Science Poland, 33, 660 (2015).

[38] B. Touati, A. Gassoumi, I. Dobryden, M. Maria Natile, A.Vomiero, N. K. Turki, "Engineering of electronic and optical properties of PbS thin films via Cu doping." Superlattices and Microstructures, 97 (2016) 519-528.

[39] A. Molea and V. Popescu. Optoelectronics And Advanced Materials 5, 242 (2011).

[40] S. Janitabar-Darzi, A. R. Mahjoub, and A. Nilchi. Physica E 42, 176 (2009).

[41] M. Caglar and Y. Caglar, "The determination of the thickness and optical constants of the ZnO crystalline thin film by using envelope method." Optoelectron. Adv. Mater, 8, 1410 (2006).

[42] B. Choudhury and A. Choudhury, "Oxygen defect dependent variation of band gap, Urbach energy and luminescence property of anatase, anatase–rutile mixed phase and of rutile phases of TiO_2 nanoparticles." Physica E, 56, 364 (2014).

Chapter V

Comparison of characteristic properties of La and Mn – doped TiO2 thin films formed by spin – coating process

V.1. Introduction

In the field of semiconductors, doping is the action of adding impurities in small quantities to a pure substance in order of producing dramatic changes in its properties (in particular electrical properties). The properties of semiconductors are largely governed by the amount of charge carriers they contain. These carriers are electrons or holes. The doping of a material consists in introducing, into its matrix, atoms of another material. These atoms will replace certain initial atoms and thus introduce more electrons or holes.

This chapter presents a detailed explanation of the preparation and characterization of ***La-doped TiO_2*** and ***Mn-doped TiO_2*** thin films deposited using sol-gel (spin coating) technique , where the atomic ratio of ***La*** and ***Mn*** in the precursor solution had 0, 3, 5, 7 and 9 $at.\%$ .Hence, The influence of ***La*** and ***Mn*** concentration on the properties of TiO_2 thin films is also discussed in detail.

V.2. Experimental details

V.2.1. Preparation of La and Mn- doped TiO_2

lanthanum ***(La***) and Manganese ***(Mn)*** - doped titanium oxide thin films with different concentrations were prepared on glass substrates by sol gel spin coating technique, using 0.605 ml Titanium Tetra Isopropoxide (TTIP) Ti $[OCH(CH_3)_2]_4$, 10 ml of methanol (CH_3OH) and 0.210 ml of acetylacetone (CH_3COCH) were used as the starting precursor, solvent and stabilizer, respectively then we add : *Lanthanum (III) Cholride Heptahydrate* ***[$LaCl_3$,7H_2O]*** ($Molecular\ weight$ = 371.37 g/mol), and *Manganese (II) Chloride Tetrahydrate* ***[$MnCl_2$,4H_2O]*** ($Molecular\ weight$ = 197.91 g/mol***)***,

The prepared solutions were stirred at 50 °C for one hours to yield clear and homogenous solutions, the resultant solutions were dropped on to glass substrates, which were rotated at 4000 rpm for 30 s. After each coating step, the films dried at 250 °C for 10 min to evaporate the solvent and remove organic residuals. The spin coating process was repeated seven times to achieve the desired film thickness. Finally, all the samples were annealed in furnace at 500 °C for 2 h to obtain good crystalline films.

V.2.2. Characterization methods

The phase and crystal structure were investigated using aby X-ray diffractometer (XRD) spectra (Model: Bruker D8) using Cu Kα (λ =1.5418 Å) radiation within the 2θ range of 20° – 60°, with the steps of 0.02°, respectively. Besides, Perkin Elmer Lambda 950 UV/VIS spectrometer using a blank substrate as the reference position examined the optical properties

of deposited thin film (film thickness, transmittance, gap energy, Urbach energy) ranging from 300 to 1100 nm. Furthermore, the FT-IR spectra were obtained with a Fourier transform infrared spectrometer (Perkin Elmer UATR Two). The scanning wavelength of infrared was 400 – 4000 cm^{-1}. Finally, The electrical resistivity measurement was done using four probe method.

The shematic diagram of sol-gel process of Mn and La-doped TiO_2 preparation is shown in Figure V.1.

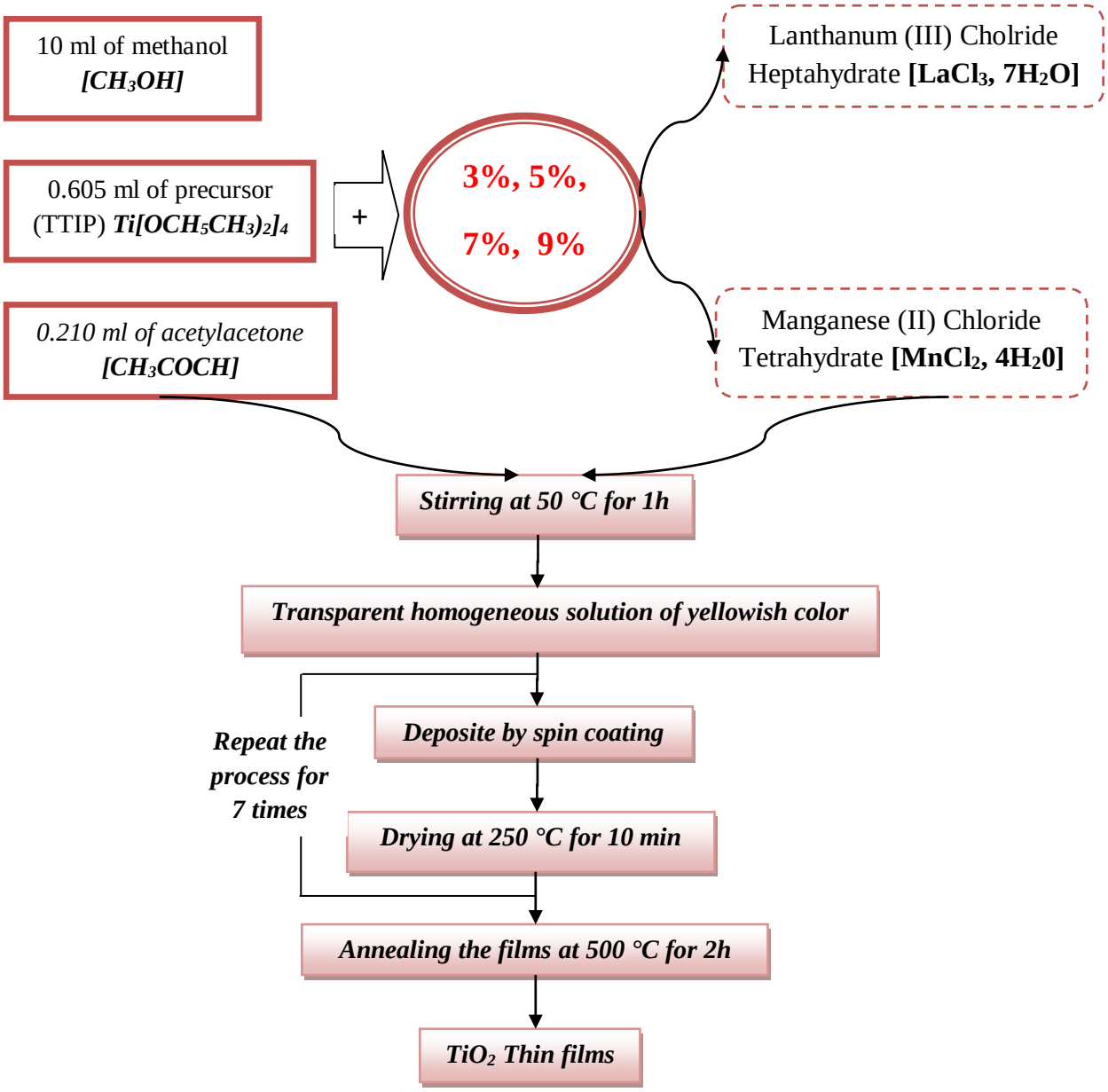

Figure V.1. The shematic diagram of sol-gel process of La and Mn- doped TiO_2 preparation.

V.3. Effect of La-doped TiO_2

V.3.1. Structural study

Figure V.2. shows the XRD spectra of pure and Lanthanum doped TiO_2 nanoparticle samples. XRD analysis reveals that Ti/TiO_2 film and Ti/La-doped TiO_2 film with La concentration of 3%, 5% and 7%, that was calcined at 500 °C were comprised of anatase phase structure of TiO_2 [1], namely, the planes (101), (112) and (200) at 2θ values 25.37°, 38.00° and 48.16°. Respectively, which all are in good agreement with (JCPDS-21-1272). While, XRD analysis reveals that Ti/La-doped TiO_2 film with La concentration of 9% were comprised amorphous phase structure.

It is seen from diffraction pattern that by doping of lanthanum content upto 7 %, the position of strongest peaks (101) having a small shift towards lower values of 2θ (25.42° to 25.37°, shown in inset of Figure V.2). This is an indication that the incorporation of some La^{3+} ions into the TiO_2 lattice. Besides, there isn't any intense diffraction peaks related to the oxides of La were observed in the recorded XRD patterns, implying that either La ions were incorporated into the bulk of mesoporous TiO_2, or the La particles were very small and highly dispersed on the mesoporous TiO_2 surface [2,3] because La oxide is amorphous or highly dispersed and cannot be detected by XRD scan [4].

The La-doped film has a certain extent of peak broadening compared to the undoped film, indicating lattice distortion in the TiO_2 crystal structure (the structure disorder) and the presence of oxygen vacancies produced by La doping [5,6]. The phenomenon was explained by the fact that the La^{3+} has a large ionic radius (1.08 Å) than Ti^{4+} (0.61 Å). Therefore, it cannot enter into lattice sites of titania but La atoms only disperse on the surface of TiO_2 atoms and make stronger bonding. In addition. Here, as the concentration of La increase, the intensity of (101) peak decreased as compared to pure TiO_2, indicating a decreased crystallinity of the TiO_2 thin films. This low peak crystallinity is may be due to height in lattice mismatching between the layers.

Moreover, we found that the diffraction peaks of lanthanum modified TiO_2 films film with La concentration of 3% and 5% are nearly same as that of pure TiO_2 films which indicates that La^{3+} ions may be present in the form of La_2O_3 [7,8]. As a result, It seems that La-doping appears to causes an additional disorder in the anatase phase, and it does not exclude the presence of La-oxide in the amorphous phase in the samples doped with higher La concentration and this is what was found in TiO_2 film when the concentration of La was 9 % as shown in the Figure V.2.

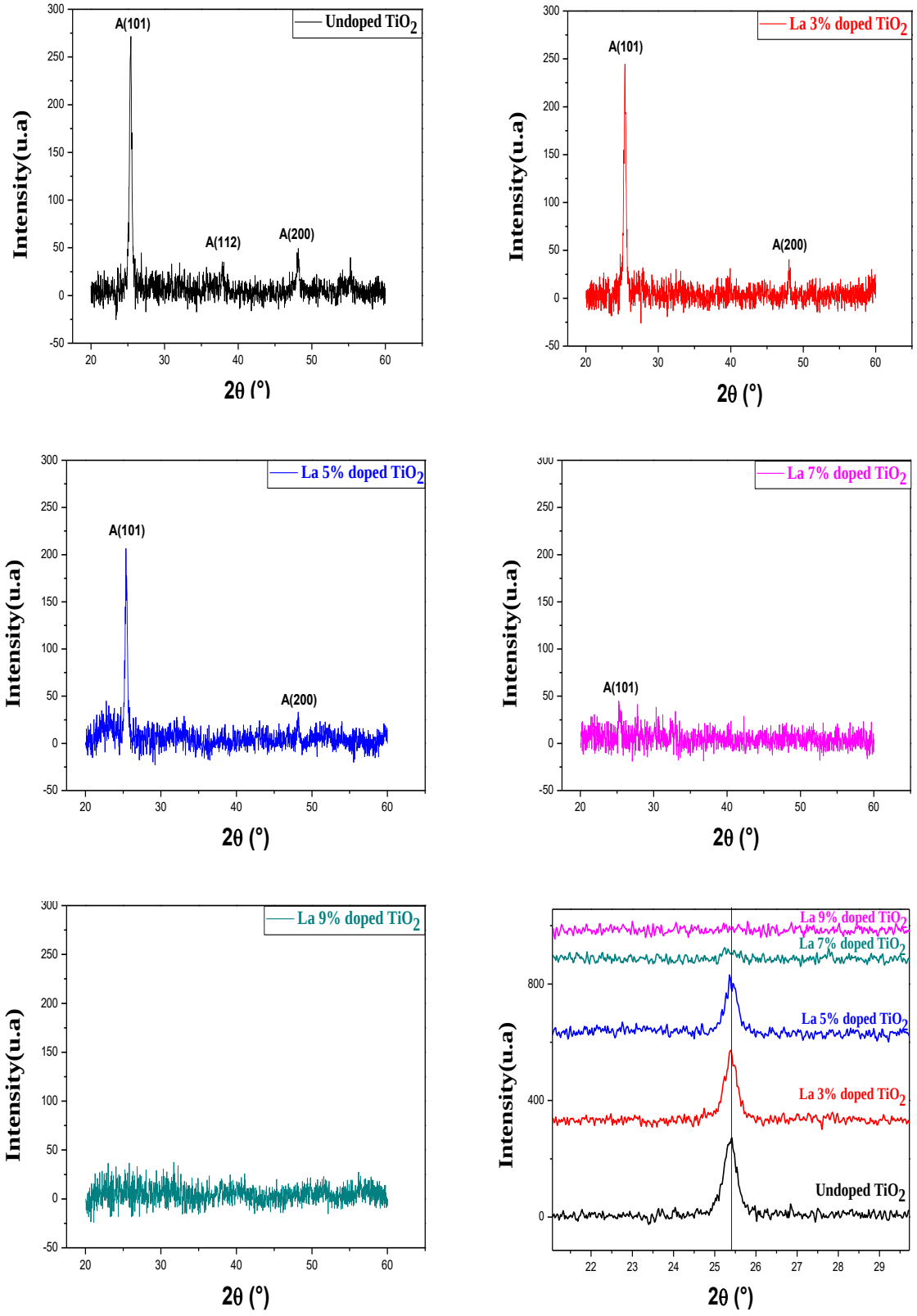

Figure V.2. XRD patterns of sol–gel synthesized pure and La-doped TiO_2.

In the present study, the crystallite size *D* was determined from Scherrer's formula (equation II.9) using the diffraction peaks at 25.37°. From Figure V.3 and Table V.1 we observe that the FWHM slightly increases with increase in La doping percentage. Increasing in the FWHM value leads to decrease in crystallite size of the TiO_2 anatase phase. The crystallite sizes of the nanoparticles obtained from the XRD spectra were 21.27, 20.87, 20.25 and 18.41 nm for 0%, 3%, 5% and 7% La-doped TiO_2 respectively. This decrease in the crystallite size can be attributed to the fact that the dopant La^{3+} ions inhibits the growth of the nanoparticles because relatively large size difference between La^{3+} (1.216 Å) and Ti^{4+} (0.745 Å) prevent La^{3+} ions enter into Ti lattice. Also, the decrease in the crystal size can be attributed to the presence of La_2O_3 produced on the surface and on the interstitial sites of the samples, this prevents TiO_2 nanoparticles from clumping and inhibit the growth of crystal grains [5,9,10].

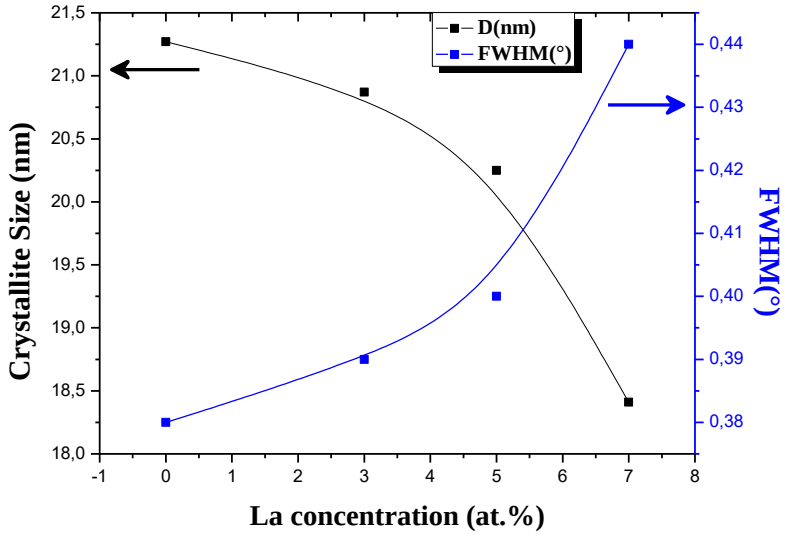

Figure V.3. Crystallite size (D) and Full width at half maximum (FWHM) of TiO_2 thin film as a function of La concentration (at.%).

The dislocation density is defined as the length of dislocation lines per unit volume of the crystal, and it is calculated using Williamson and Smallman simple approach (relation II.13). Figure V.4 shows that when the percentage of La dopant increases, the dislocation density increases. This is because the presence of dislocations has a significant impact on the characteristics of TiO_2 thin films. Where, a large dislocation density signifies a higher hardness.

In addition, the lattice strain (ε) have also been estimated for all the films by applying the following relation (II.12). The strain values for the TiO_2 films deposited at the La doping

concentration of 0, 3, 5 and 7 (at.%) are 1.62, 1.66, 1.71 and 1.88 ($x10^{-3}$) respectively. Our results revealed of strain increases with the increase of the La-doping content, because that the ionic radius of La was larger than that of Ti, strain is produced in the TiO_2 lattice. Hence, this strain is due to the lattice imperfection during the film deposition (see Figure V.4 and Table V.1).

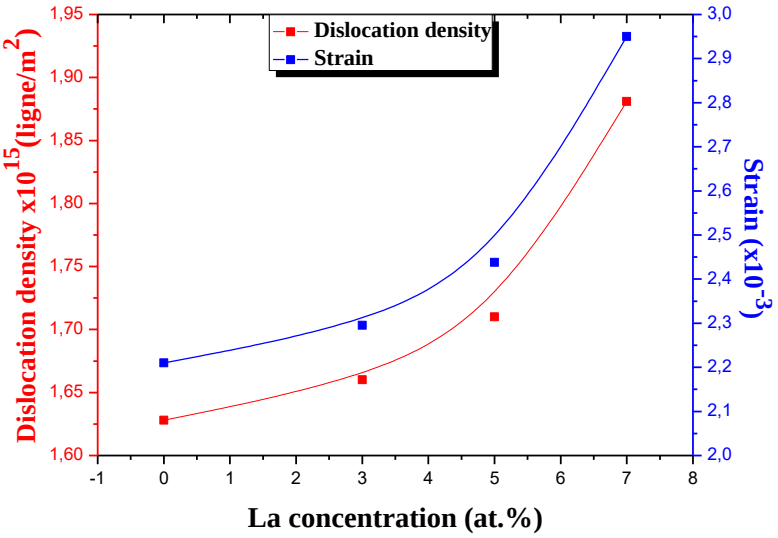

Figure V.4. Dislocation density **δ** and strain **ε** as a function of La concentration (at%).

Table V.1. Crystallite sizes, dislocation density and strain values of pure and La doped TiO_2 thin films extracted from XRD analysis.

La Concentration (at%)	Peak (hkl)	2θ°	FWHM (β°)	Crystallite size D (nm)	Dislocation density(δ)x10^{15} (Lines /m^2)	Strain (ε)x10^{-3}
0	(101)	25.37	0.38	21.27	2.21	1.62
3	(101)	25.37	0.39	20.87	2.29	1.66
5	(101)	25.42	0.40	20.25	2.43	1.71
7	(101)	25.38	0.44	18.41	2.95	1.88
9	—	—	—	—	—	—

The lattice constants ‘a’ and ‘c’ of anatase TiO_2 films were calculated from the relation (II.11) and the stress of films are calculated by relation (II.14) and given in Table V.2 . We can see from this table that the ‘a’ and ‘c’ values are lower than the TiO_2 standard values.

(a = 3.7852 Å and c = 9.5139 Å) JCPDS (n° : 21 − 1272) [11], which indicate that the stress is compressive for La doping concentration of 0%, 3% and 5%. With an increase in La concentration, the lattice parameters fall slightly. These changes are due to the internal structure of TiO_2 film is affected by La doping. This is because the difference between ionic La^{3+} and Ti^{4+} radii .Where, this variation of lattice parameters will effect on the optoelectronic characteristics of film. In addition, it is observed in the literature that differences in ionic radius play a very effective role in lattice variations. When the La doping concentration reaches 7%, the lattice constants become greater than the standard values, and the stress is changed to tensile stress. This variation in stress can be related to lattice mismatch (shown in Figure V.5).

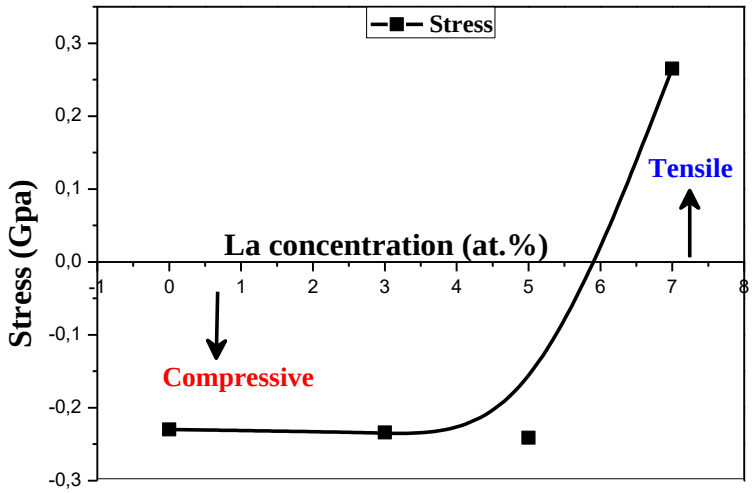

Figure V.5. The stress of TiO_2 thin films as a function of La concentration (at.%).

The surface states will play an important role in the nanoparticles, due to their large surface to volume ratio with a decrease in particle size [12]. The Specific surface area (SSA) defines the total area occupied by the particles/mass [13], with the help of the equation (II.15) SSA is measured. As shown in Table V.2, we notice that the specific surface area (SSA) increase dramatically as the crystallite size (D) of materials decreases. On the other hand, the specific surface area of the thin films is in the range 66.68–77.04 (m^2/ g). In addition that, The specific surface area (SSA) is increasing with increase in La doping concentration because crystals are actually gathered together on the surface of the films. As results as, a high surface area absorbs more sunlight and boosts surface reactivity, resulting in increased efficiency.

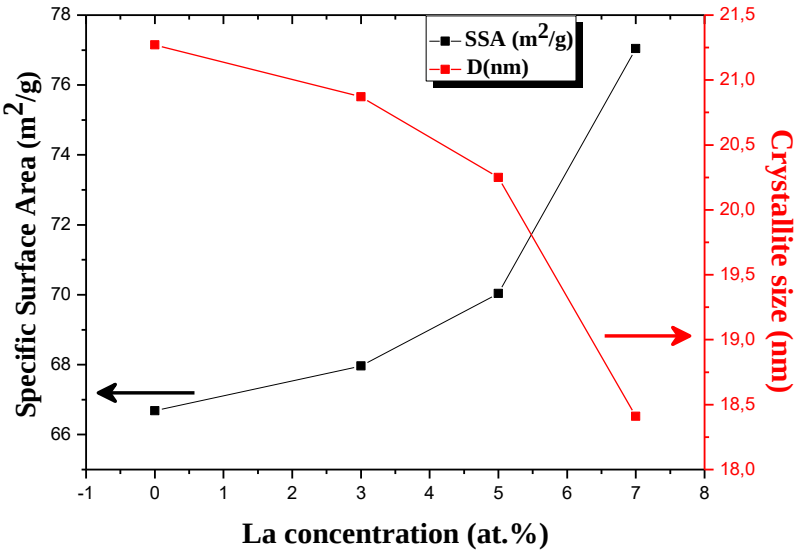

Figure V.6. Effect of La concentration on specific surface area (SSA) and crystallite size (D) of TiO_2 thin film.

Table V.2. Structural parameters for undoped and TiO_2: La thin films.

La Concentration (at%)	hkl planes	2θ°	Calculated parameters			Reference parameter (JCPDS card No 21- 1272)	Stress (Gpa)	Specific surface area (m^2/g)
			d-spacing (Å)	Lattice constant a (Å)	Lattice constant c (Å)			
0	(101)	25.37	3.5067	3.7752	9.4678		-0.230	66.68
3	(101)	25.37	3.5065	3.7841	9.3271	a_0 = 3.7852Å	-0.234	67.96
5	(101)	25.42	3.5010	3.7765	9.3380	c_0 = 9.5139Å	-0.241	70.04
7	(101)	25.38	3.5054	3.7901	9.6533	d_0 = 3.521 Å 2θ = 25.28°	0.265	77.04
9	—	—	—	—	—		—	—

The volume of the unit cell for all the films were calculated according to the following relation (II.16). As Table V.3 illustrates, the lattice volume increase with increasing concentration of dopant which confirms the ionic size difference between the radii of La^{3+} and

Ti^{4+}. Where we find it expansion of host occurred, that's because La^{3+} entering into TiO_2 lattice.

The X-ray density was calculated using the relation (II.17). Besides, the X-ray density depends on molecular weight and lattice constant 'a'. From Table V.3 we observed that the values of the X-ray density slightly increased because due to difference between atomic weights of La^{3+} (138.905 amu) and Ti^{4+} (47.867 amu), this results in a slightly increase in unit cell volume and, as a result, an increase in X-Ray density.

The degree of crystallinity of the films was calculated using the relationship (II.18). In Table V.3 we present the degree of crystallinity decreased with increase in La concentration because due to difference in ionic radii of host atom Ti^{4+} (0.61 Å) and the dopant atom La^{3+} (1.08 Å).

Table V.3. The data extracted from XRD patterns of undoped and La-doped TiO_2 films.

La Concentration (at%)	**The volume of the unit cell ($Å^3$)**	**X-ray density ($g/mol.Å^3$) ($x10^{-23}$)**	**Degree of crystallinity (X_C)**
0	116.854	7.016	0.393
3	115.661	6.966	0.378
5	115.332	7.008	0.356
7	120.111	6.896	0.294
9	—	—	—

V.3.2. Fourier Transform Infrared (FTIR) Spectroscopic Analysis

FTIR spectroscopy was used for finding the nature of the chemical bond in the titanium oxide (TiO_2) thin films. Fourier transform-infrared spectra of La-doped TiO_2 nanoparticles are shown in Figure V.7. At the range of 400 – 4000 cm^{-1}. The FTIR analysis of these TiO_2 nanoparticles show the characteristics of the formation of high purity products, with peaks corresponding to anatase titania. TiO_2 shows a broad band at 509 cm^{-1} range due to the vibration of Ti–O bonds in TiO_2 lattice as reported in literatures [14,15]. Also, the broad peaks appear at 735 cm^{-1} are assigned to the to the stretching vibration mode of Ti–O–Ti groups [16]. Furthermore, we note that a very weak two peak appears in the pure TiO_2 film at 904 cm^{-1} and 1055 cm^{-1} which gradually increases with increase in La doping concentration to reach its strength at 9%, corresponds probably to absorption peaks bands O–Ti–O. As

noticed also by DU Jun et al. [17] and Ti–O–Ti. Chin-Chieh Ho et al. [18], respectively. By the way, Absorption intensity of the peaks decreases with increasing La doping concentration which indicated to the decreasing of the crystallization degree ,that supported by DRX results. Moreover, the peak of feeble absorption intensity positioned at 1563 cm^{-1} in the FTIR spectra of films are associated with the H–O–H bending vibration of the absorbed water molecules [19]. Hence, the presence of OH bands in the spectrum was owing to chemically and physically adsorbed H_2O on the surface of nanoparticles [20]. Besides, There are also traces of CO_2 (2360 cm^{-1}). This last band is due to the fact that the FTIR analysis of TiO_2 thin films was carried out in ambient air [21]. Also, In the FTIR spectra, main bands were observed at 2858 and 2911 cm^{-1}. Respectively, is allocated to the distinctive frequencies of leftover organic species that were not entirely eliminated by ethanol and distilled water washing and is attributed to the C–H stretching vibrations of alkane groups, the symmetric and asymmetric CH_2 stretching vibration modes could be attributed to them [22]. Also, FTIR spectra of TiO_2 show a band at about 3389 cm^{-1}, is attributed to stretching vibration of hydroxyl O–H groups. As reported by K.P. Priyanka et al. [23].

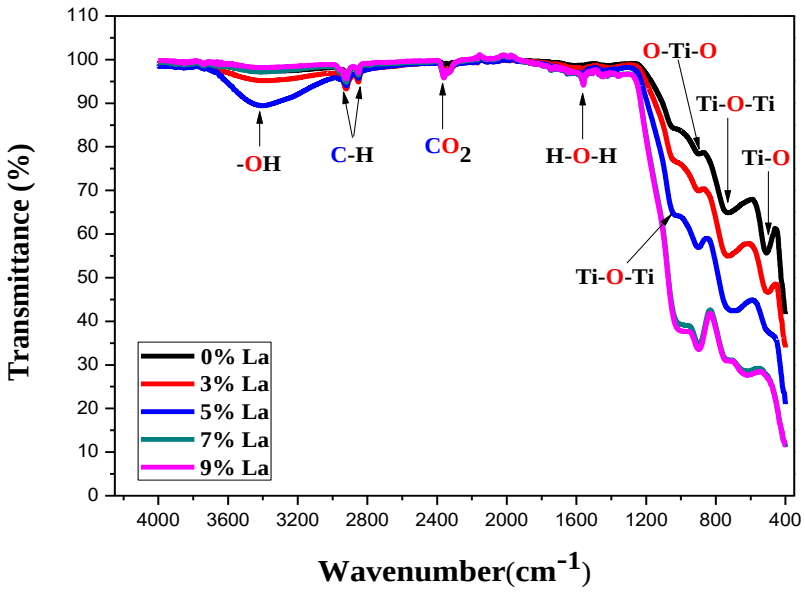

Figure V.7. FTIR spectra of pure and La doped TiO_2 nanoparticles.

V.3.3. Optical study

Figure V.8 shows the transmittance spectra of undoped and TiO_2: La films recorded between 300 nm to 1100 nm wavelength range. From the Figure V.8 we notice that all the

spectra show almost similar curve shape. In the visible wavelength region (400 – 800 nm), a high transmittance with an average of up to 91% is observed with the presence of interference fringes (corrugations), which are due to the multiple refections of the radiation on the two sides of the film [24]. On the other hand, this is due to the fact that the prepared films are uniform and homogenous with a smooth surface area consequently of interference oscillation between films and substrate surface. Furthermore, we notice that the undoped TiO_2 has absorption edge at 380 nm which is similar to the anatase TiO_2 nanoparticles (386 nm). The minimum shift has been observed for higher La percentage (9 at.%) at 344 nm. Besides, it is worth noting that the doping concentration increases caused a notable blue shift in the UV region ($\lambda <$ 385nm), because due to the reduction in size of the particles caused by doping, which confirms the quantum confinement [25]. Also, this may be attributed to the interaction between surface oxidic site of TiO_2 and La^{3+} may also be the cause for blue shift [26]. This shift is followed by a increasing of the TiO_2 network's band gap energy.

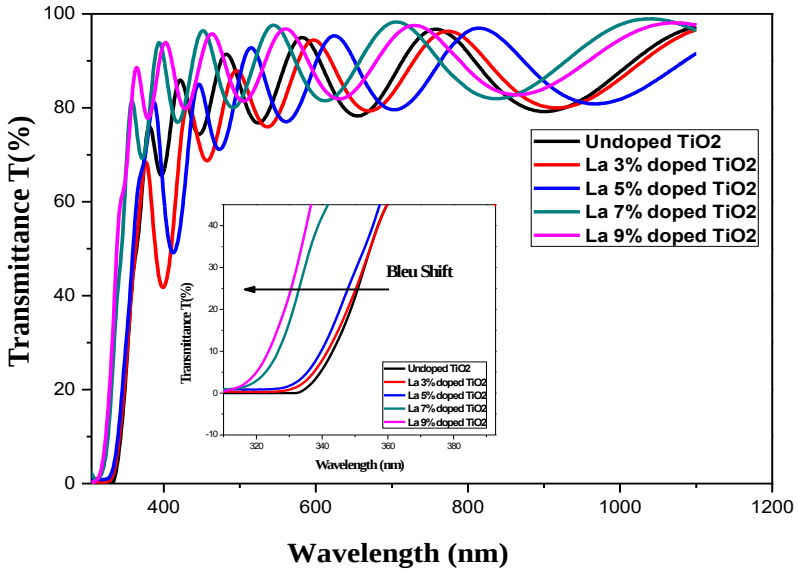

Figure V.8. UV–Visible spectra of pure and La-doped TiO_2 films.

The optical band gap energy of undoped, 3%, 5%, 7% and 9% La-doped of TiO_2 thin films is calculated by plotting a curve between $(\alpha h\nu)^2$ and $(h\nu)$ as shown in Figure V.9. The Tauc's equation was used to determination the band gap energy, according to the relationship (II.20). As shown in Figure V.9, the optical band gap energy Eg increases from 3.67 to 3.75 eV with increasing La dopant levels from 0 at.% to 9 at.%. This increase in energy gap is attributed to the presence of a large interaction between the TiO_2 and La sites [25]. Also, the

broadening of the bandgap energy with increasing thickness of the films could be due to the Borstein-Mohs effect [27,28]. This phenomenon is associated with an increase in carrier concentration leading to Fermi level shifts to higher energy [29]. Where, doping with La^{3+} ions in TiO_2 lattice will provide free electrons in the valence band. Because the bottom of the conduction band is filled with La free electrons, so that high energy is needed for electrons in valence to move to higher energy states in the conduction band. Hence, Eg increased tremendously with increase in La percentage to 9 (at.%) due to the high electron density. It applies that higher electron concentration density dominates over crystal defects which increased band gap [4].

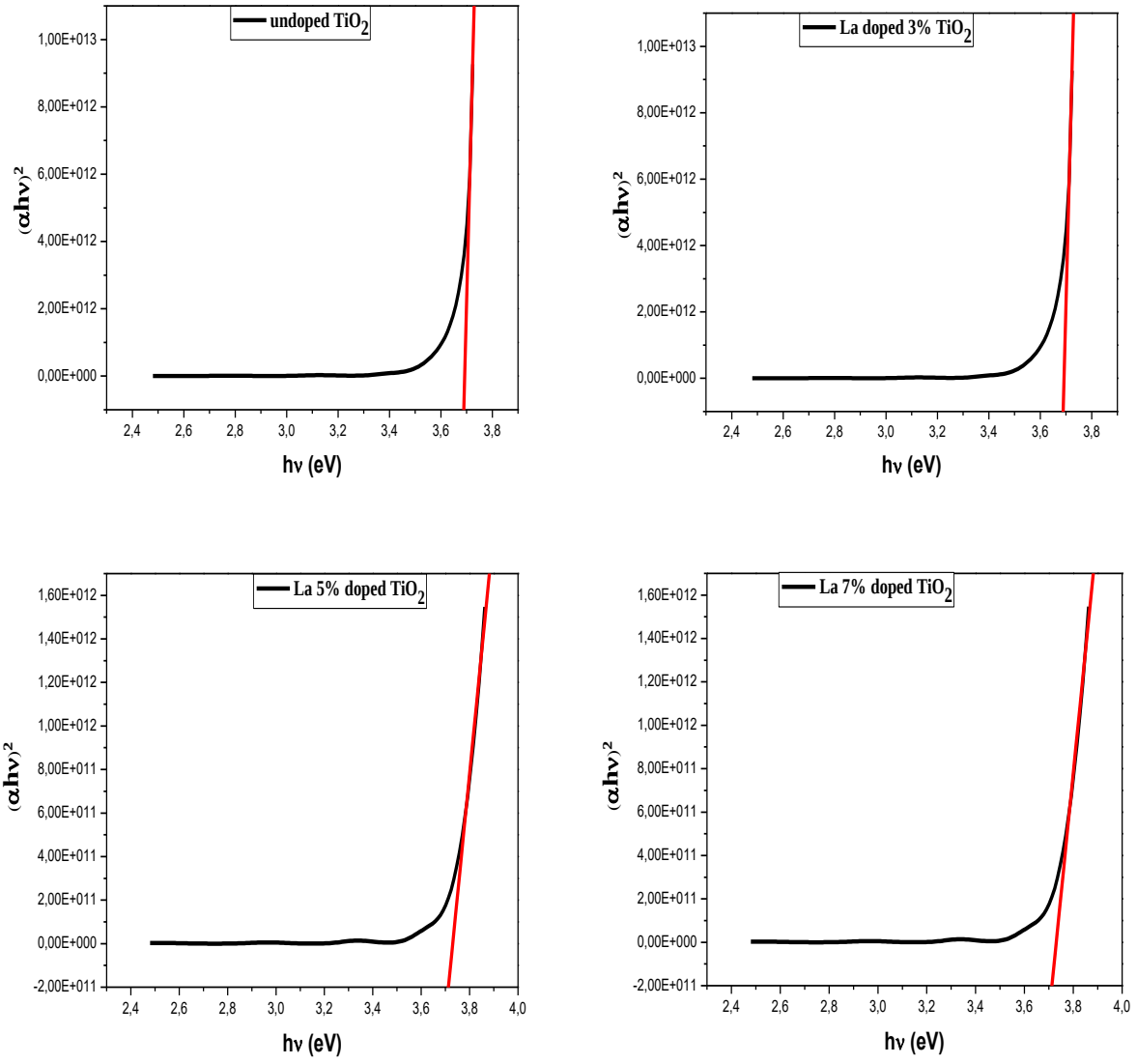

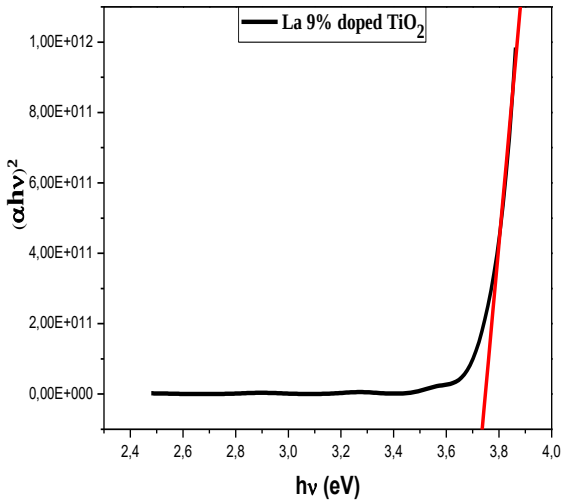

Figure V.9. The plot of $(\alpha h\nu)^2$ versus hν of pure and La-doped TiO_2 films.

The Urbach energy (Eu) is the band tail width and describes the disorder in a film network. It is determinited by plotting a curve between ln(α) and (hν) as shown in Figure V.10. Hence, Urbach energy can be calculated using the formula (II.21).

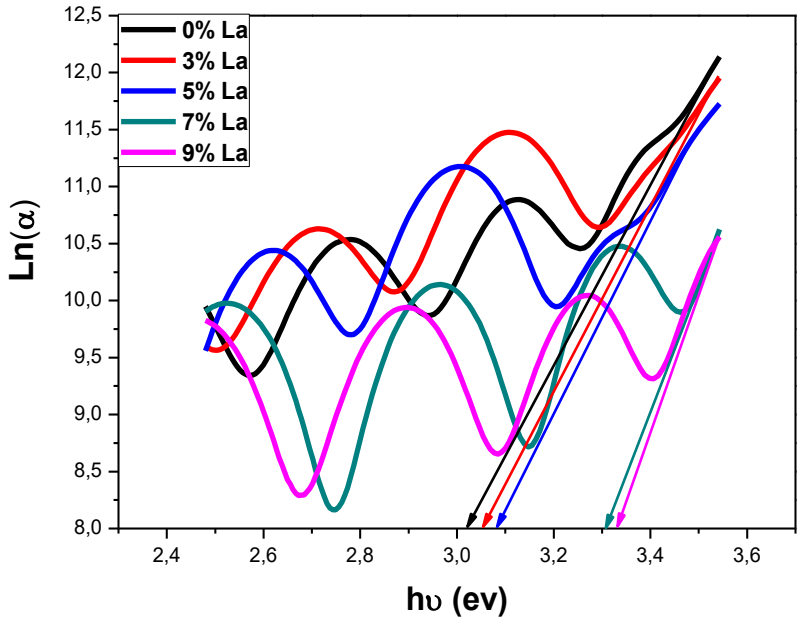

Figure V.10. Ln(α) vs hν plots of undoped and La-doped TiO_2 nanoparticles.

Variation in Urbach energy for undoped and TiO_2: La thin films are summarised in Table V.4. We have observed an decrease in Urbach energy with increase in Lanthanum (La)

concentration from 0 to 9 at.% from 0.140 eV to 0.126 eV. Zebbar et al [30] interpreted the Urbach energy Eu as being the width of the bands of the localized states inside the width of the forbidden band. This decrease in disorder with increasing La concentration can be interpreted as structural disorder decreases (the decrease in disorder density) and defect in the structure of the films [31] because the decrease in crystallite size has formed on the surface of the films to prevent external defects and intrinsic defects [32]. This result is confirmed by Abdelhak Jrad andothers [33].

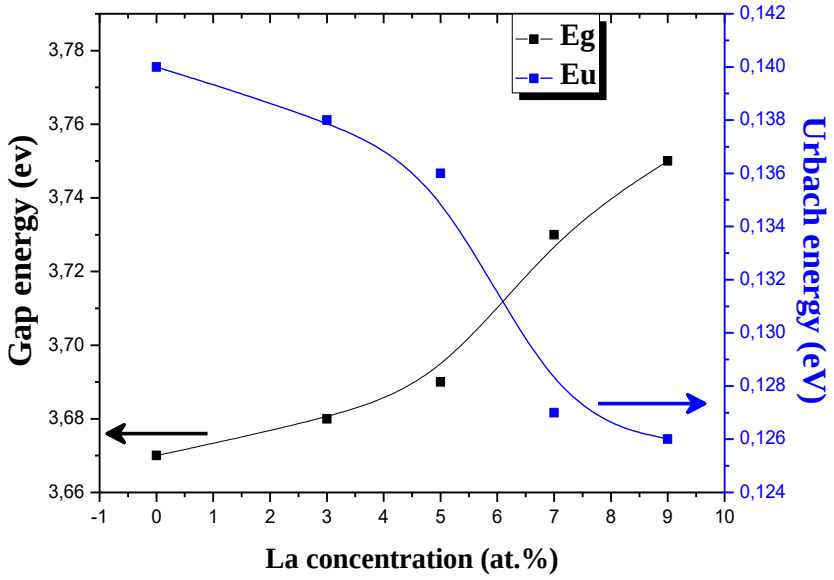

Figure V.11. Optical band gap and Urbach energy of TiO_2 films as a function of La concentration (at.%).

Table V.4. Optical and electrical properties for undoped and TiO_2: La thin films.

La Concentration (at%)	Thickness (nm)	Band Gap Energy (eV)	Urbach Energy (meV)	Rsheet $x10^6$ (Ω/sheet)	Electrical resistivity $x10^2$ (Ω.cm)	Electrical conductivity $x10^{-3}$ $(Ω.cm)^{-1}$
0	787.44	3.67	0.140	0.85	0.66	15.15
3	907.02	3.68	0.138	0.75	0.68	14.70
5	994.66	3.70	0.136	0.72	0.71	14.08
7	1034.98	3.73	0.127	0.77	0.79	12.56
9	1090.87	3.75	0.126	0.88	0.95	10.52

V.3.4. Electrical study

A four-point probe setup was used to conduct the electrical measurements.The variation of electrical conductivity of TiO_2 films as a function of La-doping concentration is shown in Figure V.12. The value of the electrical conduvtivity σ is obtained according to equation (II.28). From Figure V.12, we can observe that the electrical conductivity is decreased from 15.15 x 10^{-3} to 10.52 x 10^{-3} $(\Omega.cm)^{-1}$ as increasing La concentration. We obtained a maximum electrical conductivity value at 15.15 x 10^{-3} $(\Omega.cm)^{-1}$ for pure TiO_2 thin film. Some La atoms may occupy interstitial places and may also form generate defects in the structural lattice, which operate as carrier traps rather than electron donors, resulting in a decrease in electrical conductivity [34]. Furthermore, this reduction in electrical conductivity is attributed to the decrease of grain size means deterioration of crystalline quality of TiO_2 films with increase in La concentration and an increase of total grain boundary fraction in the films, which can enhance grain boundary scattering, thus, result in a decrease of electrical conductivity. This result confirmed by XRD and grain size variations. As a result, we may deduce that the electronic transport property of TiO_2 thin films is fully dependent on the microstructure of the films and doping concentration.

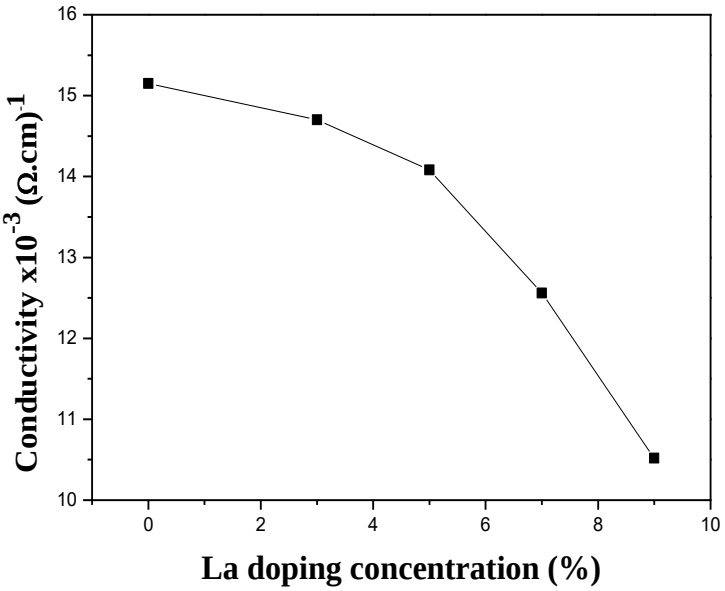

Figure V.12. Conductivity of TiO_2 thin films with different La concentration (at.%).

Conclusion

Sol-gel (spin-coating) technology was used to successfully manufacture transparent conducting titanium oxide thin films with varied compositions (0, 3, 5, 7, 9 mol.% La) on glass substrates that had been annealed at 500 °C. The effect of lanthanum (La) doping concentration on TiO_2 film structural, optical and electrical properties was examined. Following are the results reached as a result of these investigations : The X-ray diffraction analysis showed that the only detectable crystal structure is the one of anatase with strong (101) as preferential orientation, and there isn't any intense diffraction peaks related to the oxides of La were observed in the recorded XRD patterns. On the other hand, the crystallite size and strain values, were found to be around 21.27 to 18.41 nm and 1.62 x 10^{-3} to 1.88 x 10^{-3}. Besides, the stress of TiO_2 thin films changed from compressive to tensile. The optical measurements show a high transmittance with an average of up to 82 % for undoped TiO_2 films, and it was found to the transmittance increased from 83% to 91% with increased the Mn concentration from 3 at% to 9 at%. So, all TiO_2 thin films are highly transparent in the visible region and show are mark able absorption band shifts (Blue Shift) suggesting the increased in the optical band gap energy increasing with increase in La doping concentration from 3.67 eV to 3.75 eV. Correspondigly, the urbach energy decreases from 0.140 eV to 0.126 eV. On the other hand, FTIR spectra confirmed the presence of Ti–O, Ti–O–Ti, O–Ti–O, H–O–H, CO_2, C–H and O–H stretching vibration bonds. Lanthanum doping in titanium oxide thin films reduces conductivity from 15.15 to 10.52 x 10^{-3} $(\Omega.cm)^{-1}$, according to four probe measurements. As a result, we may deduce that the electronic transport property of TiO_2 thin films is fully dependent on the microstructure and doping concentration of the films.

V.4. Effect of Mn doping

V.4.1. Structural study

XRD pattern of pure TiO_2 and Mn-doped TiO_2 nanoparticles with different weight percentages (3%, 5%, 7% and 9%) respectively are shown in Figure V.13. As shown from Figure V.13, the XRD results indicated that all the films are crystallized. It was discovered that the substance seen is TiO_2 polycrystalline with an anatase tetragonal structure, no other phases (rutile or brookite) are detected. Also , the pattern of pure TiO_2 exhibits prominent peaks at 2θ values of 25.37°, 37.98°, 38.07° and 48.16° , which is represented by diffraction peaks corresponding to (101), (400), (112) and (200) this is in accordance with JCPDS (n°: 21-1272), similar structure phase are observed by other literature (S. Asha Bhandarkar et al.,2021) [35].

XRD diffraction patterns showed that the samples were polycrystalline, and had differences in peak intensities and widths. Where, as the rate Mn concentration increase, the intensity of (101) peak decreased and half-peak widths increased (FWHM), indicating not improved crystallinity of the TiO_2 thin films with decreasing thickness, this may be it indicates that the crystal growth of TiO_2 may be slightly affected by Mn doping And that's because the difference in ionic radii of host atom Ti^{4+} (0.61 Å) and the dopant atom Mn^{2+} (0.67 Å). Also, in literature it can be seen when dopant ions replace main ions in a crystal, the crystallinity declines (Li et al., 2008) [36]. Although, we have not observed any distinguished peaks of Mn or its oxides, the presence of these phases cannot be completely ruled out. Since the added dopant concentration is very less, the fraction of impurity phases are probably too less to be detected by XRD [37]. However, as the rate of Mn concentration increases, the diffraction angle (101) of TiO_2 thin films changes from 0.05° to 0.18°, which could be due to residual stresses in the films, resulting in a shift in d-spacing of a typical (101) plane. On the other hand, we have observed with the increasing ratio of Mn dopant, the crystal structure remained the same and only the peak intensities changed. Therefore, can be attributed to the fact that the samples were produced in high purity and Mn ions replaced the TiO_2 atoms without changing the crystal structure. The crystallite size (D) of the undoped and doped TiO_2 was calculated using the Debye-Scherer Formula (equation II.9), from Figure V.14 and Table V.5. We can see that crystallite size (D) decreases for the doped films with increase in concentration of dopant, where is the crystallite size of pure TiO_2 is 21.27 nm, where as Mn doped TiO_2 nanoparticles having 19.92, 19.39, 19.16 and 18.52 nm for 3%, 5%, 7% and 9%

of Mn, respectively. Also, we have observed that the FWHM value has increased with increase in Mn concentration indicating a decrease in crystallite size due to the presence of Mn content in TiO_2 structure [38]. Furthermore, a slight decrease in particle size with increase in doping concentration and that's because the doping inhibits grain formation and causes lattice distortion in crystal structure [39].

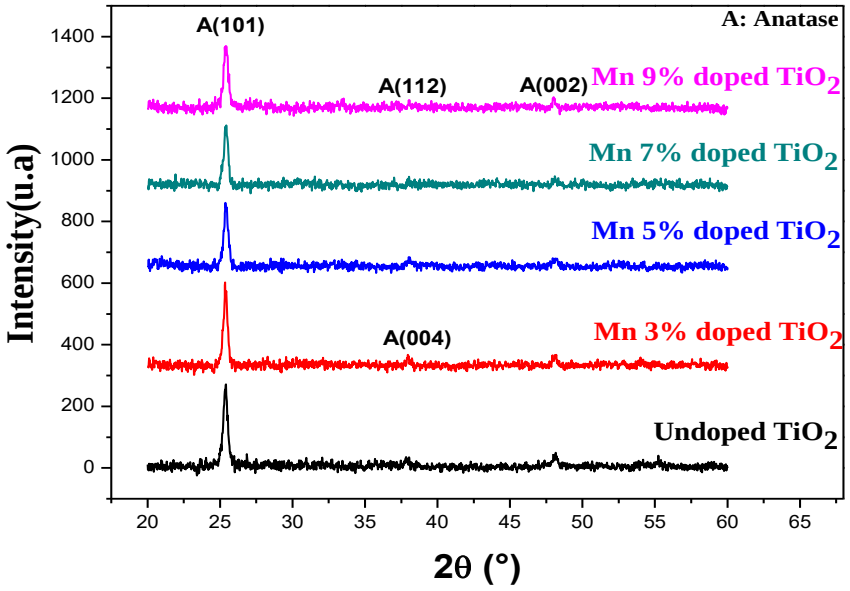

Figure V.13. XRD patterns of pure TiO_2 and Mn-doped TiO_2 nanoparticles with Mn concentration of 3%, 5%, 7% and 9% respectively.

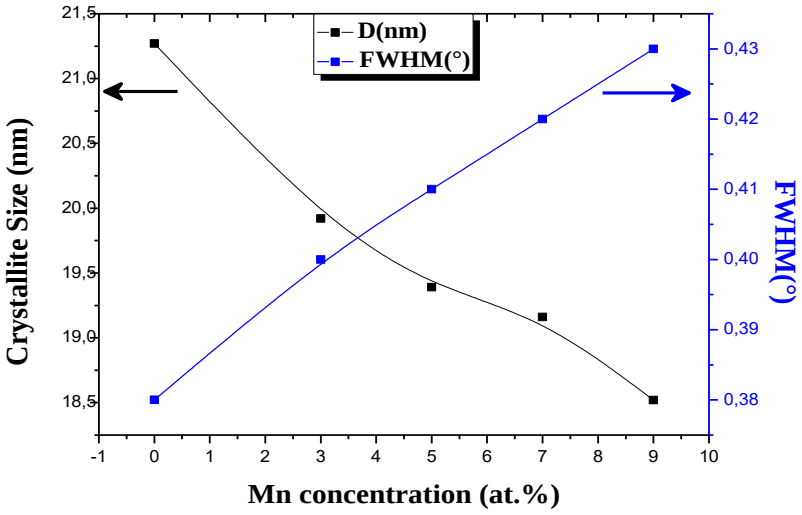

Figure V.14. Effect of Mn concentration on crystallite size (D) and Full width at half maximum (FWHM) of TiO_2 thin film.

Based on the obtained crystallite size values, the one-dimensional defects (dislocation density) were calculated according to the relationship (II.13), the strain (ε) in the deposited films have been estimated using the relation (II.12) and the stress (σ) of the prepared films were determined using the formula (II.14), these structural parameters (δ, ε, σ) in addition to the and lattice parameters 'a', 'c' of the films provide us with information about the crystal structure. From Table V.5 we observed that the dislocation density and the strain of the films were found to increase with decrease in crystallite size. This may probably be attributed to the following: the difference in ionic radii of Ti^{4+} (0.61 Å) and Mn^{2+} (0.67 Å), where we note that the ionic radius of Mn is greater than Ti. So, the substitution of Ti^{4+} by Mn^{2+} in the TiO_2 lattice when TiO_2 is doped with Mn, it causes deformation in the crystal lattice [40]. (See in the Figure V.15).

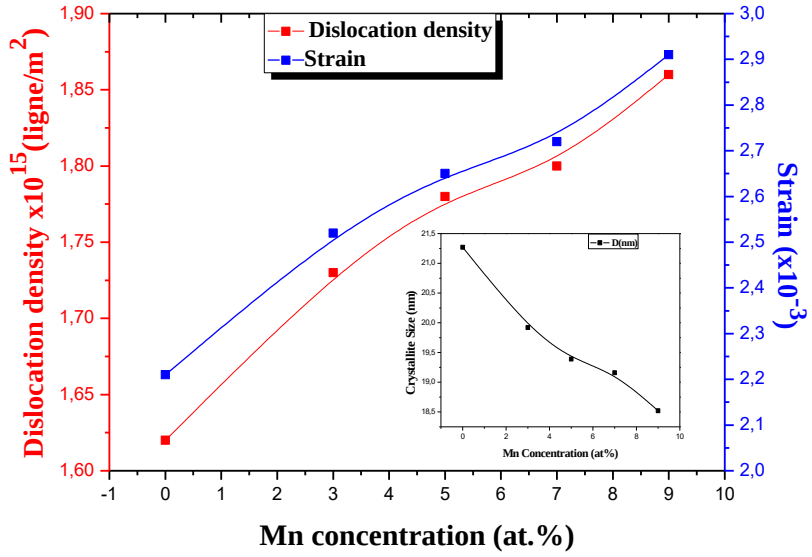

Figure V.15. Dislocation density ***δ*** and strain ***ε*** as a function of Mn concentration (at.%).

Moreover, we can deduce from the Figure V.16 and Table V.6 that the stress induced by Mn atoms in TiO_2 thin films at different Mn doping percentage, was a which indicate that the stress is compressive. This is because the difference between ionic Mn^{2+} and Ti^{4+} radii .Where we find that when it is Mn^{2+} ions are incorporated into the periodic crystal lattice of TiO_2, These ions (Mn^{2+}) occupancy of interstitial sites of oxide titanium (between the (Ti) atom and the (O) atom). Therefore, a stress is compressive is induced into the system. Hence, we find that the lattice constants 'a' and 'c' to decreased upon doping. As we can see, the lattice

constant changes little along the c-axis compared to the a-axis. This is due to Mn atoms occupying interstitial sites in addition to substitutional sites [39].

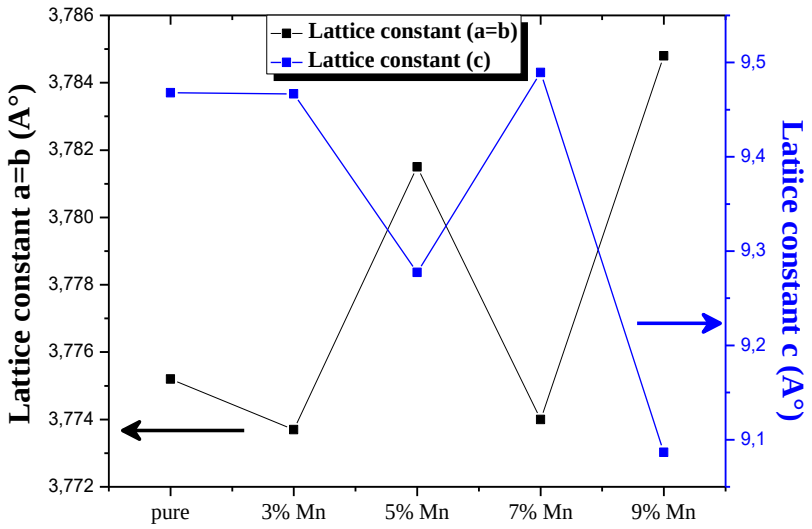

Figure V.16. Variation of lattice constants for pure and Mn doped TiO_2 nanoparticles.

Table V.5. Crystallite sizes, dislocation density and strain values of pure and Mn doped TiO_2 nanoparticles extracted from XRD analysis.

Mn Concentration (at%)	Peak (hkl)	2θ°	FWHM (β°)	Crystallite size D (nm)	Dislocation density(δ)x10^{15} (Lines /m^2)	Strain (ε)x10^{-3}
0	(101)	25.37	0.38	21.27	2.21	1.62
3	(101)	25.38	0.40	19.92	2.52	1.73
5	(101)	25.41	0.41	19.39	2.65	1.78
7	(101)	25.37	0.42	19.16	2.72	1.80
9	(101)	25.46	0.43	18.52	2.91	1.86

The specific surface area (SSA) defines the total area occupied by the particles/mass [38], with the help of the equation (II.15). It is worthwhile noting, from Table V.6 and Figure V.17, that the specific surface area (SSA) increase as the crystallite size (D) of materials decreases. On the other hand, the specific surface area of the thin films is in the range 66.68 (m^2/ g) at Mn -doped TiO_2 (0 $at.$ %) to 76.58 (m^2/ g) at Mn-doped TiO_2 (9 $at.$ %). Besides,

the specific surface area (SSA) is increasing with increase in Mn doping concentration because crystals are actually gathered together on the surface of the films. As results as, a high surface area absorbs more sunlight and boosts surface reactivity, resulting in increased efficiency.

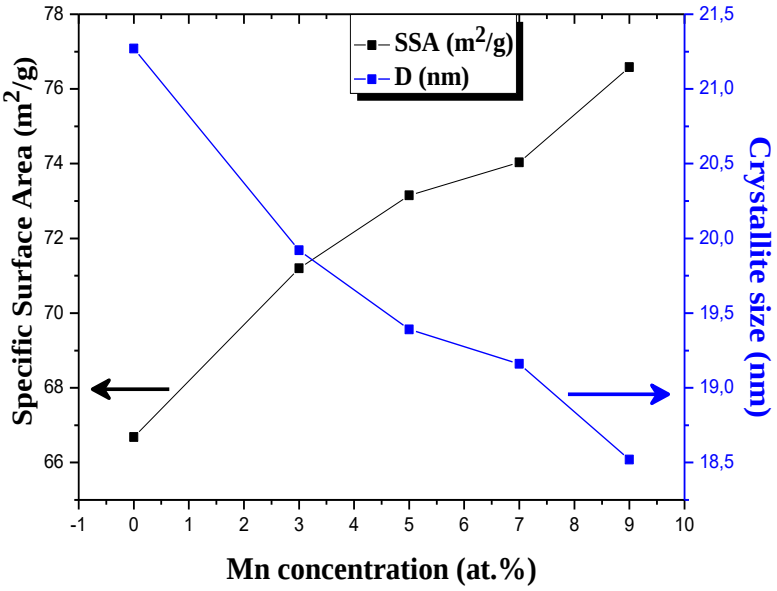

Figure V.17. Variation of specific surface area (SSA) for pure and Mn doped TiO_2 nanoparticles.

Table V.6. Structural parameters for undoped and TiO_2: Mn thin films.

Mn Concentration (at%)	hkl planes	2θ°	Calculated parameters			Reference parameter (JCPDS card No 21- 1272)	Stress (Gpa)	Specific surface area (m^2/g)
			d-spacing (Å)	Lattice constant a (Å)	Lattice constant c (Å)			
0	(101)	25.37	3.5067	3.7752	9.4678		-0.230	66.68
3	(101)	25.38	3.5054	3.7737	9.4667	a_0 = 3.7852Å	-0.245	71.20
5	(101)	25.41	3.5018	3.7815	9.2774	c_0 = 9.5139Å d_0 = 3.521 Å	-0.252	73.15
7	(101)	25.37	3.5068	3.7740	9.4893	2θ = 25.28°	-0.255	74.03
9	(101)	25.46	3.4954	3.7848	9.0866		-0.262	76.58

In addition, the volume of the unit cell (V), the X-ray density and the degree of crystallinity (Xc) have also been estimated for all the films by applying the following relations (II.16), (II.17) and (II.18) respectively. The variation of the volume of the unit cell, the X-ray density and the degree of crystallinity with La concentration (at. %) of TiO_2 films are represented in Table V.7. We notice that the volume of the unit cell increase with increasing Mn dopant percentage which confirms the ionic size difference between the radii of Mn^{2+} and Ti^{4+}. Where we find it expansion of host occurred, that's because Mn^{2+} entering into TiO_2 lattice. As a result, when some Mn^{2+} ions remain in the unit cell at Ti^{4+} ion locations, the TiO_2 bond length is enhanced. Besides, the X-ray density slightly increased because due to difference between atomic weights of Mn^{2+} (54.938 amu) and Ti^{4+} (47.867 amu). Morever, because Mn has a larger ionic radius than Ti, the degree of crystallinity decreased as the Mn concentration increased.

Table V.7. The data extracted from XRD patterns of undoped and Mn-doped TiO_2 films.

Mn Concentration (at%)	**The volume of the unit cell ($Å^3$)**	**X-ray density ($g/mol.Å^3$) ($x10^{-23}$)**	**Degree of crystallinity (X_C)**
0	116.854	7.016	0.393
3	116.748	7.024	0.344
5	114.887	6.981	0.326
7	117.045	7.022	0.319
9	112.840	6.960	0.298

V.4.2. FTIR Spectroscopic Analysis

The infrared transmission spectra of undoped and Mn-doped TiO_2 nanoparticles at 3%, 5%, 7% and 9% at the range of 400 – 4000 cm^{-1}, deposited by spin-coating technique on glasse substrates and annealed at 500 °C, are shown in Figure V.18. The FTIR study of these TiO_2 nanoparticles reveals the characteristics of high purity product production, with peaks correspond to anatase titania. The characteristic absorption bands in the pure TiO_2 film and Mn-doped TiO_2 include two strong broad peaks and clear. One is around 496 cm^{-1}, which is assigned to the stretching vibration of Ti–O groups [41], and the other is around 735 cm^{-1}, which is assigned to the stretching vibration mode of Ti–O–Ti groups. J. Wei et al. [42]. On the other hand, the spectrum of Mn-doped TiO_2 shows the appearance of new band at 894

cm^{-1} corresponds probably to absorption peaks metal bands-hydroxyl Ti–O or Mn–O. As reported by Abdelmalek Kharoubi et al. [24]. Moreover, the peaks at 1438–1558 cm^{-1} region could be attributed to carboxyl (C=O) and methylene groups. The carboxyl and methylene groups might could be resulted from residual organic species G.S. Guo et al. [43]. Furthermore, the peak of feeble absorption intensity positioned at 1656 cm^{-1} in the FTIR spectra of films is associated to water molecules H–O–H stretching vibrations (pertaining to the adsorbed water) [44]. Also, the peak at 1747 cm^{-1} can be associated to the asymmetric stretching mode of titanium carboxilate [45]. Besides, the spectrum of Mn-doped TiO_2 shows the appearance of new band at 2367 cm^{-1} represented the Mn–Ti band. M.M. Rashad et al. [46]. Additionally to two others weak peaks located at 2858 cm^{-1} and 2924 cm^{-1} respectively, is attributed to stretching vibration C–H of alkane groups, that mainly due to the residual organic species and which was not completely removed by ethanol and distilled water washing [47]. In addition, for both bare and manganese doped TiO_2 nanoparticles, a spectroscopic band in the range 3362 cm^{-1} is found, which is explained by both symmetric and asymmetric stretching vibrations of the hydroxyl group (Ti–OH). Similar in the stretching vibrations of the hydroxyl group (Ti–OH) of TiO_2 has been reported by P. Praveen et al. [41] in their studies on manganese doped TiO_2 nanoparticles.

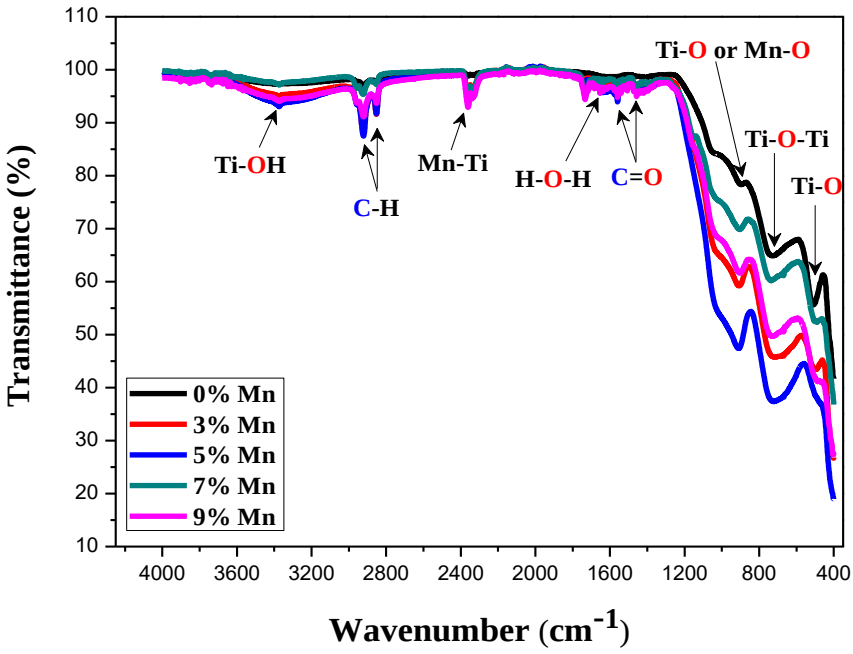

Figure V.18. FTIR spectra of pure and Mn-doped TiO_2 thin films.

V.4.3. Optical study

The optical transmittance spectra of Mn doped TiO_2 nanostructures in the wavelength range of 300 – 1100 nm for the all samples are displayed in Figure V.19. As is shown in Figure V.19, a high transmittance with an average of up to 82 % for undoped TiO_2 films is observed with the presence, and it was found to decrease from 80 % to 73 % as we increased the Mn concentration from 3 at% to 9 at%. This transmittance is consistent with that of TiO_2 thin films [41,19,20]. the primary reason for this reduction in transmittance is attributed to the deformation in lattice system with increasing Mn dopant levels. Furthermore, the transmittance spectra of our samples revealed strong absorption edges in the UV region (λ<385 nm), which suggesting that the absorption edge of the transmittance shifts towards longer wavelength (i.e. red shift) when Mn concentration were increased (see the insert image in Figure V.19), This shift is followed by a narrowing of the TiO_2 network's band gap energy. Also, all the deposited films have interference fringes in the visible region owing to the difference of the refractive index value between air-film and film-substrate interfaces [48].

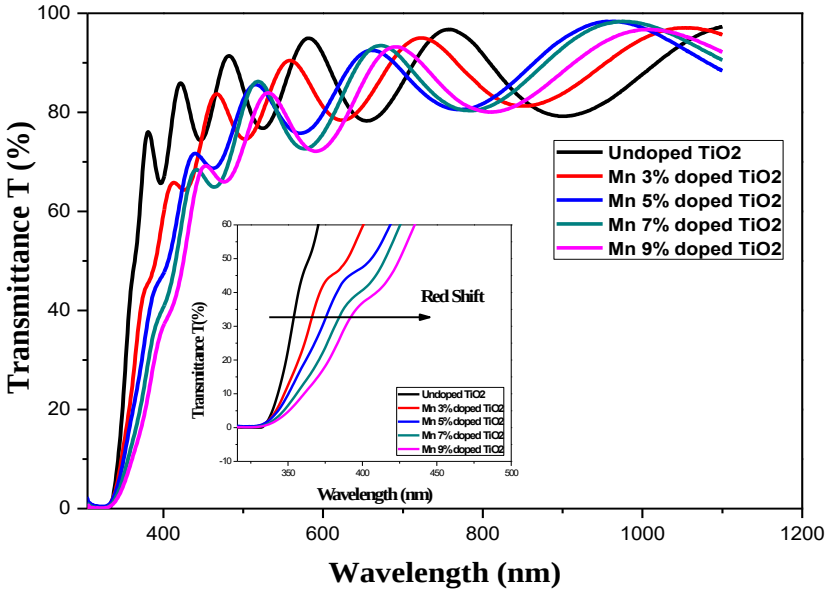

Figure V.19. Optical transmittance spectra of Mn doped TiO_2 thin films.

Tauc's plot, which represents a plot of $(\alpha h\nu)^2$ versus photon energy ($h\nu$), was used to estimated the energy band gap value of the films. The Tauc's plot for undoped and Mn doped TiO_2 samples is shown in Figure V.20. We can get the values of energy band gap of the films using to the following relation (II.20). The band gap energy for un-doped TiO_2 has been

observed 3.67 eV. Also, it has been observed that on doping the band gap energy decreases from 3.67 eV (pure TiO_2) to 3.50 eV with the increase in Mn doping percentage in TiO_2 nanoparticles. This reduction in energy gap is attributed to the network distortions produced by the introduction of impurities and to the increase in the concentration of free electrons. Furthermore, reduction in band gap can be attributed to the occupation of interstitial sites by manganese atoms in the Mn-doped TiO_2 films [49].

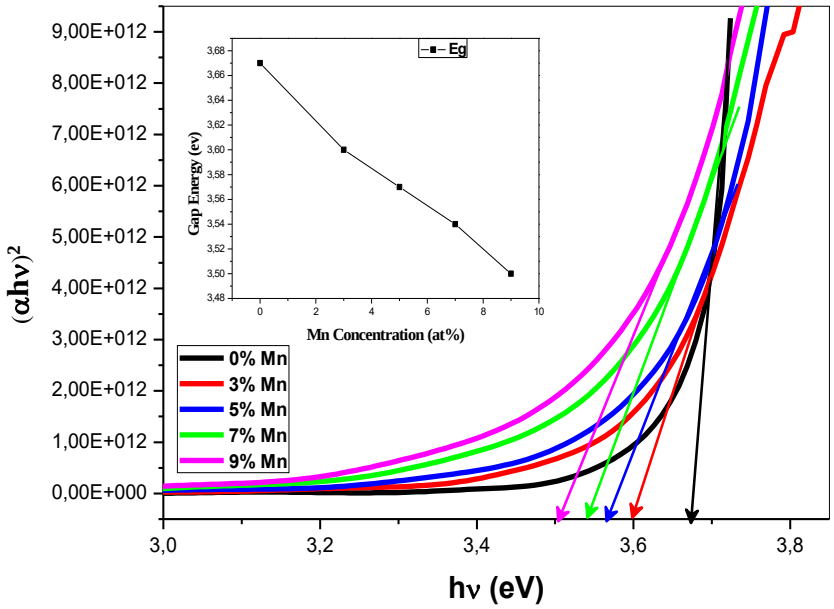

Figure V.20. The plot of $(\alpha h\nu)^2$ versus hν of pure and Mn-doped TiO_2 nanoparticles.

The presence of surface imperfections causes the absorption curve to tail, which is known as the Urbach tail, and the associated energy is known as Urbach energy (Eu). Urbach energy can be determined using the equation (II.21).

As shown in Figure V.21, which represents the plot of ln(α) versus energy of photon (hν) for pure and Mn doped TiO_2 nanoparticles and Table V.8, we have noticed an increase in Urbach energy from 0.140 eV to 0.180 eV with increase in Mn concentration from 0 to 9 at%. This is mostly owing to the presence of disordered levels in the manganese-doped films forbidden gap. These disorders may be the contributions from vacancies and interstitials and edge dislocations imperfections created in the investigating material. This is consistent with other studies [49,50].

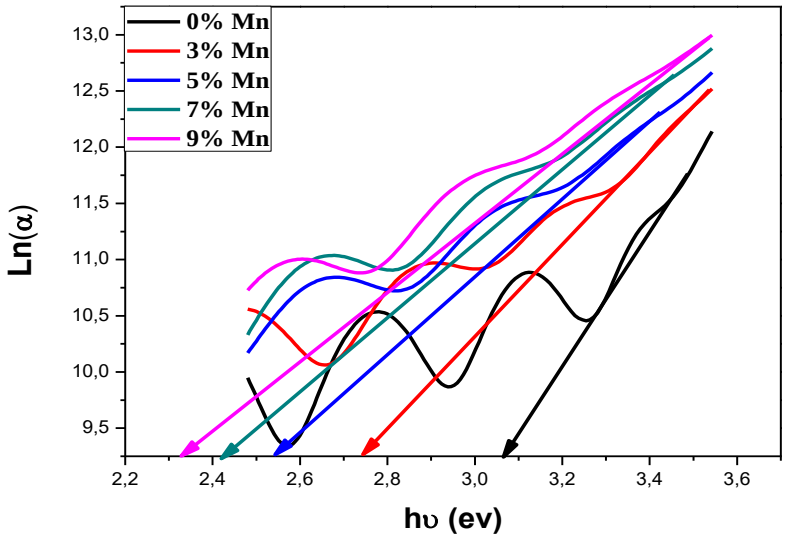

Figure V.21. Ln(α) vs hν plots of undoped and Mn-doped TiO_2 films.

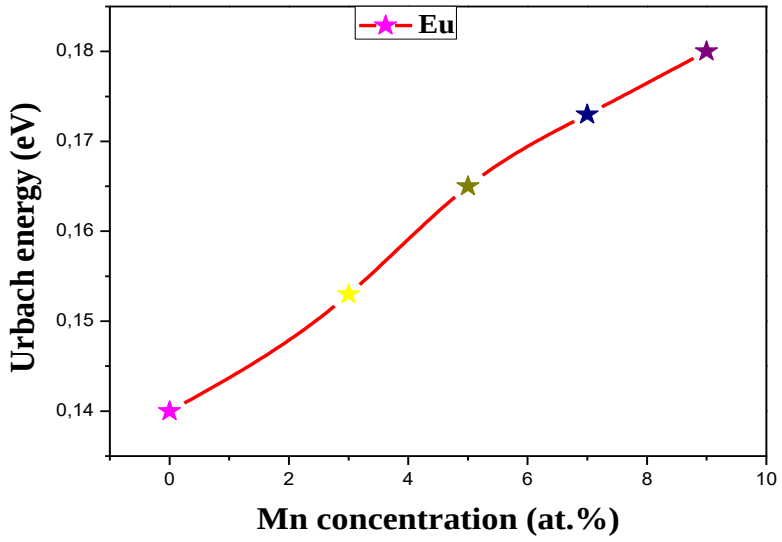

Figure V.22. Variation of Urbach energy with Mn doping concentration.

V.4.4. Electrical study

The electrical properties of the obtained TiO_2 thin films prepared at various Mn concentration (at.%). were calculated by using four point probe technique at room temperature. The value of the electrical resistivity ρ is obtained according to equation (II.27). From Figure V.23. As can be notice, We discovered that the resistivity increases from 0.66× 10^2 at 0 mol.% Mn to 3.39 × 10^2 (Ω.cm) at 5 mol.% Mn concentration. This behavior could

be owing to the electron density being compensated by holes generated by acceptors, especially substitutional Mn atoms, resulting in an increase in electrical resistivity. Increasing Mn content will result in stronger compensation and hence larger resistivity, the reason for the increase in resistivity is that some Mn atoms may form defects, which acts as a carrier traps rather than electron donors. Moreover, we found that the resistivity decrease from 2.74 x 10^2 at 7 mol.% to reach value 0.52 x 10^2 (Ω.cm) at 9 mol.% close to the resistivity value of undoped TiO_2 film. This could be linked to the deterioration of crystallinity, thereby enhancement in lattice distortion [51].

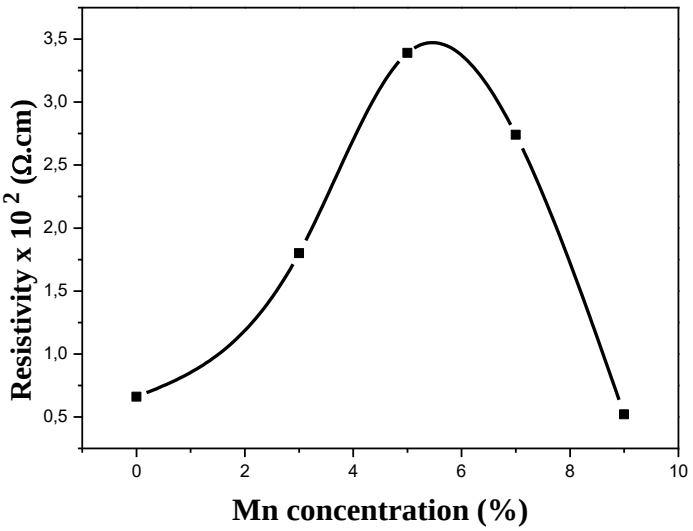

Figure V.23. Resistivity of prepared Mn doped TiO_2 thin films.

Table V.8. Optical and electrical properties for undoped and TiO_2: Mn thin films.

Mn Concentration (at%)	Thickness (nm)	Band Gap Energy (eV)	Urbach Energy (meV)	Rsheet x10^6 (Ω/sheet)	Electrical resistivity x10^2 (Ω.cm)	Electrical conductivity x10^{-3} $(Ω.cm)^{-1}$
0	787.44	3.67	0.140	0.85	0.66	15.15
3	759.55	3.60	0.153	2.37	1.80	5.55
5	734.03	3.57	0.165	4.63	3.39	2.94
7	696.01	3.54	0.173	3.95	2.74	3.64
9	692.32	3.50	0.180	0.76	0.52	19.23

Conclusion

TiO_2 nanoparticles doped with different Mn contents were synthesized through a Sol-Gel (spin coating) technique. The Mn doping TiO_2 was promoted the crystallization process of the TiO_2 particles when annealed at 500 °C. In addition, the XRD pattern of spin coated undoped and Mn doped titania films showed the presence of pure anatase phase for all samples. We have also found that the Mn doping did not affect the anatase phase. Also, the X-ray diffraction patterns of pure TiO_2 and Mn-doped TiO_2 nanoparticles are polycrystalline with preferential (101) plane of tetragonal structure. The grain size was found to decrease from 21.27 nm to 18.52 nm with increasing Mn doping. The optical measurements show a high transmittance with an average of up to 82 % for undoped TiO_2 films is observed with the presence, and it was found to decrease from 80% to 73% as we increased the Mn concentration from 3 at% to 9 at%, and show are mark able absorption band shifts towards higher wavelength (Red Shift) suggesting the reduction in the optical band gap energy from 3.67 to 3.50 eV with increasing in Mn doping concentration. Correspondigly, the urbach energy increases from 0.140 to 0.180 eV. Furthermore, the FTIR Spectroscopic Analysis of Mn doped TiO_2 films exhibit eight stretching vibration bonds is: Ti–O (at 496 cm^{-1}) ,Ti–O–Ti (at 735 cm^{-1}) , Ti–O or Mn–O (at 894 cm^{-1}), C=O (at 1438–1558 cm^{-1}) , H–O–H (at 1656 cm^{-1}) , Mn–Ti (at 2367 cm^{-1}) , C–H (at 2858 cm^{-1} and 2924 cm^{-1}) and Ti–OH (at 3362 cm^{-1}). Electrical studies show that when the Mn concentration (at.%) increases, the electrical resistivity falls, and a minimum electrical resistivity of 0.52 x 10^2 (Ω.cm) for the film coated at 9%. Finally, we can state that we generated TiO_2 thin films with excellent optical and electrical properties, and that the sol gel spin coating approach is suitable for manufacturing high-quality TiO_2 films.

Comparison of the properties of TiO_2 thin films doped with lanthanum (La) and manganese (Mn)

In this study, the influence of lanthanum and manganese doping on the characteristic structral, optical and electrical of TiO_2 thin films prepared by the sol-gel (spin-coating) process is examined. The XRD patterns reveal that undoped and doped TiO_2 nanoparticles with La and Mn concentration of 3%, 5%, 7% and 9% respectively, have a polycrystalline tetragonal structure of anatase, where as no other phases are revealed (rutile or brookite).

Due to the big difference in the radius of lanthanum and Manganese doping as compared to titanium, this clearly reduces the crystallinity of the film in the manganese-doped titanium films as well as in the lanthanum-doped titanium films, where we find that the increase in the concentration of lanthanum the anatase structure turns into an amorphous phase structure starting from La concentration of 9%. Besides, XRD measurements show that the crystallinity of the film decreases due to the increase in the dislocation density of the La, Mn doped TiO_2 thin films. Hence, the increase of the structural disorder. Also, XRD measurements reveal that all of the films for TiO_2: Mn thin films are under compressive stress. Correspondly, all of the films for TiO_2: La thin films are subject to compressive stress from 0% to 5% and tensile stress at 7%.This is mainly due to experimental conditions and the difference in radius between doping atoms and Ti. Moreover, Fourier Transform Infrared (FTIR) Spectroscopic Analysis spectra show that an additional peaks which is located at around 496 cm^{-1},735 cm^{-1} and 894 cm^{-1} in low frequency values of Mn-doped TiO_2. Also, FTIR spectra of TiO_2 show a bands at about 509 cm^{-1}, 735cm^{-1}, 904 cm^{-1} and 1055 cm^{-1} in low frequency values of La-doped TiO_2. On the other hand, ftir spectra also indicate that the intensity of the peaks decreases with increasing La doping concentration which indicated to the decreasing of the crystallization degree. Besides, a high transmittance with an average of up to 82 % by manganese doping is observed with the presence, and 91% by lanthanum doping.

As seen from optical transmittance measurements the value of the optical band gap decreases from 3.67 to 3.50 eV in pure and manganese doped TiO_2.This reduction in energy gap is attributed to the network distortions produced by the introduction of impurities and to the increase in the concentration of free electrons. Correspondly, The urbach energy increases from 0.140 eV to 0.180 eV with increase in Mn concentration from 0 to 9 at%. This is mainly

due to the presence of disordered levels in the forbidden gap for the films doped with manganese. As compared, the optical band gap values increase from 3.67 to 3.75 eV in pure and lathanum doped TiO_2, the broadening of the bandgap energy of the films could be due to the Borstein-Mohs effect and urbach's energy is decreasing from 0.140 eV to 0.126 eV, where this decrease in disorder with increasing La concentration can be interpreted as structural disorder decreases.

As seen from electrical measurements the value of the electrical conductivity decrease with increase in La concentration from 15.15 x 10^{-3} to 10.52 x 10^{-3} $(\Omega.cm)^{-1}$ at 0% to 9% .Correspondly, when the Mn doping concentration increases from 0% to 5%, the conductivity decreases and then increases with increasing Mn concentration from 5% to 9% at values 2.94 x 10^{-3} to 19.23 x 10^{-3} $(\Omega.cm)^{-1}$. According to these result, we conclude that manganese doped titanium oxide thin films are suitable for optoelectronic applications and is appropriate for producing TiO_2 films with good quality.

Finally, we can say that the XRD, FTIR, optical and electrical results are in agreement with each other but in a greater proportion in the study of manganese doped TiO_2 thin films and our results manifest that structural, optical, and electrical properties of TiO_2 film can be modified with the type of dopant atoms for producing TiO_2 films with excellent quality are suitable for photovoltaic, optoelectronic and photocatalytic applications.

Chapter V's references :

[1] B. Mehmood, et al, " Structural and optical properties of Ti and Cu co-doped ZnO thin films for photovoltaic applications of dye sensitized solar cells." Int. J. Energy Res, 4 (2020) 1–15.

[2] Hanane.Chaker, Nawel.Ameur, Karima.Saidi.Bendahou, Mustapha.Djennas, Sophie. Fourmentin,"Modeling and box-benken design optimization of photocatalytic parameters for efficient removal of dye by lanthanum-doped mesoporous TiO_2." journal of environmental chemical engineering, 9 (2021) 104584.

[3] F.B. Li, X.Z. Li, C.H. Ao, S.C. Lee, M.F. Hou, "Enhanced photocatalytic degradation of VOCs using Ln^{3+}–TiO_2 catalysts for indo or air purification." Chemosphere, 59 (2005) 787–800.

[4] Zohra.Nazir.Kayani, Sidra.Rahim, Riffat.Sagheer, Saira.Riaz, Shahzad.Naseem, "Assessment of anti bacterial and optical features of sol-gel dip coated La doped TiO_2 thin films." Materials Chemistry and Physics, 250 (2020) 123217.

[5] Fengwu Wang, Mai Xu, Lin Wei, Yijin Wei, Yunhu Hu, Wenyan Fang, Chuan Gao Zhu,"Fabrication of La-doped TiO_2 Film Electrode and investigation of its electrocatalytic activity for furfural reduction." J. Electrochemica Acta, 153(2015) 170-174.

[6] Xu, L. Feng, A. Lei, "Characterization of lanthanum trivalent ions/TiO_2 nanopowders catalysis prepared by plasma spray." J. Colloid Interface Sci, 329(2009) 395-403.

[7] Muhammad Nasir, Segomotso Bagwasi, Yanchao Jiao, Feng Chen, Baozhu Tian, Jinlong Zhang,"Characterization and activity of the Ce and N co-doped TiO_2 prepared through hydrothermal method." Chemical Engineering Journal, 236 (2014) 388–397.

[8] Joanna Reszczy'nska, Tomasz Grzyb, Janusz W. Sobczak, Wojciech Lisowski, Maria Gazda, Bunsho Ohtani, Adriana Zalesk, " Lanthanide co-doped TiO_2: The effect of metal type and amount onsurface properties and photocatalytic activity." Applied Surface Science, 307 (2014) 333–345.

[9] V. Stengl, S. Bakardjieva, N. Murafa, " Preparation and photocatalytic activity of rare earth doped TiO_2 nanoparticles." Mater. Chem. Phys, 114 (2009) 217–226.

[10] Dapeng Xu, Lajun Feng, Ali Lei, "Characterizations of lanthanum trivalent ions/ TiO_2 nanopowders catalysis prepared by plasma spray." Journal of Colloid and Interface Science, 329 (2009) 395–403.

[11] P. Semalti, S.N. Sharma,"Dye sensitized solar cells (DSSCs) electrolytes and naturaln photo-sensitizers: a review." J. Nanosci. Nanotechnol, 20 (6) (2020) 3647–3658.

[12] Chen J, Yaling Li, Wang Y, Yun J, Cao D. "Preparation and characterization of zinc sulfide nanoparticles under high-gravity environment." Mat.Res.Bull, 2004; 39(2): 185-194.

[13] R. Bomila, S. Srinivasan, S. Gunasekaran, A. Manikandan, " Enhanced photocatalytic degradation of methylene blue dye, opto-magnetic and antibacterial behaviour of pure and La-doped ZnO nanoparticles." J. Supercond. Magn, 31 (3) (2018) 855–864.

[14] Y. Zhao, C. Li, X. Liu, F. Gu, H. Giang, W. Shao, L. Zhang, Y. He, "Synthesis and optical properties of TiO_2 nanoparticles " Mater. Lett, 61 (2007) 79–83.

[15] A.N. Jose, J.T. Juan, D. Pablo, R.P. Javier, R. Diana, I.L. Marta, " Iron-doped titania powders prepared by a sol–gel method. Part II: photocatalytic properties." Appl. Catal. A Gen, 178 (1999) 191–203.

[16] W. Cui, J. He, H. Wang, J. Hu, L. Liu, Y. Liang, " Polyaniline hybridization promotes photo-electro-catalytic removal of organic contaminants over 3D network structure of rGH-PANI/TiO_2 hydrogel." Appl. Catal. B Environ, 232 (2018) 232–245.

[17] DU Jun, Buhui, HUANG Jingjing, ZHANG Wenlong, PENG Hailong, ZOU Jianguo ," Hydrophilic and photocatalytic performances of lanthanum doped titanium dioxide thin films." JOURNAL OF RARE EARTHS, Vol. 31, No. 10, Oct. 2013, P. 992.

[18] Chin-Chieh Ho, Fei Kang, Gen-Mu Chang, Sheng-Jie You, Ya-Fen Wang, "Application of recycled lanthanum-doped TiO_2 immobilized on commercial air filter for visible-light photocatalytic degradation of acetone and NO." Applied Surface Science, 465 (2019) 31–40.

[19] A. Kathiravan, R. Renganathan, " Photosensitization of colloidal TiO_2 nanoparticles with phycocyanin pigment." Journal of Colloid and Interface Science., 335 (2009) 196–202.

[20] K. Olurode, G.M. Neelgund, A. Oki, Z. Luo, "A facile hydrothermal approach for construction of carbon coating on TiO_2 nanoparticles. " Spectrochimica Acta Part A : Molecular and Biomolecular Spectroscopy., 89 (2012) 333–336.

[21] S .Chelbi, L. Hammiche, D. Djouadi, A. Chelouche, " Caracterisations structurale et optique de l'aerogel de TiO_2 elabore dans l'ethanol supercritique." Rev. Alg. Phys, Vol. 2, N° 2, 2015.

[22] E. Zanchetta, V. Auzelyte, J. Brugger, A.V. Savegnago, G. Della Giustina, G.

Brusatin, "Highly inorganic titania based sol–gel as directly patternable resist for micro and nano- structured surfaces." Microelectronic Engineering, 98 (2012) 176–179.

[23] K.P. Priyanka, V.R. Revathy, P. Rosmin, B. Thrivedu, K.M. Elsa, J. Nimmymol, K.M. Balakrishna, T. Varghese, " Influence of La doping on structural and optical properties of TiO_2 nanocrystals." Materials Characterization, 113 (2016) 144–151.

[24] Abdelmalek Kharoubi, Amar Bouaza, Bedhiaf Benrabah, Abdelkader Ammari, Hadj Benhebal, Belkacem Khiali and Cherifa Dalache,"Sol–Gel Dip Coating Method Synthesis of Mn-Doped Titanium Dioxide Thin Films." Journal of Molecular and Engineering Materials, 6 (1) (2018) 1850001 (8 pages).

[25] K.P. Priyanka, V.R. Revathy, P. Rosmin, B. Thrivedu, K.M. Elsa, J. Nimmymol, K.M. Balakrishna, T. Varghese, "Influence of La doping on structural and optical properties of TiO_2 nanocrystals." Materials Characterization, 113 (2016) 144–151.

[26] J. Choi, H. Park, M.R. Hoffmann, "Effects of single metal-ion doping on the visible-light photoreactivity of TiO_2." J. Phys. Chem, C 114 (2009) 783–792.

[27] L. Obulapathi, A.G.S. Kumar, T.S. Sarmash, D.J. Rani, G.V.V. Rao, T.S. Rao, "Effect of film thickness on physical properties of $CuCrO_2$ thin films." J. Australas. Ceram. Soc, 52 (2016) 102e105.

[28] L.Y. Chen, W.H. Chen, J.J. Wang, F.C.N. Hong, Y.K. Su, "Hydrogen-doped high conductivity ZnO films deposited by radio-frequency magnetron sputtering." Appl. Phys. Lett, 85 (2004) 5628–5630.

[29] Du-Cheng Tsai, Zue-Chin Chang, Bing-Hau Kuo, Yu-Hong Wang, Erh-Chiang Chen, Fuh-Sheng Shieu," Thickness dependence of the structural, electrical, and optical properties of amorphous indium zinc oxide thin films." Journal of Alloys and Compounds, 743 (2018) 603−609.

[30] N. Zebbar, Y. Kheireddine, K.Mokeddem, A.Hafdallah, M. Kechouane, M.S. Aida, "Structural, optical and electrical properties of n-ZnO/p-Si heterojunction prepared by ultrasonic spray**.** "Materials Science in Semiconductor Processing,14 (2011) 229–234.

[31] A.Kennedya, K.Viswanathan, K.Pradeev raj," Study of the influence of substrate temperature on structural, optical, and electrical properties of Zn-doped $MnIn_2S_4$ thin films prepared by chemical spray pyrolysis". Physics Letters A.380 (2016) 2842–2848.

[32] G. Bakiyaraj, N. Gopalakrishnan, R. Dhanasekaran, " Influence of thermal annealing on the structural, optical and electrical properties of nanostructured cadmium sulphide thin films." Chalcogenide Letters. Vol. 8, No. 7, July 2011, p. 419 – 426.

[33] Abdelhak Jrad, Wafa Naffouti, Tarek Ben Nasr, Najoua Turki-Kamoun, "Comprehensive optical studies on Ga-doped ZnS thin films synthesized by chemical bath deposition. " Journal of Luminescence., 173 (2016) 135–140.

[34] M. Islam, R.C. Roy, J. Hossain, M. Julkarnain, K.A. Khan," Electrical and optical transport characterizations of electron beam evaporated V doped In_2O_3 thin films." Mater. Res. 20 (2017) 102–108.

[35] S Asha Bhandarkar, Prathvi, Akshayakumar Kompa, M.S. Murari, Dhananjaya Kekuda, Rao K. Mohan, " Investigation of structural and optical properties of spin coated TiO_2:Mn thin films." Optical Materials, 118 (2021) 111254.

[36] Burak Ünlü, Mahmut Özacar, " Effect of Cu and Mn amounts doped to TiO_2 on the performance of DSSCs." J.Solar Energy ,196 (2020) 448-456.

[37] Biswajit Choudhury, Amarjyoti Choudhury**,** "Oxygen vacancy and dopant concentration dependent magnetic properties of Mn doped TiO_2 nanoparticle." J. Current Applied Physics ,13 (2013) 1025-1031.

[38] A. Mahmood, S.M. Ramay, Y.S. Al-Zaghayer, S. Atiq, M. Saleem, W.A. al Masary, S. Haider, "Synthesis, structural and magnetic behaviour of undoped and Mn-doped anatase TiO_2 nanoparticles." Mod. Phys. Lett, B 29 (2015) 1–7.

[39] Ruby Chauhan, Ashavani Kumar , Ram Pal Chaudhary , "Structural and photocatalytic studies of Mn doped TiO_2 nanoparticles." Spectrochimica Acta Part A: Molecular and Biomolecular Spectroscopy, 98 (2012) 256–264.

[40] A. Kharoubi, A. Bouaza, B. Benrabah, A. Ammari, H. Benhebal, B. Khiali, C. Dalache," Sol–Gel dip coating method synthesis of Mn-doped titanium dioxide thin films. " Journal of Molecular and Engineering Materials, 6 (2018) 1850001.

[41] P. Praveen, G. Viruthagiri, S. Mugundan, N. Shanmugam, " Sol–gel synthesis and characterization of pure and manganese doped TiO_2 nanoparticles – A new NLO active material." Spectrochimica Acta Part A: Molecular and Biomolecular Spectroscopy, 120 (2014) 548–557.

[42] J. Wei, L. Zhao, S. Peng, J. Shi, Z. Liu, W. Wen," Wettability of urea-doped TiO_2 nanoparticles and their high electrorheological effects." J. Sol–Gel Sci. Technol, 47 (2008) 311–315.

[43] G.S. Guo, C.N. He, Z.H. Wang, F.B. Gu, D.M. Han, " Synthesis of titania and titanate nanomaterials and their application in environmental analytical chemistry. " Talanta, 72 (2007) 1687–1692.

[44] Li-Lan Yang, Yi-Sheng Lai, and J.S. Chen, "Compositional tailored sol-gel SiO_2–TiO_2 thin films: Crystallization, chemical bonding configuration, and optical properties." J. Mater. Res, 20(11) (2005) 3141-3149.

[45] Yu Rong, Hong-Zheng Chen, Gang Wu, Mang Wang, "Preparation and characterization of titanium dioxide nanoparticle/polystyrene composites via radical polymerization. " J. Materials Chemistry and Physics, 91 (2005) 370–374.

[46] M.M. Rashad, E.M. Elsayed, M.S. Al-Kotb, A.E. Shalan, " The structural, optical, magnetic and photocatalytic properties of transition metal ions doped TiO_2 nanoparticles. " Journal of Alloys and Compounds, 581 (2013) 71–78.

[47] Yu Rong, Hong-Zheng Chen, Gang Wu, Mang Wang, "Preparation and characterization of titanium dioxide nanoparticle/polystyrene composites via radical polymerization." Materials Chemistry and Physics, 91 (2005) 370–374.

[48] Damian Wojcieszak, Michałmazur, Joanna Indyka, Aleksandra Jurkowska, Małgorzata Kalisz, Piotr Domanowski, Danuta Kaczmarek, Jarosław Domaradzki, "Mechanical and structural properties of titanium dioxide deposited by innovative magnetron sputtering process. " Materials Science-Poland, 33(3) (2015) pp 660-668.

[49] S. Ruzgar, S.A. Pehlivanoglu," The effect of Fe dopant on structural, optical properties of TiO_2 thin films and electrical performance of TiO_2 based photodiode. " Superlattice. Microst. 145 (2020) 106636.

[50] V.R. Akshay, B. Arun, G. Mandal, M. Vasundhara, "Impact of Mn-dopant concentration in observing narrowing of band-gap, Urbach tail and paramagnetism in anatase TiO_2 nanocrystals. " New J. Chem, 43 (2019) 14786–14799.

[51] P. Reunchan, X. Zhou, S. Limpijumnong, A. Janotti, C.G. Van de Walle, " Vacancy defects in indium oxide: An ab-initio study." Curr. Appl. Phys, 11 (2011) S296–S300.

Conclusion and future outlook

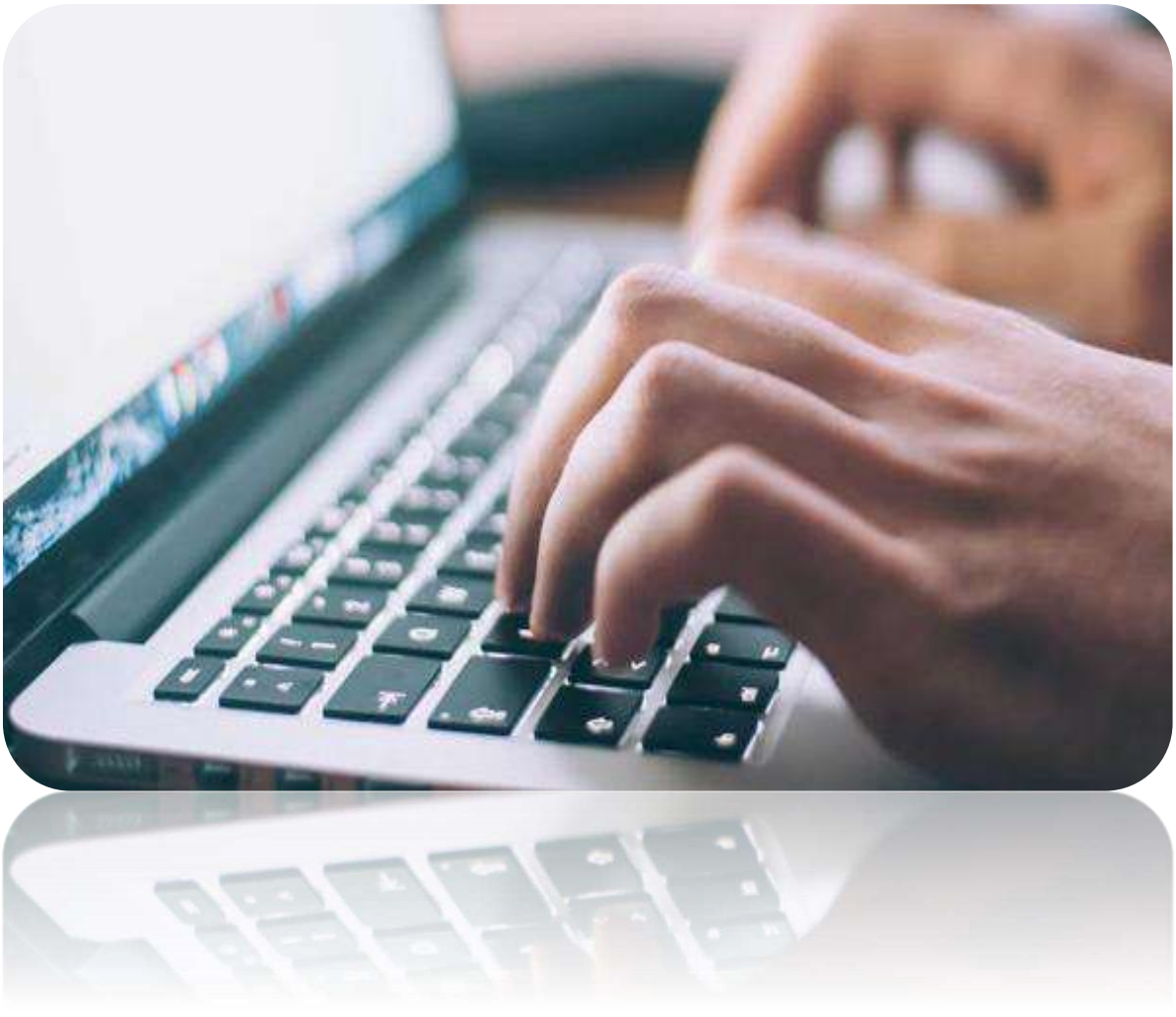

Conclusion and future outlook

In this thesis work, we have developed and characterized thin layers of pure TiO_2 and is doped with lanthanum and manganese by sol-gel (spin coating) on glass substrates at a temperature of 500°C for photovoltaic application. The choice of this method is justified by its simple, inexpensive, low energy cost, high purity and better homogeneity of the material, and Realization of multi-component deposits in a single operation and it allows to obtain deposits with controllable properties according to the conditions of development.

The analysis of the properties of these samples was carried out by different characterization methods. In this context, we carried out structural characterizations by X-ray diffraction (XRD), optical by UV-VIS spectrometry , the FT-IR spectra were obtained with a Fourier transform infrared spectrometer and finally the electrical characterization by four-point measurement .

The following conclusions are drawn based on the results obtained of the six parts of this study:

Has been investigated the Effect of the number of spin-coated layers on structural, optical and electrical properties of TiO_2 thin films which they were deposited on glass substrate via a sol-gel spin coating method. Their properties variation with number of layers were investigated. The X-ray diffraction analysis showed that the only detectable crystal structure is the anatase only with strong (101) as preferential orientation, while the films crystallite size varies from 15.31 to 18.03 nm. In addition, all TiO_2 thin films are highly transparent in the visible region and they show absorption band shifts to wards wavelength suggesting the reduction in the optical band gap energy by increasing the layers from 3.67-3.52 eV. The FTIR measurements confirmed the presence of functional groups and chemical bonding in these films. Moreover, the electrical resistivity varies with the number of layers, it rise with number of layers from 2.51×10^3 to 13.06×10^3 Ω.cm.

The effect of the mixd solvent's percentage on structural, optical and electrical properties of TiO_2 thin films has been investigated and prepared by a simple sol–gel process followed spin coating technique on microscopic glass substrates for annealed at 500 °C. we notice a increase in the thickness of TiO_2 thin films with increasing methanol solvent ratio from 477.22 to 940.78 nm. In addition, all films containe polycrystalline which is tetragonal

structure of anatase along (101) plane corresponding to TiO_2 structure. However, we notice an increase in the growth at the (101) plane for films with increasing methanol solvent ratio, that means that the crystalline state of our films will be better. Furthermore, we observe a increases in the crystallite size from 16.04 to 21.77 nm for TiO_2 nanoparticles. On the other hand , it is found that the TiO_2 films deposited at different percentages of the mixed solvent (methanol + ethanol) exhibit a high optical transparency more than 72% for all films, which gives the thin layers of TiO_2 this character. The highly transmittance of these films can be appropriated as transparent electrode of the solar cell application, In addition, we noticed that the optical band gap energy (Eg) decreases from 3.68 to 3.56 eV where the absorption band shifts towards higher wavelength. Correspondigly, Urbach energy decreases from 0.302 to 0.154 eV. The FTIR measurements confirmed the presence of functional groups and chemical bonding in these films of : Ti–O, Ti–O–Ti, C=O, CO_2 and C-H. Electrical measurements showed that methanol solvent effectively increases the electrical conductivity from 0.11 to 8.19×10^{-3} $(\Omega.cm)^{-1}$.

The drying temperature impact on the structural, optical and electrical properties of TiO2 thin films deposited on glass substrates at 500 ° C. has been discussed. The XRD results reveal that the deposited thin films have a polycrystalline having tetragonal structure of anatase, due to the minimization of free surface energy, all of the films exhibited a preferred (101) orientation. The intensity of the (101) peak grows as the drying temperature increases, showing that the crystalline quality of the deposited films improves with drying. According to UV-VIS spectra analysis, the films transmittance increased from 71% to 84% in the visible region with increasing drying temperature. Also, the crystallite size increase from 13.93 to 21.77 nm. Also, we observe that the energy band gap was increased (from 3.37 to 3.56 eV) with increasing drying temperature from 50 ℃ to 200 ℃ and then it starts to decrease to the value of 3.56 eV for 250 ℃. Correspondigly, urbach energy decreases from 0.469 to 0.154 eV. Furthermore, Fourier transform infrared transmittance spectra (FT-IR) confirmed the presence of Ti–O, Ti–O–Ti and CO_2 stretching vibration bonds. Besides, the electrical resistivity of the films decreases from 11.10 x 10^2 to 1.22 x 10^2 (Ω.cm) as drying temperature increase.

On glass substrates, titanium oxide thin films with different stirring times have been effectively deposited using the Sol - Gel (spin coating) technique. The influence of stirring time on structural, optical, and electrical properties was studied. XRD patterns revealed that prepared films have a polycrystalline having tetragonal structure of anatase along (101) plane

corresponding to TiO_2 structure. We noticed an increase in the preferential growth in the (101) plane for films , that means that the crystalline state of our films will getting better because of the increase of the stirring time. Furthermore, we observed a increases in the crystallite size with increasing the stirring time from 21.27 to 22.07 nm for TiO_2 nanoparticles. On the other hand, Films have a high optical transparency in the visible region, reaching up to 82 % at 1 hour. In addition, we observed that the optical band gap energy (Eg) decreases from 3.67 to 3.54 eV where the absorption band shifts towards higher wavelength. Correspondigly, urbach energy increases from 0.136 to 0.157 eV. Hence, the presence of Ti–O, Ti–O-Ti and CO_2 absorption bands and the stretching bonds of the organic compounds of C-H, because of the symmetric and asymmetric stretching vibration modes of CH_2 was confirmed by Fourier transform infrared transmittance spectra (FTIR). In addition, we noticed a increased in the thickness of TiO_2 thin films with increasing stirring time from 787.44 to 986.23 nm. Electrical measurements revealed that stirring time increases the electrical resistivity from 0.66 to 2.90 $\times 10^2$ $(\Omega.cm)^{-1}$.

Lanthanum doped TiO_2 thin films have been deposited on microscopic glass substrates that have been annealed at 500 °C. The influence of lanthanum (La) doping concentration on structural, optical and electrical properties of TiO_2 films was investigated. The X-ray diffraction analysis showed that the only detectable crystal structure is the one of anatase with strong (101) as preferential orientation, and there isn't any intense diffraction peaks related to the oxides of La were observed in the recorded XRD patterns. While, the values of crystallite size and strain were found to be about 21.27 to 18.41 nm and 1.62 x 10^{-3} to 1.88 x 10^{-3} , The optical measurements show a high transmittance with an average of up to 82 % for undoped TiO_2 films, and it was found to the transmittance increased from 83% to 91% with increased the La concentration from 3 at% to 9 at% .So, all TiO_2 thin films are highly transparent in the visible region and show are mark able absorption band shifts suggesting the increased in the optical band gap energy increasing with increase in La doping concentration from 3.67 eV to 3.75 eV. Correspondigly, the urbach energy decreases from 0.140 eV to 0.126 eV. On the other hand, FTIR spectra confirmed the presence of Ti–O, Ti–O–Ti, O–Ti–O, H-O-H, CO_2, C-H and –OH stretching vibration bonds. Lanthanum doping in titanium oxide thin films reduces its conductivity from 15.15 to 10.52 $\times$ 10^{-3} $(\Omega.cm)^{-1}$, according to four probe measurements.

Manganese doped TiO_2 thin films have been deposited on microscopic glass substrates a sol-gel (spin coating) technique.The XRD pattern of spin coated undoped and Mn doped

titania films showed the presence of pure anatase phase for all samples. We have also found that the Mn doping did not affect the anatase phase. Also, the X-ray diffraction patterns of pure TiO_2 and Mn-doped TiO_2 nanoparticles are polycrystalline with preferential (101) plane of tetragonal structure. The crystallite size was found to decrease from 21.27 nm to 18.52 nm with increasing Mn doping. The optical measurements show a high transmittance with an average of up to 82 % for undoped TiO_2 films is observed with the presence, and it was found to decrease from 80% to 73% as we increased the Mn concentration from 3 at% to 9 at%, and show are mark able absorption band shifts towards higher wavelength suggesting the reduction in the optical band gap energy from 3.67 to 3.50 eV with increasing in Mn doping concentration. Correspondigly, the urbach energy increases from 0.140 to 0.180 eV. Furthermore, the FTIR Spectroscopic Analysis of Mn doped TiO_2 films exhibit eight stretching vibration bonds is: Ti–O, Ti–O–Ti, Ti–O or Mn–O, C=O, H–O–H, Mn–Ti, C-H and Ti–OH. With increasing Mn concentration (at. %), the electrical resistivity decreases, and a minimum electrical resistivity of 0.52 x 10^2 Ω.cm was obtained for the film coated at 9%.

In the present research, an attempt is made to optimize transparent conducting properties of TiO_2 films using sol gel spin coating method. To achieve this goal, several process parameters like number of spin-coated layers, mixed of solvent, drying temperature, stirring time, La and Mn doping level are investigated. Among these parameters, drying temperature of TiO_2 thin films at 250 °C and preparing the TiO_2 thin films by methanol solvent and the stirring time of the solution at 1 hour are the most successful and efficient for the better electrical conductivity and optical transmittance of the films. Also, doping the TiO_2 films by manganese (Mn) give good results for the better electrical conductivity and optical transmittance of the films, These films are ideal for photovoltaic and optoelectronic applications like solar cells and gas sensors. Also, Photocatalytic application, which as a promising future fuel that protects the environment from pollutants.

Finally, These results constitute interesting performances for samples manufactured by a very simple technique. So, In the upcoming scientific research, I will carry out various applications on all the current works in order to improve their structural, optical and electrical properties more and reach perfect scientific research.

ANNEX

21-1272 Wavelength= 1.54056

TiO2

Titanium Oxide

Anatase, syn

Rad.: λ: Filter: d-sp:

Cut off: Int.: I/Icor.: 3.3

Ref: Natl. Bur. Stand. (U.S.) Monogr. 25, 7, 82 (1969)

Sys.: Tetragonal S.G.: $I4_1/amd$ (141)

a: 3.7852 b: c: 9.5139 A: C: 2.5134

α: β: γ: Z: 4 mp:

Ref: Ibid.

Dx: 3.893 Dm: SS/FOM: F_{30} = 74(.0116 , 35)

Color: Colorless

Pattern taken at 25 C. Sample obtained from National Lead Co., South Amboy, NJ, USA. Anatase and another polymorph, brookite (orthorhombic), are converted to rutile (tetragonal) by heating above 700 C. Pattern reviewed by Holzer, J., McCarthy, G., North Dakota State Univ, Fargo, ND, USA. ICDD Grant-in-Aid (1990). Agrees well with experimental and calculated patterns. O2 Ti type. PSC: tI12. Validated by calculated pattern. Mwt: 79.90. Volume[CD]: 136.31.

2θ	Int	h	k	l	2θ	Int	h	k	l
25.281	100	1	0	1	118.434	4	2	1	9
36.946	10	1	0	3	120.099	2	2	2	8
37.80	20	0	0	4	121.720	<2	4	1	3
38.575	10	1	1	2	122.331	2	4	0	4
48.049	35	2	0	0	131.029	2	4	2	0
53.890	20	1	0	5	135.991	<2	3	2	7
55.060	20	2	1	1	137.384	4	4	1	5
62.119	4	2	1	3	143.879	2	3	0	9
62.688	14	2	0	4	150.028	4	4	2	4
68.760	6	1	1	6	152.622	2	0	0	12
70.309	6	2	2	0					
74.029	<2	1	0	7					
75.029	10	2	1	5					
76.017	4	3	0	1					
80.725	<2	0	0	8					
82.136	2	3	0	3					
82.659	6	2	2	4					
83.147	4	3	1	2					
93.217	2	2	1	7					
94.178	4	3	0	5					
95.139	4	3	2	1					
98.315	2	1	0	9					
99.801	2	2	0	8					
101.218	2	3	2	3					
107.444	4	3	1	6					
108.959	4	4	0	0					
112.836	<2	3	0	7					
113.857	2	3	2	5					
114.904	2	4	1	1					

Figure.1. The ASTM sheet (No. 21-1272).